Development of Efficient and Stable Catalytic Systems for Polyolefin Plastic Waste Upcycling



Haokun Wang

Inorganic Chemistry Laboratory

Department of Chemistry

Exeter College

University of Oxford

A thesis submitted for the degree of

Doctor of Philosophy in Inorganic Chemistry

Trinity Term 2024

Table of Contents

Declaration iv

Acknowledgements v

Abstract vii

List of Abbreviations viii

List of publications xi

Journal articles xi

Patent xii

Conference xii

Chapter 1 Introduction 1

1.1 The importance of plastic products 1

1.2 The environmental, social, and economic issues of plastic waste 4

1.3 Traditional plastic waste treatment methods 9

1.4 Novel treatment methods for polyolefin plastic waste 13

1.4.1 Hydrocracking 14

1.4.2 Hydrogenolysis 19

1.4.3 Metathesis 22

1.5 Aims and objective 24

1.6 Thesis overview 26

1.7 Reference 28

Chapter 2 Experimental and Characterisation Methods 37

2.1 Catalyst synthesis 37

2.1.1 Preparation of various zeolites and amorphous silica-alumina catalysts 37

2.1.2 Preparation of γ-Al_2O_3 support 37

2.1.3 Synthesis of PtSnCe/SiAl catalysts 37

2.1.4 Synthesis of metal-loaded (Fe, Co, Ni, Cu, and Zn) ZSM-5 or ZSM-5 nanosheet catalysts 38

2.1.5 Synthesis of Ni/γ-Al_2O_3 catalyst 38

2.1.6 Synthesis NiW/ZSM-5 catalysts 38

2.1.7 Synthesis W/ZSM-5 catalyst 39
2.1.8 Synthesis lanthanum-group elements promoted PtGa/γ-Al_2O_3 catalysts 39
2.2 Characterisation methods 39
2.2.1 Structural and chemical composition analysis techniques 40
2.2.2 Surface and porosity analysis techniques 48
2.2.3 Morphological analysis techniques 52
2.2.4 Thermal and molecular weight analysis techniques 54
2.3 Catalytic tests 56
2.3.1 Catalytic procedures and product analysis 56
2.3.2 Catalytic results calculation methods 58
2.4 Process design and life-cycle assessment 60
2.4.1 Process design 60
2.4.2 Life-cycle assessment 62
2.5 Reference 64
Chapter 3 Ce-Promoted PtSn-Based Catalysts for Hydrocracking of Polyolefin Plastic Waste into High Yield of Gasoline-Range Products 67
3.1 Introduction 67
3.2 Results and discussion 69
3.2.1 Initial catalyst screening 69
3.2.2 Catalyst and solid residue characterisation 71
3.2.3 Redox properties and electronic promotion 78
3.2.4 Time-dependent reaction network and hydrocracking mechanism evaluation 82
3.2.5 Other plastic test and reusability test 86
3.3 Conclusion 89
3.4 Reference 90
Chapter 4 Efficient Hydrocracking of Plastics into High-Selectivity of Propane via Non-noble Metal-Supported ZSM-5 Nanosheet 97
4.1 Introduction 97
4.2 Results and discussion 100
4.2.1 Comparative analysis between ZSM-5 and ZSM-5 nanosheet 100

4.2.2 Metal-supported ZSM-5 nanosheet 109
4.2.3 Further evaluation of Ni/ZSM-5 nanosheet 116
4.3 Conclusion 122
4.4 Reference 122
Chapter 5 Sustainable Propane Production from Plastics with Stable W-Ni Catalysts 128
5.1 Introduction 128
5.2 Results and discussion 130
5.2.1 PP hydrocracking results 130
5.2.2 Characterisation of catalysts 138
5.2.3 Reaction mechanism study 147
5.2.4 Upcycling of other plastics and life-cycle assessment 152
5.3 Conclusion 155
5.4 Reference 156
Chapter 6 Lanthanum-Group Elements Promoted PtGa Catalysts for Propane Dehydrogenation: Exploring Key Performance Descriptors 161
6.1 Introduction 161
6.2 Results and discussion 163
6.2.1 Physicochemical properties of catalysts 163
6.2.2 Catalytic performances in propane dehydrogenation 174
6.2.3 Exploring the key catalytic performance descriptors 178
6.3 Conclusion 188
6.4 Reference 189
Chapter 7 Conclusion and Outlook 196
7.1 Conclusion 196
7.2 Further work and outlook 200
7.3 Reference 202

Declaration

I declare that the research work presented in this thesis is original and has not been submitted for any degree at any other institution. All work described, unless otherwise explicitly indicated, is my own. All external sources or materials referenced have been appropriately cited and duly acknowledged.

Haokun Wang

Acknowledgements

The past four years of my DPhil journey at Oxford have felt like a transformative expedition, and although this chapter is nearing its conclusion, the people I've met and the experiences I've had along the way have deeply influenced me. I am profoundly grateful to all those who supported me throughout this journey.

First and foremost, I extend my heartfelt thanks to my supervisor, Prof. Shik Chi Edman Tsang, for giving me the incredible opportunity to work in his group and the freedom to choose my research projects over the past four years. Under Edman's mentorship, I not only gained a deeper understanding of heterogeneous catalysis but also learned invaluable lessons in resilience, particularly during challenging times like manuscript rejections. His constant encouragement and support provided me with an exceptional platform to pursue the research I was passionate about.

My research would not have been possible without the professional assistance I received throughout my various DPhil projects. I would like to especially thank:

- Prof. Jianwei Zheng (Xiamen University) and Dr. Tatchamapan Yoskamtorn (Chulalongkorn University) for their help with catalytic tests, characterisations, and insightful project discussions;
- Dr. Shaoliang Guan (HarwellXPS) for conducting XPS measurements and Wentian Niu for assisting with XPS data analysis;
- Dr. Guangchao Li (Hong Kong Polytechnic University) for performing the ss-NMR experiments;
- Dr. Xuelei Pan for his assistance with Raman measurements at University of Surry and help with data analysis;
- Dr. Bryan Ng and Jiasi Li for conducting nitrogen adsorption-desorption isotherms at the Surface Analysis Facilities, University of Oxford;

- Dr. Tugce Ayvali, and Dr. Kwan Chee Leung for their support with NH_3-TPD and DRIFTS experiments;
- Dr. Ping-Luen Ho and Dr. Yanjie Wang for their work on TEM imaging;
- Amy Radford for obtaining SEM images;
- Prof. Volkan Degirmenic (University of Warwick) for providing access to Aspen software.

I would also like to extend my gratitude to the past and present members in Tsang group. Special thanks to Prof. Jianwei Zheng, Prof. Pu Zhao, Dr. Tugce Ayvali, and Dr. Tatchamapan Yoskamtorn for their invaluable discussions and guidance, particularly in the early stage of my research. I am also deeply thankful to Prof. Huihuang Fang, Dr. Yiyang Li, Dr. Guangchao Li, Dr. Hangjuan Ren, Dr. Yanjie Wang, and Dr. Xuelan Hou for their advice and suggestions. Additionally, I appreciate the contributions of other group members including Dr. Kwan Chee Leung, Dr. Xuelei Pan, Dr. Bryan Ng, Dr. Ping-Luen Ho, Wentian Niu, Dongpei Ye, Renzo Leeflang, Amy Radford, Jiasi Li, Sijie Huang, and Mingyu Luo, for their collaborations and scientific discussions. Special thanks to Tasha Lam (visiting student) from Hong Kong City University for her contributions to the experiments in Chapter 4.

Moreover, I own deep gratitude to my parents and family members for their unwavering support, both emotionally and financially, and for their unconditional confidence in my decisions throughout this DPhill journey. I am also grateful to my girlfriend, Yitong Xu, and her cat, Nano, whose encouragement and companionship have enriched my DPhill experience with added meaning and joy.

Lastly, I wish to acknowledge my own efforts. The consistent hard work and perseverance I have maintained over the past nine years–from my time at Beijing University of Chemical Technology, to University of Birmingham, Imperial College London, and now University of Oxford–have been critical in bringing me to this milestone. I am confident these traits will continue to drive me towards even greater accomplishments and more rewarding future destinations.

Abstract

While the widespread use of plastics has greatly benefited modern life, it has also led to significant environmental, health, social, and economic challenges due to poor waste management and low recyclability. Traditional disposal methods, such as landfilling and incineration, are energy-intensive and environmentally damaging. Recent advancements in catalytic technologies, including hydrocracking, hydrogenolysis, and metathesis, offer more sustainable approaches by converting polyolefin (PO) plastic waste into valuable products under milder conditions with lower emissions. However, more efficient and stable catalytic approaches are required to meet the demands of industrial-scale applications.

This thesis addresses these challenges by constructing two efficient and stable catalytic pathways through four complementary approaches aimed at upcycling of PO plastic waste. The first route involves introducing Ce and Sn promoters into a Pt/SiAl system to enhance the efficiency and stability of plastic-to-gasoline hydrocracking. Extensive characterisation and mechanistic studies provide a deeper understanding of improved catalytic performance.

The second route involves a two-step process to convert PO plastics into high-value products, aligning with circular economy principles. In the first step, PO plastics are converted to propane through two strategies: (1) modifying the morphology of ZSM-5 to create nanosheets, and (2) employing W-modified Ni/ZSM-5 catalysts. In the second step, propane is dehydrogenated to produce propylene using commercial $PtGa/Al_2O_3$ catalysts enhanced with four lanthanum-based promoters (La, Ce, Pr, and Nd) to improve conversion, selectivity, and stability. Detailed characterisation and mechanistic studies were undertaken to elucidate the factors contributing to catalytic performance.

By integrating these approaches, this thesis demonstrates substantial advancements in the efficiency and stability of catalytic upcycling processes for PO plastics. These findings provide promising solutions for mitigating environmental impacts and fostering the development of sustainable plastic upcycling technologies.

List of Abbreviations

BAS	Brønsted Acid Sites
BET	Brunauer-Emmett-Teller
BHT	3,5-Di-Tert-Buty-4-Hydroxytoluene
BJH	Barrett-Joyner-Halenda
BPA	Bisphenol A
CAGR	Compound Annual Growth Rate
CCP	Cubic Closest-Packed
CFRP	Carbon Fibre-Reinforced Polymer
CO-FTIR	Fourier Transform Infrared Spectroscopy using CO as a probe molecule
CP	Cross-Polarisation
DFT	Density Functional Theory
DRIFTS	Diffuse Reflectance Infrared Fourier Transform Spectroscopy
EDX	Energy-Dispersive X-ray
FCC	Fluid Catalytic Cracking
FID	Flame Ionisation Detector
FTIR	Fourier Transform Infrared Spectroscopy
FWHM	Full Width at Half Maximum
GC	Gas Chromatography
GC-MS	Gas Chromatography-Mass Spectroscopy
GDP	Gross Domestic Product
GFRP	Glass Fibre-Reinforced Polymer
GPC	Gel Permeation Chromatography
GWP	Global Warming Potential

H_2-TPR	Hydrogen-Temperature-Programmed Reduction
HDPE	High-Density Polyethylene
HRTEM	High-Resolution Transmission Electron Microscopy
IR	Infrared Spectroscopy
IUPAC	International Union of Pure and Applied Chemistry
LAS	Lewis Acid Sites
LCA	Life-Cycle Assessment
LDPE	Low-Density Polyethylene
LLDPE	Linear Low-Density Polyethylene
MAB	Metal-Acid-Balance
MAS	Magic-Angle Spinning
Mt	Million Metric Tons
MTO	Methanol-To-Olefins
NH_3-TPD	Ammonia-Temperature-Programmed Desorption
NMR	Nuclear Magnetic Resonance
PA	Polyamide
PE	Polyethylene
PET	Polyethylene Terephthalate
PO	Polyolefin
PP	Polypropylene
PR	Peng-Robinson
PS	Polystyrene
PUR	Polyurethane
PVC	Polyvinyl Chloride

Py-IR	Fourier Transform Infrared Spectroscopy using Pyridine as a probe molecule
RDS	Rate-Determining Step
RPM	Revolutions Per Minute
SBA	Santa Barbara amorphous
SC	Steam Cracking
SEM	Scanning Electron Microscopy
SiAl	Silica-Alumina
ss-NMR	Solid-State Nuclear Magnetic Resonance
STEM	Scanning Transmission Electron Microscopy
TCB	1,2,4-Trichlorobenzene
TCD	Thermal Conductivity Detector
TEM	Transmission Electron Microscopy
TG	Thermogravimetric
TOS	Time On Stream
TPD	Temperature-Programmed Desorption
TPO	Temperature-Programmed Oxidation
TPR	Temperature-Programmed Reduction
WHSV	Weight Hourly Space Velocity
XPS	X-Ray Photoelectron Spectroscopy
XRD	X-Ray Diffraction
ZSM-5 NS	ZSM-5 Nanosheets

List of publications

Journal articles

1. **Haokun Wang**, Tatchamapan Yoskamtorn, Jianwei Zheng, Ping-Luen Ho, Bryan Ng, and Shik Chi Edman Tsang*, ‘‘Ce-promoted PtSn-Based Catalyst for Hydrocracking of Polyolefin Plastic Waste into High Yield of Gasoline-Range Products,’’ ***ACS Catalysis***, 2023, 13 (24), 15886-15898.
2. **Haokun Wang***, Shik Chi Edman Tsang*, ‘‘Recent advances in polyolefin plastic waste upcycling via mild heterogeneous catalysis route from catalyst development to process design,’’ ***Cell Reports Physical Science***, 2024, 5 (7), 102075.
3. **Haokun Wang,** Xuelei Pan, Yanjie Wang, Bryan Ng, Shik Chi Edman Tsang*, ‘‘Lanthanum-group elements promoted PtGa catalysts for propane dehydrogenation: Exploring key performance descriptors,’’ ***Applied Catalysis A: General,*** *2025, 691, 120055*.
4. **Haokun Wang**[#], Sijie Huang[#], Shik Chi Edman Tsang*, ‘‘Heterogeneous catalysis strategies for polyolefin plastic upcycling: co-reactant-assisted and direct transformation under mild conditions,’’ ***Chemical Communications (ChemComm 60th Anniversary Collection),*** *2025*.
5. Pu Zhao, Lin Ye, Guangchao Li, Chen Huang, Simson Wu, Ping-Luen Ho, **Haokun Wang**, Tatchamapan Yoskamtorn, Denis Sheptyakov, Giannantonic Cibin, Augus I. Kirkland, Chiu C. Tang, Anmin Zheng, Wenjuan Xue, Donghai Mei, Kongkiat Suriye, and Shik Chi Edman Tsang*, ‘‘Rational Design of Synergistic Active Sites for Catalytic Ethene/2-Butene Cross-Metathesis in a Rhenium-Doped Y Zeolite Catalyst,’’ ***ACS Catalysis,*** 2021, 11 (6), 3530-3540.
6. **Haokun Wang**[#], Lam Ka Yin[#], Guangchao Li, Sijie Huang, Jiasi Li, Ping-Luen Ho, Amy Radford, Renzo Leeflang, Mingyu Luo, Yung-Kang Peng, and Shik Chi Edman Tsang*, ‘‘Efficient Hydrocracking of Plastics into High-Selectivity of Propane via Non-Noble Metal-supported ZSM-5 Nanosheet,’’ ***(in preparation)***.

7. **Haokun Wang**, Sijie Huang, Lam Ka Yin, Guangchao Li, Ping-Luen Ho, Jiasi Li, and Shik Chi Edman Tsang*, ‘‘Sustainable Propane Production from Plastics with Stable W-Ni Catalysts,’’ ***(in preparation)***.

Patent

1. **Haokun Wang**, Jianwei Zheng, Tatchamapan Yoskamtorn, Shik Chi Edman Tsang*, Hydrocarbon boosted thermoplastic pyrolysis into gasoline fuel, UK Patent 2200664.7 ***(under review)***.

Conference

1. **Haokun Wang**, and Shik Chi Edman Tsang*, ‘‘Ce-promoted Pt-based catalysts for hydrocracking of polyolefin plastic waste into high yield of gasoline-range products,’’ ***poster presentation at the 18th International Congress on Catalysis (18th ICC)***.

Chapter 1 Introduction

Some sections in this chapter (1.3 and 1.4) are adapted from the work by Haokun Wang, and Shik Chi Edman Tsang*, published in Cell Reports Physical Science in 2024. The tables are reproduced with permission.*[1]

1.1 The importance of plastic products

Polymers are macromolecules composed of numerous repeating units called monomers, linked by chemical bonds. They occur naturally in materials like silk, rubber, and muscle fibres but can also be synthetically produced by humans.[2,3] The development of synthetic polymers, commonly referred to plastics, began in the 1850s when English metallurgist Alexander Parkes treated cellulose with nitric acid, leading to the creation of nitrocellulose, an early semi-synthetic thermoplastic.[4,5] Subsequent advancements by American inventor John Wesley Hyatt, who developed a method to stabilise nitrocellulose, resulted in the patenting of *Celluloid* in 1870, the first commercially viable man-made polymer.[4,5]

The first fully synthetic polymer was created by Belgian-American chemist Leo Baekeland, who synthesised *Bakelite* by reacting phenol with formaldehyde, marking the invention of the first synthetic thermosetting plastic.[6] The discovery of polyvinyl chloride (PVC), an essential plastic still widely used today, occurred accidentally in 1872 by German chemist Eugen Baumann. Although the production of modern plastic began in the early 20th century, it gained significant momentum during World War II due to material shortages and the versatility of plastics.[3,7] Post-war economic expansion and the rise of consumer culture accelerated the global production of plastics. By 1950, annual global plastic production reached 2 million metric tons (Mt), a significant milestone considering that cumulative global production before 1950 was estimated between 4 and 8 Mt. This marked the beginning of large-scale plastic manufacturing.[4]

From the 1950s onward, the compound annual growth rate (CAGR) of global plastic production averaged approximately 15%, although it slowed to 8.4% for the period from the

early 1970s until 2015. Nevertheless, this growth rate was still about 1.5 times higher than the global gross domestic product (GDP) growth over the same period.[7] By 2015, an estimated 8300 Mt of plastic had been produced globally.[7] As illustrated in Figure 1.1, recent data indicate that the global plastic production reached approximately 390 Mt in 2021, underscoring society's deep reliance on plastics.[8] Projections suggest that by 2050, annual production could exceed 500 Mt, potentially accounting for 10% to 13% of the remaining carbon budget permissible for limiting global warming.[9,10] Furthermore, from an energy resource perspective, it is anticipated that plastics alone will account for around 20% of global petroleum consumption by 2050.[11]

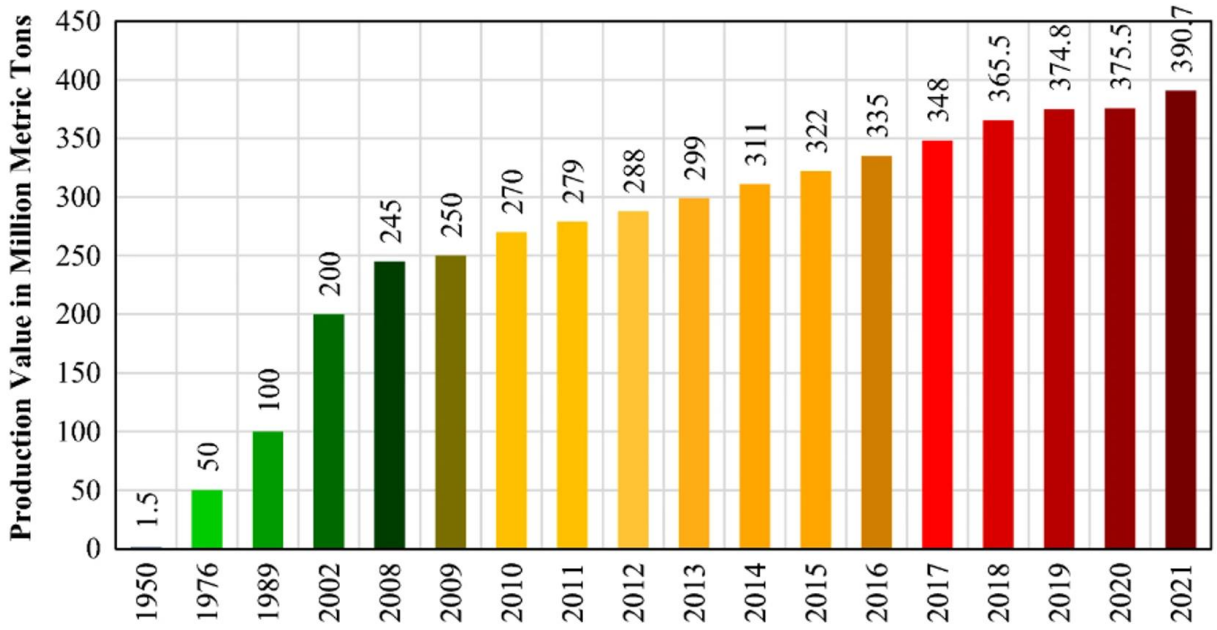

Figure 1.1 Annual worldwide production of plastics from 1950 to 2021 (in million metric tons). Reprinted with permission from reference[8].

The polynomial growth trend in global plastic production can be attributed to the extensive adoption of plastics across various sectors due to their unique characteristics, including low cost, lightweight, durability, ease of processing, and versatility in applications.[1,12,13] Plastics are widely utilised in packaging, construction, transportation, electrical and electronic devices, agriculture, furniture, household items, leisure and sports goods, and medical equipment.[14,15] This widespread use is illustrated in Figure 1.2, which shows the global primary plastics

production by sector from 1950 to 2017.[13] Packaging is by far the largest consuming sector, accounting for approximately 36% of global plastic production. The rapid increase in packaging consumption is primarily driven by the shift from reusable containers to single-use packaging. The building and construction sector follows as the second largest consumer, representing around 16% of total production by weight, with textiles coming in third at 14%.

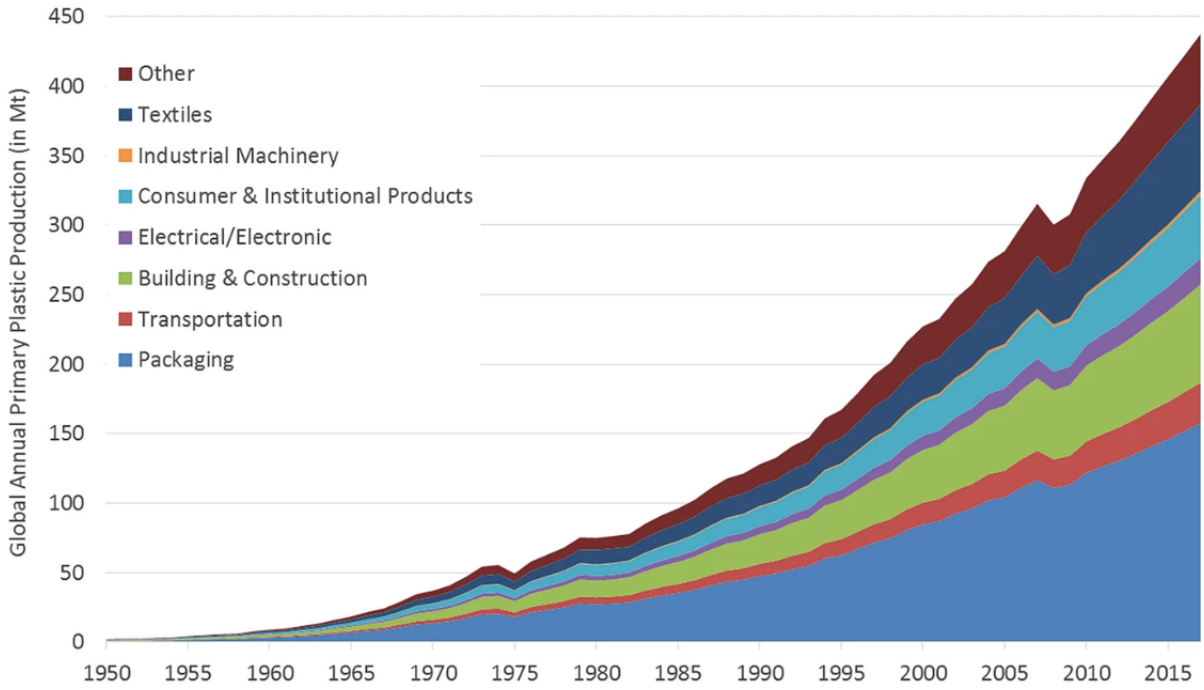

Figure 1.2 Global annual plastic production (in million metric tons) by consuming sector from 1950 to 2017. Reprinted with permission from reference[13].

While the large-scale production and usage of plastics have profoundly shaped modern life and led to a numerous application, it is important to note that plastics comprise a broad and expanding family of materials. To better understand their impact on different applications, plastics are categorised in various ways. A fundamental distinction is based on their behaviour upon heating, dividing them into thermoplastics and thermosets.[13] Thermoplastics soften when heated and harden upon cooling, and this process can be repeated, making them more amenable to recycling. This category includes some of the most widely used plastic, such as polyethylene (PE), polypropylene (PP), polystyrene (PS), PVC, polyethylene terephthalate (PET), and polyamide (PA).[3] Conversely, thermosets undergo irreversible chemical changes

when heated, forming a stable three-dimensional network that cannot be remelted or reformed, posing significant challenges for recycling. Common thermosets include polyurethanes (PUR), unsaturated polyesters, silicone, and epoxy, melamine, phenolic, and acrylic resins. Thermoplastics and thermosets can also be combined with fibres to produce composites, such as glass or carbon fibre-reinforced polymers (GFRP or CFRP).[13]

Another method of categorising the plastics is based on the source of their carbon, which can either come form from fossil fuel or biomass.[16] This classification leads to two categories: fossil-based (or petroleum-based) plastics or bio-based plastics.

The diverse technical properties of different plastics determine their suitability for specific applications. For example, high-density polyethylene (HDPE) is widely used in packaging applications, like milk bottles, toiletries, detergent, and household cleaning products. Linear low-density polyethylene (LLDPE) and low-density polyethylene (LDPE) are commonly used in bags, food packaging, and plastic films. Among all major polymers, PP has the broadest application across various sectors, although it is predominantly used in packaging. PS is often employed in packaging and insulation, such as foam products. PVC is heavily utilised in the building and construction industry, accounting for 69% of its total production, where it is used for pipes, hoses, cable insulation, and window and door frames. PET is almost exclusively used in packaging, particularly for beverage bottles, together with PE and PP, constitutes over 90% of the materials used in the packaging sector. It is increasingly being adopted for packaging clamshells and other retail items. PUR are primarily used for foam products, such as mattresses, pillows, and insulation materials. Most synthetic fibres are consumed for the textile sector, where they are used for apparel but also for many other products such as carpets, upholstery, and household textiles.[3,13,17]

1.2 The environmental, social, and economic issues of plastic waste

In the previous section, I discussed how the widespread production and use of plastic products have greatly enhanced modern life, but they have also led to significant issues, particularly in

the form of plastic waste. Plastic waste is generated during both the production process and after the plastic-containing products have reached the end of their useful life. This waste can be categorised into two types: pre-consumer (or production) waste and post-consumer (or end-of-life) waste.

Pre-consumer waste is produced during the manufacturing stages, which involve monomer production, polymerisation, part forming, product assembly, and multiple transportations steps in between. Although the production processes are complex, pre-consumer waste is generally easy to recycle. This is because it is less contaminated and more homogenous than post-consumer waste, making it simpler to reprocess into valuable secondary products. Additionally, pre-consumer waste is generated at fewer production locations, making its collection more efficient and cost-effective.

On the other hand, post-consumer waste, generated after plastic-containing products are used and discarded by consumers, presenting far more significant challenges. The large volume of this waste, coupled with inadequate management, low recyclability, complicates its processing and disposal.[3,13,18,19] As of 2015, the total plastic waste generated from primary plastics was estimated to have reached 5800 Mt.[7] Plastic waste typically follows one of the three pathways: recycling or reprocessing into secondary materials, incineration for energy recovery, or disposal in landfills and natural environment.[7,20,21]

Of the plastic waste accumulated so far, approximately 12% has been incinerated, only 9% has been recycled, and a staggering 79% remains discarded, accumulating in landfills and polluting natural ecosytems.[7,19] Alarmingly, this cumulative plastic waste is projected to exceed 25000 Mt by 2050 (Figure 1.3). If current trends persist by 2050, approximately 12000 Mt of plastic waste will have been incinerated, another 12000 Mt will be discarded, and only 9000 Mt will be recycled[7]. The rapid growth in plastic waste, poor management of plastics, and limited recyclability have led to serious environmental, health, social, and economic challenges, posing significant threats to both present and further human development.

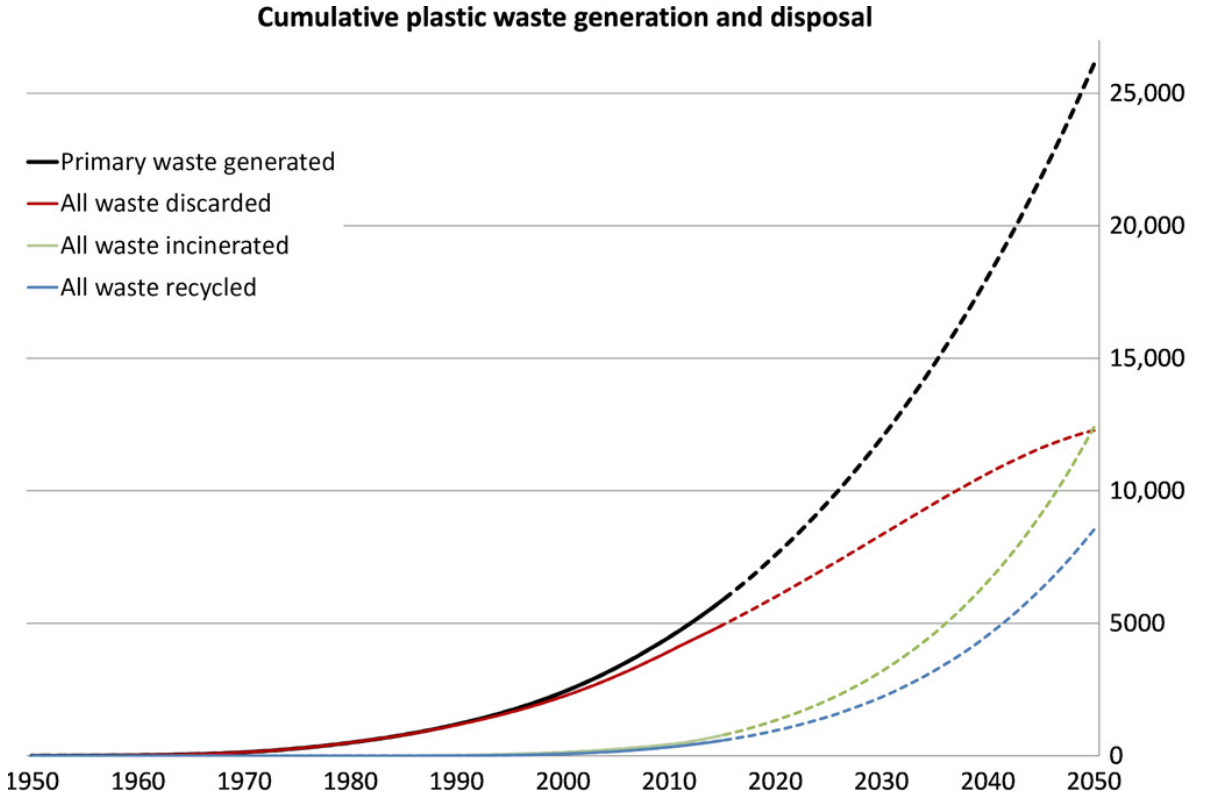

Figure 1.3 Cumulative plastic waste generation and disposal (in million metric tons). Solid lines show historical data from 1950 to 2015, while dashes lines show projections of historical trends to 2050. Reprinted with permission from reference[7].

As highlighted in the previous discussion, the majority of mismanaged plastic waste ultimately finds its way into the environment, where it persists for extended periods, often spanning centuries, due to its inherent stability, durability, and resistance to biodegradation.[22,23] This persistence results in widespread environmental impacts across terrestrial, marine, atmospheric, and human systems.[24]

On land, where plastics are predominantly produced, utilised, and discarded, a substantial portion of plastic waste accumulates within terrestrial ecosytems.[25] Over time, this waste breaks down into macroplastics and microplastics, both of which pose significant risks to biodiversity and ecological health. Macroplastics can entangle terrestrial fauna, such as birds and mammals, leading to restricted movement, injury, or even death.[26] Microplastics, on the other hand, are ingested by a wide range of organisms, including birds, insects, and large mammals like livestock, resulting in nutritional deficiencies, physical damage, and chemical

toxicity.[27] The ingestion of microplastics can also negatively impact plant health by inhibiting root and shoot growth, disrupting soil microbial communities, and alter soil properties, thereby degrading soil quality and reducing agricultural productivity.[28-31] Furthermore, as these plastic degrade, they release chemicals such as plasticisers into the soil, which can have toxic and endocrine-disrupting effects.[32,33]

Terrestrial plastic waste is transported by rivers into marine environments, exacerbating global marine plastic pollution.[34] In aquatic ecosystems, plastic pollution leads to severe consequences through entanglement and ingestion.[35] Marine species, including sea turtles and seabirds, are frequently injured or killed by becoming trapped in plastic debris. Ingested plastics can cause gastrointestinal blockages, starvation, and exposure to hazardous chemicals leading to further health complications and reproductive impairments.[35,36] Additionally, plastics can serve as artificial substrates, facilitating the spread of invasive species and disrupting natural ecosystems. This is particularly damaging to sensitive habitats like coral reefs, which suffer degradation as a result of plastic debris.[37] Moreover, plastic pollution adversely affects water quality by altering light penetration and oxygen levels, further stressing marine life.[37]

Airborne macroplastics add another layer of complexity to this issue. These particles can be transported over vast distances by wind before eventually settling back into terrestrial or aquatic environments. This cyclical exchange between land, water, and atmosphere makes microplastic pollution a persistent and widespread environmental challenge. The pervasive nature of plastic pollution across multiple ecosystems necessitates urgent and integrated strategies for mitigation and management.[24]

Plastic waste extends beyond environmental boundaries, significantly impacting human health, society, and the economy. Chemical additives, like bisphenol A (BPA), commonly found in plastic products, are known endocrine disruptor associated with severe health risks, including cardiovascular disease, kidney disorders, developmental abnormalities, and cancer.[38,39] BPA primarily enters the body through contaminated food and beverages. Similarly, plasticisers

such as phthalates, used in personal care products, toys, and food packaging, are linked to growth retardation, liver and kidney damage, depending on the specific phthalate and exposure route.[40,41] Additionally, microplastics and nanoplastics, which can be inhaled or ingested through contaminated air and food, are associated with respiratory conditions like irritation, asthma, and chronic bronchitis.[42-44] Workers in plastic manufacturing and synthetic textile industries are at high risks due to prolonged exposure to these harmful particles, leading to respiratory and other health complications. Overall, plastic waste introduces toxic substances into the environment and human body, posing significant health challenges.

Besides health issues, plastic pollution imposes direct socio-economic burdens, particularly in sectors like fisheries, tourism, and agriculture. For example, marine debris significantly hampers fish operations, leading to economic losses. In Scotland, reduced fish catches due to marine litter result in an estimated €11.7–13.0 million in annual revenue loss, representing around 5% of total income.[45] Major pollution events, such as the 2002 MV X-Press Pearl spill that released over 1700 tons of plastics into Indian Ocean, leading to widespread seafood contamination, lower consumer demand and substantial economic losses, as observed in Sri Lanka.[46] Tourism also suffers as plastic pollution diminishes the attractiveness of costal destinations, negatively affecting activities such as snorkelling and diving. The decline in tourist number translates to reduced revenue and job losses in local economies.[46] In agriculture, plastic residues alter soil physicochemical and hydrological properties, degrading soil quality and reducing crop yields. This requires additional investments in soil management and waste removal, further straining economic resources.[31,47]

Plastic waste also imposes significant financial burdens on the global economy through both direct and indirect costs. Direct costs primarily include expenditures related to waste management and environmental remediation, including the extensive efforts required for cleaning up plastic debris from affected area. Additionally, revenues losses in key sectors like fisheries and tourism are substantial. Indirect costs stem largely from public health implications associated with exposure to microplastics and toxic additives found in plastic products. These

health-related issues not only increase medical expenses but also result in reduced workforce productivity, further straining economic systems.[24]

The environmental, social, and economic impacts of plastic pollution extend across terrestrial, marine, and atmospheric ecosystems, contributing to a wide range of challenges, from biodiversity loss to deteriorating human health conditions. The interconnected nature of these issues underscores the urgent need for comprehensive and viable strategies to address plastic waste.

1.3 Traditional plastic waste treatment methods

As discussed in Sections 1.1 and 1.2, the extensive production and consumption of plastic products have greatly enhanced modern living, yet the resulting large-scale plastic waste has led to significant environmental, social, and economic issues. To mitigate these challenges, various plastic waste treatment approaches have been developed and implemented, including landfilling, incineration, mechanical recycling, and chemical recycling methods such as pyrolysis, gasification, and catalytic cracking.

Among traditional waste management practices, landfilling is one of the most commonly used methods, where plastic waste is deposited and buried beneath the soil.[48] While this approach is often seen as cost-effective, but it consumes vast areas of land and poses severe threats to soil and water quality, subsequently affecting local ecosystems and biodiversity.[49] Incineration, another widely adopted method, involves combustion plastic waste in the presence of oxygen to recover thermal energy.[50,51] Although incineration offers the advantage of high calorific output, making it valuable for energy production (e.g., electricity), it also produces harmful by-products like carbon monoxide and other pollutants that can degrade air quality and pose environment risks.[51,52] Mechanical recycling, the most widely practiced plastic recycling method, entails processes such as collection, sorting, washing and grinding plastic waste into recycled pellets.[50,53] Despite its widespread use, this approach often results in materials with diminished mechanical and rheological properties, limiting their applications in

producing high-quality products.[53,54] Additionally, mechanical recycling is constrained by challenges such as incomplete separation of mixed waste streams, limitations to specific polymer types, and the energy-intensive and labour-intensive nature of sorting and processing stages. These factors collectively hinder the operational efficiency and economic feasibility of mechanical recycling at an industrial scale.[53,55,56]

In contrast, chemical recycling is aligned with the principles of sustainable development, aiming to transform plastic waste into valuable intermediates. These intermediates can either be used to recreate the same type of plastic in a closed-loop recycling system or be reproduced into higher-value materials in an open-loop recycling process.[11] This approach is more environmentally friendly and efficient, offering higher value-added products. Current chemical recycling encompasses three primary techniques: pyrolysis, gasification and catalytic cracking.[51]

Pyrolysis, the simplest and most commonly employed chemical recycling method, involves breaking down polymers at elevated temperatures, typically above 500 °C, in the absence of oxygen. This process cleaves C-C bonds, converting plastic waste into smaller molecules.[53,57] Pyrolysis is particularly advantageous because it produces significant quantities of liquid oil products, which have broad industrial applications.[58,59] Additionally, it is versatile with respect to feedstock and generates fewer greenhouse gases and toxic emissions compared to incineration and gasification.[58,60] However, the complexity of pyrolysis reactions, especially when processing mixed feedstocks, can lead to variability in quality and purity of the resulting fuel products.[53] Gasification is a mature energy conversion technology that transforms plastic waste into high-energy gases, such as CO, H_2, CH_4 and syngas, using gasification agents like air, steam or water vapour.[61-63] The resulting syngas can be utilised in chemical synthesis, power generation, or heating applications. However, the process often produces undesirable by-products like tar and toxic gases (e.g., NO_x), which can compromise gas quality and raise environmental concerns.[64] Catalytic cracking, a technique widely adopted in the petrochemical industry for converting heavy crude oil into gasoline-range products, is also recognised as a

viable method for plastic waste recycling.[51] This approach offers high selectivity for producing fuels and commodity chemicals at relatively lower reaction temperature (approximately 400 °C) and shorter residence time compared to pyrolysis, resulting in reduced energy consumption and enhanced economic viability.[65,66] However, catalytic cracking is typically carried out in an inert atmosphere, which presents challenges such as catalyst deactivation caused by carbon deposition, contamination by toxic elements (e.g., chlorine), and pore blockage. These issues necessitate additional processing of spent catalysts and feedstock, leading to increased operational costs, heightened process complexity, and potentially compromised product quality.

The various conventional plastic waste treatment strategies–landfill, incineration, mechanical recycling, and chemical recycling (including pyrolysis, gasification, and catalytic cracking)–are summarised in Table 1.1, outlining their key processes, advantages, and disadvantages. Compared to landfill and incineration, mechanical and chemical recycling methods are more environmentally sustainable and capable of yielding higher-value products. Nonetheless, these methods require significant energy inputs; for example, mechanical recycling involves energy-intensive collection and sorting processes, while chemical recycling demands high reaction temperatures. Additionally, recycled products frequently suffer from degraded material properties and quality, limiting their broader application potential. Therefore, there is a critical need for the development of advanced techniques that are both environmentally friendly and sustainable, thereby promoting widespread adoption of plastic waste recycling initiatives globally.

Table 1.1 Summary of traditional treatment methods for plastic waste. Reproduced with permission from reference[1].

Method	Process Description	Advantages	Disadvantages
Landfill	Discarded plastic waste is buried underground.	• Cost-effective • Widely practiced	• Consuming land areas • Contaminating soil and water • Affecting ecosystems and biodiversity
Incineration	Combustion of plastic waste in the presence of oxygen to recover thermal energy.	• High calorific value • Energy generation	• Producing harmful by-products • Contribute to air pollution and environmental risks
Mechanical recycling	Involving collection, sorting, washing and grinding plastic waste into recycled pellets.	• Simple and widely practiced • Producing reusable materials	• Degraded mechanical and rheological properties of products • Energy and labour-intensive • Challenges in separating mixed waste streams
Pyrolysis	High temperature (typically > 500 °C) thermal decomposition in the absence of oxygen, breaking down plastics into smaller molecules.	• Valuable products • Feedstock versatility • Fewer greenhouse gases and toxic emissions	• Quality and purity of products variations due to complex reactions and mixed feedstock
Gasification	Converting plastic waste into high-energy gases using a gasification agent.	• Valuable products (e.g., syngas) for different applications	• Undesirable by-products (e.g., tar, NO_x) • Potential environmental concerns
Catalytic cracking	Converting plastic waste into fuels and chemicals using	• High selectivity • Lower energy consumption	• Catalyst deactivation requires additional processing, leading to

	catalysts at moderate temperatures (~400 °C).	• Economically viable	higher operating cost, process complexity

1.4 Novel treatment methods for polyolefin plastic waste

While existing plastic waste treatment methods have their own challenges, it is important to note that not all types of plastic waste are equally difficult to manage or recycle. Among various types of plastic waste, PO plastics, including LDPE, LLDPE, HDPE, and PP, stand out due to their widespread use. In 2019, these PO plastics constituted over 60% of global plastic demand and represented more than half of plastic waste due to their ubiquity and cost-effectiveness.[7,67-70] Despite their dominant presence in plastic waste streams, PO plastics have been relatively underexplored in the context of chemical recycling, particularly when compared to polymers like PET. This is largely attributed to the distinct physical and chemical characteristics of PO plastics.[71] Their high molecular weight can present challenges in chemical recycling processes, such as poor heat and mass transfer during melting and difficulty of long-chain hydrocarbon in accessing to catalytic active sites.[72] These factors necessitate energy-intensive processes to overcome the inherent kinetic and thermodynamic barriers associated with cleavage of C-C bonds in these materials.[71,73] Consequently, there is a critical need to prioritise the development of effective treatment and recycling methods specifically for PO plastic waste.

The limitations of current plastic waste management strategies, suffering from environmental drawbacks, high energy demands, and limited sustainability, have promoted the exploration of novel methods to address the pressing issue of plastic waste. Recent advancements have focused on the conversion of plastic waste, particularly PO plastics, under milder conditions, thereby offering promising new avenues for chemical recycling and garnering increased attention from researchers. These emerging methods include hydrocracking, hydrogenolysis, metathesis. Conducting these reactions presents several advantages, such as lower energy

consumption, reduced emissions of toxic and greenhouse gases, and improved selectivity for economically valuable products like naphtha, gasoline, diesel, lubricants. These innovative approaches have the potential to address the challenges of PO plastic waste management in a more environmentally friendly and sustainable manner, offering a viable path forward in the quest to mitigate plastic waste issues.

1.4.1 Hydrocracking

Hydrocracking is a catalytic process that involves the cracking of hydrocarbons in the presence of hydrogen at high pressure. While the core reaction mechanism resembles that of traditional catalytic cracking, the introduction of hydrogen alters the reaction dynamics, enhancing the activity of Brønsted acid sites (BAS) and consequently affecting the product distribution. The presence of hydrogen also serves to inhibit coke formation on the catalyst surface, thereby extending catalyst life. Hydrocracking can be classified into two main types based on the involvement of metal sites in of dehydrogenation and hydrogenation reactions: monofunctional and bifunctional hydrocracking.[1]

Monofunctional hydrocracking primarily relies on BAS for the cleavage of C-C bonds. The process begins with the protonation of the feedstock by BAS, leading to the formation of carbocation intermediates. These intermediates undergo skeletal rearrangement, followed by C-C bond scission, yielding shorter-chain carbenium ions and cleavage products. The resulting carbenium ions can then be deprotonated to form alkenes. Additionally, the carbenium ions may undergo isomerisation, leading to a variety of isomerised intermediates or products. Common solid acid catalysts, such as zeolites are frequently employed in this process, facilitating significant levels of isomerisation and generating unsaturated products.[1,66]

In bifunctional hydrocracking, the catalytic process involves the simultaneous use of both metal sites for dehydrogenation and hydrogenation, alongside BAS for cracking. As illustrated in Figure 1.4, the process starts with the dehydrogenation of feedstock on metal sites to generate alkenes. These alkenes then migrate to the BAS, where they undergo protonation, leading to the formation of carbenium intermediates. Similar to monofunctional hydrocracking,

these intermediates experience skeletal rearrangement and β-scission, producing new alkenes and additional carbenium intermediates. Subsequently, the carbenium ions are deprotonated to yield fresh alkenes, which then return to the metal sites for hydrogenation, ultimately forming the desired alkanes. Compared to monofunctional hydrocracking, bifunctional hydrocracking typically produces products with enhanced isomerisation and lower unsaturation levels. Various solid acid supports are employed in bifunctional hydrocracking, such as zeolites, WZr and WO_3. In terms of the metal sites for C-H bond activation, Pt-based catalysts are preferred. Additionally, other noble metals like Ru and Rh are used, alongside non-noble metals like Co and Ni, though the latter typically exhibiting lower reactivity for PO conversion compared to noble-metal catalysts.[1,66]

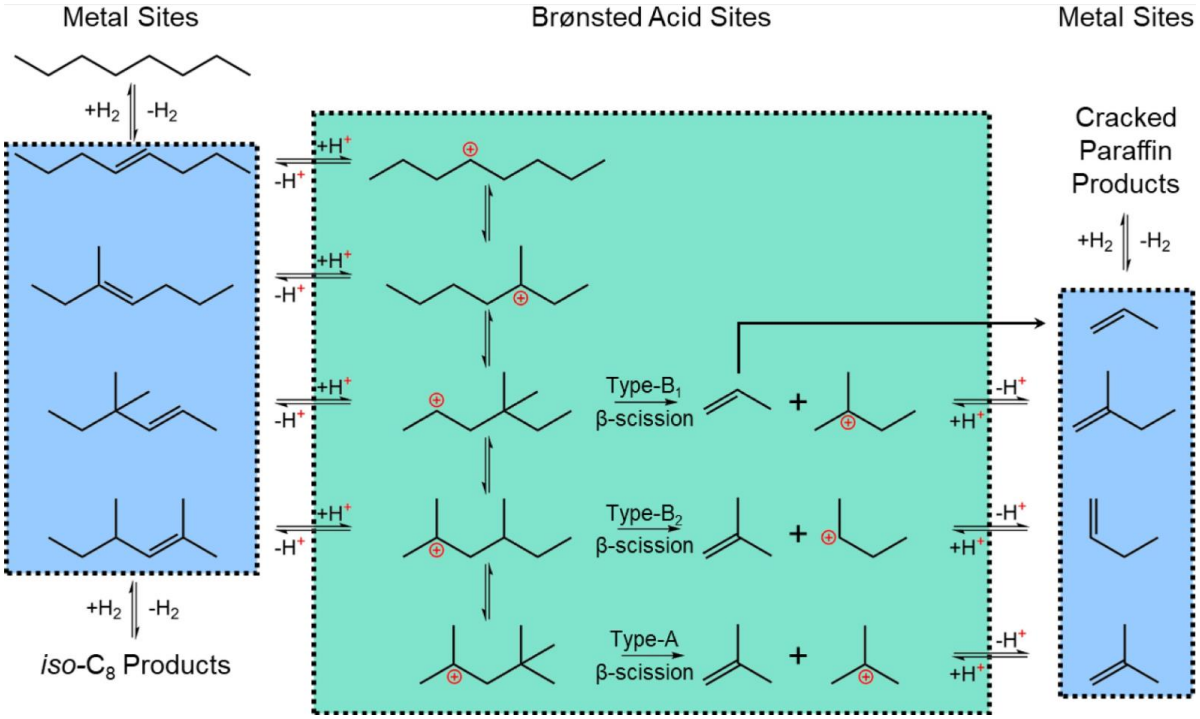

Figure 1.4 Overall reaction scheme for bifunctional hydrocracking of octane to different products. Reprinted with permission from reference[74].

Recent advancements in monofunctional hydrocracking catalysts have emphasised structural modifications aimed at reducing diffusion barriers for intermediates and improving conversion and selectivity towards desired products. For instance, Munir et al. engineered zeolite composites with enhanced mesoporosity relative to conventional BEA zeolite.[75] Their study

revealed that these micro-mesoporous composite zeolites provided improved conversion and selectivity for liquid products due to enhanced diffusion of primary cracked polymer fragments and cracked liquids through the micropores of zeolite. Similarly, Wang et al. explored ZSM-5 nanosheets (ZSM-5 NS) modified with Ce, achieving significant improvements in conversion, selectivity, and catalyst stability.[76] The nanosheet configuration, characterised by a reduced b-axis, enhanced molecular diffusion, while the introduction of Ce increased BAS density, promoting substrate adsorption, improving the formation of intermediates and product desorption.

Despite recent research into monofunctional hydrocracking, the primary focus in hydrocracking catalyst development for PO conversion remains on bifunctional systems. The inclusion of metal sites enables effective C-H bond activation, leading to higher PO conversion at lower temperatures (typically 250-300 °C) and shorter residence times (1-4 h). Research in this area is mainly directed towards two objectives: the exploration of novel catalytic systems to further enhance catalytic performances, and investigating the structure-performance relationships in PO hydrocracking, particularly evaluating whether conventional descriptors used in alkane hydrocracking, such as metal-acid-balance (MAB), metal-acid proximity remain applicable for PO feedstock.

For example, Sun et al. incorporated W species into Pt/BEA catalysts to improve the conversion of LDPE into gasoline alkanes (C_5-C_{12}).[77] The addition of W promoted the reduction and dispersion of Pt species, while introducing additional BAS, leading to a higher yield of gasoline products. Zhou et al. anchored Pt on defective two-dimensional WO_3 nanosheets for HDPE hydrocracking, demonstrating a synergistic effect that enhanced hydrogen dissociation, activated C-C cleavage, and converted intermediates into alkane products.[78] Rorrer et al. investigated Ru-based catalysts for the hydrocracking of PP, identifying a strong relationship between the number of acid sites and the yield of liquid alkanes (C_6-C_{33}), with liquid yields for 33% for non-acidic to 67% for strongly acidic Ru/FAU catalysts.[79]

Han et al. employed four distinct synthesis methods to prepare Pt/USY catalysts with varying metal-acid proximities.[80] Their findings indicate that Pt nanoparticles located exclusively on the USY surface exhibited superior activity compared to those situated within the USY crystal structure or those mixed with Pt/Al_2O_3 and USY. As shown in Figure 1.5, Pt nanoparticles inside USY pores displayed high activity and produced more cracked products for small reactants, but encountered significant diffusion limitations with larger molecules like C_{16} and C_{24}, leading to reduced conversion. The catalytic efficiency also declined as the distance between metal and acid sites increased to the micro-meter scale, impending intermediate diffusion and lowering the overall hydrocracking process efficiency. This study highlights the crucial role of metal-acid proximity in determining PO reaction pathways and efficiency.

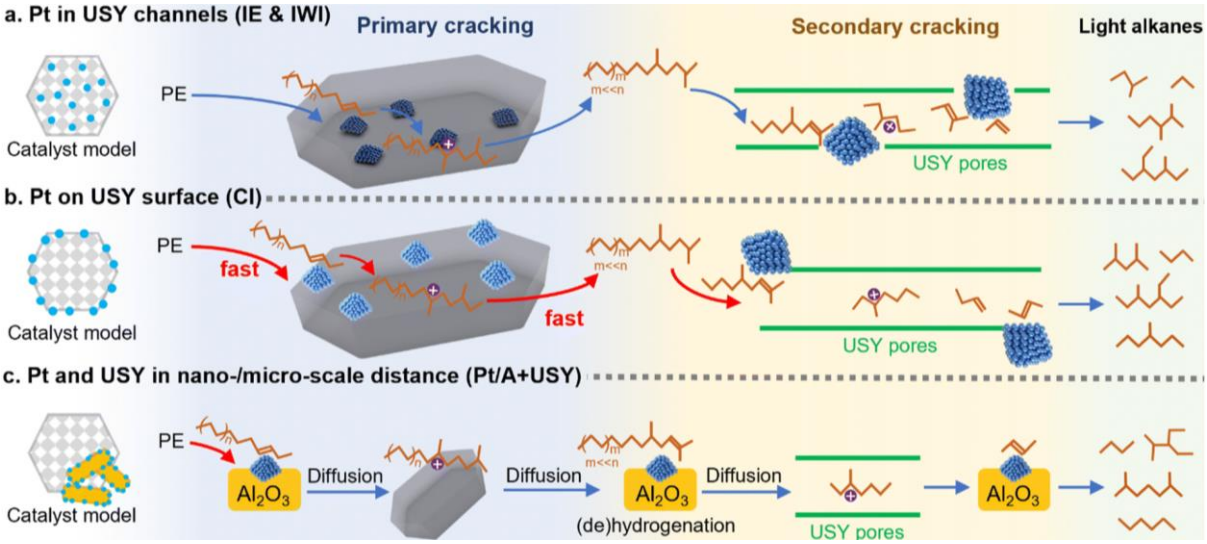

Figure 1.5 Mechanism of hydrocracking of PE on Pt/USY catalysts with different metal-acid proximity. Reprinted with permission from reference[80].

Vance et al. (2021) deviated from the conventional use of zeolite supports by investigating the WZr impregnated with Pt for LDPE hydrocracking.[74] By fine-turning the impregnation loadings of WO_3 and Pt, they successfully regulated the MAB, thereby controlling product distribution and branching degree of residues. A higher MAB ratio induced a transition from type-B β-scission to type-A β-scission (Figure 1.4), resulting in increased production of long-chain C_{9+} products and reduced yields of C_3-C_4 hydrocarbons. However, the isomerisation degree of the liquid products remained relatively constant across different MAB values, indicating that higher

molecular weight polymer chains exhibited a stronger affinity for the catalyst's active sites than lighter products. The authors proposed a new adhesive mechanism in which polymer chains are dehydrogenated at the metal sites, followed by diffusion to acid centres for isomerisation, and then back to the metal sites for hydrogenation. This process, illustrated in Figure 1.6, shows how a single polymer chain can initiate successive reaction cycles, generating branched structures and new reaction sites. This study highlights the distinct role of MAB in hydrocracking PO plastics compared to its role in light alkane hydrocracking.

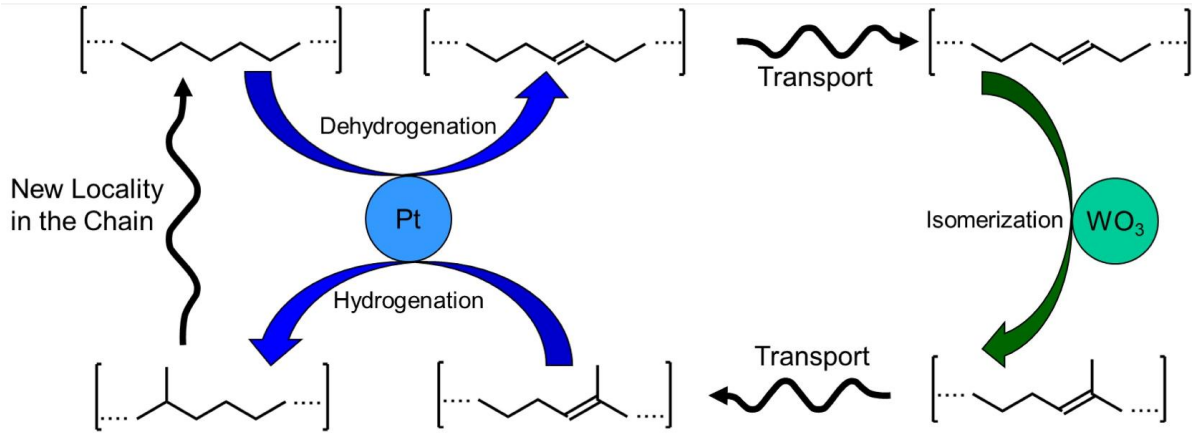

Figure 1.6 Proposed isomerisation cycle in the hydrocracking of LDPE. Reprinted with permission from reference[74].

Overall, hydrocracking represents a promising route for efficiently converting PO plastic waste into valuable products like naphtha, gasoline, diesel under relatively mild reaction conditions. Despite substantial progress in enhancing hydrocracking performances, current literature reports suboptimal results, especially regarding product selectivity. Furthermore, catalyst stability, a critical factor in catalytic performances, remains inadequately addressed in existing research. A deeper understanding of catalyst deactivation mechanisms and development of more stable hydrocracking systems are essential for advancing this approach. Additionally, the heavy reliance on noble metals for C-H bond activation poses a significant challenge to the economic viability of hydrocracking on an industrial scale. Therefore, further efforts should focus on advancing the understanding of hydrocracking mechanisms and development more efficient and cost-effective catalytic systems.

1.4.2 Hydrogenolysis

Hydrogenolysis also represents an efficient pathway for converting PO plastics into valuable products such as fuels, lubricants, and waxes, operating under high hydrogen pressure and at relatively mild temperatures (typically 200-300 °C).[1] Unlike hydrocracking–whether monofunctional hydrocracking, driven primarily by acid sites, or bifunctional hydrocracking, involving both metal and acid sites–hydrogenolysis is predominantly a metal-catalysed process. In this mechanism, alkylidyne intermediates are generated rather than carbenium ions, leading to the production of highly saturated products with minimal isomerisation. One notable feature of hydrogenolysis is the substantial formation of methane, a by-product of terminal C-C bond cleavage and the removal of methyl branches. This contrasts with hydrocracking, where methane formation is thermodynamically less favourable.[81,82]

As depicted in Figure 1.7, the hydrogenolysis process begins with the dissociative adsorption of the C-H bonds in alkanes, followed by the cleavage of C-C bonds to form two alkyl species adsorbed on the metal surface. These intermediates are then hydrogenated, and the products are subsequently desorbed.[83] The catalysts typically used in PO hydrogenolysis are primarily based on Ru supported on non-acidic materials, although other noble metals such as Pt, as well as non-noble metals like Ni and Co, have also been explored. Current research in this area is largely focused on improving the catalytic performance of PO hydrogenolysis, with particular emphasis on increasing the selectivity for liquid-range products by minimising the formation of lower-valued methane. Strategies to achieve this include manipulating geometrical and electronic properties of the metal, adjusting the basicity of the support, and the utilising confinement effects.[1,66]

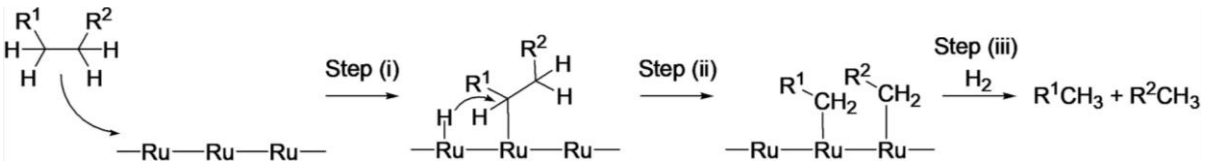

Figure 1.7 Plausible mechanism of C-C hydrogenolysis of alkanes over Ru metal. Reprinted with permission from reference[83].

Tamura et al. (2022) discovered that the conversion of LDPE hydrogenolysis follows a volcano-like trend concerning the size of Ru particles, with medium-sized Ru particles (~ 2.5 nm) achieving the highest conversion.[84] Their findings revealed the as the size of Ru particles increases up to 7 nm, the gas yield at a 30-50% conversion level progressively rises, followed by a significant spike beyond this size. This behaviour was attributed to the crucial function of Ru particle plane sites in facilitating the reaction, where the multi-point interactions between these sites and PE molecules enhance the adsorption of PE, thereby increasing catalytic activity. However, this robust adsorption can trigger continuous hydrogenolysis of the adsorbed PE's C-C bonds, leading to greater formation of gaseous product, predominantly methane. Consequently, fine-turning the size of Ru particles is essential for effectively regulating both conversion and product distribution.

In another study, Chu et al. (2024) investigated the impact of Ni incorporation into CoAl-LDH on the electronic structure of Co.[85] The introduction of Ni was found to induce electron deficiency at Co sites by redistributing electrons between Co and Ni, resulting in electron-deficient Co sites within the $NiCoAlO_x$ catalyst system. This interactions between Co and Ni not only modifies the electronic properties of the catalyst but also enhances to a synergistic interaction between the two metals. In terms of hydrogenolysis performance, the addition of Ni was observed to decrease both the overall solid conversion and extend of C−C cleavage. This reduction is likely due to the weaker C−C cleavage activity associated with Ni and the disruption of continuous Co−Co active sites by Ni atoms. Furthermore, Ni doping was found to enhance the hydrogenation capabilities of the catalyst, thereby supressing excessive hydrogenolysis of alkanes to methane (Figure 1.8), and improving the selectivity towards liquid fuel products during the hydrogenolysis process.

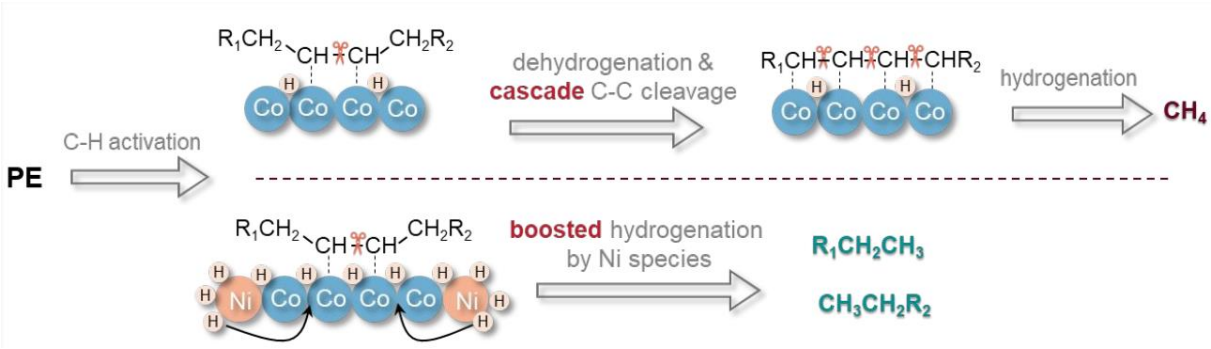

Figure 1.8 Schematic representation of methane suppression by boosted hydrogenation ability of Ni species. Reprinted with permission from reference[85].

Jaydev et al. (2023) identified a significant relationship between the scission preference in PP hydrogenolysis and the basicity of metal support.[86] Their research demonstrated that lower surface basicity correlates with a higher propensity for backbone scission, suggesting that metal oxide supports with weaker basic sites are more likely to adsorb hydrocarbon via primary carbon atoms, thereby facilitating backbone scission. In contrast, as the basicity of support increases, adsorption tends to occur through secondary and tertiary carbon atoms, which leads to more frequent demethylation and a higher yield of methane. This finding underscores the critical role of support basicity in directing reaction mechanisms and optimising catalytic performance, even in metal-driven hydrogenolysis processes.

Building on the influence of metal and support properties, Kang et al. (2023) introduced the concept of entropy confinement as a strategy to enhance catalytic performance in the upcycling of PE.[87] In contrast to conventional Ru/Santa Barbara amorphous (SBA) catalysts, where Ru nanoparticles are dispersed both within and outside the mesoporous channels, they developed p-Ru/SBA catalysts that strategically places all Ru nanoparticles uniformly within the mesoporous channels. This configuration markedly increases catalytic activity due to the stronger interaction between the SBA-15 support and alkane chains, while stabilises the adsorption of polymer chains and improves solid conversion. Furthermore, the size of mesopores within the catalyst plays a pivotal role in this process, as it significantly affects the degree of spatial confinement of polymer chains. Smaller mesopores provide enhanced

entropy confinement, resulting in higher reactivity. However, if the channels are too small, mass diffusion may be restricted, whereas larger pores could reduce the effectiveness of entropy confinement. This interplay between pore size and entropy confinement also influences product distribution, with smaller pores potentially increasing diffusion resistance, which lead to excessive cracking into methane. This innovative design effectively manages the confinement of polymer chains, reducing their entropy and thus offering a refined approach to regulate the catalytic performance.

Overall, hydrogenolysis represents a viable method for converting PO plastic waste into valuable products such as fuels, lubricants, wax under relative mild reaction conditions. However, the inherent tendency of hydrogenolysis to cleavage terminal C-C bonds and remove methyl branches often leads to substantial methane production. To enhance the efficiency of hydrogenolysis, particularly in minimising methane formation, further research is needed to optimise catalytic performance. Similar to hydrocracking, the issue of catalyst stability in hydrogenolysis has been largely overlooked in current studies, indicating a need for deeper investigation into catalyst deactivation mechanisms and the development of more robust catalytic systems. Although hydrogenolysis is primarily driven by metal catalysis, the influence of the catalyst support remains poorly understood. Further research should focus on elucidating these mechanisms and advancing the development of more selective and stable catalytic systems.

1.4.3 Metathesis

Metathesis offers another approach to convert PO plastics at relatively mild temperatures (below 300 °C) without the use of hydrogen. This process typically involves olefin intermediates derived from polymers, where C=C double bond is either directly inherent in the polymers or generated through dehydrogenation catalysis, such as by using $PtSn/Al_2O_3$. These intermediates can undergo metathesis reactions with additional olefins (either as solvent or reaction gases) to reconstruct the C-C bond, thereby producing various final products. Beyond generating liquid-range fuels, metathesis can also produce propylene by

utilising ethylene as co-reactant. Despite its potential advantages, research on metathesis remains limited, particularly within fully heterogeneous catalysis systems.[1,66]

Eills et al. (2021) developed a fully heterogeneous catalytic system combining $SnPt/Al_2O_3$ for dehydrogenation/hydrogenation and Re_2O_7/Al_2O_3 for metathesis, with n-pentane facilitating the decomposition of PE.[88] This integrated approach involves the Pt-based catalyst initially removing hydrogen from PE and light alkanes to generate unsaturated olefins. The Re-based catalyst then catalyses the metathesis of these olefins, cleaving the PE chains into shorter alkenes. These shorter alkenes are subsequently hydrogenated by the Pt-based catalyst, leading to a progressive reduction in PE chain length. The products formed during this process continue to react with excess light alkanes, ultimately converting the PE into short hydrocarbons. In a related study, Kim et al. (2023) explored alternative WO_x-based catalysts for the metathesis step.[89] Their newly developed WO_x/SiO_2 system, in conjunction with Pt-based dehydrogenation/hydrogenation catalysts, demonstrated efficient conversion of various plastics within short reaction times and at low solvent-to-LDPE mass ratios, producing products with a narrow molecular weight distribution.

Contrastingly, Wang et al. (2022) investigated both homogeneous and heterogeneous metathesis systems designed to produce propylene as the primary product by using an excess ethylene at temperature below 100 °C.[90] This process, known as ethenolysis, breaks C=C bonds in the polymer, generating propylene and other olefinic products. The process includes a rate-limiting isomerisation step to enhance the propylene selectivity (Figure 1.9). While monounsaturated PE can be selectively converted to propylene, fully saturated PE requires an additional step of single-transfer dehydrogenation. The resulting propylene can then be recycled for production of new PP, thus supporting a circular economy for PO plastics.

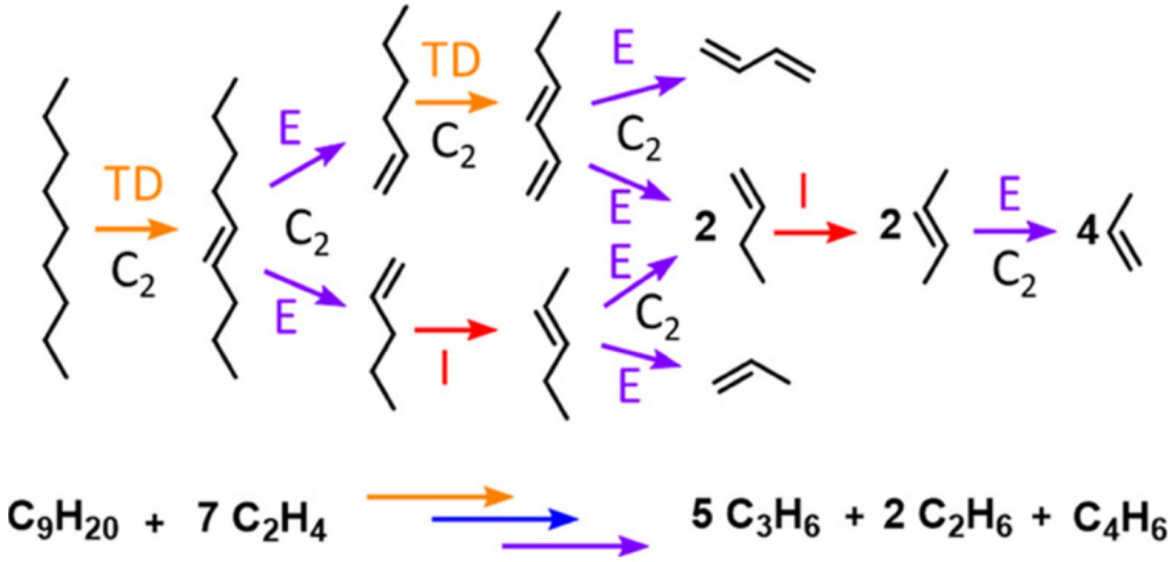

Figure 1.9 Example of the complete conversion of n-nonane into five molecules of propylene, two molecules of ethane, and one molecule of butadiene via two transfer dehydrogenation steps, two isomerisation steps, and eight ethenolysis steps. Reprinted with permission from reference[90].

Despite the promising results of metathesis for the conversion of PO plastic under mild conditions, research in this area, particularly concerning fully heterogeneous catalytic systems, remains limited. Typically, these systems involve with separate catalysts for dehydrogenation/hydrogenation and metathesis, which can lead to an underestimation of the interaction between two catalysts and its impact on overall reaction kinetics. Further studies are needed to deepen the understanding of the reaction mechanisms and to clarify the structure-performance relationships. Additionally, while metathesis has proven effective for the upcycling of PE, its application to PP is hindered by the challenge associated with cleaving tri-substituted chains, indicating a need for further research in this area.[91]

1.5 Aims and objective

The extensive production and widespread use of plastic products have significantly enhanced modern life by enabling a broad range of applications. However, the vast quantities of plastic produced, coupled with inadequate waste management practices and the inherent low recyclability of plastic waste, have led to severe environmental, health, social, and economic

challenges. Conventional plastic waste management strategies, including landfill, incineration, mechanical recycling, and chemical recycling methods such as pyrolysis, gasification, and catalytic cracking, are often associated with significant environmental drawbacks, high energy consumption, and limited sustainability. These limitations have driven the need to explore novel approaches to effectively address the growing plastic waste crisis.

Recent advances in catalytic processes, such as hydrocracking, hydrogenolysis, and metathesis, have shown promise in converting plastic waste, particularly PO plastic waste, under milder conditions. These methods offer several advantages, including lower energy requirements, reduced emissions of toxic and greenhouse gases, and improved selectivity towards economically valuable products. Despite the progress and potential benefits of these innovative strategies for PO upcycling, there remains a critical need to develop catalytic systems that are not only more cost-effective but also more efficient and stable to meet the demands of industrial-scale applications. In response to these challenges, this thesis focuses on the development of two robust and efficient catalytic routes for the conversion of PO plastic waste into valuable products via hydrocracking (Figure 1.10).

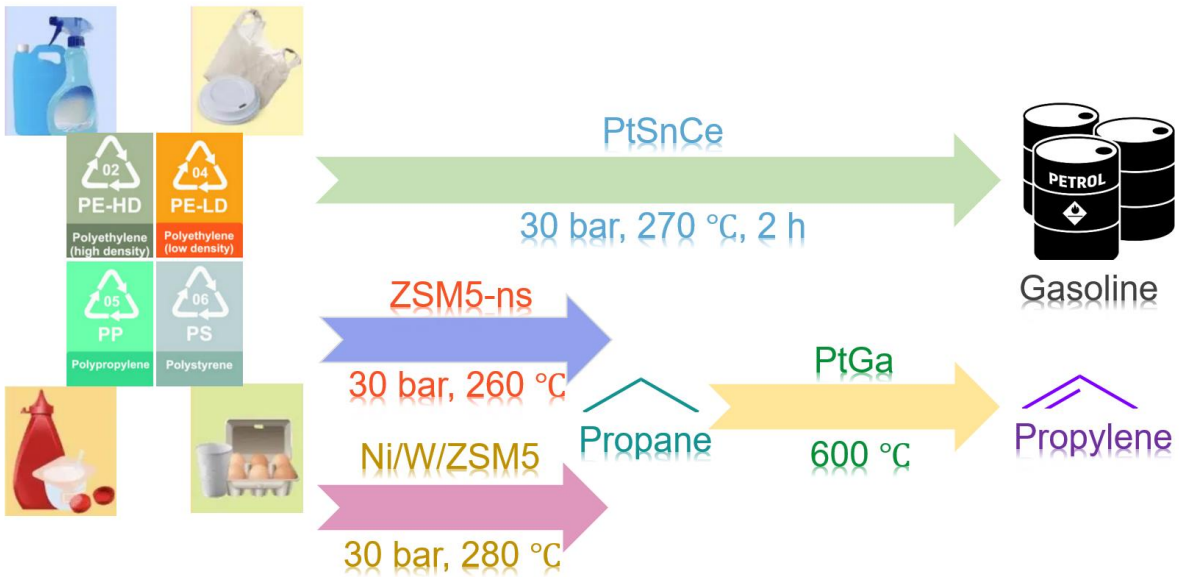

Figure 1.10 Summary of two catalytic routes developed for plastic upcycling in this thesis.

As illustrated in Figure 1.10, the first route leverages Ce-modified PtSn-based catalysts to directly convert a wide range of plastics–including HDPE, LDPE, PP, PO mixtures and commercial plastics–into high yields of gasoline-range hydrocarbons. This method highlights the effectiveness of Ce modification in enhancing catalytic performance, leading to efficient plastic-to-fuel conversion.

Building on this direct conversion route, the second pathway adopts a two-step process to enhance the versatility and efficiency of catalytic upcycling. Initially, various plastics are hydrocracked using two approaches to achieve high yields of propane. In the subsequent step, a dehydrogenation catalytic system is developed to convert this propane into propylene. By coupling plastic hydrocracking with propane dehydrogenation, this route enables the production of propylene, which can then be reused to manufacture new PP plastic. This process not only promotes the recycling of plastic into valuable monomers but also contributes significantly to the circular economy and addresses the urgent need for sustainable plastic waste management.

These two complementary routes provide innovative insights into the management of PO plastic waste, offering efficient and environmentally friendly solutions for the upcycling of plastics. The development of such approaches could play a crucial role in mitigating the environmental impact of plastic waste, advancing the field of plastic waste conversion, and paving the way for more sustainable industrial applications.

1.6 Thesis overview

This thesis is structured into seven chapters, with Chapters 3 to 6 detailing the experimental and computational research conducted during my DPhil project.

Chapter 1 provides a historical overview of plastic production and utilisation, emphasising its importance in modern society. It then addresses the environmental and human health, societal, and economic issues arising from plastic waste and evaluates the advantages and disadvantages of existing plastic waste management strategies. Additionally, this chapter

introduces novel plastic waste treatment methods reported in the literature, highlighting their advancements and identifying research gaps in each approach. Based on this background, this chapter concludes by presenting the aims and objectives of this thesis, along with an overview of its structure.

Chapter 2 focuses on the methodologies employed throughout the research, including catalysts synthesis, characterisation techniques, catalytic testing, process design and life-cycle assessment (LCA). A detailed discussion of the characterisation techniques and their underlying principles is provided, emphasising their application in this thesis.

Chapter 3 explores the development of a Ce-modified PtSn-based catalytic system designed to convert HDPE plastic into gasoline-range hydrocarbons. This chapter investigates the impact of various reaction parameters, employing comprehensive characterisation techniques and mechanistic studies to elucidate the role of Ce in enhancing catalytic performances. Furthermore, the versatility of this catalytic system is demonstrated through tests on other plastics, including LDPE, PP, plastic mixtures, and commercial plastics.

Chapter 4 reveals the efficacy of ZSM-5 NS in the hydrocracking of PP into propane. Given the superior performances of these nanosheets compared to conventional ZSM-5 zeolite, this chapter introduces different non-noble metals (Fe, Co, Ni, Cu, and Zn) into the system to further enhance catalytic activity. Detailed catalytic tests, characterisations, and mechanistic studies are discussed to explain the enhanced conversion, selectivity, and stability of these catalytic systems.

Chapter 5 examines the use of a W-modified Ni/ZSM-5 catalytic system for the conversion of PP into high yields of propane. This chapter includes extensive catalytic and recyclability tests, demonstrating the system’s superior conversion and stability. Subsequent characterisation and mechanistic analyses are conducted to identify the factors contributing to its superior performance. Additionally, this chapter describes the process scale-up and LCA evaluation, comparing its carbon emissions with those of other plastic treatment methods.

Chapter 6 investigates the enhancement of catalytic performance in commercial propane dehydrogenation catalysts ($PtGa/Al_2O_3$) through the incorporation of four lanthanide elements (La, Ce, Pr, and Nd) at various loadings. Based on catalytic performances and characterisations, this chapter utilises different descriptors to predict conversion, selectivity, and stability, constructing clear structure-performance relationship in this reaction and offering insights into the optimisation of these catalytic systems.

Finally, Chapter 7 summarises the findings presented in the previous chapters and provides novel perspectives on the future of plastic upcycling research.

1.7 Reference

1. Wang, H., and Edman Tsang, S.C. (2024). Recent advances in polyolefin plastic waste upcycling via mild heterogeneous catalysis route from catalyst development to process design. Cell Reports Physical Science *5*, 102075. 10.1016/j.xcrp.2024.102075.
2. Doi, M. (1996). Introduction to polymer physics (Oxford university press).
3. Streit-Bianchi, M., Cimadevila, M., and Trettnak, W. (2020). Mare Plasticum-The Plastic Sea (Springer).
4. Freinkel, S. (2011). A brief history of plastic's conquest of the world. Sci Am.
5. Rasmussen, S.C. (2021). From Parkesine to Celluloid: The Birth of Organic Plastics. Angewandte Chemie International Edition *60*, 8012-8016. 10.1002/anie.202015095.
6. National Historic Chemical Landmarks. Bakelite: The World's First Synthetic Plastic. http://www.acs.org/content/acs/en/education/whatischemistry/landmarks/bakelite.html.
7. Geyer, R., Jambeck, J.R., and Law, K.L. (2017). Production, use, and fate of all plastics ever made. Science Advances *3*, e1700782. 10.1126/sciadv.1700782.
8. Haque, M.K., Uddin, M., Kormoker, T., Ahmed, T., Zaman, M.R.U., Rahman, M.S., Rahman, M.A., Hossain, M.Y., Rana, M.M., and Tsang, Y.F. (2023). Occurrences, sources, fate and impacts of plastic on aquatic organisms and human health in global perspectives: What Bangladesh can do in future? Environmental Geochemistry and Health *45*, 5531-5556. 10.1007/s10653-023-01646-0.
9. Hamilton, L.A., and Feit, S. (2019). Plastic & climate: The hidden costs of a plastic planet.
10. Sardon, H., and Dove, A.P. (2018). Plastics recycling with a difference. Science *360*, 380-381. 10.1126/science.aat4997.

11. Ellis, L.D., Rorrer, N.A., Sullivan, K.P., Otto, M., McGeehan, J.E., Román-Leshkov, Y., Wierckx, N., and Beckham, G.T. (2021). Chemical and biological catalysis for plastics recycling and upcycling. Nature Catalysis *4*, 539-556. 10.1038/s41929-021-00648-4.
12. Zheng, K., Wu, Y., Hu, Z., Wang, S., Jiao, X., Zhu, J., Sun, Y., and Xie, Y. (2023). Progress and perspective for conversion of plastic wastes into valuable chemicals. Chemical Society Reviews *52*, 8-29. 10.1039/D2CS00688J.
13. Geyer, R. (2020). Chapter 2 - Production, use, and fate of synthetic polymers. In Plastic Waste and Recycling, T.M. Letcher, ed. (Academic Press), pp. 13-32. 10.1016/B978-0-12-817880-5.00002-5.
14. PlasticsEurope, E. (2019). Plastics—the facts 2019. An analysis of European plastics production, demand and waste data. PlasticEurope.
15. Council, A.C. (2013). 2013 Resin Report: The Annual Statistical Report of the North American Plastics Industry. (ACC Washington, DC, USA).
16. Bioplastics, E. (2014). What are bioplastics. Material Types, Terminology and Labels, an Introduction. European Bioplastic Fact Sheet.
17. Mackenzie, P.W. (2017). Global Fibres supply demand report 2017. PCI Wood Mackenzie, Oberursel, Germany.
18. Chen, H., Wan, K., Zhang, Y., and Wang, Y. (2021). Waste to Wealth: Chemical Recycling and Chemical Upcycling of Waste Plastics for a Great Future. ChemSusChem *14*, 4123-4136. 10.1002/cssc.202100652.
19. Wang, H., Yoskamtorn, T., Zheng, J., Ho, P.-L., Ng, B., and Tsang, S.C.E. (2023). Ce-Promoted PtSn-Based Catalyst for Hydrocracking of Polyolefin Plastic Waste into High Yield of Gasoline-Range Products. ACS Catalysis *13*, 15886-15898. 10.1021/acscatal.3c03996.
20. Mutha, N.H., Patel, M., and Premnath, V. (2006). Plastics materials flow analysis for India. Resources, Conservation and Recycling *47*, 222-244. 10.1016/j.resconrec.2005.09.003.
21. Kuczenski, B., and Geyer, R. (2010). Material flow analysis of polyethylene terephthalate in the US, 1996–2007. Resources, Conservation and Recycling *54*, 1161-1169. 10.1016/j.resconrec.2010.03.013.
22. Wang, C., Zhao, L., Lim, M.K., Chen, W.-Q., and Sutherland, J.W. (2020). Structure of the global plastic waste trade network and the impact of China's import Ban. Resources, Conservation and Recycling *153*, 104591. 10.1016/j.resconrec.2019.104591.
23. Huang, S., Wang, H., Ahmad, W., Ahmad, A., Ivanovich Vatin, N., Mohamed, A.M., Deifalla, A.F., and Mehmood, I. (2022). Plastic Waste Management Strategies and Their Environmental Aspects: A Scientometric Analysis and Comprehensive Review.

International Journal of Environmental Research and Public Health *19*, 4556. 10.3390/ijerph19084556.

24. Nayanathara Thathsarani Pilapitiya, P.G.C., and Ratnayake, A.S. (2024). The world of plastic waste: A review. Cleaner Materials *11*, 100220. 10.1016/j.clema.2024.100220.
25. Hurley, R., Horton, A., Lusher, A., and Nizzetto, L. (2020). Chapter 7 - Plastic waste in the terrestrial environment. In Plastic Waste and Recycling, T.M. Letcher, ed. (Academic Press), pp. 163-193. 10.1016/B978-0-12-817880-5.00007-4.
26. Townsend, A.K., and Barker, C.M. (2014). Plastic and the Nest Entanglement of Urban and Agricultural Crows. PLOS ONE *9*, e88006. 10.1371/journal.pone.0088006.
27. Provencher, J.F., Bond, A.L., Avery-Gomm, S., Borrelle, S.B., Bravo Rebolledo, E.L., Hammer, S., Kühn, S., Lavers, J.L., Mallory, M.L., Trevail, A., and van Franeker, J.A. (2017). Quantifying ingested debris in marine megafauna: a review and recommendations for standardization. Analytical Methods *9*, 1454-1469. 10.1039/C6AY02419J.
28. Rillig, M.C., Lehmann, A., de Souza Machado, A.A., and Yang, G. (2019). Microplastic effects on plants. New Phytologist *223*, 1066-1070. 10.1111/nph.15794.
29. van Weert, S., Redondo-Hasselerharm, P.E., Diepens, N.J., and Koelmans, A.A. (2019). Effects of nanoplastics and microplastics on the growth of sediment-rooted macrophytes. Science of The Total Environment *654*, 1040-1047. 10.1016/j.scitotenv.2018.11.183.
30. Awet, T.T., Kohl, Y., Meier, F., Straskraba, S., Grün, A.L., Ruf, T., Jost, C., Drexel, R., Tunc, E., and Emmerling, C. (2018). Effects of polystyrene nanoparticles on the microbiota and functional diversity of enzymes in soil. Environmental Sciences Europe *30*, 11. 10.1186/s12302-018-0140-6.
31. Wan, Y., Wu, C., Xue, Q., and Hui, X. (2019). Effects of plastic contamination on water evaporation and desiccation cracking in soil. Science of The Total Environment *654*, 576-582. 10.1016/j.scitotenv.2018.11.123.
32. Lithner, D., Damberg, J., Dave, G., and Larsson, Å. (2009). Leachates from plastic consumer products – Screening for toxicity with Daphnia magna. Chemosphere *74*, 1195-1200. 10.1016/j.chemosphere.2008.11.022.
33. Lithner, D., Nordensvan, I., and Dave, G. (2012). Comparative acute toxicity of leachates from plastic products made of polypropylene, polyethylene, PVC, acrylonitrile–butadiene–styrene, and epoxy to Daphnia magna. Environmental Science and Pollution Research *19*, 1763-1772. 10.1007/s11356-011-0663-5.
34. Jambeck, J.R., Geyer, R., Wilcox, C., Siegler, T.R., Perryman, M., Andrady, A., Narayan, R., and Law, K.L. (2015). Plastic waste inputs from land into the ocean. Science *347*, 768-771. doi:10.1126/science.1260352.

35. Gall, S.C., and Thompson, R.C. (2015). The impact of debris on marine life. Marine Pollution Bulletin *92*, 170-179. 10.1016/j.marpolbul.2014.12.041.

36. Lithner, D., Larsson, Å., and Dave, G. (2011). Environmental and health hazard ranking and assessment of plastic polymers based on chemical composition. Science of The Total Environment *409*, 3309-3324. 10.1016/j.scitotenv.2011.04.038.

37. Thushari, G.G.N., and Senevirathna, J.D.M. (2020). Plastic pollution in the marine environment. Heliyon *6*, e04709. 10.1016/j.heliyon.2020.e04709.

38. Rezg, R., El-Fazaa, S., Gharbi, N., and Mornagui, B. (2014). Bisphenol A and human chronic diseases: Current evidences, possible mechanisms, and future perspectives. Environment International *64*, 83-90. 10.1016/j.envint.2013.12.007.

39. Campanale, C., Massarelli, C., Savino, I., Locaputo, V., and Uricchio, V.F. (2020). A Detailed Review Study on Potential Effects of Microplastics and Additives of Concern on Human Health. International Journal of Environmental Research and Public Health *17*, 1212. 10.3390/ijerph17041212.

40. Wang, Y., and Qian, H. (2021). Phthalates and Their Impacts on Human Health. Healthcare *9*, 603. 10.3390/healthcare9050603.

41. Hauser, R., and Calafat, A.M. (2005). PHTHALATES AND HUMAN HEALTH. Occupational and Environmental Medicine *62*, 806-818. 10.1136/oem.2004.017590.

42. Enyoh, C.E., Verla, A.W., Verla, E.N., Ibe, F.C., and Amaobi, C.E. (2019). Airborne microplastics: a review study on method for analysis, occurrence, movement and risks. Environmental Monitoring and Assessment *191*, 668. 10.1007/s10661-019-7842-0.

43. Li, P., Wang, X., Su, M., Zou, X., Duan, L., and Zhang, H. (2021). Characteristics of Plastic Pollution in the Environment: A Review. Bulletin of Environmental Contamination and Toxicology *107*, 577-584. 10.1007/s00128-020-02820-1.

44. Wang, Y., Huang, J., Zhu, F., and Zhou, S. (2021). Airborne Microplastics: A Review on the Occurrence, Migration and Risks to Humans. Bulletin of Environmental Contamination and Toxicology *107*, 657-664. 10.1007/s00128-021-03180-0.

45. Arabi, S., and Nahman, A. (2020). Impacts of marine plastic on ecosystem services and economy: State of South African research. South African Journal of Science *116*, 1-7. 10.17159/sajs.2020/7695

46. Ratnayake, A.S. (2023). Marine pollution after the MV X-Press Pearl maritime disaster: Societal impacts based on research outcomes. Societal Impacts *1*, 100003. 10.1016/j.socimp.2023.100003.

47. Qi, Y., Beriot, N., Gort, G., Huerta Lwanga, E., Gooren, H., Yang, X., and Geissen, V. (2020). Impact of plastic mulch film debris on soil physicochemical and hydrological properties. Environmental Pollution *266*, 115097. 10.1016/j.envpol.2020.115097.

48. Evode, N., Qamar, S.A., Bilal, M., Barceló, D., and Iqbal, H.M.N. (2021). Plastic waste and its management strategies for environmental sustainability. Case Studies in Chemical and Environmental Engineering *4*, 100142. 10.1016/j.cscee.2021.100142.
49. Steensgaard, I.M., Syberg, K., Rist, S., Hartmann, N.B., Boldrin, A., and Hansen, S.F. (2017). From macro-to microplastics-Analysis of EU regulation along the life cycle of plastic bags. Environmental Pollution *224*, 289-299. 10.1016/j.envpol.2017.02.007.
50. Davidson, M.G., Furlong, R.A., and McManus, M.C. (2021). Developments in the life cycle assessment of chemical recycling of plastic waste – A review. Journal of Cleaner Production *293*, 126163. 10.1016/j.jclepro.2021.126163.
51. Pan, D., Su, F., Liu, C., and Guo, Z. (2020). Research progress for plastic waste management and manufacture of value-added products. Advanced Composites and Hybrid Materials *3*, 443-461. 10.1007/s42114-020-00190-0.
52. Ni, H.-G., Lu, S.-Y., Mo, T., and Zeng, H. (2016). Brominated flame retardant emissions from the open burning of five plastic wastes and implications for environmental exposure in China. Environmental Pollution *214*, 70-76. 10.1016/j.envpol.2016.03.049.
53. Ragaert, K., Delva, L., and Van Geem, K. (2017). Mechanical and chemical recycling of solid plastic waste. Waste Management *69*, 24-58. 10.1016/j.wasman.2017.07.044.
54. Al-Salem, S.M., Behbehani, M.H., Al-Hazza'a, A., Arnold, J.C., Alston, S.M., Al-Rowaih, A.A., Asiri, F., Al-Rowaih, S.F., and Karam, H. (2019). Study of the degradation profile for virgin linear low-density polyethylene (LLDPE) and polyolefin (PO) plastic waste blends. Journal of Material Cycles and Waste Management *21*, 1106-1122. 10.1007/s10163-019-00868-8.
55. Hopewell, J., Dvorak, R., and Kosior, E. (2009). Plastics recycling: challenges and opportunities. Philosophical Transactions of the Royal Society B: Biological Sciences *364*, 2115-2126. 10.1098/rstb.2008.0311.
56. Bioplastics, E. (2010). Mechanical recycling fact sheet.
57. Angyal, A., Miskolczi, N., and Bartha, L. (2007). Petrochemical feedstock by thermal cracking of plastic waste. Journal of Analytical and Applied Pyrolysis *79*, 409-414. 10.1016/j.jaap.2006.12.031.
58. Jiang, J., Shi, K., Zhang, X., Yu, K., Zhang, H., He, J., Ju, Y., and Liu, J. (2022). From plastic waste to wealth using chemical recycling: A review. Journal of Environmental Chemical Engineering *10*, 106867. 10.1016/j.jece.2021.106867.
59. Anuar Sharuddin, S.D., Abnisa, F., Wan Daud, W.M.A., and Aroua, M.K. (2016). A review on pyrolysis of plastic wastes. Energy Conversion and Management *115*, 308-326. 10.1016/j.enconman.2016.02.037.
60. Dai, L., Zhou, N., Lv, Y., Cheng, Y., Wang, Y., Liu, Y., Cobb, K., Chen, P., Lei, H., and Ruan, R. (2022). Pyrolysis technology for plastic waste recycling: A state-of-the-art

review. Progress in Energy and Combustion Science *93*, 101021. 10.1016/j.pecs.2022.101021.

61. Kannan, P., Al Shoaibi, A., and Srinivasakannan, C. (2013). Energy recovery from co-gasification of waste polyethylene and polyethylene terephthalate blends. Computers & Fluids *88*, 38-42. 10.1016/j.compfluid.2013.09.004.
62. Acomb, J.C., Wu, C., and Williams, P.T. (2014). Control of steam input to the pyrolysis-gasification of waste plastics for improved production of hydrogen or carbon nanotubes. Applied Catalysis B: Environmental *147*, 571-584. 10.1016/j.apcatb.2013.09.018.
63. Janajreh, I., Adeyemi, I., and Elagroudy, S. (2020). Gasification feasibility of polyethylene, polypropylene, polystyrene waste and their mixture: Experimental studies and modeling. Sustainable Energy Technologies and Assessments *39*, 100684. 10.1016/j.seta.2020.100684.
64. Arena, U., and Di Gregorio, F. (2014). Energy generation by air gasification of two industrial plastic wastes in a pilot scale fluidized bed reactor. Energy *68*, 735-743. 10.1016/j.energy.2014.01.084.
65. Cardona, S.C., and Corma, A. (2000). Tertiary recycling of polypropylene by catalytic cracking in a semibatch stirred reactor: Use of spent equilibrium FCC commercial catalyst. Applied Catalysis B: Environmental *25*, 151-162. 10.1016/S0926-3373(99)00127-7.
66. Sun, J., Dong, J., Gao, L., Zhao, Y.-Q., Moon, H., and Scott, S.L. (2024). Catalytic Upcycling of Polyolefins. Chemical Reviews. 10.1021/acs.chemrev.3c00943.
67. Celik, G., Kennedy, R.M., Hackler, R.A., Ferrandon, M., Tennakoon, A., Patnaik, S., LaPointe, A.M., Ammal, S.C., Heyden, A., Perras, F.A., et al. (2019). Upcycling Single-Use Polyethylene into High-Quality Liquid Products. ACS Central Science *5*, 1795-1803. 10.1021/acscentsci.9b00722.
68. Chitalia, A. (2020). Why Polyolefins Are the Polymers to Watch. Wood Mackenzie.
69. Britt, P.F., Coates, G.W., Winey, K.I., Byers, J., Chen, E., Coughlin, B., Ellison, C., Garcia, J., Goldman, A., Guzman, J., et al. (2019). Report of the Basic Energy Sciences Roundtable on Chemical Upcycling of Polymers. United States. https://www.osti.gov/biblio/1616517.
70. Rorrer, J.E., Beckham, G.T., and Román-Leshkov, Y. (2021). Conversion of Polyolefin Waste to Liquid Alkanes with Ru-Based Catalysts under Mild Conditions. JACS Au *1*, 8-12. 10.1021/jacsau.0c00041.
71. Vollmer, I., Jenks, M.J.F., Roelands, M.C.P., White, R.J., van Harmelen, T., de Wild, P., van der Laan, G.P., Meirer, F., Keurentjes, J.T.F., and Weckhuysen, B.M. (2020). Beyond Mechanical Recycling: Giving New Life to Plastic Waste. Angewandte Chemie International Edition *59*, 15402-15423. 10.1002/anie.201915651.

72. Bin Jumah, A., Anbumuthu, V., Tedstone, A.A., and Garforth, A.A. (2019). Catalyzing the Hydrocracking of Low Density Polyethylene. Industrial & Engineering Chemistry Research *58*, 20601-20609. 10.1021/acs.iecr.9b04263.

73. Mark, L.O., Cendejas, M.C., and Hermans, I. (2020). The Use of Heterogeneous Catalysis in the Chemical Valorization of Plastic Waste. ChemSusChem *13*, 5808-5836. 10.1002/cssc.202001905.

74. Vance, B.C., Kots, P.A., Wang, C., Hinton, Z.R., Quinn, C.M., Epps, T.H., Korley, L.T.J., and Vlachos, D.G. (2021). Single pot catalyst strategy to branched products via adhesive isomerization and hydrocracking of polyethylene over platinum tungstated zirconia. Applied Catalysis B: Environmental *299*, 120483. 10.1016/j.apcatb.2021.120483.

75. Munir, D., Amer, H., Aslam, R., Bououdina, M., and Usman, M.R. (2020). Composite zeolite beta catalysts for catalytic hydrocracking of plastic waste to liquid fuels. Materials for Renewable and Sustainable Energy *9*, 9. 10.1007/s40243-020-00169-3.

76. Wang, X., Wu, X., Zhao, M., Zhang, R., Wang, Z., Li, Y., Zhang, L., Wang, X., Song, S., and Zhang, H. (2024). High-efficiency Ce-modified ZSM-5 nanosheets for waste plastic upgrading. Nano Research *17*, 5645-5650. 10.1007/s12274-024-6475-y.

77. Sun, M., Zhu, L., Liu, W., Zhao, X., Zhang, Y., Luo, H., Miao, G., Li, S., Yin, S., and Kong, L. (2022). Efficient upgrading of polyolefin plastics into C5–C12 gasoline alkanes over a Pt/W/Beta catalyst. Sustainable Energy & Fuels *6*, 271-275. 10.1039/D1SE01778K.

78. Zhou, Q., Wang, D., Wang, Q., He, K., Lim, K.H., Yang, X., Wang, W.-J., Li, B.-G., and Liu, P. (2023). Mechanistic Understanding of Efficient Polyethylene Hydrocracking over Two-Dimensional Platinum-Anchored Tungsten Trioxide. Angewandte Chemie International Edition *62*, e202305644. 10.1002/anie.202305644.

79. Rorrer, J.E., Ebrahim, A.M., Questell-Santiago, Y., Zhu, J., Troyano-Valls, C., Asundi, A.S., Brenner, A.E., Bare, S.R., Tassone, C.J., Beckham, G.T., and Román-Leshkov, Y. (2022). Role of Bifunctional Ru/Acid Catalysts in the Selective Hydrocracking of Polyethylene and Polypropylene Waste to Liquid Hydrocarbons. ACS Catalysis *12*, 13969-13979. 10.1021/acscatal.2c03596.

80. Han, X., Zhou, X., Ji, T., Zeng, F., Deng, W., Tang, Z., and Chen, R. (2024). Boosting the catalytic performance of metal–zeolite catalysts in the hydrocracking of polyolefin wastes by optimizing the nanoscale proximity. EES Catalysis *2*, 300-310. 10.1039/D3EY00180F.

81. Weitkamp, J. (2012). Catalytic Hydrocracking—Mechanisms and Versatility of the Process. ChemCatChem *4*, 292-306. 10.1002/cctc.201100315.

82. Lee, W.-T., van Muyden, A., Bobbink, F.D., Mensi, M.D., Carullo, J.R., and Dyson, P.J. (2022). Mechanistic classification and benchmarking of polyolefin depolymerization over silica-alumina-based catalysts. Nature Communications *13*, 4850. 10.1038/s41467-022-32563-y.

83. Nakaji, Y., Tamura, M., Miyaoka, S., Kumagai, S., Tanji, M., Nakagawa, Y., Yoshioka, T., and Tomishige, K. (2021). Low-temperature catalytic upgrading of waste polyolefinic plastics into liquid fuels and waxes. Applied Catalysis B: Environmental *285*, 119805. 10.1016/j.apcatb.2020.119805.

84. Tamura, M., Miyaoka, S., Nakaji, Y., Tanji, M., Kumagai, S., Nakagawa, Y., Yoshioka, T., and Tomishige, K. (2022). Structure-activity relationship in hydrogenolysis of polyolefins over Ru/support catalysts. Applied Catalysis B: Environmental *318*, 121870. 10.1016/j.apcatb.2022.121870.

85. Chu, M., Wang, X., Wang, X., Xu, P., Zhang, L., Li, S., Feng, K., Zhong, J., Wang, L., Li, Y., et al. (2024). Layered Double Hydroxide Derivatives for Polyolefin Upcycling. Journal of the American Chemical Society *146*, 10655-10665. 10.1021/jacs.4c00327.

86. Jaydev, S.D., Usteri, M.-E., Martín, A.J., and Pérez-Ramírez, J. (2023). Identifying selective catalysts in polypropylene hydrogenolysis by decoupling scission pathways. Chem Catalysis, 100564. 10.1016/j.checat.2023.100564.

87. Kang, Q., Chu, M., Xu, P., Wang, X., Wang, S., Cao, M., Ivasenko, O., Sham, T.-K., Zhang, Q., Sun, Q., and Chen, J. (2023). Entropy Confinement Promotes Hydrogenolysis Activity for Polyethylene Upcycling. Angewandte Chemie International Edition *62*, e202313174. 10.1002/anie.202313174.

88. Ellis, L.D., Orski, S.V., Kenlaw, G.A., Norman, A.G., Beers, K.L., Román-Leshkov, Y., and Beckham, G.T. (2021). Tandem Heterogeneous Catalysis for Polyethylene Depolymerization via an Olefin-Intermediate Process. ACS Sustainable Chemistry & Engineering *9*, 623-628. 10.1021/acssuschemeng.0c07612.

89. Kim, D., Hinton, Z.R., Bai, P., Korley, L.T.J., Epps, T.H., and Lobo, R.F. (2022). Metathesis, molecular redistribution of alkanes, and the chemical upgrading of low-density polyethylene. Applied Catalysis B: Environmental *318*, 121873. 10.1016/j.apcatb.2022.121873.

90. Wang, N.M., Strong, G., DaSilva, V., Gao, L., Huacuja, R., Konstantinov, I.A., Rosen, M.S., Nett, A.J., Ewart, S., Geyer, R., et al. (2022). Chemical Recycling of Polyethylene by Tandem Catalytic Conversion to Propylene. Journal of the American Chemical Society *144*, 18526-18531. 10.1021/jacs.2c07781.

91. Motta, A., Szeto, K.C., Taoufik, M., and Nicholas, C.P. (2016). Energetic pathways and influence of the metallacyclobutane intermediates formed during isobutene/2-butene

cross-metathesis over WH3/Al2O3 supported catalyst. Catalysis Science & Technology *6*, 3386-3393. 10.1039/C5CY02154E.

Chapter 2 Experimental and Characterisation Methods

2.1 Catalyst synthesis

2.1.1 Preparation of various zeolites and amorphous silica-alumina catalysts

The zeolites and amorphous silica-alumina (SiAl) used for catalytic testing or as support in Chapters 3, 4 and 5 were obtained from various sources. ZSM-5 (H-type, Si/Al =20), SAPO-34 (H-type, Si/Al =20) were procured from Nankai University, while HY (Si/Al =20) and SiAl Grade 135 (H-type) were sourced from Sigma-Aldrich. Additionally, ZSM-5 NS (H-type) were supplied by Sinopec Shanghai Petrochemical Co., Ltd.

Prior to use in catalytic tests or further catalyst synthesis, these materials were pretreated by heating at 400 °C in air flow for 3 h with a heating rate of 5°C min^{-1}. This treatment was performed to eliminate the adsorbed moisture and other volatile species present in the materials.

2.1.2 Preparation of γ-Al_2O_3 support

The γ-Al_2O_3 support employed in Chapters 4, 5, and 6 was synthesised by calcining boehmite (SCG Ltd.) at 600 °C for 8 h under an air flow.

2.1.3 Synthesis of PtSnCe/SiAl catalysts

PtSn/SiAl catalysts (with 1 wt% Pt, 1.8 wt% Sn) containing varying amounts of Ce (0 to 3 wt%) in Chapter 3 were synthesised using a co-impregnation method. The precursors, including chloroplatinic acid hydrate, tin (II) chloride dihydrate, and cerium (III) nitrate hexahydrate, were sourced from Sigma-Aldrich. The synthesis procedure involved dissolving these precursors in 20 mL deionised water, followed by impregnation of the 2 g SiAl support at room temperature under continuous stirring for 2 hours. The choice of 20 mL of water was based on the pore volume of the support, determined via BET analysis, which indicated a minimum requirement of approximately 1 mL for adequate wetting of 2 g of support. The use of 20 mL ensured complete dissolution of the metal salts and facilitated uniform impregnation.

After impregnation, the resulting slurry was dried at 120 °C overnight, followed by calcination at 500 °C for 4 h in air with a heating rate of 2 °C min^{-1}. The calcined catalysts were then reduced in 5 wt % H_2/N_2 flow at 400 °C for 3 h prior to their use in catalytic studies and characterisation. Pt/SiAl and Sn/SiAl catalysts were prepared following the same procedure and loadings for comparison.

2.1.4 Synthesis of metal-loaded (Fe, Co, Ni, Cu, and Zn) ZSM-5 or ZSM-5 nanosheet catalysts

Metal-loaded catalysts with a metal loading of 2 wt% were synthesised in Chapter 4 via the incipient wetness impregnation method. Metal precursors, including iron (III) nitrate nonahydrate, cobalt (II) nitrate hexahydrate, nickel (II) nitrate hexahydrate, copper (II) nitrate hemipentahydrate, and zinc nitrate hexahydrate were obtained from Sigma-Aldrich. The precursors were dissolved in 20 mL deionised water and stirred with 2 g of ZSM-5 or ZSM-5 NS support at room temperature for 5 h. The resulting slurries were dried at 100°C overnight, ground into powder, and calcined at 550 °C in air for 5 h at a heating rate of 5 °C min^{-1}. The final reduction was carried out at 700 °C in 5% H_2/N_2 flow for 3 h at a heating rate of 5 °C min^{-1} before the catalysts were used in catalytic studies and certain characterisations.

2.1.5 Synthesis of Ni/γ-Al_2O_3 catalyst

The Ni/γ-Al_2O_3 (2 wt% Ni) used in Chapters 4 and 5 was synthesised using the same precursor and methodology as described for Ni/ZSM-5 NS in section 2.1.4.

2.1.6 Synthesis NiW/ZSM-5 catalysts

Ni/ZSM-5 catalysts (2 wt% Ni) with varying W loadings (0 to 2 wt%) in Chapter 5 were synthesised using the co-impregnation method. Nickel (II) nitrate hexahydrate and ammonium metatungstate hydrate, both sourced from Sigma-Aldrich, were used as precursors. These were dissolved in 20 mL deionised water, and 2 g of ZSM-5 support was impregnated with the solution at room temperature for 5 h under continues stirring. The slurry was then dried overnight at 100 °C, followed by calcination at 550 °C for 5 h in air at a heating rate of 5 °C

min^{-1}. The calcined catalysts were reduced in 5 wt % H_2/N_2 flow at 700 °C for 3 h with a heating rate of 5 °C min^{-1} before being used in catalytic studies and for certain characterisations.

2.1.7 Synthesis W/ZSM-5 catalyst

W/ZSM-5 catalysts (0.25 wt% W) in Chapter 5 were synthesised using ammonium metatungstate hydrate as the precursor. The precursor was dissolved in 20 mL deionised water, and 2 g of ZSM-5 support was impregnated with this solution at room temperature for 5 h under continues stirring. The resulting slurry was dried overnight at 100 °C, followed by calcination at 550 °C for 5 h in air at a heating rate of 5 °C min^{-1} before being used as catalysts.

2.1.8 Synthesis lanthanum-group elements promoted PtGa/γ-Al_2O_3 catalysts

PtGa/γ-Al_2O_3 catalysts (1 wt% Pt and 3 wt% Ga) with varying loadings (0 to 5 wt%) of promoters (La, Ce, Pr, and Nd) were synthesised using a co-impregnation method. Precursors including chloroplatinic acid hydrate, gallium (III) nitrate hydrate, lanthanum (III) nitrate hexahydrate, cerium (III) nitrate hexahydrate, praseodymium (III) nitrate hexahydrate, and neodymium (III) nitrate hexahydrate were sourced from Sigma-Aldrich. These were pre-dissolved in 20 mL deionised water before impregnation of the 2 g of γ-Al_2O_3 support into the solution at room temperature for 5 h under continuous stirring. The slurry was then dried overnight at 100 °C and calcined at 550 °C for 6 h in air at a heating rate 5 °C min^{-1}. The Pt/γ-Al_2O_3 and Ga/γ-Al_2O_3 catalysts were synthesised following the same procedure and loadings for comparison.

2.2 Characterisation methods

Characterising materials is fundamental in the field of heterogeneous catalysis, as it provides critical insights into the catalyst performance by linking activity to specific different properties. While a wide range of characterisation techniques is available, this thesis focuses on 11 key methods. For clarity and streamlined discussion, these methods are organised into four main categories: structural and chemical composition analysis, surface and porosity analysis, morphological analysis, and thermal and molecular weight analysis.

2.2.1 Structural and chemical composition analysis techniques

2.2.1.1 X-ray diffraction

X-ray diffraction (XRD) is a fundamental technique for analysing the bulk structure of catalysts. X-rays are generated by bombarding a target material with electrons produced by heating of a filament. The resulting monochromatic X-ray beam is directed at the sample where it interacts with atomic lattice and scatters. At certain angles, the scattered X-rays are in phase, leading to constructive interference and the formation of diffraction peaks with measurable intensities. This process, depicted in Figure 2.1, adheres to Bragg's law, which states that constructive interference occurs only when the following condition is met:

$$n\lambda = 2d\sin\theta \tag{2.1}$$

Here, n is the order of reflection, λ is the wavelength of the X-ray, d is the spacing between the crystal planes, and θ is the angle between the incident X-ray and the scatter plane.[1]

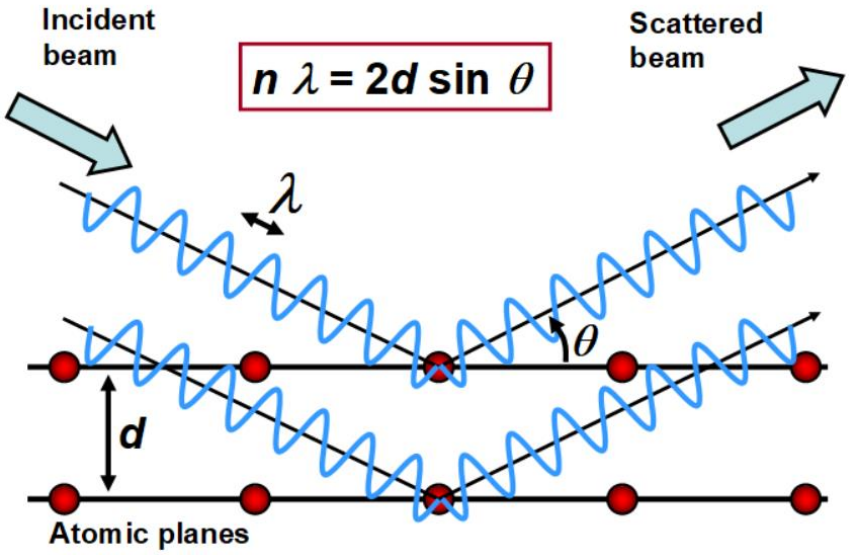

Figure 2.1 Principle of XRD. Reprinted with permission from reference[2].

Crystalline materials typically contain multiple sets of planes, each characterised by its orientation and interplanar spacing. These planes are described by three integers, known as Miller indices (h, k, l), which define the points where the plane intersects the Cartesian axes

(x, y, z). To account for all the possible planes which satisfy Bragg's law, the latter in a cubic system is usually expressed as follows:

$$\frac{1}{d_{hkl}^2} = \frac{h^2 + k^2 + l^2}{a^2} \tag{2.2}$$

where a is the lattice constant of the cubic crystal, which can be calculated once d_{hkl} (interplanar spacing with Miller indices hkl) is determined from XRD measurements.[3]

The broadening of XRD peaks is indicative of the structural order within the material. Single-crystal materials and large crystalline particles exhibit sharp, narrow peaks due to their well-ordered, long-range structure. In contrast, amorphous materials show either no diffraction peaks or very board ones, reflecting the absence of planes capable of generating Bragg diffraction. Catalysts, which are often characterised by structural domains of medium-range order, typically consist of nanoparticles. For nanoscale crystallites, the crystallite size can be estimated from the broadening of the diffraction peak using the Debye-Scherrer's equation:

$$\tau = \frac{K\lambda}{B\cos\theta} \tag{2.3}$$

where τ represents the crystalline size perpendicular to the reflecting plane, K is a shape factor typically close to unity, λ is the X-ray wavelength, B is the full width at half maximum (FWHM) of the diffraction peak, and θ is the diffraction angle. However, this method provides an estimation of crystalline size, as peak broadening can also be affected by lattice distortions, twinning internal stresses, surface and boundaries of crystalline, etc., which may introduce inaccuracies.[4]

In this thesis, XRD patterns were obtained using a Brucker D8 Advanced Eco X-ray diffractometer operated at 40 kV and 25 mA, with a step size at 0.019°, a time per step of 0.10 s, and a total 4368 steps, utilising Cu $K\alpha_1$ radiation. The samples were pressed onto a glass and attached to a sample holder, with all measurements conducted in a 2θ range of 5-90°.

2.2.1.2 X-ray photoelectron spectroscopy

X-ray photoelectron spectroscopy (XPS) is a highly surface-sensitive technique commonly employed to study the composition and electronic structures of solid surfaces. With a sampling depth ranging from 5 to 10 nm, XPS operates on the principle of photoelectric effect, where electrons are emitted from a sample after it is irradiated by X-rays under high vacuum conditions. Unlike XRD, which typically uses Cu source (Cu Kα: 8047.8 eV), XPS utilises an aluminium source (Al Kα: 1486.7eV) to generate $K\alpha_{1,2}$ radiation. This results in shallower penetration depth, making XPS signals more sensitive to surface characteristics. Figure 2.2 illustrates the photoelectric effect mechanism. The balance between the energy of the incident X-ray photos (hν) and the kinetic energy of the ejected electron (E_k) is described by Einstein's equation:

$$E_k = h\nu - E_b - \phi \qquad (2.4)$$

where E_b is the binding energy of electron relative to the Fermi level, and ϕ is the work function, which is dependent on both the sample and the spectrometer used.[5]

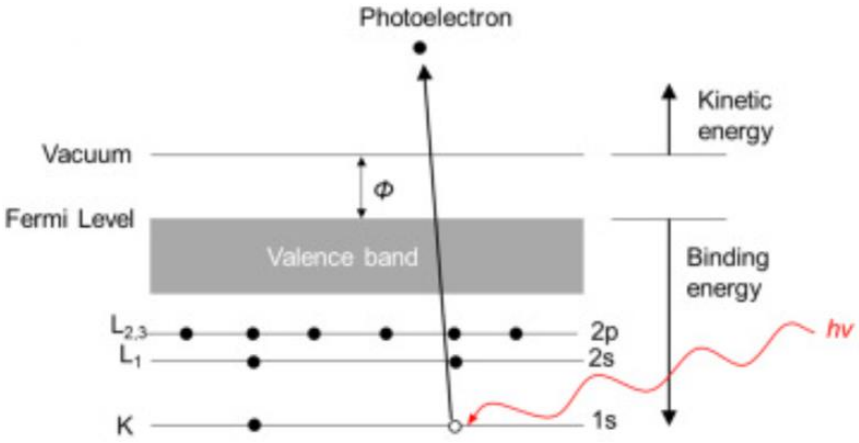

Figure 2.2 Schematic of photoemission process involved in XPS. Reprinted with permission from reference[6].

In the context of heterogeneous catalysis, XPS is instrumental in elucidating the relationship between catalytic surfaces and their performance. It allows for the quantification of the elemental composition on the catalyst surface, the identification of the oxidation states of

elements, and the detection of any variation, manifested as shifts in binding energy. Typical laboratory-based XPS experiments are conducted under high vacuum conditions to prevent photoelectrons from colliding with gas molecules and to protect moisture-sensitive detectors.

A survey scan covering a binding energy range from 0 eV to 1400 eV is performed to determine the chemical composition by assigning peaks to different elements. The elemental ratios are calculated based on the integrated peak areas and the corresponding relative sensitivity factors. High-resolution scans within specific binding energy ranges are conducted to investigated the oxidation states of the interesting elements. The oxidation state influences the electron density, thereby altering the binding energies. By comparing these experimental binding energies with the database values, the chemical states of elements can be identified.

In this thesis, XPS was primarily used to study the chemical states of various materials. Ex-situ XPS measurements were performed using a PHI Quantum-2000 photoelectron spectrometer (Al Kα: 1486.7 eV) equipped with an Omicron Sphera II hemispherical electron energy analyser on a Thermo Scientific Nexsa model. The aluminium anode tube voltage was set to 12 kV. Samples were prepared by affixing them to the stage with silicone-free double-side tape to avoid contamination. Survey scans were conducted with a pass energy of 200 eV at 1 eV/step, repeated 5 times. High-resolution XPS spectra were measured with 10 scans at 0.1 eV/step and 50 eV pass energy. All data were recorded at a pressure below 10^{-8} Torr and at room temperature. Data analysis was carried out using CasaXPS v2.3.20PR1.0, with the characteristic C 1s peak at approximately 284.8 eV used for calibration to mitigate sample charging during measurements. Peaks were fitted with a Shirley background prior to component analysis. The XPS measurements were performed at Harwell XPS by Dr. Shaoliang Guan.

2.2.1.3 Solid-state nuclear magnetic resonance

Nuclear magnetic resonance (NMR) spectroscopy is a powerful technique used to explore the molecular structure of materials by examining the interactions between nuclear spins within a magnetic field. When exposed to a magnetic field, NMR-active nuclei, such as ^{1}H and ^{13}C,

absorb electromagnetic radiation at isotope-specific frequencies. The resulting NMR spectrum, which plots signal intensity against chemical shift (δ), reflects the resonant frequency of the nuclei relative to a standard reference in the magnetic field.

Solid-state NMR (ss-NMR) is an essential tool in the analysis of heterogeneous catalysts, particularly zeolite.[7] Unlike liquid-state NMR, which benefits from Brownian motion to average out anisotropic effects, ss-NMR deals with the solid-state environment where anisotropic interactions dominate, leading to boarder and more complex spectral lines. However, spectral resolution in ss-NMR can be significantly enhanced using magic-angle spinning (MAS). In MAS, the sample is rapidly rotated (up to 60000 revolutions per second) around an axis titled at 54.7 degrees relative to the magnetic field, resulting in narrow spectral lines and improved resolution.

In the field of heterogeneous catalysis, ss-NMR is valuable for identifying specific atomic sites based on nuclear spins that produces spectral lines at frequencies characteristic of their local environments. The NMR frequencies are influenced by interactions between nuclear spins and electrons in either localised orbitals (chemical shifts) or metallic conduction bands (Knight shift), enabling differentiation between sites such as Si and Al in zeolites.[8] Additionally, ss-NMR can access catalyst surface acidity by analysing properties such as acid types (Brønsted or Lewis), acid strength, and acid site concentration. For instance, ^{1}H MAS NMR can detect OH groups acting as BAS on the catalyst surface.[7] Moreover, ss-NRM can be used to investigate reaction mechanisms by quantifying reactants, products, and intermediates.

In this thesis, ss-NMR was primary used to examine the chemical environments and surface acidity of different zeolites, as discussed in Chapters 4 and 5. Prior to analysis, the samples were dehydrated under vacuum, with the temperature gradually increased at a rate of 1 °C min^{-1}, reaching a final temperature of 400 °C and maintaining a pressure below 10^{-3} Pa overnight. After cooling to room temperature, the samples were flame-sealed in tubes and transferred into a ZrO_2 rotor with a Kel-F endcap under a dry nitrogen atmosphere in a glove box.

All NMR experiments were conducted on a Jeol ECZ500R spectrometer equipped with 4 mm and 8 mm MAS probes, operating at resonance frequencies of 495.13 MHz for ^{1}H, 129.02 MHz for ^{27}Al, 98.37 MHz for ^{29}Si, and 125.72 for ^{13}C. The ^{1}H MAS spectra were recorded at a 12 kHz spinning rate, using a 2.7 μs pulse width (approximately a π/2 pulse), a 5-second recycle delay, and 32 scans. The ^{1}H chemical shifts were referenced to solid adamantane at 1.78 ppm. The ^{27}Al MAS NMR spectra were collected at a 12 kHz spinning rate with a 0.5-second recycle delay and 1024 scans, using a small flip angle (π/12) and short pulse duration (0.16 μs) for uniform signal excitation. The ^{27}Al chemical shifts were referenced to 1.0 M aqueous $Al(NO_3)_3$ solutions at 0 ppm. The ^{29}Si MAS NMR spectra were obtained at a 4 kHz spinning rate with an 8 mm probe, using a 7.61 μs pulse width, a 60-secdon recycle delay, and 60 scans, with the ^{29}Si chemical shifts referenced to kaolinite at -91.5 ppm. The ^{13}C cross-polarisation (CP) MAS NMR spectra were collected using a 4 mm probe, with a spinning rate of 12 kHz. The pulse width was set at 2.5 μs (equivalent to a π/2 pulse), with a recycle delay of 3 s. Chemical shifts for ^{13}C were referenced to solid adamantane at 29.9 ppm. All ss-NMR experiments were performed by Dr. Guangchao Li.

2.2.1.4 Infrared and Raman spectroscopy

Vibrational spectroscopy, encompassing several techniques, such as infrared (IR) and Raman spectroscopy, plays a pivotal role in catalyst characterisation. These techniques are complementary, each offering unique insights into molecular fingerprinting. Although some vibrational modes are active in both Raman and IR spectroscopy, they operate through distinct mechanisms (Figure 2.3 (a)).

In IR spectroscopy, absorption leads to a transition from ground vibrational state to an excited state via one-photon event, where the energy of the IR photon is transferred to the molecule, altering its dipole moment. This interaction occurs when the vibrational frequency of a particular normal mode resonates with the frequency of the IR radiation. The relevant vibrational modes are illustrated in Figure 2.3 (b).

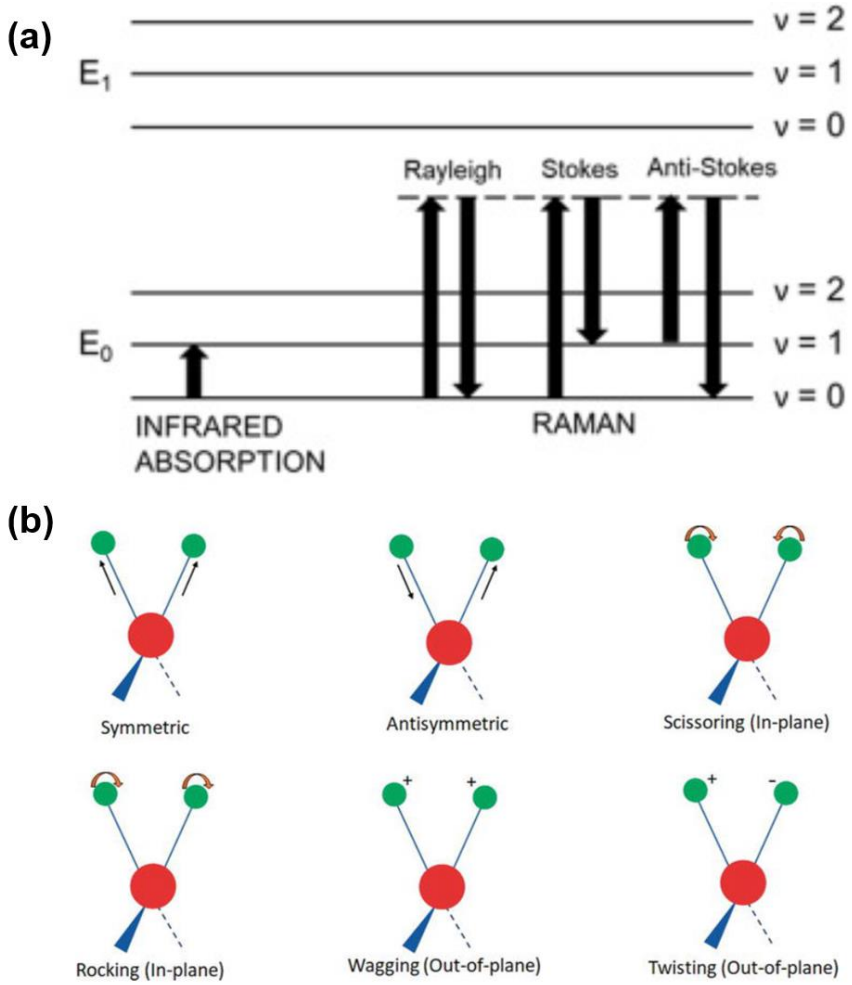

Figure 2.3 (a) Schematic of energy transitions in IR absorption and Raman scattering. v and E denote vibrational level and electronic level, respectively. Reprinted with permission from reference[6]. (b) Types of molecular vibrational modes. Reprinted with permission from reference[9].

Similarly, Raman spectroscopy involves transitions between vibrational states. However, unlike IR spectroscopy, which uses broadband IR sources and depends on changes in the dipole moment, Raman spectroscopy relies on the inelastic scattering of narrow-band monochromatic radiation. This scattering occurs when light interacts with the sample, causing the molecule to relax into a different energy state. While Rayleigh scattering is elastic and returns the molecule to its original state, inelastic scattering results in Raman scattering, where the energy of the scattered photon differs from that of the incident photon. The difference in energy determines the vibrational transition, leading to either Stokes (lower energy), or anti-

Stokes (higher energy) Raman shifts, as depicted in Figure 2.3 (a).[10] The resulting Raman displays peaks corresponding to these shifts, providing detailed molecular information.

Regarding IR spectroscopy, diffuse reflectance infrared Fourier transform spectroscopy (DRIFTS) is the most widely used mode, particularly suitable for probing highly absorbing catalysts with weak transmission signals. DRIFTS offers high surface sensitivity, making it ideal for quantifying catalyst acidity, identifying active sites, and studying reaction mechanisms through time-resolved spectra. The molecular vibrations of interest in catalysis typically occur in the mid-IR (400-4000 cm^{-1}).

Raman spectroscopy, in contrast, is more sensitive to homonuclear and nonpolar bonds, while IR spectroscopy excels at detecting heteronuclear functional groups and polar bonds. Raman also effectively probes the region below 400 cm^{-1}, which can be challenging for traditional IR instruments. Furthermore, Raman spectroscopy can provide insights into crystal phases, making it particularly valuable for characterising amorphous phases undetectable by XRD. Additionally, Raman is sensitive to carbon materials, making it useful for characterising such substances.

In this thesis, IR spectroscopy was employed to quantify catalyst acidity and investigate the reaction mechanisms. Fourier transform IR (FTIR) measurements were conducted using pyridine (Py-IR) as a probe molecule in Chapters 3, 5 and 6, CO (CO-FTIR) in Chapters 4 and 6, or in-situ DRIFTS using propylene in Chapter 6 and in-situ DRIFTS for reaction mechanism studies in Chapters 4 and 5. These experiments were carried out in a vacuum cell using a Thermo Scientific Nicole at 6700 spectrometers, equipped with ZnSe windows and a mercury cadmium telluride detector cooled by liquid nitrogen. Spectra were obtained with 128 scans at a resolution of 4 cm^{-1} and presented in absorbance units.

For Py-IR, samples were reduced under a 5% H_2/N_2 flow in vacuum at 400 °C for 3 h. After cooling to 150 °C, background spectra were acquired under N_2 flow. Pyridine vapor was then introduced and allowed to adsorb for 1 h, followed by evacuation for 40 min to remove excess

pyridine. Py-IR spectra were recorded at 200 °C to quantify total concentration of BAS and Lewis acid sites (LAS), or at 350 °C to quantify the total concentration of strong BAS and LAS. For CO-FTIR, samples underwent same pretreatment as in Py-IR, followed by background recording at room temperature. CO was introduced for 1 h, then evacuated for another 1 h before CO-FTIR spectra were recorded.

For in-situ DRIFTS using propylene as a probe molecule in Chapter 6, samples were reduced as described for CO and pyridine adsorption, with background spectra recorded at 30 °C. Propylene was introduced and allowed to adsorb for 1 h, followed by a nitrogen purge and spectra collection at this temperature. The temperatures were then gradually increased to 50, 100, 150, 200, 250, 300 °C with spectra collected at each step. In-situ DRIFTS for investigating the reaction mechanisms of PP hydrocracking involved pretreating the PP and catalyst mixture at 150 °C for 3 h under N_2, followed by cooling to 20 °C to collect background spectra. Subsequently, 5 bar of pure hydrogen was introduced at a flow rate of 10 (or 5) mL min^{-1}, and the temperature was increased to 280 (or 260) °C before spectra were collected over time.

Raman spectra of spent catalysts in Chapter 6 were obtained using a Renishaw Microraman spectrometer with a 532 nm laser beam, conducted at room temperature at University of Surry. Dr. Xuelei Pan provided valuable assistance in performing all the Raman measurements.

2.2.2 Surface and porosity analysis techniques

2.2.2.1 Nitrogen adsorption-desorption isotherms

The adsorption process is commonly analysed through isotherms, which depict the relationship between the quantify of adsorbate on the adsorbent and the partial pressure at a constant temperature. According to the International Union of Pure and Applied Chemistry (IUPAC), isotherms are categorised into six types, as shown in Figure 2.4. However, in catalyst characterisation, types I, II, IV, and VI are predominantly observed.[11,12] The pores are also classified by size into micropores (< 2 nm), mesopores (2-50 nm), and macropores (> 50 nm).[11]

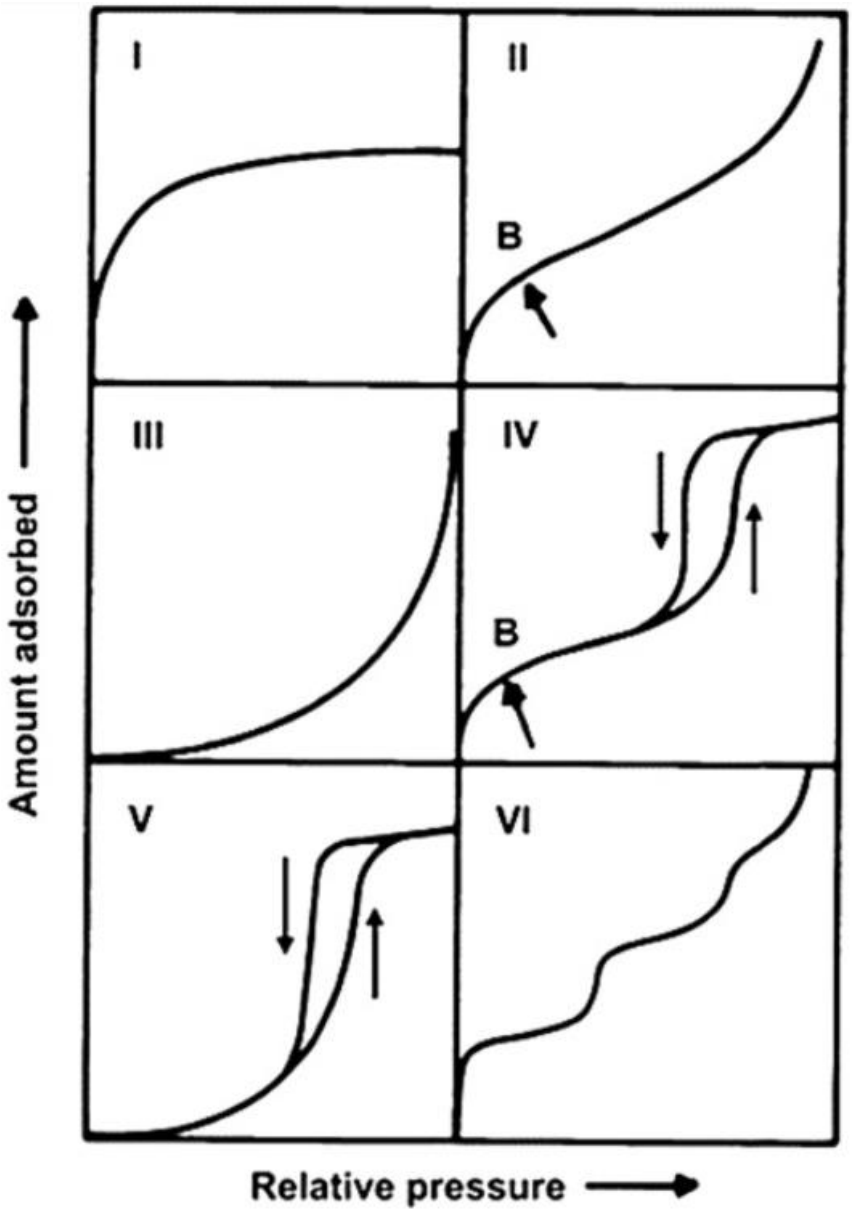

Figure 2.4 IUPAC classification of adsorption-desorption isotherms (Type I-VI). Reprinted with permission from reference[13].

Among these isotherms, type IV is most frequently associated with catalytic materials investigated in this thesis.[14] This type of isotherm characterises mesoporous solids and is distinguished by a hysteresis loop and a plateau at relative pressure (P/P_0) of 0.6-0.95. The presence of the hysteresis loop is attributed to capillary condensation occurring in the mesopores as the relative pressure increases. At low relative pressure, the curve resembles that of microporous solids, where the surface is covered by a monolayer. As the pressure increases, multilayer adsorption occurs, followed by capillary condensation, leading to a

marked increase in the adsorbed volume. Once the mesopores are fully filled, adsorption continues on external surface area.

To interpret different isotherm curves, various theoretical and experimental methods have been developed, with the Brunauer-Emmett-Teller (BET) model being the most commonly applied. The BET equation is expressed as:

$$\frac{P}{V(P_0 - P)} = \frac{1}{V_m C} + \frac{C - 1}{V_m C}\left(\frac{P}{P_0}\right) \quad (2.5)$$

Plotting $P/[V(P_0-P)]$ versus P/P_0 yields a straight line with a slope of $(C-1)/(V_mC)$ and an intercept of $1/(V_mC)$. This linearity is typically maintained in regions where P/P_0 is sufficiently low (typically<1/3) to avoid nonlinearity caused by condensation in mesopores. From this, the volume of the monolayer, V_m, is determined, allowing for the calculation of the specific surface area, S_g, of the adsorbent using the equation:

$$S_g = \frac{V_m}{0.0224} \times (6.023 \times 10^{23}) \times A \quad (2.6)$$

where 6.023×10^{23} is Avogadro's number, and A represents the area occupied by each adsorbate molecule (for nitrogen, this value is 16.2×10^{-20} m^2).[15]

In this thesis, the BET surface area was determined through N_2 adsorption-desorption isotherms, analysed using Micrometrics TriStar II Plus software. Pore size distribution was evaluated using the Density Functional Theory (DFT) model within the same software. For the catalysts studied in Chapters 3 and 6, samples were outgassed under vacuum for 1 h at 300 °C before adsorption measurements. In contrast, the catalysts from Chapters 4 and 5 were degassed under vacuum at 300 °C for 16 h. All N_2 adsorption-desorption experiments were conducted using a Micromeritics Tristar instrument with high-purity gases, performed at the Surface Analysis Facilities, Chemistry Research Laboratory, University of Oxford, with the assistance of Dr. Bryan Ng and Ms. Jiasi Li.

2.2.2.2 Temperature-programmed methods

Temperature-programmed methods are highly effective for characterising catalyst activation and reactivity. These techniques involve gradually increasing the temperature of the catalyst at a constant rate while monitoring the concentration of reacting or desorbing species as a function of temperature. These methods are generally categorised into two primary types: temperature-programmed desorption (TPD), which focuses on surface processes, and temperature-programmed oxidation (TPO) or reduction (TPR), which encompass both surface and bulk reactions.

In TPD characterisation, the desorption rate initially rises exponentially with temperature due to the gradual depletion of adsorbed gas on the catalyst surface. Once the maximum rate is reached, it then declines to zero, signifying the complete desorption of the adsorbate. A key application of TPD in this thesis is ammonia-TPD (NH_3-TPD), used to assess the strength and concentration of acid sites. However, due to the inability of NH_3-TPD to differentiate between types of acid sites, it is often complemented by Py-IR spectroscopy for a more detailed acidity analysis.

In TPR and TPO, a reducing or oxidising gas interacts with samples while as the temperature is increased at a controlled rate. The concentration of these gases is continuously monitored, providing insights into the various reduction or oxidation temperatures among different catalysts, the presence of various species during these reactions, and the amount of gas consumption for specific species.[16] In this thesis, TPR of hydrogen (H_2-TPR) is extensively utilised to examine the reducibility of various catalysts.

All NH_3-TPD and H_2-TPD experiments were performed on Chem BET Pulsar TPR/TPD instrument in this thesis. For NH_3-TPD experiments detailed in Chapters 3-5, samples (0.2 g) were placed into a quartz U-type tube between two quartz wool plugs. The samples were pretreated under an Argon flow (20 mL min^{-1}) at 300 °C for 1 h. After cooling to 50 °C, the samples were exposed to a stream of ammonia gas (10% NH_3/N_2) at same flow rate for 1 h. The baseline was stabilised at same temperature for 2 h before switching the gas back to

Argon flow, followed by heating to 800 °C at a rate 5 °C min^{-1}, while the NH_3-TPD profile was monitored using a thermal conductivity detector (TCD). In Chapter 6, the same procedure was followed, except the final temperature was 600 °C.

For H_2-TPR experiments described in Chapters 4-6, samples (0.2 g) were pretreated at 300 °C for 1 h under Argon flow. After cooling to 50 °C, the baseline was stabilised for 2 h under a 5% H_2/N_2 flow (20 mL min^{-1}). The reactor was then heated to 800 °C at a rate of 10 °C min^{-1}, and the H_2-consumption profile was recorded. For the catalysts used in Chapter 3, sample mass of 0.12 g was used, and the target heating temperature was 1000 °C; the other procedures remained consistent with the descriptions above.

2.2.3 Morphological analysis techniques

2.2.3.1 Scanning electron microscopy and transmission electron microscopy

Electron microscopy employs electrons to produce high-resolution images of samples. This technique encompasses a variety of methods that capture signals generated by the interaction between an electron beam and the sample, providing critical information about the structural features, surface morphology, and material composition. Due to the much shorter wavelength of electrons compared to visible light, electron microscopy achieves far higher resolution than optical instruments.[17] Two of the most commonly utilised electron microscopy techniques in heterogeneous catalysis are scanning electron microscopy (SEM) and transmission electron microscopy (TEM).

The operating principles of SEM and TEM are illustrated in Figure 2.5 (a) and (b). Both instruments utilise a set of lenses to focus the electron beam onto the sample surface. In SEM, the electron beam is rastered across the sample's surface by scanning coils, and the signals generated are captured by a detector. The detected signals are synchronised with the beam position on the sample, allowing image formation by mapping signal intensity to pixel brightness (Figure 2.5 (a)). In contrast, TEM projects the electron beam onto a specific area of an ultra-thin sample (preferably < 100 nm). Electrons passing through the samples are

collected by a detector, forming an image based on electron transmission (Figure 2.5 (b)). TEM can also be operated in scanning mode (STEM), as depicted in Figure 2.5 (c).

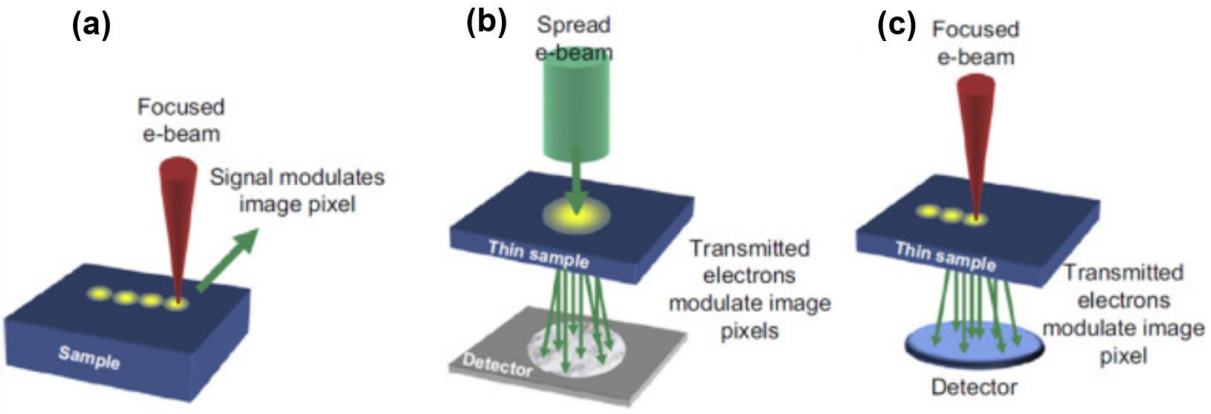

Figure 2.5 (a) Serial collection of data points in SEM. (b) Parallel image acquisition in TEM. (c) Serial collection of transmitted electrons in STEM. Reprinted with permission from reference[18].

SEM is widely used for routine catalyst characterisation, offering valuable insights into the micro- and nanostructure of materials, including particle size, agglomeration, porosity, and aspect ratio.[14] For example, Figure 2.6 (a)–(d) shows SEM images of CeO_2 catalysts with four distinct morphologies: (a) rods with diameter of approximately 20 nm and lengths of 100-300 nm; (b) cubes measuring 30-50 nm; (c) spheres with an average diameter of ~ 300nm; (d) random nanoparticles sized 10-50 nm.[19] TEM, on the other hand, provides atomic-scale resolution (as high as 0.1 nm, compared to 10 nm typical of SEM), making it ideal for studying catalyst structure at the nano and atomic scale. TEM is used to analyse nanoparticle shape and size distribution, phase spatial distributions, atomic ordering, and lattice parameter measurements. Additionally, TEM can be paired with energy-dispersive X-ray (EDX) spectroscopy in STEM mode to map local elemental composition and analyse electronic structures.

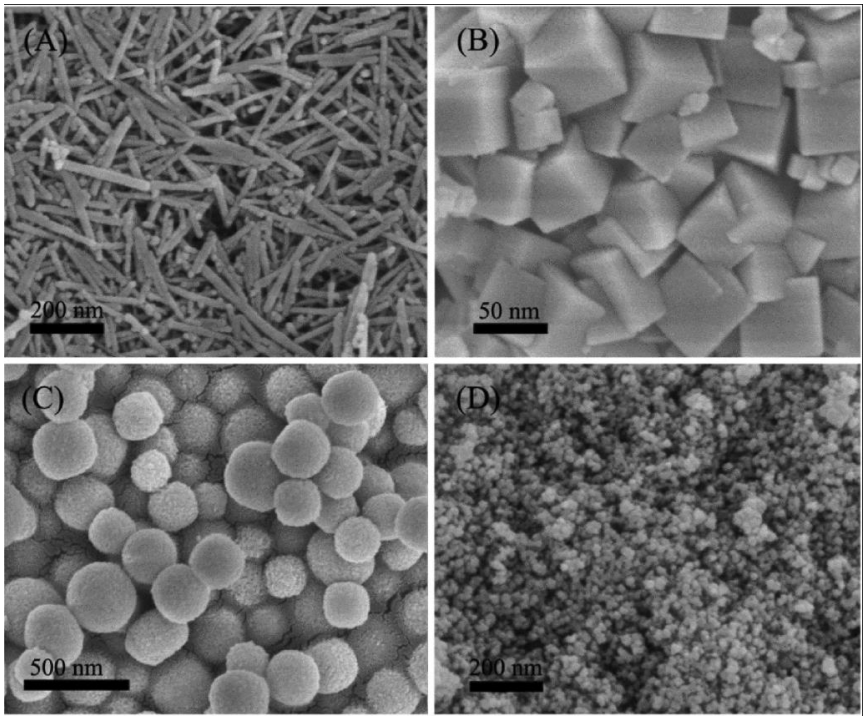

Figure 2.6 (a)-(d) SEM images of CeO_2 catalysts with different morphologies. Reprinted with permission from reference[19].

In this thesis, SEM images in Chapter 4 were obtained using a Zeiss Sigma 300 Field Emission Gun SEM with a 2 kV electron beam. Catalyst samples were suspended in ethanol and drop-cast onto a Si (100) wafer prior to scanning. All SEM images are acquired with the assistance of Amy Radford. High-resolution TEM (HRTEM) images were acquired using a JEM-2100 analytical electron microscope operated at 200 kV, with bright-field imaging enabled by a Gatan Orius charge-coupled device camera. An EDX spectroscopy detector was employed for elemental mapping, achieving a peak integration of 8 cps/eV. All TEM images in Chapters 3-5 were obtained with the assistance of Dr. Ping-Luen Ho, while the TEM images in Chapter 6 were acquired with the assistance of Dr. Yanjie Wang.

2.2.4 Thermal and molecular weight analysis techniques

2.2.4.1 Thermogravimetric analysis

Thermogravimetric (TG) analysis is a technique closely related to temperature-programmed methods, employed to study the response of a catalyst to temperature variations. In TG analysis, the sample's weight is continuously monitored over time using a microbalance as

the sample undergoes controlled heating within a furnace. This method is primarily used to access the thermal stability of materials in different atmospheres, such as inert or oxidising environments, and provides crucial date on decomposition temperatures, moisture content, and degradation mechanisms. Additionally, TG analysis can quantify the humidity of a catalyst and its hydroxyl group content.[20]

In this thesis, TG analysis is primarily utilised to determine the total coke content of spent catalysts. All TG experiments were performed using an SDT-Q600 instrument. Approximately 20 mg of each sample was loaded into the microbalance. Prior to initiating the measurement, the samples were stabilised in an airflow of 40 mL min^{-1} at room temperature for 20 min, during which the initial weight of the samples was normalised to 100%. The heating program was then initiated, with a temperature ramp of 10 °C min^{-1} up to 700 °C.

2.2.4.2 Gel permeation chromatography

Gel permeation chromatography (GPC) is a widely utilised technique for determining the molecular weight distribution of polymers. This method separates dissolved molecules based on their size, as they elute through a column packed with a porous gel. Essentially, GPC functions as a form of molecular sieving chromatography, wherein the sample is dissolved in a mobile phase (solvent) and then passed through the column. The different components of sample traverse the stationary phase at varying speeds, depending on their ability to penetrate the pores of the gel, leading to separation–a process known as differential partitioning.

In this thesis, GPC experiments were conducted using a high-temperature GPC system with an IR5 detector. The samples were prepared by dissolving them in 1,2,4,-trichlorobenzne (TCB) containing approximately 300 ppm of 3,5-di-tert-buty-4-hydroxytoluene (BHT) at 160 °C for 90 min. After dissolution, the solutions were filtered through a 10 µm stainless steel filter before being introduced into the GPC column. The samples were analysed under a flow rate of 0.5 mL min^{-1} using TCB with 300 ppm of BHT as the mobile phase. Additionally, 1 mg mL^{-1} of BHT was added as a flow rate marker. The GPC column was maintained at 145 °C, while the detector temperature was operated at 160 °C.

2.3 Catalytic tests

2.3.1 Catalytic procedures and product analysis

For the plastic hydrocracking experiments detailed in Chapters 3, 4, 5, the following general procedures was employed: A 50 mL stainless steel Parr autoclave (Figure 2.7 (a)) without a liner was utilised as a batch reactor, equipped with internal and external thermocouples at different depths to ensure accurate temperature control. The reactor's volume was determined by fully filling it with water and measuring the volume of contained liquid. The plastic feedstock, typically 2 g of PP fine powder (or other types of plastics) was mixed with 0.2 g of solid catalyst, maintaining a plastic-to-catalyst ratio 10:1. The autoclave was purged three times with hydrogen before being pressurised to 30 bar (unless otherwise specified) with hydrogen gas. The reactor was then heated to the target temperature over 40 min, with continuous stirring at 400 revolution per minute (RPM), unless otherwise specified, using a glass-coated stirrer. The choice of 400 RPM was based on our investigations into the effect of stirring speed. It is demonstrated that low stirring speeds (e.g., 200 RPM) or the absence of stirring limited the diffusion between the molten polymer and catalysts, resulting in a higher yield of solid residues. Stirring speed above 400 RPM effectively mitigated this diffusion limitation. Additionally, control experiments confirmed that negligible reaction occurred during the heating phase. Once the desired reaction time was complete, the system was cooled to room temperature.

After cooling, gas-phase products were analysed using gas chromatography (GC), while the autoclave was depressurised for further analysis of liquid and solid products. Gaseous products were sampled from the reactor headspace using a 250 µL glassy syringe and injected into an online Shimadzu GC-2014 equipped with a flame ionisation detector (FID) and a TCD for quantification. Liquid-phase products were analysed via GC-mass spectroscopy (Agilent GC-MS 6890), with chloroform used to extract the liquid from the solid–liquid mixture in the autoclave. The quantification of both gas and liquid products was performed using a normalised method.

To separate the liquid from the solid, the solid-liquid mixture was centrifuged. In Chapter 3, the solid residue was dried under vacuum at 60 °C overnight and weighed at room temperature. In Chapters 4 and 5, the solid residue was air-dried at room temperature before weighing.

The total product mass was divided into gas, liquid, and solid phases. The mass of the autoclave, including the stirrer, was measured using a balance with a capacity and accuracy of 10 kg ± 0.05 g. The combined mass of the liquid and solid phases was determined by subtracting the weight of emptied autoclave after gas release. The solid mass was determined by subtracting the catalyst weight, and the liquid mass was calculated by subtracting the solid residue and catalyst weight from the total liquid–solid mass.

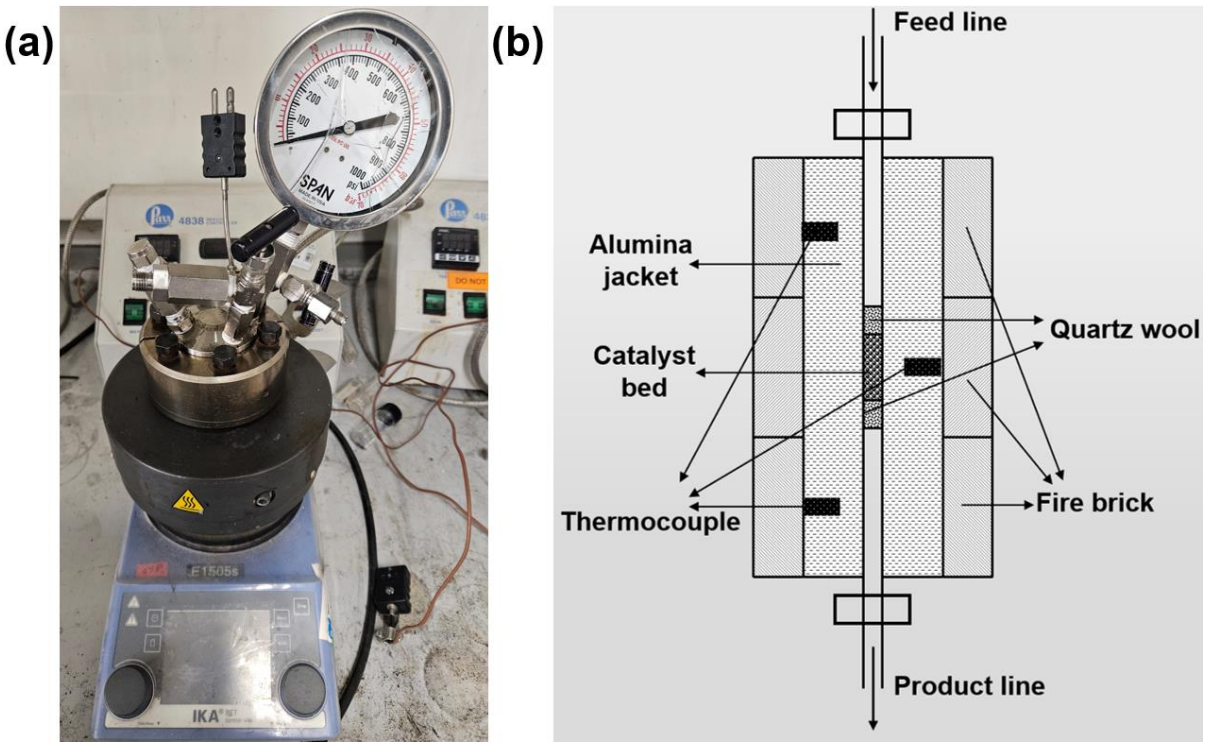

Figure 2.7 (a) Batch reactor for plastic hydrocracking. (b) Schematic diagram of the fixed-bed reactor for propane dehydrogenation.

For propane dehydrogenation tests described in Chapter 6, a fixed-bed reactor with an internal diameter of 3/8 inches and a length of 15 inches (Figure 2.7 (b)) was employed. In each test, 0.1 g of fine powdered catalyst without dilution was placed in the centre of the reactor, held in place with quartz wool. The catalyst was heated to 600 °C over 1 h, followed by reduction

under a 20 mL min^{-1} flow of H_2 for 2 h. Two gas mixtures were used: one containing 10 vol % H_2 and 20 vol % C_3H_8, balanced with N_2 at a total flow rate 25 mL min^{-1}, and second mixture containing 20 vol% C_3H_8 balanced with N_2 at a total flow rate 25 mL min^{-1}. The weight hourly space velocity (WHSV) of propane was maintained at 5.4 h^{-1} in both conditions. After 10 min of reaction, the gas products were analysed using an online Shimadzu GC-2014 equipped with FID and TCD detectors.

Long-term stability tests were conducted using the hydrogen-free gas mixture. After each 14-hours reaction, the catalysts were regenerated by flowing 20 mL min^{-1} of air at 600 °C for 1 h, followed by reduction with 20 mL min^{-1} of H_2 flow for 2 h before the next cycle.

2.3.2 Catalytic results calculation methods

For the plastic hydrocracking experiments in Chapters 3, 4, and 5, the yield of a specific product i or solid was calculated using the following equation:

$$\text{Yield } [\text{wt\%}] = \frac{m_i}{m_{gas} + m_{liquid} + m_{solid}} \times 100\% \quad (2.7)$$

where m_i represents the mass of the specific product i or solid, and m_{gas}, m_{liquid}, and m_{solid} are the masses of the gas, liquid, and solid phases, respectively.

The selectivity of a product group with i-numbered carbons was determined as follows:

$$\text{Selectivity } [\text{wt\%}] = \frac{m_i}{\sum m_i} \times 100\% \quad (2.8)$$

where $\sum m_i$ is the total mass of all reaction products collected in the gas and liquid phases, excluding solid residues.

The mass balance was defined as:

$$\text{Mass balance } [\%] = \frac{m_{gas} + m_{liquid} + m_{solid}}{m_{input}} \times 100\% \quad (2.9)$$

All results reported in Chapters 3, 4, 5 achieved mass balances with a range of 97 ± 3 %.

The degree of branching in Chapter 3 was assessed by calculating the fraction of isomerised hydrocarbons in liquid the phase (C_{iso}) relative to the total liquid hydrocarbon products (C_n and C_{iso}). In Chapter 5, this was calculated based on the isomerised C_4-C_6 hydrocarbons (C_{iso}) relative to the total C_4-C_6 products (C_n and C_{iso}), excluding C_1-C_3 gas products due to the lack of isomerism in these gases.

$$\text{Degree of branching } [\%] = \frac{C_{iso}}{C_{iso} + C_n} \times 100\% \quad (2.10)$$

For propane dehydrogenation results in Chapter 6, propane conversion, propylene selectivity, and carbon balance were calculated using the following expressions:

$$C_3H_8 \text{ conversion } (\%) = \frac{[F_{C_3H_8}]_{in} - [F_{C_3H_8}]_{out}}{[F_{C_3H_8}]_{in}} \times 100\ \% \quad (2.11)$$

$$C_3H_6 \text{ selectivity } (\%) = \frac{[F_{C_3H_6}]_{out}}{[F_{C_3H_6}]_{out} + \frac{2}{3}[F_{C_2H_6}]_{out} + \frac{2}{3}[F_{C_2H_4}]_{out} + \frac{1}{3}[F_{CH_4}]_{out}} \times 100\ \% \quad (2.12)$$

$$\text{Carbon balance } (\%) = \frac{[F_{C_3H_8}]_{out} + [F_{C_3H_6}]_{out} + \frac{2}{3}[F_{C_2H_6}]_{out} + \frac{2}{3}[F_{C_2H_4}]_{out} + \frac{1}{3}[F_{CH_4}]_{out}}{[F_{C_3H_8}]_{in}} \times 100\ \% \quad (2.13)$$

The terms $[F_i]_{in}$ and $[F_i]_{out}$ denote the flow rate of specific compound i at inlet or outlet in mL min^{-1}, respectively.

The deactivation rate constant k_d (h^{-1}) and expected catalyst lifetime τ (h) were determined by fitting propane conversion data to a first-order deactivation model, using the equation:

$$k_d(h^{-1}) = \frac{\ln\left(\frac{1 - con_{end}}{con_{end}}\right) - \ln\left(\frac{1 - con_{start}}{con_{start}}\right)}{t} \quad (2.14)$$

$$\tau(h) = \frac{1}{k_d} \quad (2.15)$$

Here, con_{stat} and con_{end} represent the initial and final propane conversions, and t denotes the reaction time. A higher k_d value and lower τ value indicate lower catalyst stability.[21]

The WHSV of propane (h^{-1}) was determined using the following equation:

$$\mathrm{WHSV}\ (\mathrm{h}^{-1}) = \frac{\mathrm{F}_{\mathrm{C_3H_8\,in}} \times \mathrm{M}_{\mathrm{C_3H_8}}}{\mathrm{V_m} \times \mathrm{W_{cat}}} \tag{2.16}$$

In this equation, $\mathrm{F}_{\mathrm{C_3H_8\,in}}$ (L h^{-1}) represents the inlet flow rate of propane, $\mathrm{M}_{\mathrm{C_3H_8}}$ (44 g mol^{-1}) is the molar mass of propane, V_m (22.4 mol L^{-1}) corresponds to the standard molar volume at standard temperature and pressure, and W_{cat} (g) denotes the mass of catalyst used in the fixed-bed reactor.

2.4 Process design and life-cycle assessment

2.4.1 Process design

To evaluate the life-cycle impact of the novel plastic-to-propane process discussed in Chapter 5, the laboratory-scale setup was scaled up and simulated using a larger process model. A key consideration in this design was the selection of an appropriate reactor type. Batch reactors (autoclaves) are commonly employed in laboratory experiments due to their simplicity and capability to accommodate multi-product processes. However, they exhibit notable limitations, including batch-to-batch variability, discontinuous operations for industrial applications. Furthermore, the stagnant accumulation of intermediates and products within batch reactors can supress reaction rates and necessitate additional separation steps.

In contrast, continuous reactors, such as fixed-bed reactors, offer superior reaction control and facilitate in-situ analysis of gaseous products. Nonetheless, these systems face significant challenges when handling liquid and solid products. Moreover, the inherent properties of polymers during the reaction, coupled with the absence of internal mixing between the catalysts and the highly viscous melted polymers within the reactor, result in a substantial increase in diffusion resistance. This, in turn, reduces the overall reaction rate compared to batch reactors with continuous stirring.

Both reactor types process distinct advantages and limitations for plastic upcycling. While future research should aim to develop reactor configurations specially tailored to the address

unique properties of molten polymers, a batch reactor was chosen for this simulation to ensure consistency with lab-scale experiments.

The key assumptions used in the process simulation include:

1. **Hydrocracking Conditions**: The reaction parameters were based on experimental data, with the process operating at 30 bar, 280 °C, and a residence time of 8 h.
2. **Membrane Separation**: The separation of hydrogen and flare gases (a mixture of methane, ethane, and minor quantities of propane) was achieved using membrane technology. Separation efficiencies and operating parameters were derived from published data.[22] Using differential permeabilities (H_2/CH_4 = 73.4, H_2/C_2H_6 = 242.9, H_2/C_3H_8 > 1000), the separation efficiencies were estimated as 98.2% for hydrogen, 1.3% for methane, 0.4% for butane, and 0.1% for propane. The pressure drop across the membrane was estimated to be around 4 bar.
3. **Solid Retention**: Solids were assumed to remain entirely within Reactor R-1, and only gaseous products were considered to exit the system.
4. **Reaction Simplification**: The process in Reactor R-1, assumed complete conversion of the plastic feedstock into 3 wt% methane, 13 wt% ethane, 68 wt% propane, 13 wt% butane, 2 wt% pentane, and 1 wt% hexane. The formation of coke was disregarded, as it was not included in subsequent reaction stages.
5. **Steady-State Operation**: All reactors were assumed to function under steady-state conditions throughout the simulation.
6. **Feedstock Consistency**: The plastic feedstock was assumed to have uniform particle size for the entire process.
7. **Uniform Reactor Conditions**: Both temperature and pressure were assumed to be consistent throughout the reactor, with any pressure losses in the system being neglected.
8. **Core Design Parameters**:

- **Batch Reaction**: Each batch cycle, including feedstock loading, hydrogen injection, heating to the required temperature, conducting the hydrocracking reaction, and product recovery, was estimated to take approximately 10 h.
- **Processing Capacity**: Each batch handles about 2.5 tonnes of plastic, with an estimated annual operating time of around 8000 h (about 800 batches per year), giving a total processing capacity of 2000 tonnes of plastic annually.
- **Catalyst Usage**: A plastic-to-catalyst ratio of 10:1 was maintained, consistent with experimental conditions. Catalysts were replaced after every 40 batches, resulting in an annual consumption of 5 tonnes of catalysts. No deactivation was assumed during these cycles.
- **Distillation Parameters**: For distillation DL-1, the reflux ratio was set at 5, with a distillate gas phase fraction of 0.17 and a column pressure drop of approximately 1.3 bar. For DL-2, the reflux ratio was 2.79, with a distillate gas phase fraction of 0.08 and a compressor pressure of approximately 27 bar.

9. **Downstream Process Simplifications**: This study provides a preliminary estimation of downstream operations for propane and other hydrocarbons, with isomer separation excluded from the current design. The separation process has been simplified, and future work should focus on refining separation techniques and optimising downstream processes for a more detailed design.

2.4.2 Life-cycle assessment

LCA is a robust tool for evaluating the environmental impact of processes by analysing key indicators such as global warming potential (GWP). The primary goal of the LCA in Chapter 5 is to access the GWP associated with hydrocracking 1 kg of plastic waste into propane and compare these results with reported GWP values from similar processes.

This LCA adopts a cradle-to-gate system boundary, as depicted in Figure 2.8, encompassing all stages from the collection and sorting of plastic waste to transportation and the hydrocracking process that generates the final products. The hydrocracking process system

involves the hydrocracking operation, dual-stages distillation, membrane separation, and hydrogen recycling (detailed in Chapter 5). Key inputs consist of catalysts, hydrogen, electricity, steam for heating, refrigeration, and cooling water.

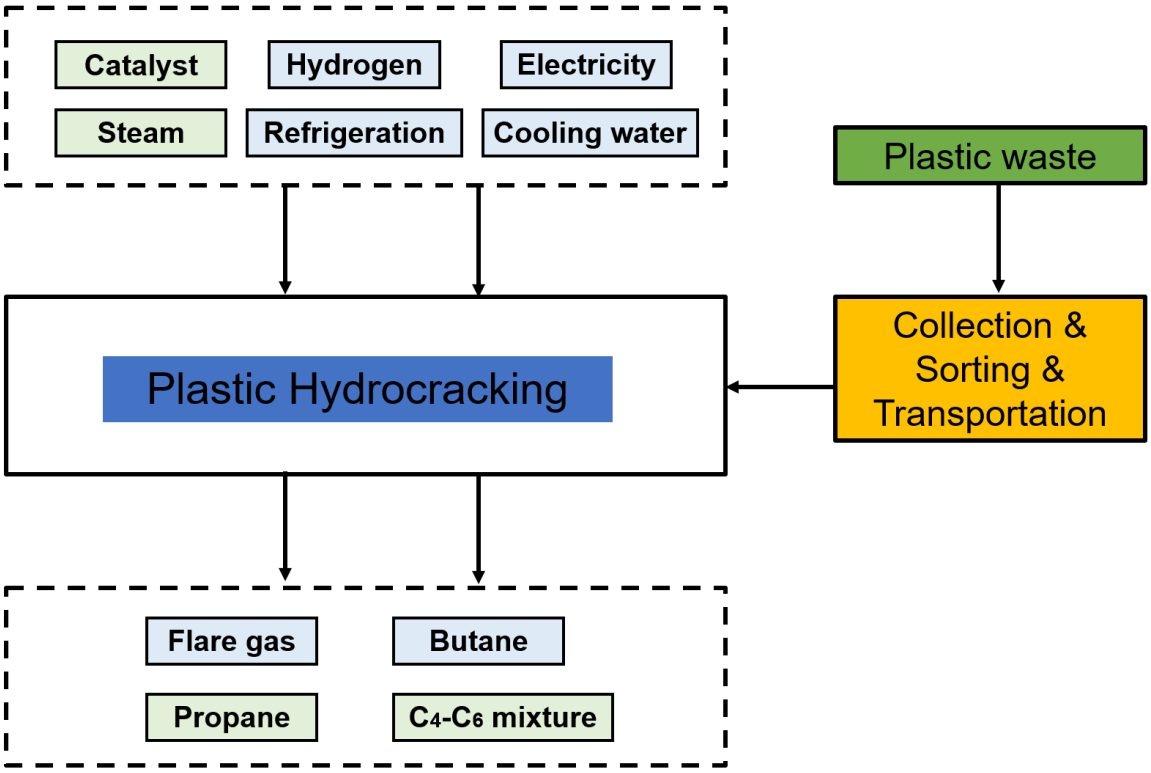

Figure 2.8 Summary of LCA boundaries for plastic hydrocracking to propane.

The GWP was calculated using OpenLCA 2.0 software, drawing on data from the Ecoinvent v3.8 database. Environmental impacts were assessed via the ReCiPe 2016 Midpoint (H) method, with GWP values expressed in kg CO_2e per kg of plastic treated. Comparative GWP data for alternative plastic treatment methods were obtained from relevant literature sources.[23-26]

The major data inputs and assumptions for this LCA are summarised as follows:

- **Catalyst Usage**: The plastic-to-catalyst ratio was set at 10:1, aligned with experimental conditions. Catalysts replacement was assumed every 40 batches, resulting in an estimated annual consumption of 5 tonnes.

- **Hydrogen Consumption**: Hydrogen use accounted for both the reaction itself and losses incurred during separation processes.
- **Power Consumption**: Power requirements were derived from process simulations, factoring in the energy needed to operate the reactors.
- **Heating Steam**: It was assumed that steam for heating was generated using fuel gas.
- **Cooling Requirements**: Ambient-temperature cooling water was used for standard cooling procedures, while refrigeration system was employed for processes requiring temperatures below freezing.

2.5 Reference

1. Waseda, Y., Matsubara, E., and Shinoda, K. (2011). Scattering and Diffraction. In X-Ray Diffraction Crystallography: Introduction, Examples and Solved Problems, Y. Waseda, E. Matsubara, and K. Shinoda, eds. (Springer Berlin Heidelberg), pp. 67-106. 10.1007/978-3-642-16635-8_3.
2. Nasir, S., Hussein, M., Zainal, Z., Yusof, N., Zobir, S., and Alibe, I. (2018). Potential Valorization of By-product Materials from Oil Palm: A review of Alternative and Sustainable Carbon Sources for Carbon-based Nanomaterials Synthesis. Bioresources *14*. 10.15376/biores.14.1.Nasir.
3. Birkholz, M. (2006). Principles of X-ray Diffraction. Thin Film Analysis by X-Ray Scattering *1*, 1-40.
4. Garlisi, C., Scandura, G., Szlachetko, J., Ahmadi, S., Sa, J., and Palmisano, G. (2016). E-beam evaporated TiO2 and Cu-TiO2 on glass: Performance in the discoloration of methylene blue and 2-propanol oxidation. Applied Catalysis A: General *526*, 191-199. 10.1016/j.apcata.2016.08.022.
5. Van der Heide, P. (2011). X-ray photoelectron spectroscopy: an introduction to principles and practices (John Wiley & Sons).
6. Palmisano, G., Jitan, S.A., and Garlisi, C. (2022). Chapter 7 - Characterization techniques. In Heterogeneous Catalysis, G. Palmisano, S.A. Jitan, and C. Garlisi, eds. (Elsevier), pp. 243-314. 10.1016/B978-0-323-89845-4.00008-4.
7. Deng, F., Yang, J., and Ye, C. (2006). Solid State NMR Characterization of Solid Surface of Heterogeneous Catalysts. In Modern Magnetic Resonance, G.A. Webb, ed. (Springer Netherlands), pp. 205-211. 10.1007/1-4020-3910-7_25.
8. Bell, A.T. (1994). NMR techniques in catalysis (CRC Press).

9. Marwa, E.-A. (2018). Introductory Chapter: Infrared Spectroscopy - A Synopsis of the Fundamentals and Applications. In Infrared Spectroscopy, E.-A. Marwa, ed. (IntechOpen), pp. Ch. 1. 10.5772/intechopen.82210.
10. Bañares, M.A., and Wachs, I.E. Raman Spectroscopy of Catalysts. In Encyclopedia of Analytical Chemistry. 10.1002/9780470027318.a9034.
11. Sing, K.S.W. (1985). Reporting physisorption data for gas/solid systems with special reference to the determination of surface area and porosity (Recommendations 1984). Pure and Applied Chemistry *57*, 603-619. doi:10.1351/pac198557040603.
12. Leofanti, G., Padovan, M., Tozzola, G., and Venturelli, B. (1998). Surface area and pore texture of catalysts. Catalysis Today *41*, 207-219. 10.1016/S0920-5861(98)00050-9.
13. ALOthman, Z.A. (2012). A Review: Fundamental Aspects of Silicate Mesoporous Materials. Materials *5*, 2874-2902.
14. Yurdakal, S., Garlisi, C., Özcan, L., Bellardita, M., and Palmisano, G. (2019). Chapter 4 - (Photo)catalyst Characterization Techniques: Adsorption Isotherms and BET, SEM, FTIR, UV–Vis, Photoluminescence, and Electrochemical Characterizations. In Heterogeneous Photocatalysis, G. Marcì, and L. Palmisano, eds. (Elsevier), pp. 87-152. 10.1016/B978-0-444-64015-4.00004-3.
15. Thomas, J.M., and Thomas, W.J. (2014). Principles and practice of heterogeneous catalysis (John Wiley & Sons).
16. Gervasini, A. (2013). Temperature Programmed Reduction/Oxidation (TPR/TPO) Methods. In Calorimetry and Thermal Methods in Catalysis, A. Auroux, ed. (Springer Berlin Heidelberg), pp. 175-195. 10.1007/978-3-642-11954-5_5.
17. Williams, D.B., and Carter, C.B. (1996). The Transmission Electron Microscope. In Transmission Electron Microscopy: A Textbook for Materials Science, D.B. Williams, and C.B. Carter, eds. (Springer US), pp. 3-17. 10.1007/978-1-4757-2519-3_1.
18. Inkson, B.J. (2016). 2 - Scanning electron microscopy (SEM) and transmission electron microscopy (TEM) for materials characterization. In Materials Characterization Using Nondestructive Evaluation (NDE) Methods, G. Hübschen, I. Altpeter, R. Tschuncky, and H.-G. Herrmann, eds. (Woodhead Publishing), pp. 17-43. 10.1016/B978-0-08-100040-3.00002-X.
19. Zheng, X., Li, Y., Zhang, L., Shen, L., Xiao, Y., Zhang, Y., Au, C., and Jiang, L. (2019). Insight into the effect of morphology on catalytic performance of porous CeO2 nanocrystals for H2S selective oxidation. Applied Catalysis B: Environmental *252*, 98-110. 10.1016/j.apcatb.2019.04.014.
20. Loganathan, S., Valapa, R.B., Mishra, R.K., Pugazhenthi, G., and Thomas, S. (2017). Chapter 4 - Thermogravimetric Analysis for Characterization of Nanomaterials. In

Thermal and Rheological Measurement Techniques for Nanomaterials Characterization, S. Thomas, R. Thomas, A.K. Zachariah, and R.K. Mishra, eds. (Elsevier), pp. 67-108. 10.1016/B978-0-323-46139-9.00004-9.

21. Nakaya, Y., Hirayama, J., Yamazoe, S., Shimizu, K.-i., and Furukawa, S. (2020). Single-atom Pt in intermetallics as an ultrastable and selective catalyst for propane dehydrogenation. Nature Communications *11*, 2838. 10.1038/s41467-020-16693-9.
22. Topuz, B., Yilmaz, L., and Kalipcilar, H. (2012). Development of alumina supported ternary mixed matrix membranes for separation of H2/light-alkane mixtures. Journal of Membrane Science *415-416*, 725-733. 10.1016/j.memsci.2012.05.060.
23. Kilgore, G. (2024). 2023 Plastic Carbon Footprint: Official Emissions Numbers + Calculator. https://8billiontrees.com/carbon-offsets-credits/carbon-ecological-footprint-calculators/plastic-carbon-footprint/.
24. GAIA (2023). Plastic is Carbon Unwrapping the "net zero" myth. https://www.no-burn.org/wp-content/uploads/2021/11/Plastic-is-Carbon-Oct2021.pdf.
25. Xayachak, T., Haque, N., Lau, D., Parthasarathy, R., and Pramanik, B.K. (2023). Assessing the environmental footprint of plastic pyrolysis and gasification: A life cycle inventory study. Process Safety and Environmental Protection *173*, 592-603. 10.1016/j.psep.2023.03.061.
26. Li, L., Luo, H., Shao, Z., Zhou, H., Lu, J., Chen, J., Huang, C., Zhang, S., Liu, X., Xia, L., et al. (2023). Converting Plastic Wastes to Naphtha for Closing the Plastic Loop. Journal of the American Chemical Society *145*, 1847-1854. 10.1021/jacs.2c11407.

Chapter 3 Ce-Promoted PtSn-Based Catalysts for Hydrocracking of Polyolefin Plastic Waste into High Yield of Gasoline-Range Products

This chapter is adapted from the work by Haokun Wang, Tatchamapan Yoskamtorn, Jianwei Zheng, Ping-Luen Ho, Bryan Ng, and Shik Chi Edman Tsang, published in ACS Catalysis in 2023.[1] The figures and tables are reproduced with permission. Copyright 2023 CC-BY 4.0.[1]*

3.1 Introduction

Since the onset of large-scale plastic production in the 1950s, these materials have profoundly impacted modern society owing to their cost-effectiveness, lightweight properties, durability, and versatility, which enabled their widespread applications across numerous fields.[2-6] However, the extensive use of plastics has also led to significant environmental challenges due to inadequate waste management practices, low recycling rate, and persistent nature of plastic, resulting in considerable losses of material value.[3,7-11] In 2019, global plastic production reached approximately 380 million tons, with projections indicating that this figure will surpass 1200 million tons annually by 2050.[12,13] Alarmingly, only around 9% of plastic waste is recycled, while roughly 79% accumulates in landfills, polluting the natural environment.[2] The situation has been further exacerbated by the increased use of single-use personal protective equipment (PPE) during the COVID-19 pandemic, including items such as surgical masks, gloves, gowns.[14,15]

Traditional approaches to plastic management, such as mechanical recycling, are often energy-intensive and tend to yield products of reduced material quality and value.[3-5,16-18] Incineration is another widely adopted method, which facilitates energy recovery through combustion. However, it also results in the emission of carcinogenic gases due to incomplete combustion, posing significant risks to both human health and the environment.[7,19,20] Chemical recycling, in contrast, offers a more promising solution by converting plastic waste into monomers or high-value fuels, such as gasoline (C_5-C_{12}) and diesel (C_9-C_{22}).[12,21] Among

chemical recycling methods, pyrolysis is particularly notable, involving the thermal decomposition of plastics at high temperatures (typically above 500 °C) in the absence of oxygen to produce fuel oils, natural gas, and solid fuels.[20,22-24] However, pyrolysis presents challenges such as high energy consumption, complex operational demands, and low selectivity for fuel oils, limiting its economic viability on an industrial scale. Hydroconversion-based chemical recycling, on the other hand, provides an alternative approach with the potentials to efficiently convert plastic waste into valuable products under milder conditions.

In recent years, hydroconversion processes have attracted considerable attention due to their ability to operate at relatively low reaction temperatures (typically from 200 to 300 °C) while achieving high selectivity for fuel-range products.[25] Significant advancements have been made in the hydroconversion of various PO, including LDPE, HDPE, PP, which together constitute a large proportion of plastic waste due to their widespread and low cost.[26] These studies have demonstrated the feasibility of achieving high yields of fuel-range products at low temperatures and have provided valuable insights into the underlying reaction mechanisms.[9,12,27-31] Despite these advances, challenges persist in optimising selectivity for fuel products, such as gasoline, and in maintaining the stability of hydrocracking catalysts. The mechanisms governing product distribution and catalyst deactivation remain inadequately understood, hindering efforts to improve catalyst performance and scale up for industrial applications.

In this chapter, a comprehensive study on the incorporation of Ce into PtSn hydrocracking catalysts supported on amorphous SiAl was introduced. Through systematic optimisation of Ce loading, hydrogen pressure, reaction temperature, and reaction time, a substantial gasoline yield of 77.1 wt% from HDPE conversion using a catalyst with 0.5 wt% Ce loading was achieved, under reaction conditions of 270 °C and 30 bar H_2 for 2 h. Additionally, high yield and selectivity were observed across a range of plastics and mixtures, including commercial plastics containing impurities. The catalysts also demonstrated stable

performance during recycling tests, thus indicating their potentials for reuse in practical applications.

3.2 Results and discussion

3.2.1 Initial catalyst screening

Hydrocracking of PO plastics typically employs bifunctional catalysts, which consist metals like Pt, Ru, Rh to activate C-H bonds, in conjunction with solid acid supports, such as zeolites, to facilitate the cracking process.[25,28] Pt has been chosen for this study due to its established superiority in industrial processes, particularly for its robust dehydrogenation and hydrogenation functions.[26] The selection of support material is a critical factor as well; the microporous and mesoporous structures within the support can greatly influence the product distribution. Zeolites with a high ratio of micropores to mesopores (e.g., ZSM-5, MOR and BEA) tend to cause higher diffusion resistance, leading to deeper polymer cracking and an increased yield of low-value gaseous byproducts. Conversely, amorphous SiAl, which processes a lower micropore-to-mesopore ratio, can mitigate diffusion resistance and favour the production of larger, more valuable products. This study focuses on this characteristic, thus Pt/SiAl was selected as the baseline catalyst for further examination.

As illustrated in Figure 3.1 (a), the initial Pt/SiAl catalyst exhibited limited efficiency, producing a relatively small fraction of fuel-range products (C_5-C_{12} for gasoline and C_9-C_{22} for diesel) when applied to the conversion of HDPE (Mw, ~97 kDa) under 30 bar of hydrogen for 2 h. The process primarily generated low-value outputs, including 22.0% extensively cracked gaseous hydrocarbons (C_1-C_4) and 35.8% solid residues (comprising non-solvent extractable carbonaceous species and coke). However, by incorporating Sn into the Pt/SiAl system, a significant enhancement in performance was observed, with substantial reduction in solid residues and a shift towards a narrower range of fuel products (Figure 3.1 (a)). This improvement can be attributed to the formation of PtSn alloys, which confers both ‘‘geometric’’ and ‘‘electronic’’ benefits to the catalyst. Geometrically, the additions of Sn facilitates the creation of smaller Pt ensembles, improving Pt dispersion across the support surface and

reducing coke formation by preventing excessive C-C cleavage during the reaction.[32] Electronically, Sn donates electrons to Pt atoms, thereby weakening molecular adsorption on Pt and promoting the migration of carbonaceous species from Pt to the support interface.[33]

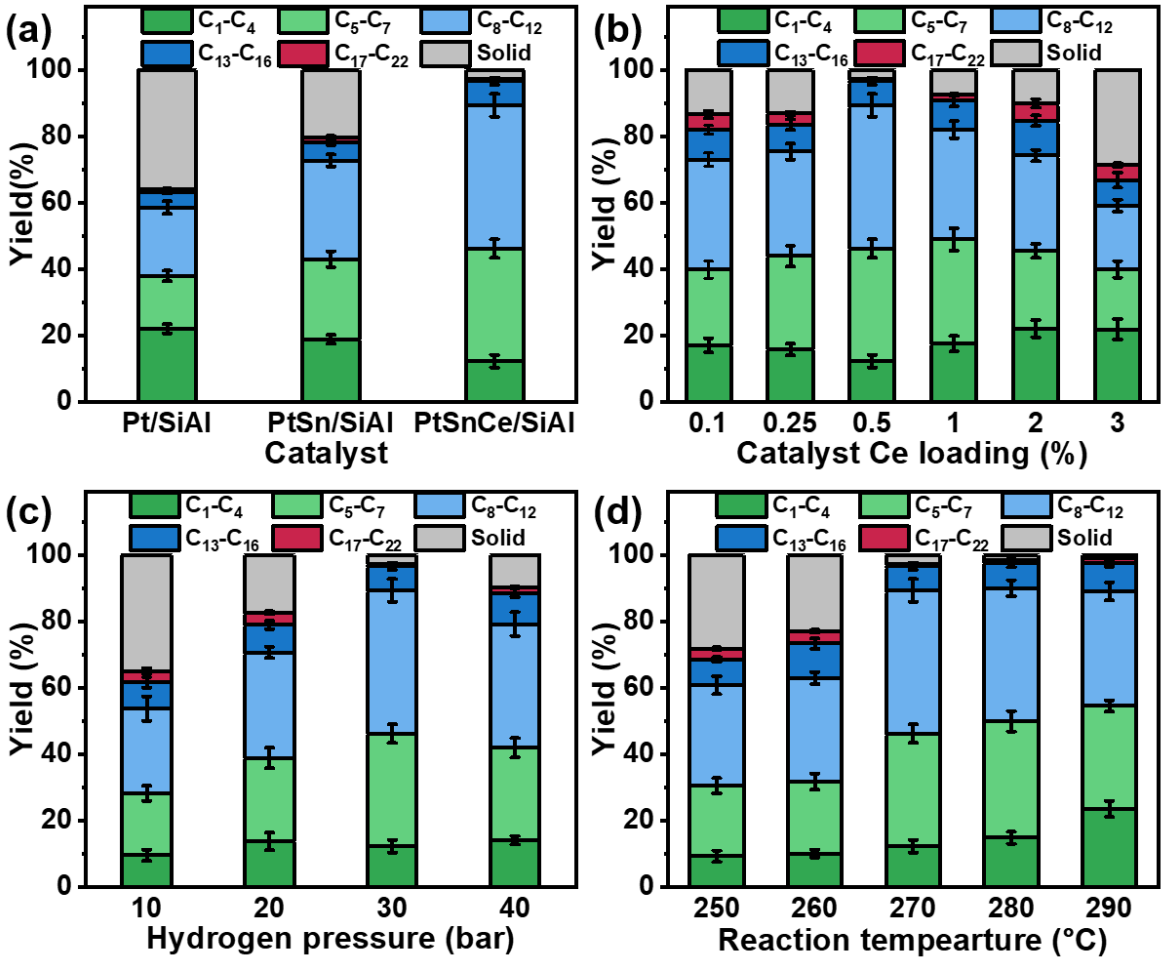

Figure 3.1 Product distribution over different Pt-based catalysts under different reaction conditions. (a) Different Pt-based catalysts at 270 °C, 2 h, 30-bar H_2, 2 g HDPE, 0.2 g catalysts. (b) 270 °C, 2 h, 30-bar H_2, 2 g HDPE, 0.2g PtSnCe/SiAl catalyst with different Ce loadings. (c) 270 °C, 2 h, 2 g HDPE, 0.2 g PtSn-0.5Ce/SiAl catalyst with different hydrogen pressures. (d) 2 h, 2 g HDPE, 0.2 g PtSn-0.5Ce/SiAl catalyst with different reaction temperatures. All mass balances are in the range of 97±3%.

Additionally, the inclusion of an optimal amount of Ce into the PtSn/SiAl catalyst further refines the C-C bond cleavage process within HDPE framework, achieving 77.1% gasoline yield while significantly reducing the production of solid residues from 20.3% to 2.6% and gaseous byproducts from 18.9% to 12.3%. The impact of varying Ce loadings on product distribution is

further demonstrated in Figure 3.1 (b), showing a progression from light (gaseous) and solid byproducts towards mid-range hydrocarbons (gasoline and diesel) as Ce loading increases from 0.1 wt% to 0.5 wt%. However, a Ce content exceeding 1 wt% leads to a reversal of this trend, characterised by an increase in solid residues. This could be due to the physical blocking of micropores, limiting access to the internal PtSn surface, or the deposition of thick Ce layers on the active sites, leading to catalyst passivation. Further characterisation is required to determine the precise cause.

An increase in hydrogen pressure to 30 bar, as depicted in Figure 3.1 (c), significantly enhances HDPE decomposition, reaching a peak gasoline yield of 77.1%. However, further increase in pressure (e.g., 40 bar) disrupt the alkane-olefin equilibrium, reducing the formation of active olefin intermediates, and resulting in increased solid residues and the production of more deeply cracked gaseous products.[12,34] An examination of reaction temperature (Figure 3.1 (d)) indicates that HDPE conversion is highly temperature-sensitive, with negligible solid residues observed above 270 °C. Further increase in temperature results in higher production of deeply cracked gaseous products, which detracts from gasoline yields.

3.2.2 Catalyst and solid residue characterisation

To address the possibility of pore blockage at higher Ce loadings, a detailed examination of the physicochemical properties of the fresh catalysts was conducted. The PtSn-based catalysts demonstrated consistent adsorption-desorption isotherm profiles (Figure 3.2 (a)) and similar pore size distributions (Figure 3.2 (b)). Notably, increasing Ce content up to 3 wt% did not significantly impact the specific surface areas and pore characteristics of the catalysts, as outlined in Table 3.1. Additionally, negative t-plot micropore values indicated that the SiAl support is predominantly mesoporous, with negligible microporosity. This suggests that even at 3 wt% Ce loadings, the risk of micropore blockage is minimal, thus eliminating it as a contributing factor to the observed decrease in catalytic efficiency.

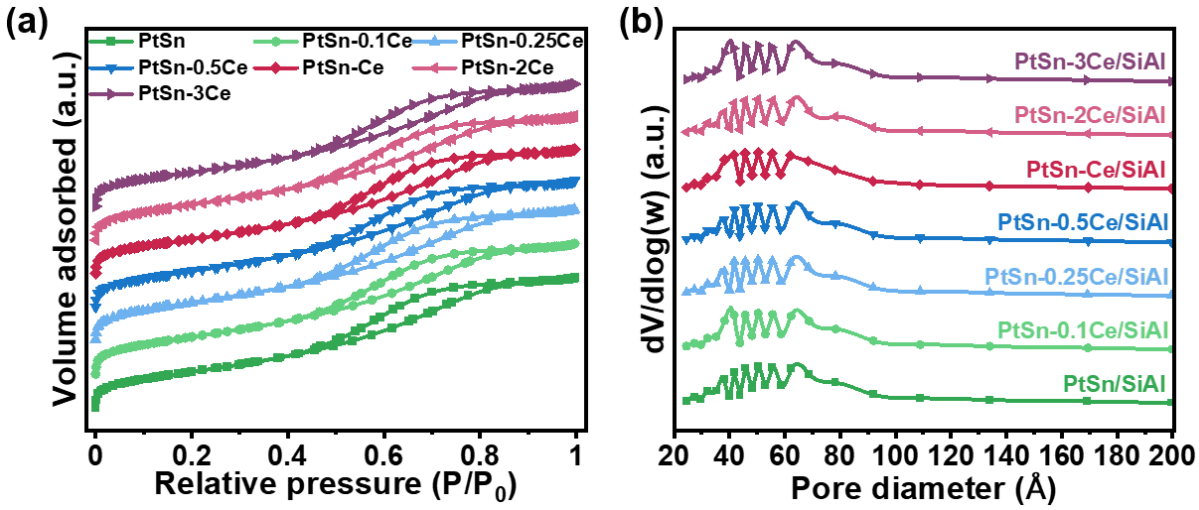

Figure 3.2 Surface area and pore characterisation of different PtSn-based catalysts. (a) N_2 adsorption-desorption isotherms of different catalysts. (b) Pore size distribution over different catalysts.

Table 3.1 Physicochemical characterisation of PtSn-based catalysts.

Catalyst	Specific area (m^2g^{-1})	Pore volume (cm^3g^{-1})	Average pore size (nm)
PtSn/SiAl	410	0.69	6.11
PtSn-0.1Ce/SiAl	421	0.69	5.97
PtSn-0.25Ce/SiAl	429	0.69	5.89
PtSn-0.5Ce/SiAl	412	0.67	5.93
PtSn-Ce/SiAl	400	0.66	6.01
PtSn-2Ce/SiAl	408	0.66	5.89
PtSn-3Ce/SiAl	398	0.65	5.94

Further insights were gained through XRD analysis, shown in Figure 3.3. In the Pt/SiAl catalyst, characteristic diffraction peaks corresponding to metallic Pt were observed at 39.8°, 46.3°, 67.5° and 81.4°, representing the (111), (200), (220), and (311) planes of cubic closest-packed (CCP) structure (AMCSD no:0011157). The addition of Sn resulted in the formation of PtSn alloys, as indicated by diffraction peaks at 25.1° (100), 30.1°(101), 41.9°(102), 44.2°(110), 62.5° (202), and 79.7°(212) (AMCSD no: 0011591). However, with Ce loadings of 2 wt% or

higher, the relative intensities of these PtSn peaks diminished significantly. This suggests that thicker Ce deposits on PtSn metallic sites might disrupt the crystalline structure of PtSn alloys, potentially altering the adsorption-desorption dynamics of intermediates and affecting catalytic performance. Despite variations in Ce loading, the XRD patterns of Ce-modified PtSn/SiAl catalysts remained consistent, likely due to the low Ce concentration (≤3 wt%) and the small size of cerium crystallites, which may fall below the detection limit of XRD.[35]

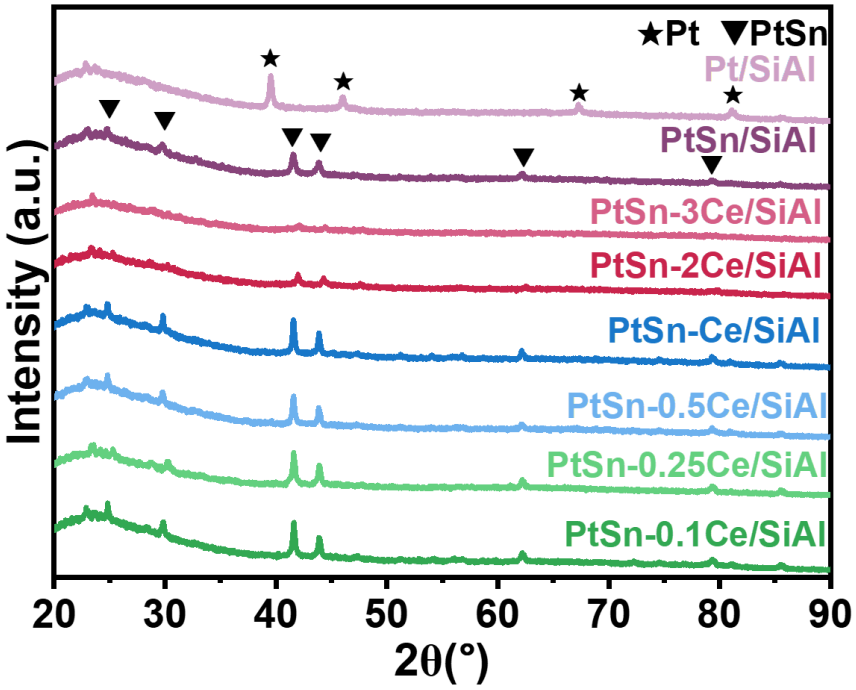

Figure 3.3 XRD patterns of all catalysts.

To further assess the properties of solid residues post-reaction, GPC was employed. The molecule weight distribution profiles of these residues are illustrated in Figure 3.4. The curves generally exhibit two main peaks centred around logMw values of 2.3 and 4.8, corresponding to heavy wax products and unreacted polymer, respectively. The addition of Sn to the Pt/SiAl system significantly enhanced its hydrocracking efficiency, as evidenced by the reduction in unreacted polymer content and an increase in wax products. Moreover, increase Ce loading from 0 wt% to 0.5 wt% further increased heavy wax yield while reducing the amount of unreacted polymer. This suggests that Ce effectively promotes C-C bond cleavage, facilitating HDPE decomposition and resulting in the formation of heavy wax residues within the catalysts.

This evidence points that incorporating Ce considerably enhances the conversion of unprocessed polymer into wax products, with this promotion having a direct correlation with Ce content. However, when Ce loading is increased beyond 0.5 wt% to 3 wt%, there was a noticeable increase in unreacted polymer, coupled with a reduction in heavy wax production. The substantial rise in total peak areas observed in Figure 3.4 suggests that excessive Ce doping impedes complete plastic conversion, leading to a larger fraction of unreacted polymer. The dynamic relationship between unreacted polymer and heavy wax production suggests that the amount of heavy wax products can serve as a key indicator of hydrocracking efficiency, with optimal catalysts producing more heavy wax products and leaving minimal unreacted polymer.

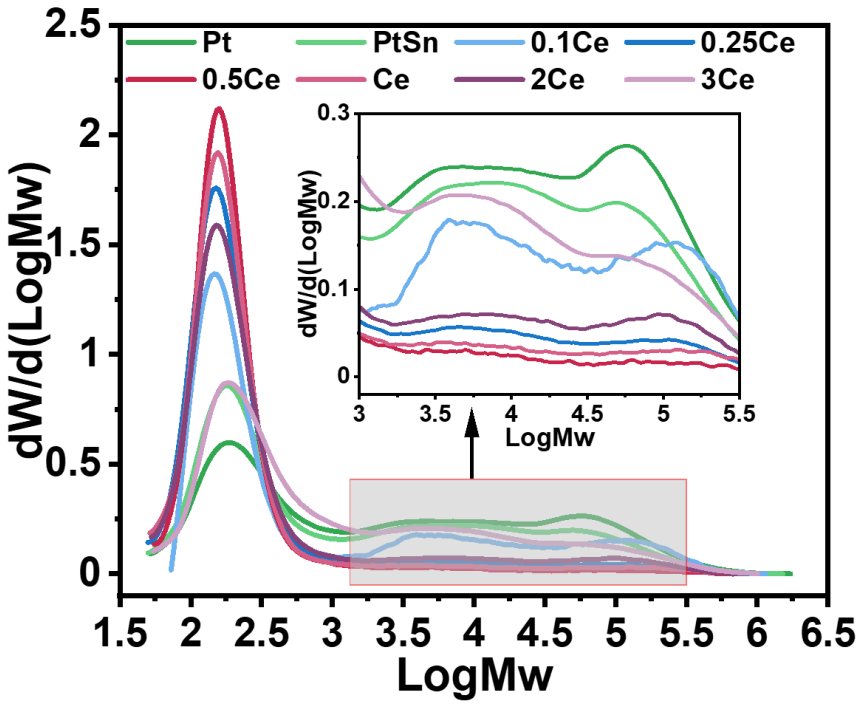

Figure 3.4 GPC analysis of solid residues obtained over various catalysts, with an enlarged inset highlighting detailed results in the LogMw range of 3 to 5.5.

To quantify the coke content in spent catalysts, TG analysis was performed under an air atmosphere up to 700 °C. As illustrated in Figure 3.5, the spent PtSn-0.5Ce/SiAl catalyst exhibited significantly lower coke content (approximately 1.2 wt%) than that of other Ce-

containing catalysts and those without Ce (around 2.9 wt%), indicating its superior coke resistance capability and higher stability.

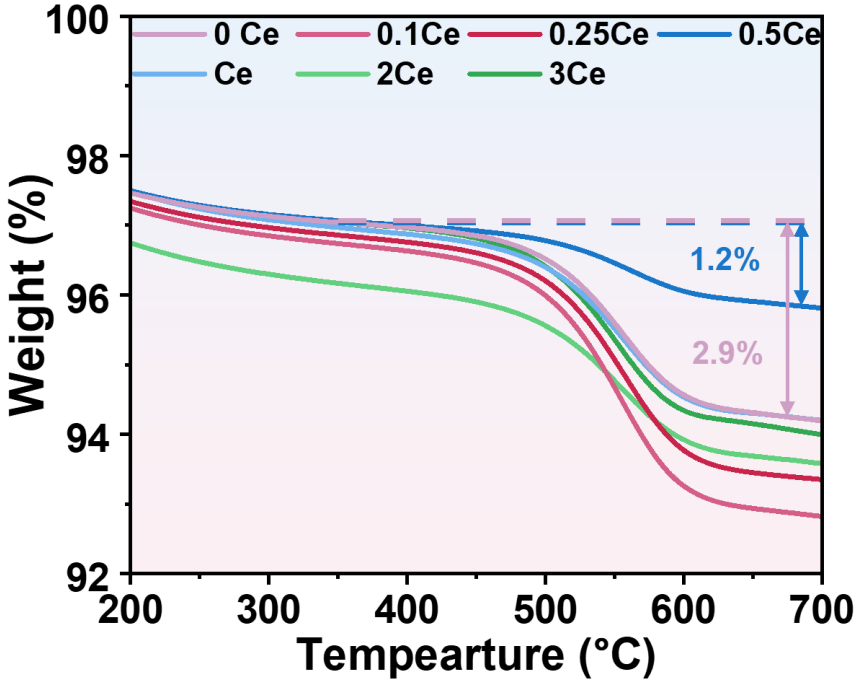

Figure 3.5 TG analysis for all spent catalysts in air.

The efficiency of hydrocracking reactions is strongly influenced by acidity of catalysts involved. To assess this relationship, NH_3-TPD and Py-IR were employed. As shown in Figure 3.6, the NH_3-TPD analysis reveals three distinct deconvoluted peaks within the temperature range of 50 to 800 °C. These peaks correspond to weak acid sites (red dashed lines), medium acid sites (blue dashed lines), and strong acid sites (green dashed lines), classified by their respective desorption temperatures. The strong acid sites, which correlate with NH_3 desorption above 400 °C, are particularly critical in hydrocracking due to their association with strong BAS. When compared to the PtSn/SiAl system, all Ce-modified catalysts displayed higher desorption temperatures for each peak (Table 3.2), reflecting an enhancement in acid site strength. Specially, while the strength of weak and medium acid sites showed a moderate increase, the strong acid sites exhibited a substantial rise, exceeding 60 °C. The total acid site concentration increased with Ce content up to 0.5 wt%, stabilising around 80 (a.u.) total area beyond this loading. Despite the overall rise in acid site concentration, the increase in weak

and medium acid sites was relatively modest compared to the significant enhancement observed in strong acid sites.

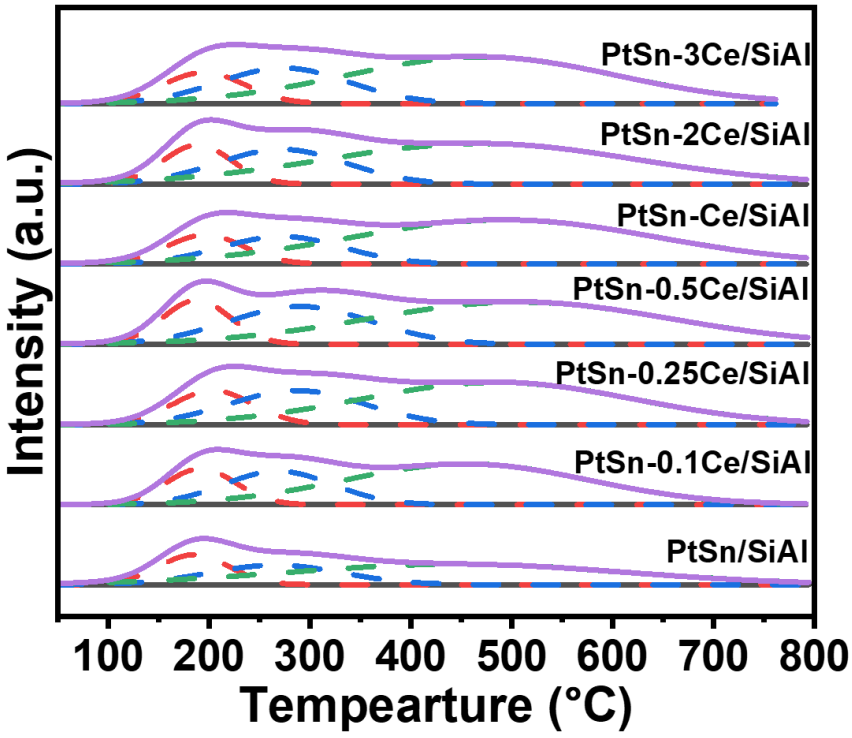

Figure 3.6 NH_3-TPD profiles for all catalysts.

Table 3.2 Summary of acidity results from NH_3-TPD and Py-IR.

Catalyst	Tm (°C) from NH_3-TPD			NH_3-TPD peak area (a.u.)	Acidity from Py-IR (μmol g cat^{-1})		LAS/BAS ratio from Py-IR
	I	II	III		LAS	BAS	
PtSn/SiAl	185	266	446	44	24.3	14.0	1.7
PtSn-0.1Ce/SiAl	192	268	455	62	27.0	19.8	1.4
PtSn-0.25Ce/SiAl	204	287	486	73	32.5	23.4	1.4
PtSn-0.5Ce/SiAl	188	290	508	80	41.1	37.4	1.1
PtSn-Ce/SiAl	196	272	493	74	44.9	27.1	1.7
PtSn-2Ce/SiAl	191	272	470	76	44.2	25.8	1.7
PtSn-3Ce/SiAl	194	274	470	76	47.2	27.1	1.7

Given the limitation of NH_3-TPD in characterising the nature of strong acid, Py-IR spectroscopy was further conducted at a desorption temperature of 350 °C to quantify the concentration of strong BAS and LAS. Figure 3.7 shows peaks at approximately 1450 cm^{-1} and 1550 cm^{-1}, which correspond to the interactions between pyridine and LAS and BAS, respectively. These measurements, consistent with Beer-Lambert-Bouguer law, allowed for the calculation of acid site concentrations, as summarised in Table 3.2.[36] The trends observed in the strong LAS and BAS concentrations mirror those obtained from NH_3-TPD. Specially, both LAS and BAS concentrations increased as Ce loading rose from 0 wt% to 0.5 wt%. Beyond this point, further increases in Ce loading resulted in a slight increase in LAS, while BAS concentrations remained relatively unchanged, with 0.5 wt% Ce exhibiting the highest strong BAS concentration among all catalysts, correlating with optimal catalytic performance.

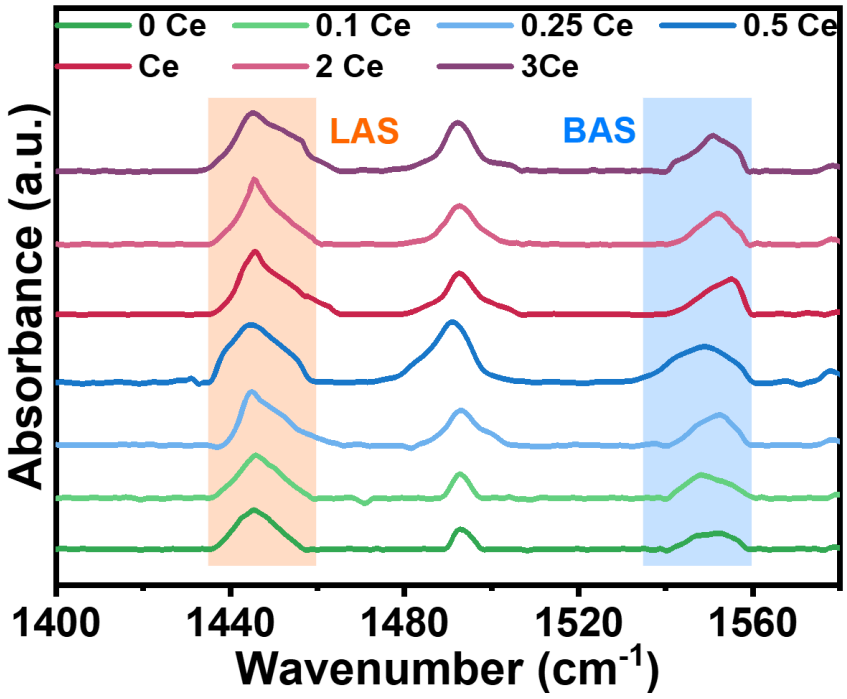

Figure 3.7 Py-IR profiles for all catalysts at desorption temperature of 350 °C.

Previous studies have shown that doping rare earth metals, such as La, Ce Pr, Nd, Sm, Eu into ZSM-5 zeolite enhances the strength and concentration of solid acids.[37] This enhancement is primarily attributed to the increased hydrothermal stability of the zeolite, which arises from the coordination of these cations with oxygen atoms in the pore channels. During

calcination and pretreatment, the coordination mitigates framework dealumination, thereby preserving acid centres. Additionally, the polarisation and induction effects of cerium cations on silicon and aluminium hydroxyl groups within SiAl framework increase electron density, resulting in stronger acidity. The enhanced strength and concentration of BAS due to Ce doping facilitate skeletal rearrangement and β-scission processes in the hydrocracking reaction, thereby explaining the superior catalytic performance observed.

3.2.3 Redox properties and electronic promotion

To explore the potential redox interactions between Pt and Ce in the catalytic system, H_2-TPR was employed on a series of freshly synthesised catalysts. The H_2-TPR profiles of the Pt/SiAl catalyst, depicted in Figure 3.8, reveals two distinct reduction peaks at 290 °C and 470 °C. These peaks correspond to weak and strong interactions between Pt oxides and the support, likely due to the variation in Pt oxide particle sizes supported on the substrate.[38,39] Previous research suggests that Sn^{4+} is reduced to Sn^{2+} at temperatures below 500 °C, correlating with a significant reduction peak observed in the Sn/SiAl catalyst at 446 °C.[40,41] Reduction peaks observed at higher temperature may be attributed to the transition from bulk Sn^{4+} to Sn^{2+} and the subsequent conversion of Sn^{2+} to Sn^0.[40,42] When Sn is integrated into Pt/SiAl matrix, a broad reduction peak emerges at 338 °C, indicating strong Pt-Sn interactions and suggesting the formation of a PtSn alloy phase, as confirmed by XRD analysis.[43] The total hydrogen consumption by PtSn/SiAl catalyst is notably higher than that required for Pt oxide reduction alone, but still lower than the amount needed for complete SnO_2 reduction. This suggests that some SnO_2 species undergo partial reduced without full conversion to Sn^0, a hypothesis that will be supported by XPS data later.

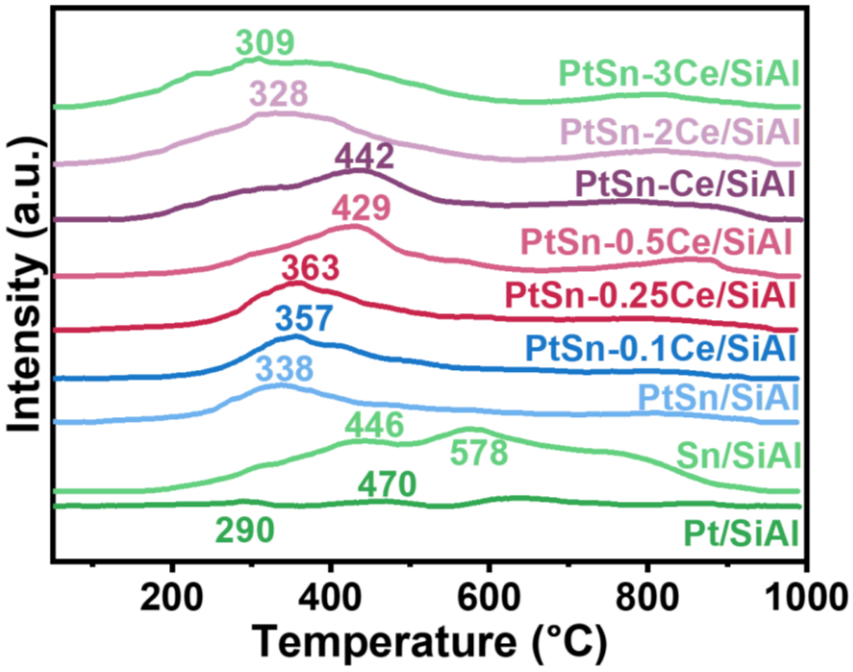

Figure 3.8 H_2-TPR profiles of different catalysts.

As the Ce content increases from 0 wt% to 3 wt%, the primary reduction peak broadens considerably, and the onset reduction temperature for reduction decreases, indicating stronger redox interactions within the catalytic components. This could be associated with the reversible hydrogen spillover from metal sites to the redox-active support.[35] Additionally, the total area under the reduction peaks increases with higher Ce loading, reflecting greater hydrogen consumption. However, the presence of Ce appears to inhibit the reduction of Sn oxides, likely due to its preferential reduction, as confirmed by XPS later.[44] Thus, the increased hydrogen consumption can be ascribed to the reduction of Ce species (from Ce^{4+} to Ce^{3+} in substituted lattice) and the facilitated reduction of Pt species in the presence of Ce. Literature also suggests that Ce imparts a significant electronic influence on Pt surfaces, thereby enhancing Pt's redox characteristics.[45] Notably, the maximum reduction peak temperatures shift to higher values at lower Ce loadings, while at higher Ce loadings (2-3 wt%), the peak maxima shift to lower temperatures, possibly due to the reduction of the CeO_x phase.

XPS analysis was employed to analyse the chemical states, and surface electronic properties of the reduced catalysts, as shown in Figure 3.9 (a) and (b). The binding energies for $Pt4d_{5/2}$

and $Sn3d_{5/2}$ are detailed in Table 3.3. Although Pt typically exhibits its most intense photoemission in the 4f orbital, this region is obscured by a strong Al 2p peak, necessitating the analysis of Pt 4d lines.[46,47] The Pt $4d_{5/2}$ peak, as shown in Figure 3.9 (a), can be deconvoluted into two components: one at lower binding energy corresponding to the metallic Pt^0, and another at higher binding energy representing oxidised Pt species.[44,48] Notably, the introduction of Ce enhances the reduction of Pt oxides, leading to an increased proportion of Pt^0 (as shown in Table 3.3), which enhances the catalyst's dehydrogenation and hydrogenation capabilities during the hydrocracking of HDPE. Interestingly, the catalyst with the highest Pt^0 content is observed at a Ce loading of 0.5 wt%, whereas higher Ce contents appear to obstruct active sites, thereby hindering the reduction of Pt oxides to metallic Pt.

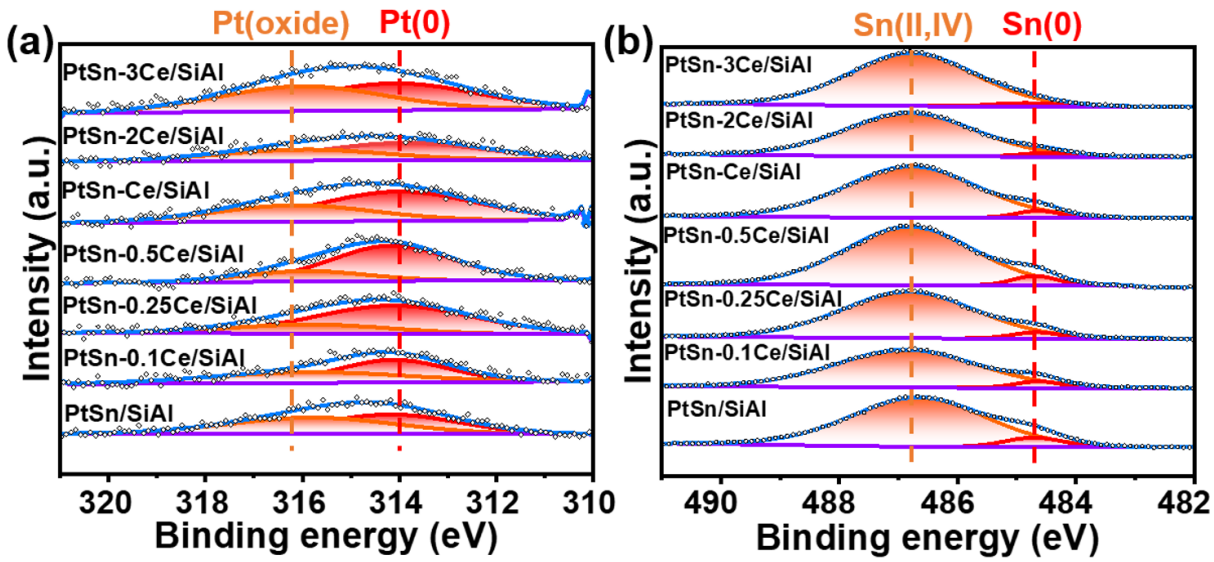

Figure 3.9 XPS spectra of (a) Pt $4d_{5/2}$ and (b) Sn $3d_{5/2}$ over different reduced catalysts.

Table 3.3 Curve-fitting parameters for XPS spectra over different reduced catalysts.

Catalyst	Binding Energy (eV)			
	Pt $4d_{5/2}$		$Sn3d_{5/2}$	
PtSn/SiAl	314.2 (49.1%)	315.8 (50.9%)	484.7 (7.9%)	486.7 (92.1%)
PtSn-0.1Ce/SiAl	314.1 (54.2%)	315.8 (45.8%)	484.6 (5.3%)	486.9 (94.7%)
PtSn-0.25Ce/SiAl	314.1 (75.6%)	315.8 (24.4%)	484.7 (4.5%)	486.8 (95.5%)
PtSn-0.5Ce/SiAl	314.1 (77.2%)	315.9 (22.8%)	484.7 (5.3%)	486.8 (94.7%)
PtSn-Ce/SiAl	314.0 (64.3%)	316.1 (35.7%)	484.6 (4.4%)	486.8 (95.6%)
PtSn-2Ce/SiAl	313.9 (61.2%)	315.9 (38.8%)	484.5 (3.6%)	486.8 (96.5%)
PtSn-3Ce/SiAl	314.0 (52.1%)	316.0 (47.9%)	484.9 (3.2%)	486.8 (96.8%)

The XPS results for Sn $3d_{5/2}$, depicted in Figure 3.9 (b), display an asymmetric peak, reflecting contributions from the sum of two different contributions [Sn^{ox}(Sn^{2+}, Sn^{4+}) and Sn^0].[49] The lower binding energy component corresponds to metallic Sn^0, while the higher binding energy component is associated with oxidised Sn (Sn^{2+}, Sn^{4+}).[49,50] Interestingly, the presence of Ce, known for its strong redox activity, suppresses the reduction of Sn oxides to Sn^0, an effect that becomes more pronounced with increasing Ce loading. This finding aligns with previous reports indicating competitive reduction effects between Ce doping on Sn oxides.[44,51] The oxidation state of Sn is crucial to catalytic performances, as excessive reduction to Sn^0 can deactivate Pt, whereas Sn oxides (Sn^{2+}, Sn^{4+}) function as effective promotors.[52] The formation of Sn^0 can inhibit catalytic activity over PtSn by enriching the catalytic surface with an inactive Sn layer.[53] Thus, maintaining a higher ratio of Sn oxides (Sn^{2+}, Sn^{4+}) in the presence of Ce is likely to enhance the catalytic performance of the PtSn system. Similar trends have been observed in La_2O_3-modified PtSn catalysts, where an increase in La content resulted in a reduction of metallic Sn content.[54] The XPS spectra of the Ce 3d region were collected and analysed; however, no meaningful insights could be derived from the data, and thus these spectra are not presented here. Additionally, surface atomic ratios obtained via XPS were not determined, as the primary focus of the XPS analysis was to examine the modifications in the electronic environment of Pt and Sn species induced by varying cerium loadings.

3.2.4 Time-dependent reaction network and hydrocracking mechanism evaluation

To access the progression of HDPE hydrocracking reaction and gain deeper mechanistic understanding, time-dependent experiments were conducted over intervals ranging from 0.5 to 3 h, as shown in Figure 3.10 (a). In the early stages of the reaction, a variety of products were formed, including gaseous hydrocarbons (C_1-C_4), gasoline-range liquids (C_5-C_{12}), and heavier liquid products (C_{13}-C_{22}), resulting in a marked reduction in solid residues. Extending the reaction time from 0.5 to 1 h led to continued conversion of solid residues, while the selectivity of the product distribution remained relatively stable. This indicates that the formation of gaseous (C_1-C_4) and liquid (C_5-C_{22}) products primarily occurred through the consumption of solid residues, with minimal conversion of heavy products to lighter fractions during this period.

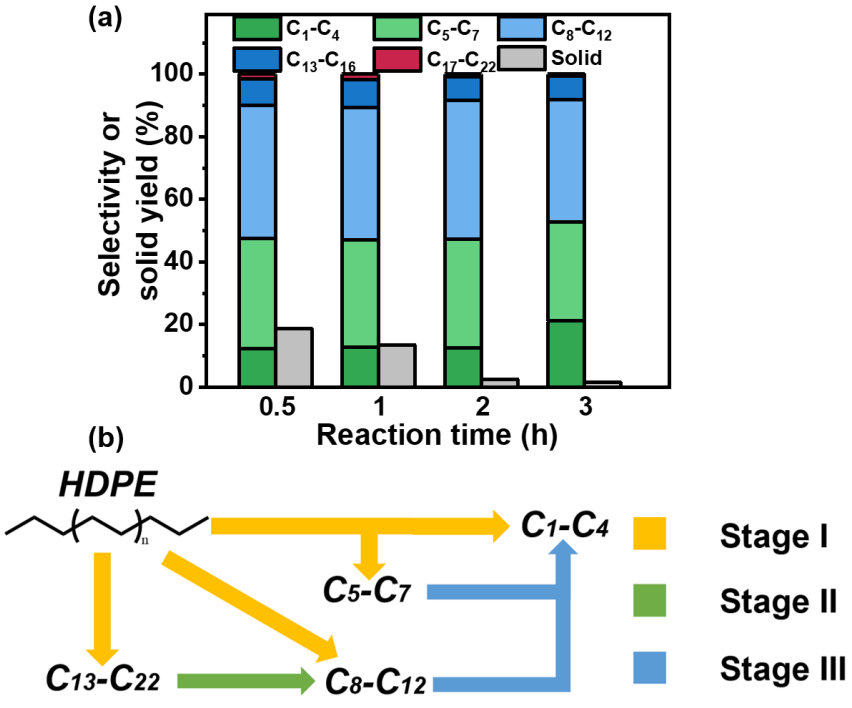

Figure 3.10 (a) Time-dependent reaction results from 0.5 to 3 h at 270 °C, 30-bar H_2, 2 g HDPE, 0.2 g PtSn-0.5Ce/SiAl catalyst. (b) Reaction network according to time-dependent reaction.

Significantly, when the reaction time was increased from 1 to 2 h, the solid residues were almost entirely consumed. During this stage, the selectivity of heavy liquid products (C_{13}-C_{22}) decreased by approximately 2.3%, while the selectivity for middle-range products (C_8-C_{12}) increased by about 2.1%. This suggests that a portion of the heavier products underwent further cracking, yielding intermediate-range products. However, at a reaction time of 3 h, there was a notable shift in the production distribution towards gas products, resulting in a decline in the selectivity for gasoline-range products from 79% to 69%. These three distinct stages of the reaction are summarised in the reaction network diagram presented in Figure 3.10 (b). By carefully optimising the reaction time to 2 h, the selectivity of gasoline-range products can be maximised, thereby preventing the deep cracking of these products into gaseous products (stage III) and promoting the conversion of heavier liquid products into gasoline-range hydrocarbons (stage II). Moreover, the cracking of heavy alkanes into lighter alkanes predominantly occurs at low solid residue yields, rather than during the initial stage when the solid residue yield is high. This observation suggests competitive adsorption allows higher molecular weight polymer chains to preferentially adsorb onto the active sites over heavier liquid products.[9]

The hydrocracking mechanism has been extensively studied, providing valuable insights for optimising catalysts and reaction conditions to enhance catalytic performance.[9,17,28,34,55] The MAB is a crucial factor, widely regarded as a key determinant of reaction pathways and product distributions in bifunctional metal-acid site catalysis during hydrocracking.[56] Initially, reactants such as n-alkanes (n-C_iH_{2i+2}) undergo dehydrogenation at the metal sites, forming a mixture of n-alkenes (n-C_iH_{2i}). These intermediates then desorb from the metal sites and adsorb onto BAS on the catalyst support. However, excessive dehydrogenation can lead to carbon deposition on the metal phase, resulting in catalyst deactivation. Therefore, it is essential to carefully control hydrogen pressure and temperature, utilise appropriate modifiers on the metal to reduce adsorption strength, and incorporate active species to maintain the integrity of the metallic phase and minimise carbon deposition.

Key intermediates in hydrocracking, such as carbocations, can be generated through two primary pathways: protonation of n-alkenes by BAS on the support surface (route A) or direct protonation to alkanes followed by dehydrogenation of the resulting carbocations at metal sites (route B). Within the BAS, alkenes and carbocations undergo competitive adsorption and desorption processes. This competition dictates whether the carbocations will undergo skeletal rearrangement or cleavage via β-scission. In general, β-scission requires more robust and extensive adsorption on BAS. If the rate-determining step (RDS) involves the skeletal rearrangement of carbocations on the acid site, the resulting isomerised alkenes can desorb and migrate back to metal sites, where they are swiftly hydrogenated into isomerised alkanes. Thus, the formation of isomerised products can serve as an indicator of acid function activity. Conversely, if the RDS involves β-scission, the reaction yields smaller carbocations and alkenes, which are immediately hydrogenated.

In high MAB hydrocracking, characterised by weaker adsorption, the cracking step involves acid centres undergoing isomerisation, leading to the generation of more isomerised products that are rapidly hydrogenated to alkanes (type-A β-scission, Figure 3.11 (b)).[57,58] On the other hand, low MAB with strong adsorption can result in deeper, simultaneous cracking and isomerisation through a slower type-B β-scission process (Figure 3.11 (b)), producing fewer isomerised products with lighter molecular weights.[57-59]

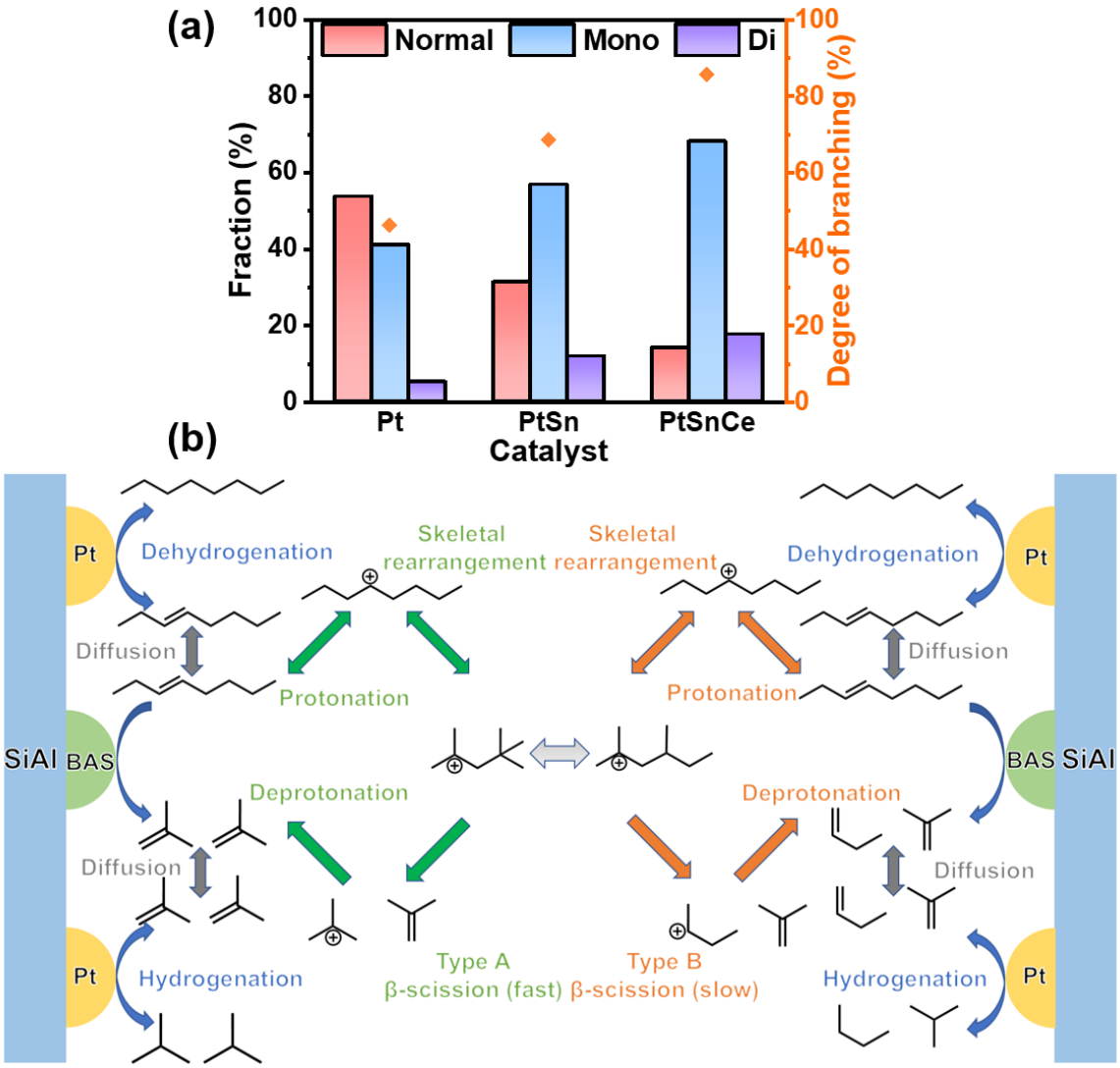

Figure 3.11 (a) The reaction mechanism study for hydrocracking at 270 °C, 2 h, 30-bar H_2, 2 g n-octadecane, 0.1 g Pt/SiAl or PtSn/SiAl or PtSn-0.5Ce/SiAl catalyst. (d) Reaction mechanism for hydrocracking where n-octane is used as reactant model.

To further elucidate the distinct reaction mechanisms of Pt/SiAl, PtSn/SiAl and PtSn-0.5Ce catalysts, n-octadecane was used as a model substrate. The product distributions obtained were similar to those observed with HDPE. The fraction of normal, monobranched, and dibranched products in the liquid phase, along with the degree of branching, were calculated to determine the reaction pathways associated with each catalyst. As illustrated in Figure 3.11 (a), the Pt/SiAl catalyst exhibited a branching degree of approximately 46%, consistent with the type-B β-scission model shown in Figure 3.11 (b), with an approximately 1:1 ratio of normal to branched products. The larger Pt particles likely result in stronger and more extensive

adsorption of HDPE and its fragments, leading to predominantly to deep cracking via type-B mechanism, yielding gaseous products (C_1 to C_4). Introducing Sn as a promotor into Pt/SiAl system decreases the fraction of normal alkane products and shifted the selectivity towards more isomerised products, as demonstrated in Figure 3.11 (a). The increase in both monobranched and dibranched products, along with the persistence of around 30% normal products, suggests the coexistence of both type A and type B β-scission mechanisms. The Sn promotor appears to mitigate Pt adsorption by reducing particle sizes and providing electronic promotion, favouring the type A mechanism of hydrocracking for the heavier carbonaceous materials. Further incorporation of Ce into the PtSn/SiAl system resulted in a higher branching degree, reaching around 86%, and an increased fraction of both monobranched and dibranched products, with normal products constituting less than 15% (Figure 3.11 (a)). This indicates that the type A mechanism predominates in this catalyst under the given reaction conditions. The selectivity for isomers is significantly higher than with the PtSn/SiAl catalyst alone. This enhancement suggests that the redox-active Ce plays a crucial role in amplifying the synergistic effect of Pt metal sites during hydrocracking. Additionally, Ce introduction enhances both the concentration and strength of highly reactive BAS. Therefore, it is proposed that the integration of Ce promotes a shift from type-B to type-A pathways, driven by the generation of stronger acid sites and intensified Ce-PtSn redox interactions.

3.2.5 Other plastic test and reusability test

While numerous studies have explored plastic decomposition under mild conditions, the majority focus extensively on pure plastic feedstocks. However, the distinct properties of various plastics, along with the presence of additives, like dyes and plasticisers, make the recycling of mixed plastic streams and commercial plastics particularly challenging [3,12] To address these complexities in real-world plastic upcycling, catalytic tests were conducted on both mixed plastic materials and commercial plastics, employing the same reaction conditions previously established. As shown in Figure 3.12 (a), different PO, including LDPE, PP, and PS, were effectively converted using 0.5 wt% Ce-modified PtSn catalyst, resulting in a

significant yield of fuel-range products. The gaseous product yield (C_1-C_4) for LDPE is slightly higher than that for HDPE, likely due to the lower molecular weight of LDPE. Conversely, PS produced more solid residues and fewer gaseous products, indicating greater difficulty in cleaving C-C bonds of aromatic hydrocarbons.

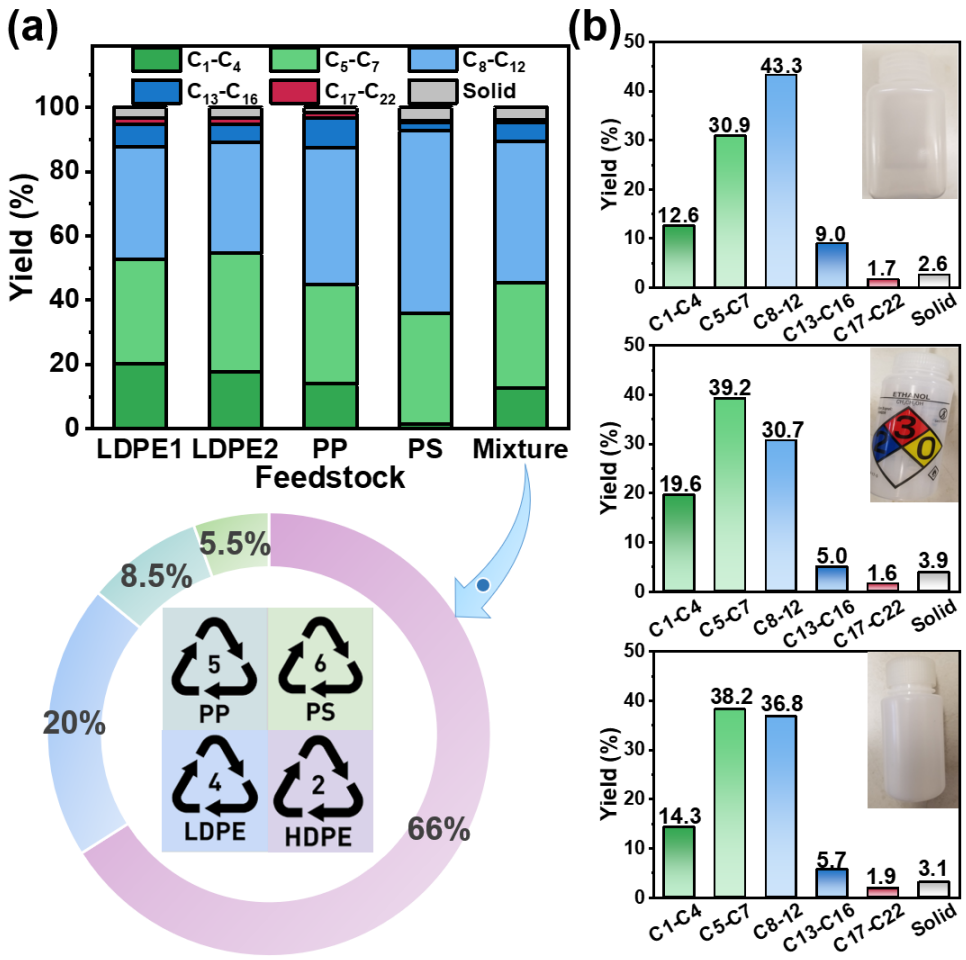

Figure 3.12 Catalytic performances over (a) other plastics and (b) commercial plastics.

To evaluate the catalyst's performance in processing mixed plastic streams, we prepared a mixture of four different plastic types–LDPE, HDPE, PP, and PS–reflecting the composition of municipal plastic waste (Figure 3.12 (a)).[60] The catalyst achieved an approximately 76.7% yield of gasoline-range products from this mixed plastic stream, demonstrating its efficiency in handling diverse plastic waste. Additionally, as illustrated in Figure 3.12 (b), even commercially used plastic bottles with external dye were efficiently converted using this catalyst, highlighting

its potential as a robust solution for both mixed-streams and commercial plastic waste treatment.

To assess the stability of the catalysts, reusability tests were conducted on spent catalysts under identical reaction conditions, with the results summarised in Figure 3.13. Initially, the recycled PtSn/SiAl catalyst without Ce showed poor activity, yielding over 55% solid residues, indicative of significant catalyst deactivation after the first cycle. HRTEM images (Figure 3.13), revealed disordered structures, highlighted by red circles, attributed to amorphous coke deposits, distinctly differing from the surrounding areas. These coke deposits were primarily located on or near the metal sites, leading to severe deactivation.[61] In contrast, the Ce-containing catalyst maintained consistent conversion and selectivity over at least three recycling cycles. The introduction of Ce significantly reduced the amount of coke deposits, from 2.9 wt% in the absence of Ce to 1.2 wt% at 0.5 wt% Ce loading, as confirmed by TG analysis shown in Figure 3.5. Furthermore, HRTEM images indicated that the distribution and location of coke deposits were altered by the presence of Ce. In the Ce-containing recycled catalyst (Figure 3.13), coke deposits were found far away from the metal centres and near the edges of the amorphous support. This suggests that Ce species not only inhibit the accumulation of coke near active sites by acting as redox agents but also facilitate the migration of coke to the support, thereby preserving the metal centres and extending the catalyst's operational lifespan.[62] In summary, the enhanced stability of this catalyst is attributed to its improved resistance to coke formation and its ability to promote coke migration, both of which are significantly enhanced by the incorporation of Ce.

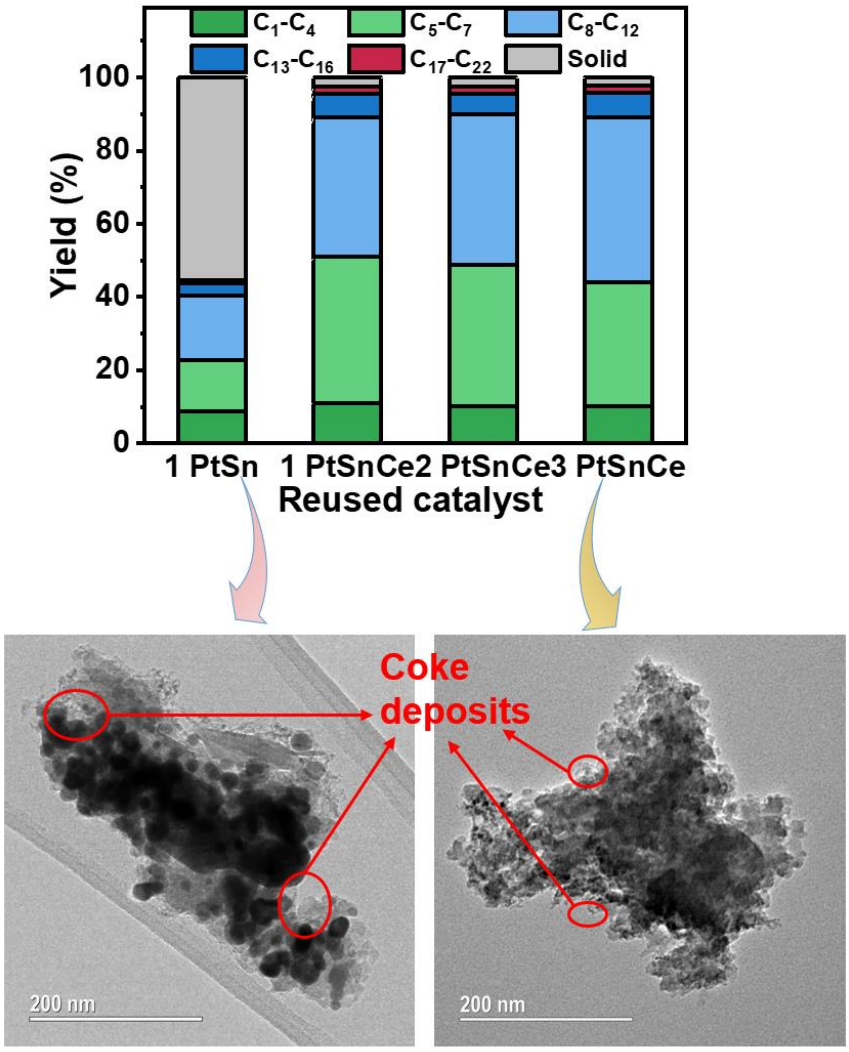

Figure 3.13 Catalytic performances over reused catalysts and reused catalysts with HRTEM images for the first recycled PtSn/SiAl catalyst and third-recycled PtSn-0.5Ce/SiAl catalyst. Reaction conditions: 270 °C, 2 h, 30-bar H_2, 2 g HDPE for reused PtSn/SiAl and PtSn0.5Ce/SiAl catalysts, and all mass balances are in the range of 97±3%.

3.3 Conclusion

The incorporation of Ce into PtSn/SiAl catalyst has been demonstrated to significantly enhance their catalytic performance in converting plastic waste into gasoline-range products. The addition of Ce not only increases the concentration and strength of BAS, thereby improving cracking efficiency, but also leverages Ce's unique redox properties to enhance the reducibility of the PtSn catalysts. This modification helps to prevent the excessive reduction of Sn oxides to Sn^0, bolstering the catalyst's dehydrogenation and hydrogenation capabilities,

and resulting in higher yields of isomerised products with minimal carbon deposition. The robust interactions between Pt, Sn and Ce are crucial in suppressing coke formation near the active metal sites, thereby significantly extending the catalyst's operational lifespan. Additionally, this Ce-modified catalyst has demonstrated promising efficacy in processing both mixed-stream and commercial plastics, indicating its potential for broader applications in plastic waste treatment. These results underscore the catalyst's potential in overcoming the challenges associated with plastic waste recycling and upcycling, contributing to more sustainable waste management practices. Ongoing research and development in this field could lead to further improvements in catalytic technologies for plastic waste valorisation, fostering a greener and more environmentally conscious approach to plastic utilisation.

3.4 Reference

1. Wang, H., Yoskamtorn, T., Zheng, J., Ho, P.-L., Ng, B., and Tsang, S.C.E. (2023). Ce-Promoted PtSn-Based Catalyst for Hydrocracking of Polyolefin Plastic Waste into High Yield of Gasoline-Range Products. ACS Catalysis *13*, 15886-15898. 10.1021/acscatal.3c03996.
2. Geyer, R., Jambeck, J.R., and Law, K.L. (2017). Production, use, and fate of all plastics ever made. Science Advances *3*, e1700782. 10.1126/sciadv.1700782.
3. Chen, H., Wan, K., Zhang, Y., and Wang, Y. (2021). Waste to Wealth: Chemical Recycling and Chemical Upcycling of Waste Plastics for a Great Future. ChemSusChem *14*, 4123-4136. 10.1002/cssc.202100652.
4. Vollmer, I., Jenks, M.J.F., Mayorga González, R., Meirer, F., and Weckhuysen, B.M. (2021). Plastic Waste Conversion over a Refinery Waste Catalyst. Angewandte Chemie *60*, 16101-16108. 10.1002/anie.202104110.
5. Vollmer, I., Jenks, M.J.F., Roelands, M.C.P., White, R.J., van Harmelen, T., de Wild, P., van der Laan, G.P., Meirer, F., Keurentjes, J.T.F., and Weckhuysen, B.M. (2020). Beyond Mechanical Recycling: Giving New Life to Plastic Waste. Angewandte Chemie International Edition *59*, 15402-15423. 10.1002/anie.201915651.
6. Zheng, K., Wu, Y., Hu, Z., Wang, S., Jiao, X., Zhu, J., Sun, Y., and Xie, Y. (2023). Progress and perspective for conversion of plastic wastes into valuable chemicals. Chemical Society Reviews *52*, 8-29. 10.1039/D2CS00688J.

7. Zhang, F., Zhao, Y., Wang, D., Yan, M., Zhang, J., Zhang, P., Ding, T., Chen, L., and Chen, C. (2021). Current technologies for plastic waste treatment: A review. Journal of Cleaner Production *282*, 124523. 10.1016/j.jclepro.2020.124523.
8. Duan, J., Chen, W., Wang, C., Wang, L., Liu, Z., Yi, X., Fang, W., Wang, H., Wei, H., Xu, S., et al. (2022). Coking-Resistant Polyethylene Upcycling Modulated by Zeolite Micropore Diffusion. Journal of the American Chemical Society *144*, 14269-14277. 10.1021/jacs.2c05125.
9. Vance, B.C., Kots, P.A., Wang, C., Hinton, Z.R., Quinn, C.M., Epps, T.H., Korley, L.T.J., and Vlachos, D.G. (2021). Single pot catalyst strategy to branched products via adhesive isomerization and hydrocracking of polyethylene over platinum tungstated zirconia. Applied Catalysis B: Environmental *299*, 120483. 10.1016/j.apcatb.2021.120483.
10. Hoseini, M., and Bond, T. (2022). Predicting the global environmental distribution of plastic polymers. Environmental Pollution *300*, 118966. 10.1016/j.envpol.2022.118966.
11. Sullivan, K.P., Werner, A.Z., Ramirez, K.J., Ellis, L.D., Bussard, J.R., Black, B.A., Brandner, D.G., Bratti, F., Buss, B.L., Dong, X., et al. (2022). Mixed plastics waste valorization through tandem chemical oxidation and biological funneling. Science *378*, 207-211. 10.1126/science.abo4626.
12. Liu, S., Kots, P.A., Vance, B.C., Danielson, A., and Vlachos, D.G. (2021). Plastic waste to fuels by hydrocracking at mild conditions. Science Advances *7*, eabf8283. 10.1126/sciadv.abf8283.
13. Jing, Y., Wang, Y., Furukawa, S., Xia, J., Sun, C., Hülsey, M.J., Wang, H., Guo, Y., Liu, X., and Yan, N. (2021). Towards the Circular Economy: Converting Aromatic Plastic Waste Back to Arenes over a Ru/Nb2O5 Catalyst. Angewandte Chemie International Edition *60*, 5527-5535. 10.1002/anie.202011063.
14. Haque, M.S., Uddin, S., Sayem, S.M., and Mohib, K.M. (2021). Coronavirus disease 2019 (COVID-19) induced waste scenario: A short overview. Journal of Environmental Chemical Engineering *9*, 104660. 10.1016/j.jece.2020.104660.
15. Patrício Silva, A.L., Prata, J.C., Walker, T.R., Duarte, A.C., Ouyang, W., Barcelò, D., and Rocha-Santos, T. (2021). Increased plastic pollution due to COVID-19 pandemic: Challenges and recommendations. Chemical Engineering Journal *405*, 126683. 10.1016/j.cej.2020.126683.
16. Fu, L., Xiong, Q., Wang, Q., Cai, L., Chen, Z., and Zhou, Y. (2022). Catalytic Pyrolysis of Waste Polyethylene Using Combined CaO and Ga/ZSM-5 Catalysts for High Value-Added Aromatics Production. ACS Sustainable Chemistry & Engineering *10*, 9612-9623. 10.1021/acssuschemeng.2c02881.

17. Dong, Z., Chen, W., Xu, K., Liu, Y., Wu, J., and Zhang, F. (2022). Understanding the Structure–Activity Relationships in Catalytic Conversion of Polyolefin Plastics by Zeolite-Based Catalysts: A Critical Review. ACS Catalysis, 14882-14901. 10.1021/acscatal.2c04915.
18. Wang, N.M., Strong, G., DaSilva, V., Gao, L., Huacuja, R., Konstantinov, I.A., Rosen, M.S., Nett, A.J., Ewart, S., Geyer, R., et al. (2022). Chemical Recycling of Polyethylene by Tandem Catalytic Conversion to Propylene. Journal of the American Chemical Society *144*, 18526-18531. 10.1021/jacs.2c07781.
19. Shen, M., Hu, T., Huang, W., Song, B., Qin, M., Yi, H., Zeng, G., and Zhang, Y. (2021). Can incineration completely eliminate plastic wastes? An investigation of microplastics and heavy metals in the bottom ash and fly ash from an incineration plant. Science of The Total Environment *779*, 146528. 10.1016/j.scitotenv.2021.146528.
20. Jiao, X., Zheng, K., Hu, Z., Zhu, S., Sun, Y., and Xie, Y. (2021). Conversion of Waste Plastics into Value-Added Carbonaceous Fuels under Mild Conditions. Advanced Materials *n/a*, 2005192. 10.1002/adma.202005192.
21. Ellis, L.D., Rorrer, N.A., Sullivan, K.P., Otto, M., McGeehan, J.E., Román-Leshkov, Y., Wierckx, N., and Beckham, G.T. (2021). Chemical and biological catalysis for plastics recycling and upcycling. Nature Catalysis *4*, 539-556. 10.1038/s41929-021-00648-4.
22. Chen, D., Yin, L., Wang, H., and He, P. (2014). Pyrolysis technologies for municipal solid waste: A review. Waste Management *34*, 2466-2486. 10.1016/j.wasman.2014.08.004.
23. Jahirul, M.I., Rasul, M.G., Schaller, D., Khan, M.M.K., Hasan, M.M., and Hazrat, M.A. (2022). Transport fuel from waste plastics pyrolysis – A review on technologies, challenges and opportunities. Energy Conversion and Management *258*, 115451. 10.1016/j.enconman.2022.115451.
24. Radhakrishnan, K., Senthil Kumar, P., Rangasamy, G., Praveen Perumal, L., Sanaulla, S., Nilavendhan, S., Manivasagan, V., and Saranya, K. (2022). A critical review on pyrolysis method as sustainable conversion of waste plastics into fuels. Fuel, 126890. 10.1016/j.fuel.2022.126890.
25. Kots, P.A., Vance, B.C., and Vlachos, D.G. (2022). Polyolefin plastic waste hydroconversion to fuels, lubricants, and waxes: a comparative study. Reaction Chemistry & Engineering *7*, 41-54. 10.1039/D1RE00447F.
26. Wang, H., and Edman Tsang, S.C. (2024). Recent advances in polyolefin plastic waste upcycling via mild heterogeneous catalysis route from catalyst development to process design. Cell Reports Physical Science *5*, 102075. 10.1016/j.xcrp.2024.102075.

27. Bin Jumah, A., Anbumuthu, V., Tedstone, A.A., and Garforth, A.A. (2019). Catalyzing the Hydrocracking of Low Density Polyethylene. Industrial & Engineering Chemistry Research *58*, 20601-20609. 10.1021/acs.iecr.9b04263.
28. Lee, W.-T., van Muyden, A., Bobbink, F.D., Mensi, M.D., Carullo, J.R., and Dyson, P.J. (2022). Mechanistic classification and benchmarking of polyolefin depolymerization over silica-alumina-based catalysts. Nature Communications *13*, 4850. 10.1038/s41467-022-32563-y.
29. Ding, W., Liang, J., and Anderson, L.L. (1997). Hydrocracking and Hydroisomerization of High-Density Polyethylene and Waste Plastic over Zeolite and Silica−Alumina-Supported Ni and Ni−Mo Sulfides. Energy & Fuels *11*, 1219-1224. 10.1021/ef970051q.
30. Venkatesh, K.R., Hu, J., Wang, W., Holder, G.D., Tierney, J.W., and Wender, I. (1996). Hydrocracking and Hydroisomerization of Long-Chain Alkanes and Polyolefins over Metal-Promoted Anion-Modified Zirconium Oxides. Energy & Fuels *10*, 1163-1170. 10.1021/ef960049j.
31. Escola, J.M., Aguado, J., Serrano, D.P., García, A., Peral, A., Briones, L., Calvo, R., and Fernandez, E. (2011). Catalytic hydroreforming of the polyethylene thermal cracking oil over Ni supported hierarchical zeolites and mesostructured aluminosilicates. Applied Catalysis B: Environmental *106*, 405-415. 10.1038/s41467-022-32563-y.
32. Chen, S., Pei, C., Sun, G., Zhao, Z.-J., and Gong, J. (2020). Nanostructured Catalysts toward Efficient Propane Dehydrogenation. Accounts of Materials Research *1*, 30-40. 10.1021/accountsmr.0c00012.
33. Chen, S., Chang, X., Sun, G., Zhang, T., Xu, Y., Wang, Y., Pei, C., and Gong, J. (2021). Propane dehydrogenation: catalyst development, new chemistry, and emerging technologies. Chemical Society Reviews *50*, 3315-3354. 10.1039/D0CS00814A.
34. Sun, M., Zhu, L., Liu, W., Zhao, X., Zhang, Y., Luo, H., Miao, G., Li, S., Yin, S., and Kong, L. (2022). Efficient upgrading of polyolefin plastics into C5–C12 gasoline alkanes over a Pt/W/Beta catalyst. Sustainable Energy & Fuels *6*, 271-275. 10.1039/D1SE01778K.
35. Yu, C., Ge, Q., Xu, H., and Li, W. (2006). Effects of Ce addition on the Pt-Sn/γ-Al2O3 catalyst for propane dehydrogenation to propylene. Applied Catalysis A: General *315*, 58-67. 10.1016/j.apcata.2006.08.038.
36. Zholobenko, V., Freitas, C., Jendrlin, M., Bazin, P., Travert, A., and Thibault-Starzyk, F. (2020). Probing the acid sites of zeolites with pyridine: Quantitative AGIR measurements of the molar absorption coefficients. Journal of Catalysis *385*, 52-60. 10.1016/j.jcat.2020.03.003.

37. Xiaoning, W., Zhen, Z., Chunming, X., Aijun, D., Li, Z., and Guiyuan, J. (2007). Effects of Light Rare Earth on Acidity and Catalytic Performance of HZSM-5 Zeolite for Catalytic Cracking of Butane to Light Olefins. Journal of Rare Earths *25*, 321-328. 10.1016/S1002-0721(07)60430-X.

38. Merlen, E., Beccat, P., Bertolini, J.C., Delichère, P., Zanier, N., and Didillon, B. (1996). Characterization of Bimetallic Pt–Sn/Al2O3Catalysts: Relationship between Particle Size and Structure. Journal of Catalysis *159*, 178-188. 10.1006/jcat.1996.0077.

39. Armendáriz, H., Guzmán, A., Toledo, J.A., Llanos, M.E., Vázquez, A., and Aguilar-Ríos, G. (2001). Isopentane dehydrogenation on Pt-Sn catalysts supported on Al-Mg-O mixed oxides: effect of Al/Mg atomic ratio. Applied Catalysis A: General *211*, 69-80. 10.1016/S0926-860X(00)00836-X.

40. Chai, S., Bai, X., Li, J., Liu, C., Ding, T., Tian, Y., Liu, C., Xian, H., Mi, W., and Li, X. (2017). Effect of phase interaction on catalytic CO oxidation over the SnO2/Al2O3 model catalyst. Applied Surface Science *402*, 12-20. 10.1016/j.apsusc.2017.01.058.

41. Zhu, Y., An, Z., Song, H., Xiang, X., Yan, W., and He, J. (2017). Lattice-Confined Sn (IV/II) Stabilizing Raft-Like Pt Clusters: High Selectivity and Durability in Propane Dehydrogenation. ACS Catalysis *7*, 6973-6978. 10.1021/acscatal.7b02264.

42. Auroux, A., Sprinceana, D., and Gervasini, A. (2000). Support effects on de-NOx catalytic properties of supported tin oxides. Journal of Catalysis *195*, 140-150. 10.1006/jcat.2000.2970.

43. Lu, Z., Ji, S., Liu, H., and Li, C. (2008). Preparation and Characterization of Pt-Sn/SBA-15 Catalysts and Their Catalytic Performances for Long Chain Alkane Dehydrogenation. Chinese Journal of Chemical Engineering *16*, 740-745. 10.1016/S1004-9541(08)60149-4.

44. Serrano-Ruiz, J.C., Huber, G.W., Sánchez-Castillo, M.A., Dumesic, J.A., Rodríguez-Reinoso, F., and Sepúlveda-Escribano, A. (2006). Effect of Sn addition to Pt/CeO2–Al2O3 and Pt/Al2O3 catalysts: an XPS, 119Sn Mössbauer and microcalorimetry study. Journal of catalysis *241*, 378-388. 10.1016/j.jcat.2006.05.005.

45. Damyanova, S., and Bueno, J.M.C. (2003). Effect of CeO2 loading on the surface and catalytic behaviors of CeO2-Al2O3-supported Pt catalysts. Applied Catalysis A: General *253*, 135-150. 10.1016/S0926-860X(03)00500-3.

46. Navarro, R.M., Álvarez-Galván, M.C., Sánchez-Sánchez, M.C., Rosa, F., and Fierro, J.L.G. (2005). Production of hydrogen by oxidative reforming of ethanol over Pt catalysts supported on Al2O3 modified with Ce and La. Applied Catalysis B: Environmental *55*, 229-241. 10.1016/j.apcatb.2004.09.002.

47. Riguetto, B.A., Damyanova, S., Gouliev, G., Marques, C.M.P., Petrov, L., and Bueno, J.M.C. (2004). Surface Behavior of Alumina-Supported Pt Catalysts Modified with

Cerium as Revealed by X-ray Diffraction, X-ray Photoelectron Spectroscopy, and Fourier Transform Infrared Spectroscopy of CO Adsorption. The Journal of Physical Chemistry B *108*, 5349-5358. 10.1021/jp031167s.

48. Ivanova, A.S., Slavinskaya, E.M., Gulyaev, R.V., Zaikovskii, V.I., Stonkus, O.A., Danilova, I.G., Plyasova, L.M., Polukhina, I.A., and Boronin, A.I. (2010). Metal–support interactions in Pt/Al2O3 and Pd/Al2O3 catalysts for CO oxidation. Applied Catalysis B: Environmental *97*, 57-71. 10.1016/j.apcatb.2010.03.024.
49. Sexton, B.A., Hughes, A.E., and Foger, K. (1984). An X-ray photoelectron spectroscopy and reaction study of Pt□Sn catalysts. Journal of Catalysis *88*, 466-477. 10.1016/0021-9517(84)90024-1.
50. Tang, X., Zhang, B., Li, Y., Xu, Y., Xin, Q., and Shen, W. (2005). The role of Sn in Pt–Sn/CeO2 catalysts for the complete oxidation of ethanol. Journal of Molecular Catalysis A: Chemical *235*, 122-129. 10.1016/j.molcata.2005.03.018.
51. Xue, M., Zhou, Y., Zhang, Y., Liu, X., Duan, Y., and Sheng, X. (2012). Effect of cerium addition on catalytic performance of PtSnNa/ZSM-5 catalyst for propane dehydrogenation. Journal of Natural Gas Chemistry *21*, 324-331. 10.1016/S1003-9953(11)60372-1.
52. Shi, Y., Li, X., Rong, X., Gu, B., Wei, H., and Sun, C. (2017). Influence of support on the catalytic properties of Pt–Sn–K/θ-Al 2 O 3 for propane dehydrogenation. RSC advances *7*, 19841-19848. 10.1039/C7RA02141K.
53. Weishen, Y., Liwu, L., Yining, F., and Jingling, Z. (1992). Surface structure and catalytic performance of supported PtSn catalysts. Catalysis Letters *12*, 267-275. 10.1007/BF00767209.
54. Del Angel, G., Bonilla, A., Peña, Y., Navarrete, J., Fierro, J.L.G., and Acosta, D.R. (2003). Effect of lanthanum on the catalytic properties of PtSn/γ-Al2O3 bimetallic catalysts prepared by successive impregnation and controlled surface reaction. Journal of Catalysis *219*, 63-73. 10.1016/S0021-9517(03)00140-4.
55. Munir, D., Irfan, M.F., and Usman, M.R. (2018). Hydrocracking of virgin and waste plastics: A detailed review. Renewable and Sustainable Energy Reviews *90*, 490-515. 10.1016/j.rser.2018.03.034.
56. Thybaut, J.W., Laxmi Narasimhan, C.S., Denayer, J.F., Baron, G.V., Jacobs, P.A., Martens, J.A., and Marin, G.B. (2005). Acid−Metal Balance of a Hydrocracking Catalyst: Ideal versus Nonideal Behavior. Industrial & Engineering Chemistry Research *44*, 5159-5169. 10.1021/ie049375+.
57. Alvarez, F., Ribeiro, F.R., Perot, G., Thomazeau, C., and Guisnet, M. (1996). Hydroisomerization and Hydrocracking of Alkanes: 7. Influence of the Balance

between Acid and Hydrogenating Functions on the Transformation ofn-Decane on PtHY Catalysts. Journal of Catalysis *162*, 179-189. 10.1006/jcat.1996.0275.

58. Degnan, T.F., and Kennedy, C.R. (1993). Impact of catalyst acid/metal balance in hydroisomerization of normal paraffins. AIChE Journal *39*, 607-614. 10.1002/aic.690390409.
59. Maesen, T.L.M., Calero, S., Schenk, M., and Smit, B. (2004). Alkane hydrocracking: shape selectivity or kinetics? Journal of Catalysis *221*, 241-251. 10.1016/j.jcat.2003.07.003.
60. Areeprasert, C., Asingsamanunt, J., Srisawat, S., Kaharn, J., Inseemeesak, B., Phasee, P., Khaobang, C., Siwakosit, W., and Chiemchaisri, C. (2017). Municipal Plastic Waste Composition Study at Transfer Station of Bangkok and Possibility of its Energy Recovery by Pyrolysis. Energy Procedia *107*, 222-226. 10.1016/j.egypro.2016.12.132.
61. Wang, H.-Z., Sun, L.-L., Sui, Z.-J., Zhu, Y.-A., Ye, G.-H., Chen, D., Zhou, X.-G., and Yuan, W.-K. (2018). Coke Formation on Pt–Sn/Al2O3 Catalyst for Propane Dehydrogenation. Industrial & Engineering Chemistry Research *57*, 8647-8654. 10.1021/acs.iecr.9b00867.
62. Ma, Z., Wang, J., Li, J., Wang, N., An, C., and Sun, L. (2014). Propane dehydrogenation over Al2O3 supported Pt nanoparticles: Effect of cerium addition. Fuel Processing Technology *128*, 283-288. 10.1016/j.fuproc.2014.07.031.

Chapter 4 Efficient Hydrocracking of Plastics into High-Selectivity of Propane via Non-noble Metal-Supported ZSM-5 Nanosheet

This chapter is adapted from the work by Haokun Wang[#], Lam Ka Yin[#], Guangchao Li, Sijie Huang, Jiasi Li, Ping-Luen Ho, Amy Radford, Renzo Leeflang, Mingyu Luo, Yung-Kang Peng, and Shik Chi Edman Tsang, unpublished paper draft.*

4.1 Introduction

Plastics are highly regarded for their distinctive attributes such as low density, durability, and resistance to chemicals, which have led to their widespread applications across various industries including packaging, textiles, manufacturing, and transportation.[1,2] The exceptional properties of plastics have driven a remarkable increase in global production. Data from Plastics Europe indicates that global plastic production has experienced a dramatic rise since the late 20th century, with output reaching approximately 400 Mt annually by 2022.[3] This substantial growth highlights the extensive global reliance on plastics in modern society. However, this pervasive usage has been accompanied by significant environmental challenges, primarily due to inadequate waste management systems, resulting in severe ecological degradation and harmful impacts on wildlife.[4,5]

The complex and heterogeneous nature of plastics poses significant challenges in developing effective waste management strategies.[6,7] Despite progress in this area, current methods remain less than ideal. Traditional landfilling, often viewed as a cost-effective solution for municipal solid waste, is inadequate for plastic waste management due to the material's prolonged degradation period. Additionally, landfills not only occupy substantial land resources but also produce toxic leachates during the degradation process, leading to soil and water contamination while failing to recover the inherent energy content of plastics.[8,9] Moreover, incineration, another conventional method, while partially recovering energy in the

form of electricity, releases hazardous pollutants and greenhouse gases, further exacerbating environmental challenges.[8,10]

In response to these limitations, chemical recycling, particularly tertiary recycling methods, has gained attention as a promising approach to mitigate the growing plastic waste crisis. Within this category, pyrolysis has emerged as a focus point. This technique involves the thermal cracking of long-chain polymers into fuel oil in an oxygen-free environment, offering the potential to process a wide range of plastic types and recover valuable resources.[8] However, pyrolysis faces significant challenges, including the complexity of the reactions involved, the high energy demands associated with the elevated temperatures required, and the low selectivity of the resulting products, which collectively hinder its scalability for large-scale plastic waste treatment.[8,11] Additionally, gasification, which converts plastics into high-calorific gaseous products, such as syngas or hydrogen, also presents limitations due to its energy-intensive nature and the need for extensive purification of the resulting products.[8,11]

Given the intrinsic limitations of these existing plastic waste treatment methods, hydrocracking has emerged as a compelling alternative. This process allows for the selective decomposition of plastics into liquid-range products under relatively mild conditions, offering a more controlled and efficient approach to plastic waste valorisation.[8] Hydrocracking typically employs bifunctional catalysts, where acid sites catalyse the cracking reactions, and metal sites, often comprising noble metals such as Pt, Pd and Ru, drive dehydrogenation and hydrogenation processses.[12-14] Despite the effectiveness of these noble metal catalysts, their high cost presents significant economic barriers to their widespread industrial applications.[15] Moreover, the product distribution in hydrocracking tends to favour liquid hydrocarbons, such as gasoline and naphtha, which may limit the versability of the process and complicate the attainment of specific product outputs.

In this chapter, the hydrocracking of PP over a series of catalysts was explored, with a focus on achieving propane as the primary product–a novel finding in the context of hydrocracking. Unlike traditional approaches, such as incineration for electricity generation or hydrocracking

for fuel production, the production of propane offers a distinct advantage. Propane can be readily dehydrogenated and polymerised through established commercial processes to remanufacture PP, thereby contributing to a circular economy in the plastic industry. This process is illustrated in Figure 4.1.

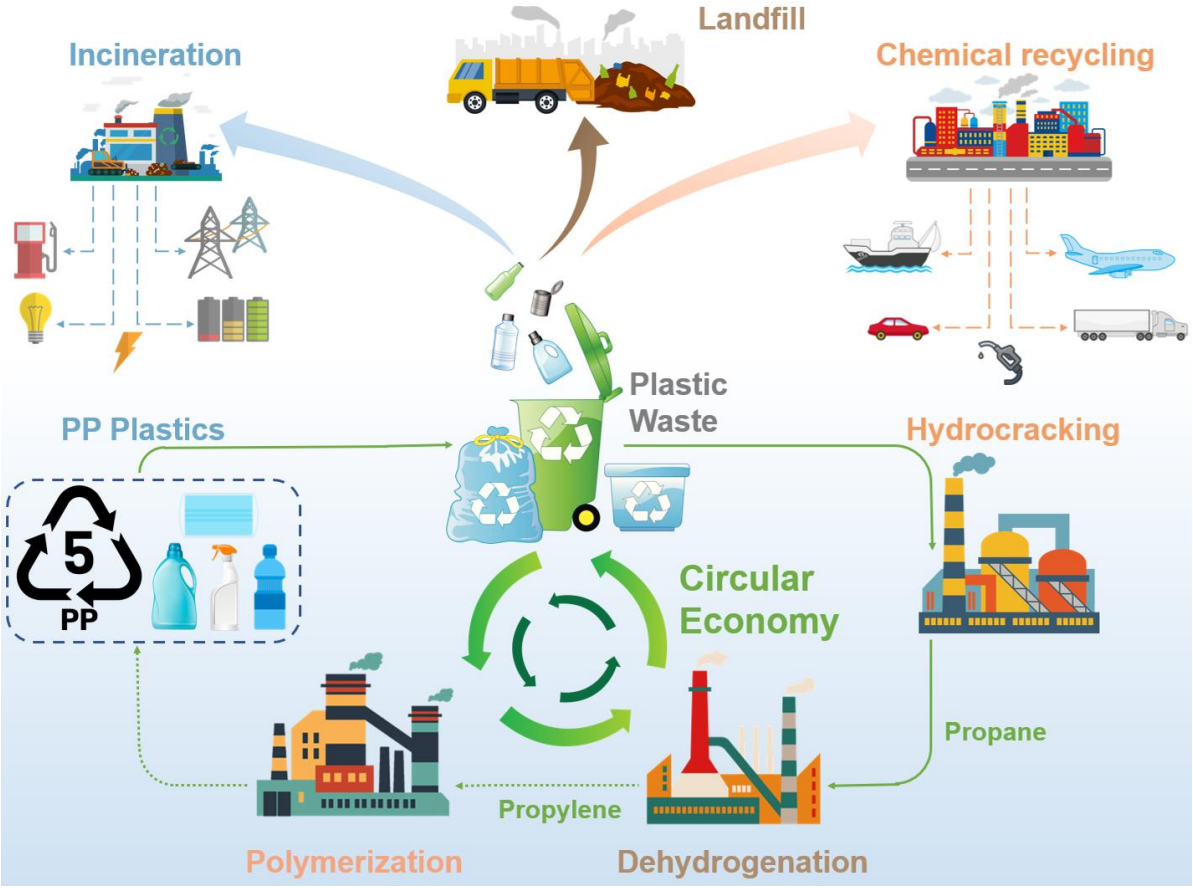

Figure 4.1 New route of plastic waste management.

The comparative analysis of ZSM-5 and ZSM-5 NS revealed that ZSM-5 NS demonstrates superior catalytic activity and stability. This enhancement is attributed to the increased accessibility of active sites and improved mass transfer of intermediates within the nanosheet structure. Building on these findings, ZSM-5 NS was further modified with non-noble metals. Alongside Ni, chemically similar elements such as Fe, Co, Cu, and Zn were incorporated to evaluate their potential in augmenting the catalytic performance of ZSM-5 NS. Remarkably, the Ni/ZSM-5 NS catalyst exhibited a high selectivity for propane (75.7%) and conversion of 99.4% at 260 °C over a 10-hours period under 30 bar H_2. Beyond its good stability and efficacy

in catalysing the hydrocracking of various plastics, including commercial grades, Ni/ZSM-5 NS represents a significant advancement towards realizing circular economy principles in industrial plastic production and waste management.

4.2 Results and discussion

4.2.1 Comparative analysis between ZSM-5 and ZSM-5 nanosheet

As outlined earlier, conventional hydrocracking processes primarily produce liquid-range hydrocarbons, such as those discussed in Chapter 3 for gasoline-range outputs. However, fine-tuning product distribution to achieve specific target outputs remains a challenging task. Zeolites, known for their molecular sieving capabilities, high thermal stability, and adjustable acidity, are critical in numerous industrial processes, including methanol-toluene alkylation and methanol-to-olefins (MTO) reactions.[16,17] Given these attributes, ZSM-5 zeolite was chosen for this study to explore its molecular sieving properties. However, conventional ZSM-5 faces limitations due to its extended diffusion paths within the micropores, which can impede reaction kinetics, particularly for macromolecules intermediates derived from polymers. This often leads to coke formation and undesired product distribution.[18]

To address these issues, ZSM-5 NS have been developed. These nanosheets offer shortened diffusion pathways and facilitate faster product desorption, thereby enhancing catalytic efficiency.[12] To better understand the morphological differences between ZSM-5 and ZSM-5 NS, SEM and HRTEM were employed. As shown in Figure 4.2 (a) and (b), the ZSM-5 NS exhibits a significantly reduced b-axis thickness (approximately 300 nm), which is nearly half that of the conventional ZSM-5. Additionally, the c-axis length of ZSM-5 NS (740 nm) is also notably shorter compared to conventional ZSM-5, which measures approximately 2800 nm. TEM images (Figure 4.2 (c) and (d)) reveal a morphological shift from the traditional thick coffin-like structure to a thin, regular hexagonal prism. It is well-established that ZSM-5 zeolites possess two distinct diffusion pathways: straight channels (5.4 × 5.6 Å) along the b-axis and sinusoidal channels (5.1 × 5.4 Å) parallel to the a-axis.[19] The modifications in ZSM-5 NS effectively shorten the diffusion distances in both the straight and sinusoidal channels,

potentially enhancing the mass transfer of reaction intermediates and enabling more rapid desorption of products, which collectively improve catalytic performance.[20]

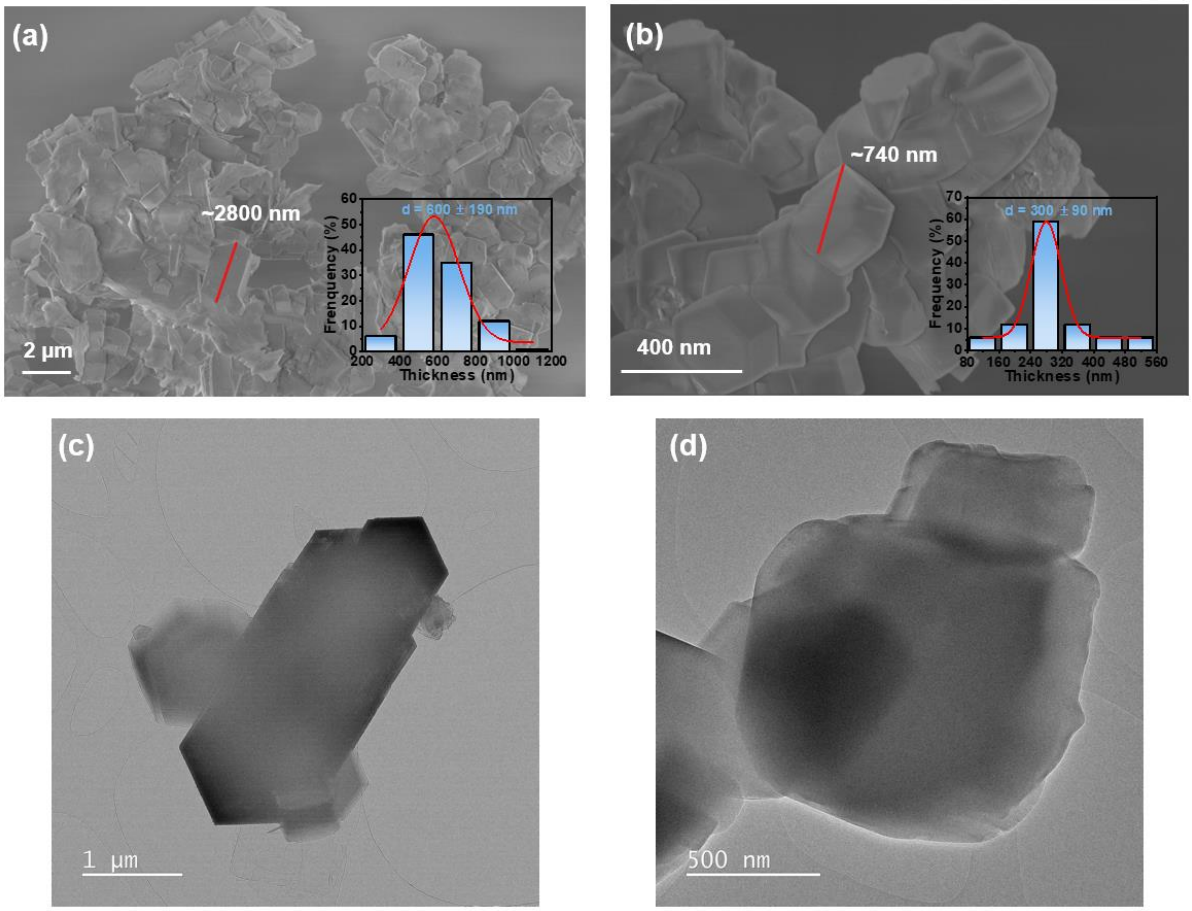

Figure 4.2 SEM images of (a) ZSM-5 and (b) ZSM-5 NS, including b-axis length distributions, and HRTEM images of (c) ZSM-5 and (d) ZSM-5 NS.

In terms of the crystalline structures, both ZSM-5 and ZSM-5 NS exhibit five well-defined diffraction peaks in the 2θ ranges of 7° to 10° and 22° to 25°, as observed in the XRD patterns (Figure 4.3). These peaks are characteristic of the MFI frameworks.[21] Notably, the diffractions peaks of ZSM-5 NS exhibit a slight shift towards lower angles, along with a decrease in intensity, which may indicate a reduction in crystallinity. This alteration is likely attributed to changes in the material's morphology.

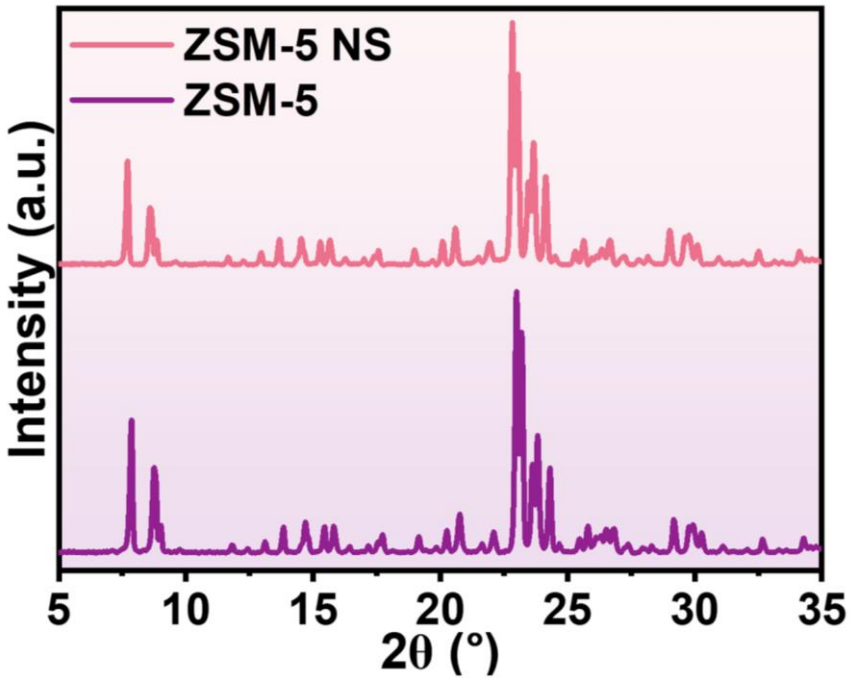

Figure 4.3 XRD patterns over ZSM-5 and ZSM-5 NS.

The nitrogen adsorption-desorption isotherms (Figure 4.4) for both ZSM-5 and ZSM-5 NS exhibit hysteresis loops, which are characteristic of mesopore capillary condensation occurring at high relative pressures (0.4 to 1.0). This behaviour is typical of type IV isotherms combined with a type H4 hysteresis loop, confirming the presence of mesopores and slit-like pores within the structures.[22] A comprehensive analysis of surface areas and pore characteristics (Table 4.1) reveals that ZSM-5 NS has a considerably larger surface area, encompassing both micropores and external surfaces, and also possesses a higher pore volume compared to conventional ZSM-5. The increased in surface area enhances the accessibility of reactants to acid sites, thereby improving catalytic activity. Additionally, ZSM-5 NS features a narrower average pore diameter, reduced from 29.6 Å to 25.8 Å, which favours the selectivity for smaller hydrocarbons. This reduction in pore size is particularly advantageous for the production of propane, as the channels' size and shape impose constraints that enhance selectivity.

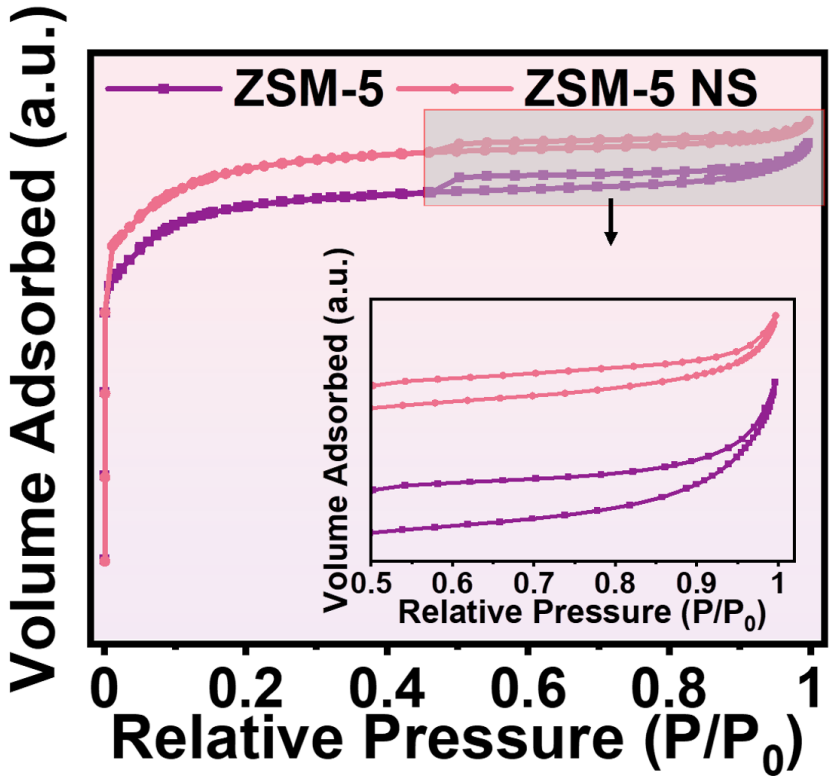

Figure 4.4 Adsorption-desorption isotherms over ZSM-5 and ZSM-5 NS, with an enlarged inset highlighting the isotherms in the relative pressure range from 0.5 to 1.

Table 4.1 Summary of specific surface area and pore features over ZSM-5 and ZSM-5 NS.

Sample	S_{BET} (m^2/g)	S_{Micro} (m^2/g)	S_{Ex} (m^2/g)	V_{Micro} (cm^3/g)	D (Å)
ZSM-5	391	227	164	0.092	29.6
ZSM-5 NS	422	247	175	0.100	25.8

where S_{BET} refers to BET surface area, S_{Micro} refers to t-Plot micropore area, S_{Ex} refers to t-Plot external surface area, V_{Micro} refers to t-Plot micropore volume, and D refers to Barrett-Joyner-Halenda (BJH) adsorption average pore diameter.

To investigate the coordination environments of atoms in ZSM-5 and ZSM-5 NS, an extensive ss-NMR analysis was conducted, as shown in Figure 4.5. The ^{29}Si NMR spectra revealed peaks at chemical shifts of approximately -94 ppm and -113 ppm, corresponding to $Si(OH)_2$ (Q^2) and Si(0Al) (Q^4) framework environments, respectively.[23,24] Notably, ZSM-5 presented an additional peak at around -103 ppm, associated with SiOH (Q^3), while ZSM-5 NS exhibited a peak at approximately -106 ppm, indicating the presence of 3Si(1Al) (Q^4).[23-25] In the ^{27}Al NMR spectra, both materials displayed a prominent peak at around 55 ppm, characteristic of

tetrahedral framework aluminium. ZSM-5 NS also showed an additional peak near 0 ppm, attributed to octahedral extra-framework aluminium species, suggesting a degree of dealumination specific to ZSM-5 NS.[25,26] However, given the relatively low intensity of this peak compared to prominent one at 55 ppm, this dealumination appears to have minimal impact on the overall properties and catalytic performance of the material.

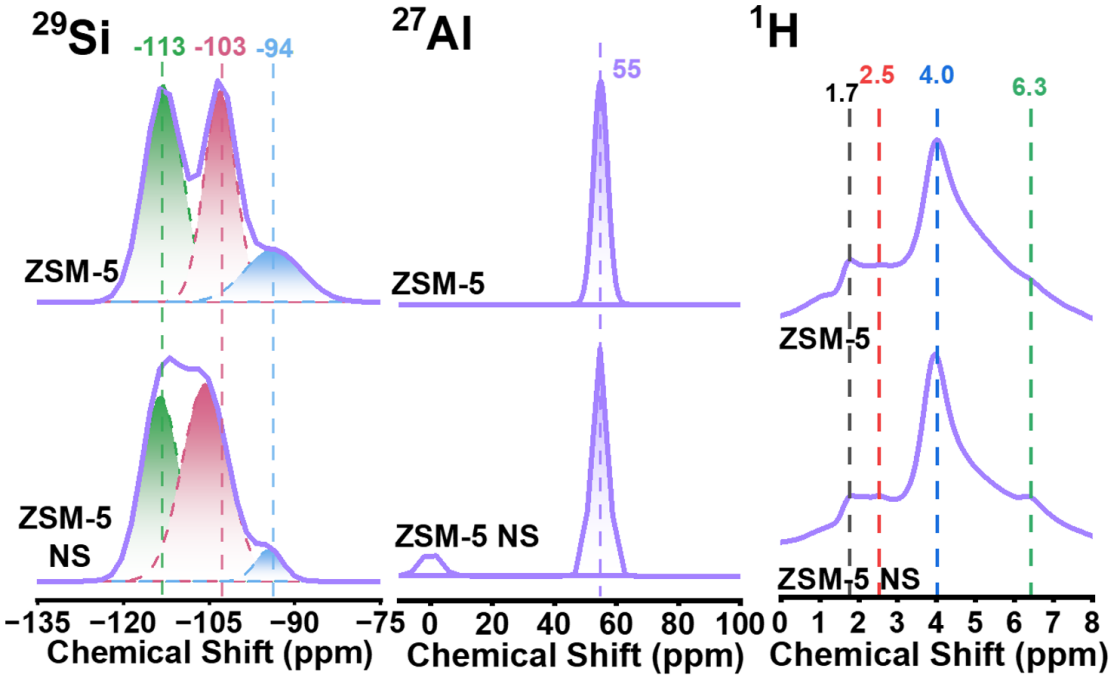

Figure 4.5 ^{29}Si, ^{27}Al, and ^{1}H ss-NMR spectra over ZSM-5 and ZSM-5 NS.

The ^{1}H NMR spectra revealed peaks at chemical shifts of approximately 1.7 ppm, 4.0 ppm, and 6.3 ppm, corresponding to SiOH, BAS, and protons bonded to framework oxygen, respectively.[25,27-29] The chemical shifts and intensities of BAS signals were similar for both ZSM-5 and ZSM-5 NS, indicating that both zeolites have comparable concentrations and strength. Additionally, in line with the ^{27}Al NMR results, ZSM-5 NS displayed an extra peak at around 2.5 ppm in the ^{1}H NMR spectrum, which suggests the presence of extra-framework AlOH species that may contribute to additional acidic sites on the external surface.[25,29] These results highlight that while ZSM-5 and ZSM-5 NS have similar chemical environments, there are subtle differences in their structural and chemical properties.

The catalytic performance in hydrocracking is closely linked to the acidity of the catalysts, particularly the properties of BAS. To complement the initial BAS evaluations using ^{1}H ss-NMR, a comprehensive acidity assessment of ZSM-5 and ZSM-5 NS using NH_3-TPD was performed, as illustrated in Figure 4.6. This technique allowed for a semi-quantitative comparison of total ammonia desorption, the distribution of desorption sites, and strength of these sites through Gaussian peaks deconvolution. The fitting results are summarised in Table 4.2. Both ZSM-5 and ZSM-5 NS exhibited two distinct peaks: one at approximately 300-400°C, indicating weak acid sites, and another at around 500-600°C, representing strong acid sites. This finding is consistent with previous studies on ZSM-5, where NH_3-TPD curves typically reveal at least two peaks.[30] The first peak, in the lower temperature range, corresponds to the desorption of weakly bound ammonia, which has limited catalytic significance. In contrast, the second peak, in the high-temperature range, reflects ammonia desorption from the BAS.[30,31]

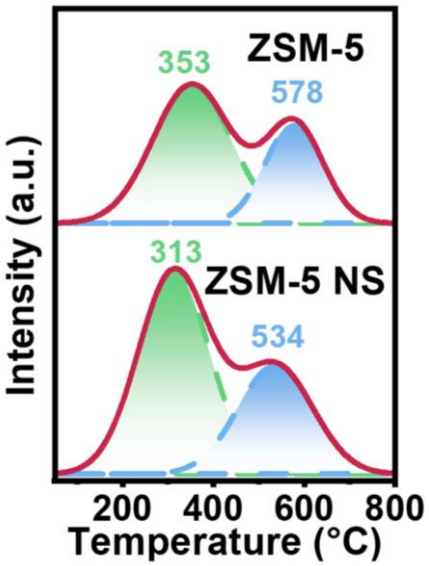

Figure 4.6 NH_3-TPD profiles over ZSM-5 and ZSM-5 NS.

Table 4.2 Semi-quantitative results of acid sites from NH_3-TPD over ZSM-5 and ZSN-5 NS.

Catalyst	Weak Acid (°C)	Peak Area (a.u.)	Strong Acid (°C)	Peak Area (a.u.)	Total Area (a.u.)
ZSM-5	353	34	578	22	56
ZSM-5 NS	313	46	534	24	70

Significantly, ZSM-5 NS demonstrated a substantial increase in the concentration of weak acid sites compared to conventional ZSM-5. This enhancement is likely due to the presence of extra-framework of AlOH spices on the external surface of ZSM-5 NS, as a result of its unique morphological modifications, which is corroborated by the ^{1}H ss-NMR data. However, the differences in strong acid sites between ZSM-5 and ZSM-5 NS were relatively minor. ZSM-5 NS showed a slight decrease in the strength of strong acid sites and a marginal increase in their concentration, but these minor variations in strong acid sites did not significantly affect their hydrocracking performances. Consequently, further evaluation through the catalytic hydrocracking of PP was undertaken to more precisely assess the catalysts' effectiveness.

The catalytic hydrocracking of PP with an average molecular weight of approximately 181 kDa was carried out over ZSM-5 and ZSM-5 NS at 260 °C, 30 bar H_2 for a duration of 12 h. As illustrated in Figure 4.7 (a), the results reveal an unexpected outcome: both catalysts exclusively yielded gaseous products with only trace amounts of liquid-phase products. This phenomenon is likely attributable to the molecular sieving properties inherent to ZSM-5 zeolite. Although both catalysts exhibited high propane selectivity, surpassing 69%, ZSM-5 NS achieved an even higher propane selectivity at 76.3%, compared to 69.1% for conventional ZSM-5. This superior performance can be attributed to the narrower average pore diameter of ZSM-5 NS, as confirmed by BET analysis (Table 4.1). Furthermore, ZSM-5 NS demonstrated a significant enhancement in conversion, approximately 20% higher under the same reaction conditions. Given the comparable acidic properties of ZSM-5 and ZSM-5 NS, it can be inferred that reduced diffusion pathways in ZSM-5 NS effectively enhance the reaction kinetics of PP hydrocracking, thereby minimising solid formation. Additionally, the increased surface area of ZSM-5 NS improves the accessibility of reactant intermediates to the acid sites, further boosting overall conversion.

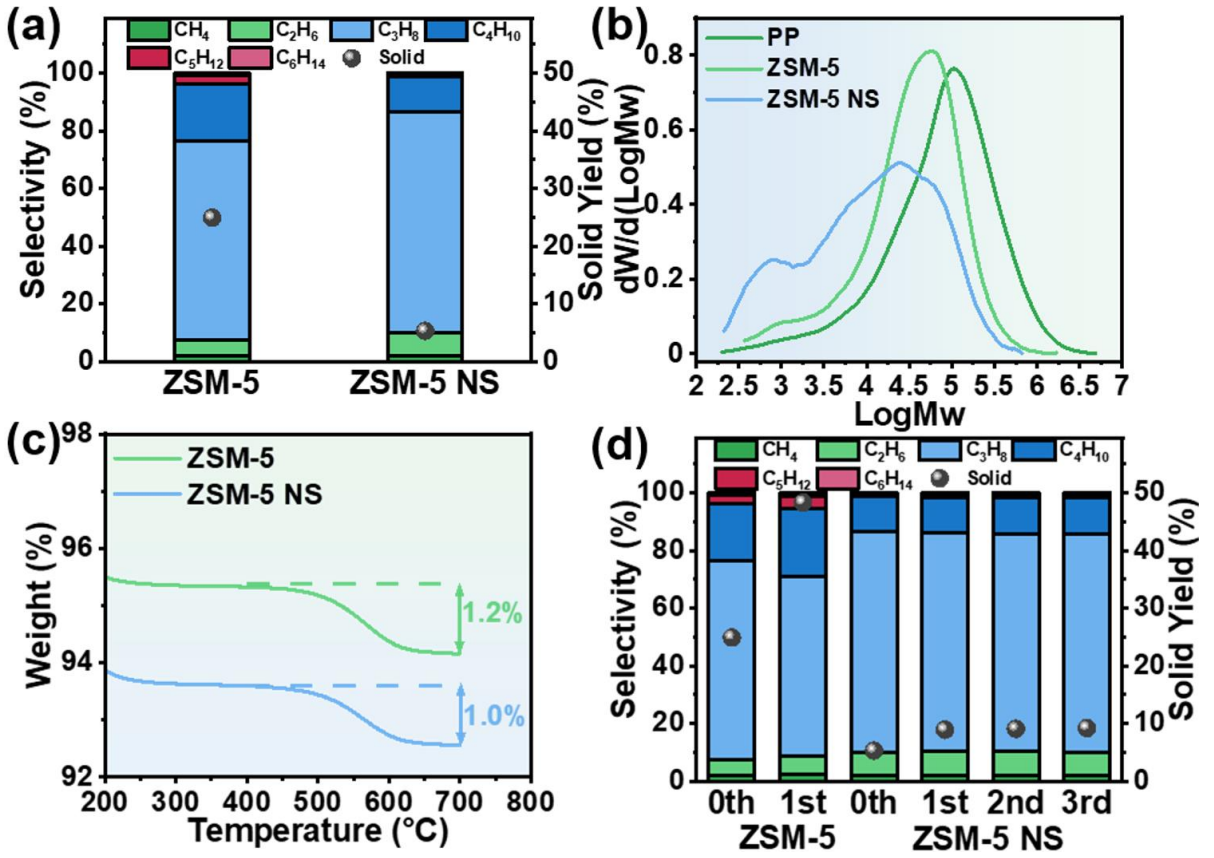

Figure 4.7 Catalytic performance of ZSM-5 and ZSM-5 NS under different reaction conditions: (a) Product distributions over ZSM-5 and ZSM-5 NS. (b) GPC profiles of solid residues over ZSM-5 and ZSM-5 NS after reaction at 260 °C, 30 bar H_2, 12 h. (c) TG analysis results of spent ZSM-5 and ZSM-5 NS after reaction at 260 °C, 30 bar H_2, 12 h. (d) Recyclability tests over ZSM-5 and ZSM-5 NS. Reaction conditions: 260 °C, 30 bar H_2, 12 h, 0.2 g catalyst mixed with 2 g PP for the initial run, with only PP added for the subsequent recycling tests, stirring speed 400 RPM. All the mass balances are within the range of 97 ± 3%.

This conclusion is further corroborated by the results from GPC of the solid residues (Figure 4.7 (b)). Both catalysts exhibit a shift in the molecular weight distribution towards lower values relative to the virgin PP, indicating a reduction in polymer size. However, the shift is more pronounced for ZSM-5 NS, confirming its superior hydrocracking activity. Moreover, ZSM-5 NS displayed an additional peak at logMw ~2.9, which suggests the formation of medium molecular weight intermediates, such as heavy wax. This observation implies that the shorter diffusion pathways in ZSM-5 NS favour the generation of these intermediates.[32] TG analysis (Figure 4.7 (c)) indicates minimal coke formation, approximately 1 wt%, for both catalysts, with

ZSM-5 NS showing a slightly lower coke accumulation. These results suggest that ZSM-5 NS may possess enhanced coking resistance and improved stability.

To further access the stability of both catalysts, recyclability tests were performed under the same reaction conditions. As depicted in Figure 4.7 (d), the first recycle test with ZSM-5 resulted in a significant increase in solid yield from 25 % to approximately 48 %, along with a decrease in propane selectivity, indicating substantial deactivation after first cycle. This deactivation is supported by the TG analysis results (Figure 4.8 (a)), which reveal a doubling of coke content. This increase in coke likely obstructs the migration of hydrocarbon intermediates into the pores, hindering access to active sites and consequently reducing conversion. In contrast, ZSM-5 NS exhibited less deactivation compared to ZSM-5, maintaining similar propane selectivity, with only a slight increase in solid yield to approximately 9% (Figure 4.7 (d)). This improved resilience is attributed to the larger specific surface and shorter pore channels of ZSM-5 NS, which offer more accessible acid sites, thus mitigating the impact of potential pore blockage by coke accumulation. Furthermore, ZSM-5 NS demonstrated consistent catalytic performance and coking resistance over three consecutive cycles, with no further deactivation observed, underscoring its superior stability relative to conventional ZSM-5.

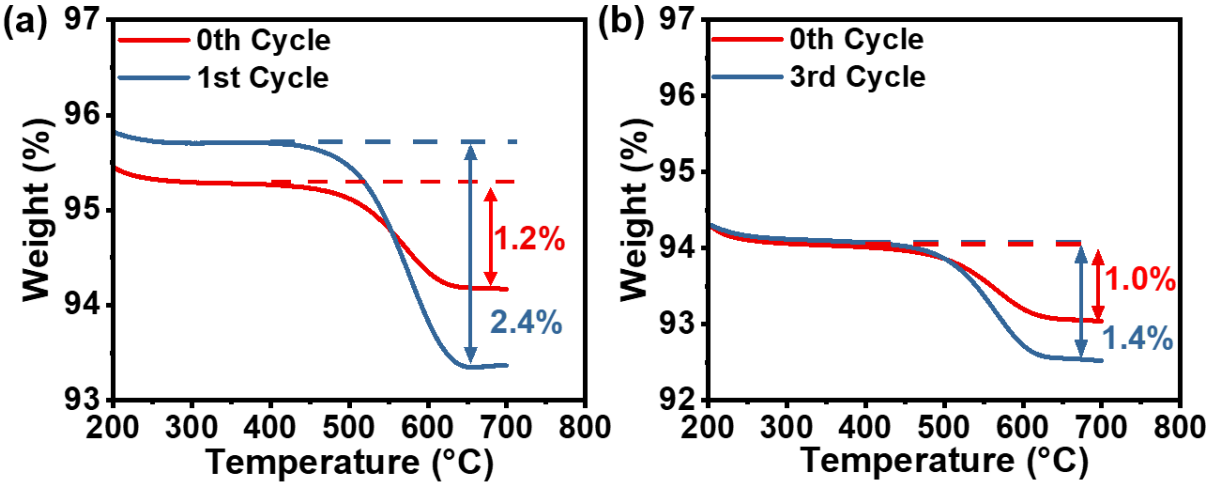

Figure 4.8 TG analysis results over ZSM-5 (a) and ZSM-5 NS (b) after different cycles at reaction conditions of 260 °C, 30 bar H_2, 12 h.

4.2.2 Metal-supported ZSM-5 nanosheet

Although ZSM-5 NS have shown improvements in conversion, selectivity, and stability over conventional ZSM-5 in the hydrocracking of PP, there remains significant potential for further enhancing catalytic performance. This can be achieved through the incorporation of metals known for their ability to activate C-H bonds, such as Pt, Pd, and Ru. These noble metals are widely recognised for their dehydrogenation and hydrogenation properties and have been extensively employed in various industrial catalytic processes. However, their high costs pose economic challenges, limiting their broader applications. To address this issue, the use of five non-noble metals–Fe, Co, Ni, Cu, and Zn–were explored as cost-effective alternatives to enhance C-H bond activation in the catalytic process.

The XRD patterns of the synthesised metal-supported ZSM-5 NS samples (Figure 4.9) demonstrate the retention of the characteristic five diffraction peaks associated with the MFI framework, albeit with a slight shift towards lower angles. This shift is indicative of the incorporation of larger metal atoms, leading to an expansion of lattice structure. While a minor reduction in peak intensity was observed, the structure integrity of the ZSM-5 NS support remained largely intact, even with the introduction of metals at a low concentration of 2 wt%. Moreover, the absence of distinct metals peaks suggests a well-dispersed distribution of metal particles within the framework, confirming the successful synthesis of the metal-supported ZSM-5 NS materials.

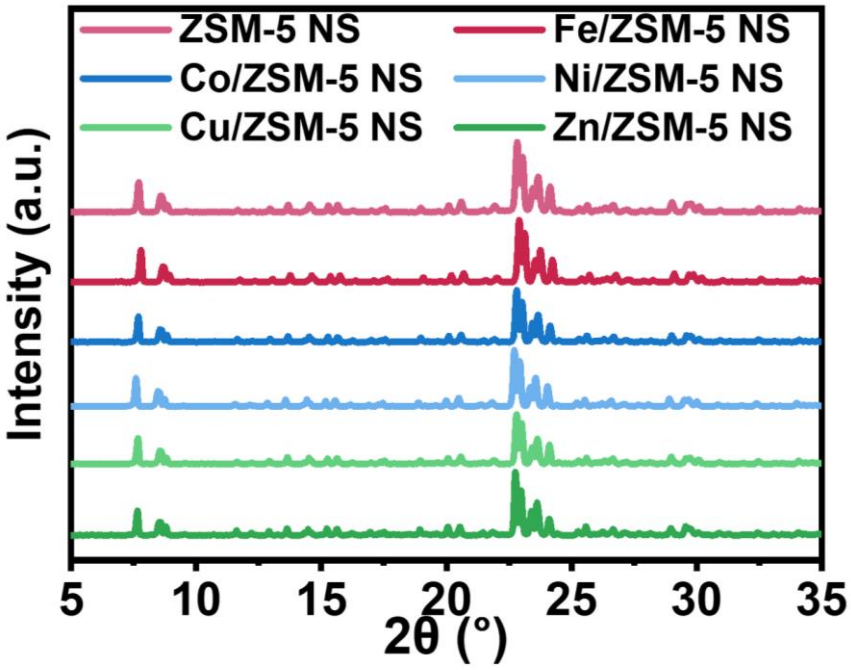

Figure 4.9 XRD patterns over different metal-supported ZSM-5 NS.

In the terms of textural properties, all metal-supported ZSM-5 NS samples displayed hysteresis loops consistent with those of the unmodified ZSM-5 NS (Figure 4.10), indicating that the pore characteristics of the parent zeolite were preserved following metal incorporation. Detailed analysis of the specific surface areas and pore structures (Table 4.3) revealed that the external surface areas of the metal-supported samples were slightly reduced compared to unsupported ZSM-5 NS. This reduction suggests that the metals were primarily incorporated on the external surfaces of the ZSM-5 NS. The presence of these C-H bond activation metals on the external surface is likely to facilitate the dehydrogenation of polymer feedstock, leading to the formation of olefin intermediates, and thereby accelerating primary cracking reactions. Conversely, the observed slight increase in micropore areas in the metal-loaded ZSM-5 NS samples suggests improved accessibility to active sites within the micropores, promoting secondary cracking reactions. Additionally, the modest increase in pore volumes and diameters observed confirms that the metal incorporation did not block pore mouths or channels, thus maintaining efficient mass transfer. Notably, the Ni/ZSM-5 NS sample exhibited the highest surface area, while the Cu/ZSM-5 NS sample demonstrated the smallest average pore diameter.

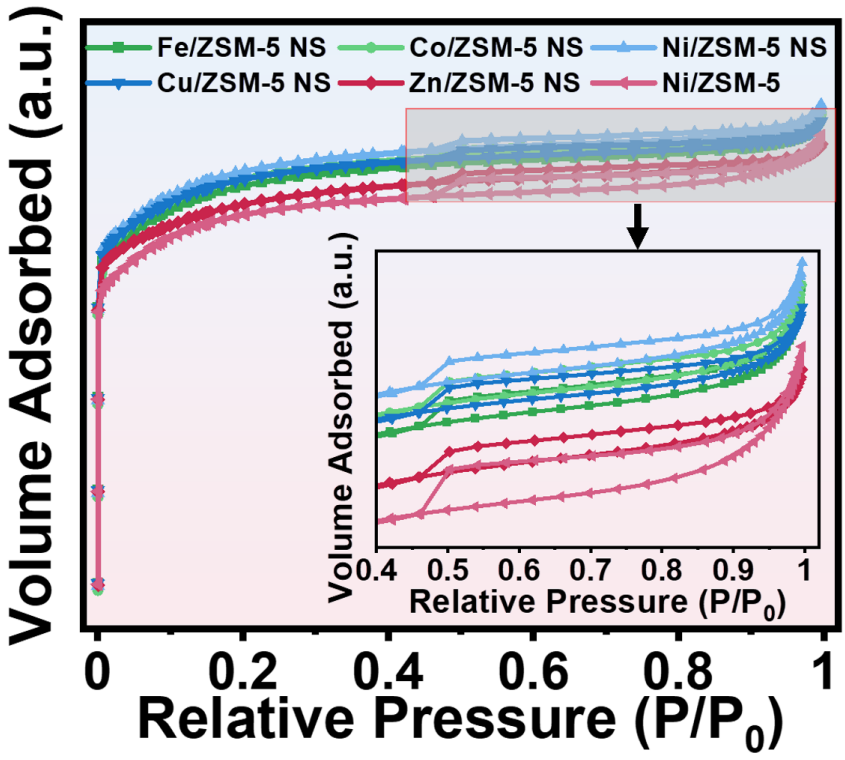

Figure 4.10 Nitrogen adsorption-desorption isotherms for metal-loaded ZSM-5 and ZSM-5 NS, with an enlarged inset highlighting the isotherms in the relative pressure range of 0.4 to 1.

Table 4.3 Summary of specific surface area and pore features over metal-loaded ZSM-5 NS.

Sample	S_{BET} (m^2/g)	S_{Micro} (m^2/g)	S_{Ex} (m^2/g)	V_{Micro} (cm^3/g)	D (Å)
Fe/ZSM-5 NS	393	248	145	0.100	28.7
Co/ZSM-5 NS	400	256	145	0.103	28.2
Ni/ZSM-5 NS	404	255	150	0.103	28.0
Cu/ZSM-5 NS	399	256	143	0.104	27.4
Zn/ZSM-5 NS	380	264	116	0.106	28.9
Ni/ZSM-5	369	224	145	0.091	30.5

where S_{BET} refers to BET surface area, S_{Micro} refers to t-Plot micropore area, S_{Ex} refers to t-Plot external surface area, V_{Micro} refers to t-Plot micropore volume, and D refers to BJH adsorption average pore diameter.

To investigate the redox behaviour of the metal-supported ZSM-5 NS, H_2-TPR experiments were performed. As illustrated in Figure 4.11, a distinct feature around 92 °C was consistently observed across all TPR profiles, including that of the unsupported ZSM-5 NS. This feature is attributed to residual He trapped within the zeolite channels or the TPR system, rather than the reduction of metal sites.[33,34] The TPR profiles reveal that Ni- and Cu-ZSM-5 NS samples

displayed significantly broader main reduction peaks, indicative of stronger metal-support interactions compared to the other metals. The Fe/ZSM-5 NS catalyst exhibited dual reduction peaks at approximately 418 °C and 443 °C, which are likely associated with stepwise reduction of Fe^{3+} to Fe^{2+} occurring outside and inside the ZSM-5 NS pores, respectively. Additionally, a broader peak observed at around 666 °C corresponds to the reduction of Fe^{2+} to Fe^{0}.[34,35] For Co/ZSM-5 NS, two distinct peaks were identified at approximately 484 °C and 618 °C, which can be ascribed to the reduction of isolated Co^{2+} and more stable cobalt silicate or aluminate to Co^{0}, respectively.[36] In the case of Ni/ZSM-5 NS, the main reduction peak centred at around 538 °C is associated with the reduction of Ni^{2+} within the support's pores, while a shoulder peak near 455 °C is attributed to the reduction of Ni^{2+} species located outside the pores.[37,38] The TPR profile for Cu/ZSM-5 NS displayed a peak at approximately 313 °C, corresponding to the reduction of CuO to Cu^{0}, with a shoulder peak around 256 °C that may be attributed to either the same reduction process or the reduction of isolated Cu^{2+} to Cu^{+}, followed by the subsequent reduction of Cu^{+} to Cu^{0} at approximately 534 °C.[39-41] For Zn/ZSM-5 NS, the TPR profile exhibited smaller bumps around 463 °C and 642 °C, likely resulting from the reduction of $Zn(OH)^{+}$ species, which form due to the interactions between Zn^{2+} and BAS during synthesis.[42-44] These smaller peaks suggests a weakened metal-zeolite interaction, possibly due to the formation of hydroxide species rather than direct metallic cations.[43]

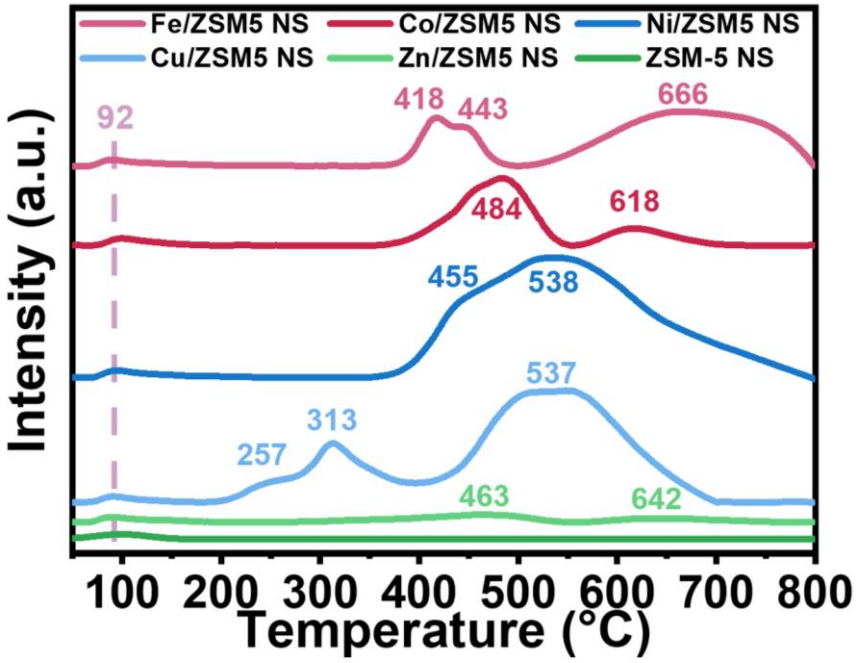

Figure 4.11 H_2-TPR profiles of meta-loaded ZSM-5 NS.

To further evaluate the acidity of metal-doped ZSM-5 NS, NH_3-TPD experiments were conducted, with the results presented in Figure 4.12 and summarized in Table 4.4. The analysis revealed that all metal-loaded catalysts exhibited smaller total peak areas compared to the unmodified ZSM-5 NS, indicating a reduction in overall number of acid sites. This decrease can be attributed to introduction of metal sites through ion exchange with H^+ at BAS. Interestingly, the peaks corresponding to weak acid sites in all metal-loaded catalysts, with the exception of Co/ZSM-5 NS, shifted to higher temperatures relative to the parent zeolite. In contrast, the peaks representing strong acid sites, except in the case of Fe/ZSM-5 NS, shifted to lower temperatures. These trends suggest that metal doping generally enhances the prevalence of weak acid sites while diminishing the strength of strong acid sites. Notably, the Ni- and Co-based catalysts exhibited a higher concentration of strong acid sites compared to the other metal-doped samples, while Fe/ZSM-5 NS showed the highest strength of strong acid sites despite having the lowest concentration. These variations indicate that the specific metal modifications impact distinct catalytic behaviours.[12] Additionally, the low concentration of acid sites observed in Zn/ZSM-5 NS can be attributed to the introduction of hydroxyl species through interactions between Zn and BAS.

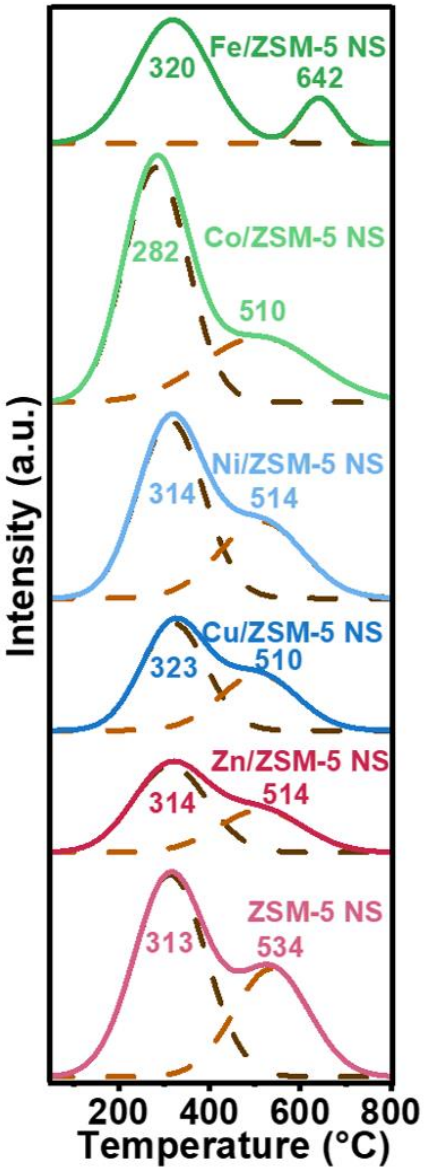

Figure 4.12 NH_3-TPD profiles of metal-loaded ZSM-5 NS.

Table 4.4 Semi-quantitative results of acid sites from NH_3-TPD over metal-loaded ZSN-5 NS.

Catalyst	Weak Acid (°C)	Peak Area (a.u.)	Strong Acid (°C)	Peak Area (a.u.)	Total Area (a.u.)
Fe/ZSM-5 NS	320	30	642	5	35
Co/ZSM-5 NS	282	47	510	23	70
Ni/ZSM-5 NS	314	37	514	20	57
Cu/ZSM-5 NS	323	22	510	14	35
Zn/ZSM-5 NS	314	20	514	11	31

Catalytic hydrocracking tests of PP using metal-doped ZSM-5 NS were carried out at 260 °C, 30 bar of hydrogen for 10 h, as shown in Figure 4.13 (a). All metal-loaded ZSM-5 NS catalysts demonstrated high conversion with solid yields remaining below 5 wt%, and propane selectivity exceeding 73%, except for Zn-based catalyst, which exhibited a slightly lower selectivity at 69%. The Ni-based catalyst was particularly notable, achieving the lowest solid yield at approximately 0.6 wt%, which is consistent with its high concentration of strong acid sites and pronounced reduction properties, as identified through NH_3-TPD and H_2-TPR analyses. On the other hand, the Cu-based catalyst achieved the highest propane selectivity, around 76.2 wt%, a performance likely associated with its narrowest average pore diameter, as confirmed by BET analysis. In contrast, the Zn/ZSM-5 NS showed a higher solid yield (3.5%) and the lowest propane selectivity (69.3%) among all the catalysts. This behaviour is likely due to the presence of $Zn(OH)^+$ spices rather than metallic cations, which adversely affects its hydrocracking performance.

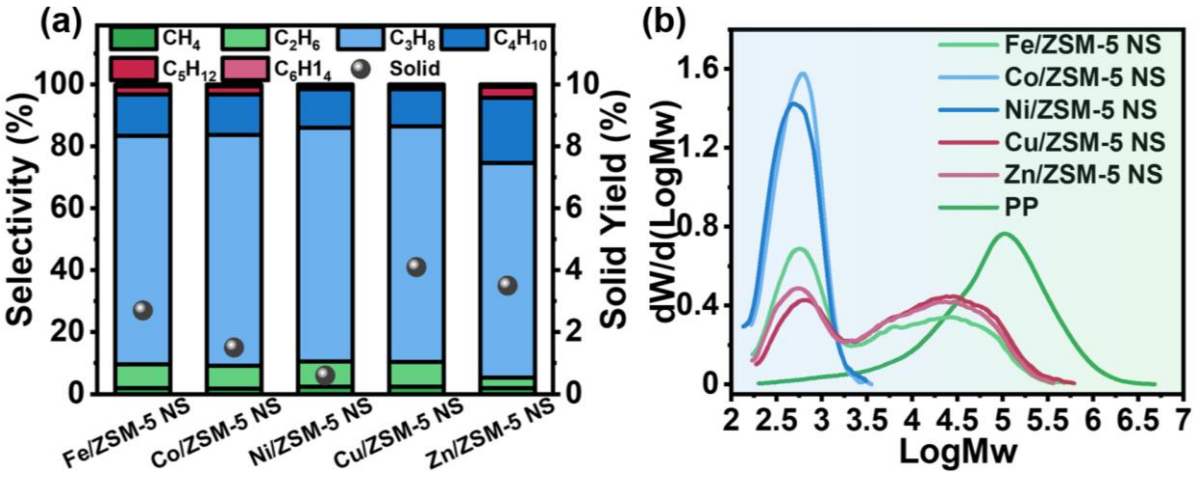

Figure 4.13 (a) Product distribution over metal-loaded ZSM-5 NS. (b) GPC profiles of solid residues over metal-loaded ZSM-5 NS after reaction. Reaction conditions: 260 °C, 30 bar H_2, 10 h, 0.2 g catalyst mixed with 2 g PP, stirring speed 400 RPM. All the mass balances are within the range of 97 ± 3%.

When evaluating both conversion and selectivity, the Ni-based catalyst stood out, achieving near-complete conversion with a moderate propane selectivity of approximately 75.7%. Conversely, while the Cu-based catalyst exhibited high propane selectivity, it retained a

significant portion of unreacted polymer, leading to a solid yield as high as 4.1 wt%. Based on these findings, the Ni-based catalyst was selected for further in-depth investigation.

This conclusion is further corroborated by GPC results, depicted in Figure 4.13 (b). The solid residues from Fe-, Cu-, and Zn-based catalysts displayed bimodal peaks centred at logMw values of approximately 2.7, and 4.5, indicating the presence of both medium molecular weight intermediates and unreacted polymer. In contrast, the Ni-based and Co-based catalysts showed peaks corresponding exclusively to medium molecular weight intermediates, highlighting their superior reaction kinetics in polymer conversion. Additionally, the GPC results for the solid residues aligned well with the observed solid yields for different catalysts, following the trend: Cu (4.1%) > Zn (3.5%) > Fe (2.7%) > Co (1.5%) > Ni (0.6%). This correlation reinforces the relationship between the average molecular weight of the residues and the solid yields obtained in catalytic testing.

4.2.3 Further evaluation of Ni/ZSM-5 nanosheet

To elucidate the differences in catalytic performance when using conventional ZSM-5 versus ZSM-5 NS as supports in bifunctional catalysts, PP hydrocracking reactions with Ni/ZSM-5 and Ni/ZSM-5 NS were performed. As illustrated in Figure 4.14 (a), the use of Ni/ZSM-5 resulted in a marked decrease in both propane selectivity and conversion, leaving approximately 35% PP unconverted. Additionally, the liquid-phase products (C_{6+}) were detected, constituting roughly 8 wt% of the overall product distribution. This observation is consistent with extensive body of literature on bifunctional ZSM-5 catalysts, which often generate both gaseous and liquid-phase products.[45,46] The reduced catalytic performance of Ni/ZSM-5 is likely due to the widening of pore diameters upon Ni incorporation, which diminishes the molecular sieve effect. Moreover, the smaller specific surface area and pore volume observed for Ni/ZSM-5 result in a reduced number of accessible active sites (Table 4.1 and 4.3). These textual characteristics likely facilitate the diffusion of larger hydrocarbon molecules into the pores, where they become trapped, leading to pore blockages and diminished mass transfer efficiency. As a consequence, the hydrocracking of PP is inhibited,

promoting the formation of liquid-phase products. Furthermore, the exclusive production of liquid hydrocarbons with Ni/ZSM-5 may be attributed to pore blockages that prevent the larger liquid molecules from migrating into the pore channels for subsequent cracking into gaseous products. Notably, the introduction of Ni into ZSM-5 significantly altered the production distribution (Figure 4.14 (a)), potentially due to an imbalance between the metal and acid sites and unfavourable changes in the textual properties caused by the presence of metal particles.

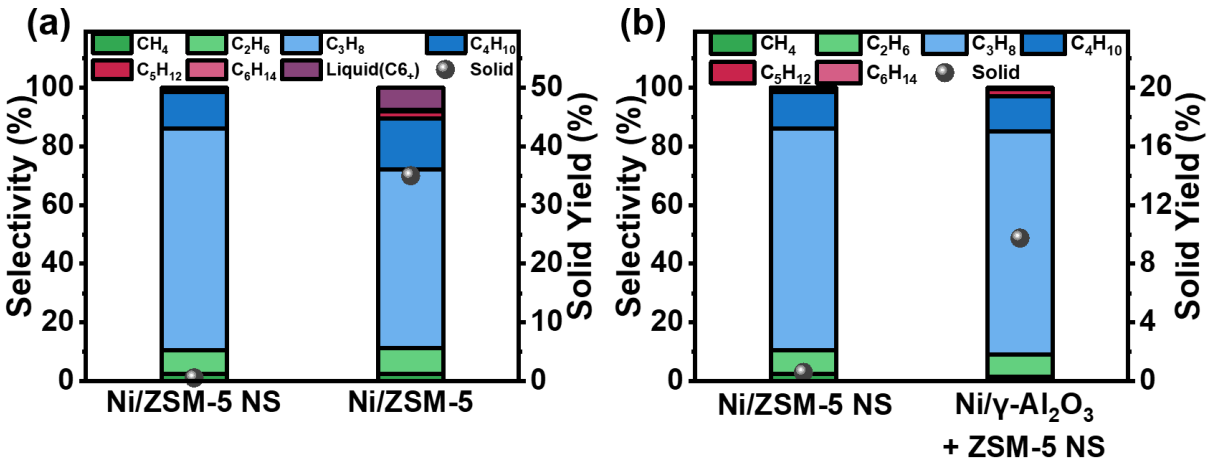

Figure 4.14 (a) Product distributions over Ni/ZSM-5 NS and Ni/ZSM-5 catalysts. (b) Product distributions over Ni/ZSM-5 NS and Ni/γ-Al_2O_3 mixed with ZSM-5 NS. Reaction conditions: 260 °C, 30 bar H_2, 10 h, 0.2 g catalyst (or 0.2 g Ni/γ-Al_2O_3 physically mixed with 0.2 g ZSM-5 NS) and 2 g PP, stirring speed 400 RPM. All the mass balances are within the range of 97 ± 3%.

Given that reactant molecules must migrate between acid and metal sites to facilitate multiple C-C bond cleavages, the spatial proximity of these sites is a crucial for catalytic efficiency. To explore this, the catalytic performances of a physical mixture of Ni/γ-Al_2O_3 and ZSM-5 NS with that of Ni/ZSM-5 NS under identical reaction conditions were compared (Figure 4.14 (b)). The increased diffusion distance between the metal and acid sites (from nanometre-scale to millimetre-scale) resulted in a slight reduction in conversion by approximately 10%. This result suggests that extending the distance between active sites increases the time required for mass transfer, thereby decreasing the frequency with which reactant molecules can access these sites within the limited reaction time. These findings underscore the importance of

optimising both the diffusion within the micropore channels and the diffusion between different active sites to maximise catalytic performance.

To further assess the stability of Ni/ZSM-5 NS, a recyclability test was conducted, with results presented in Figure 4.15 (a). Notably, the catalyst demonstrated consistent catalytic performance throughout the recycling tests, with propane selectivity exceeding 74% and solid yields remaining below 1%, highlighting its high stability. This stability is corroborated by TG analysis results (Figure 4.15 (b)), which indicate that the reused Ni/ZSM-5 NS catalyst formed a similar amount of coke as the fresh catalyst, even after 5 cycles.

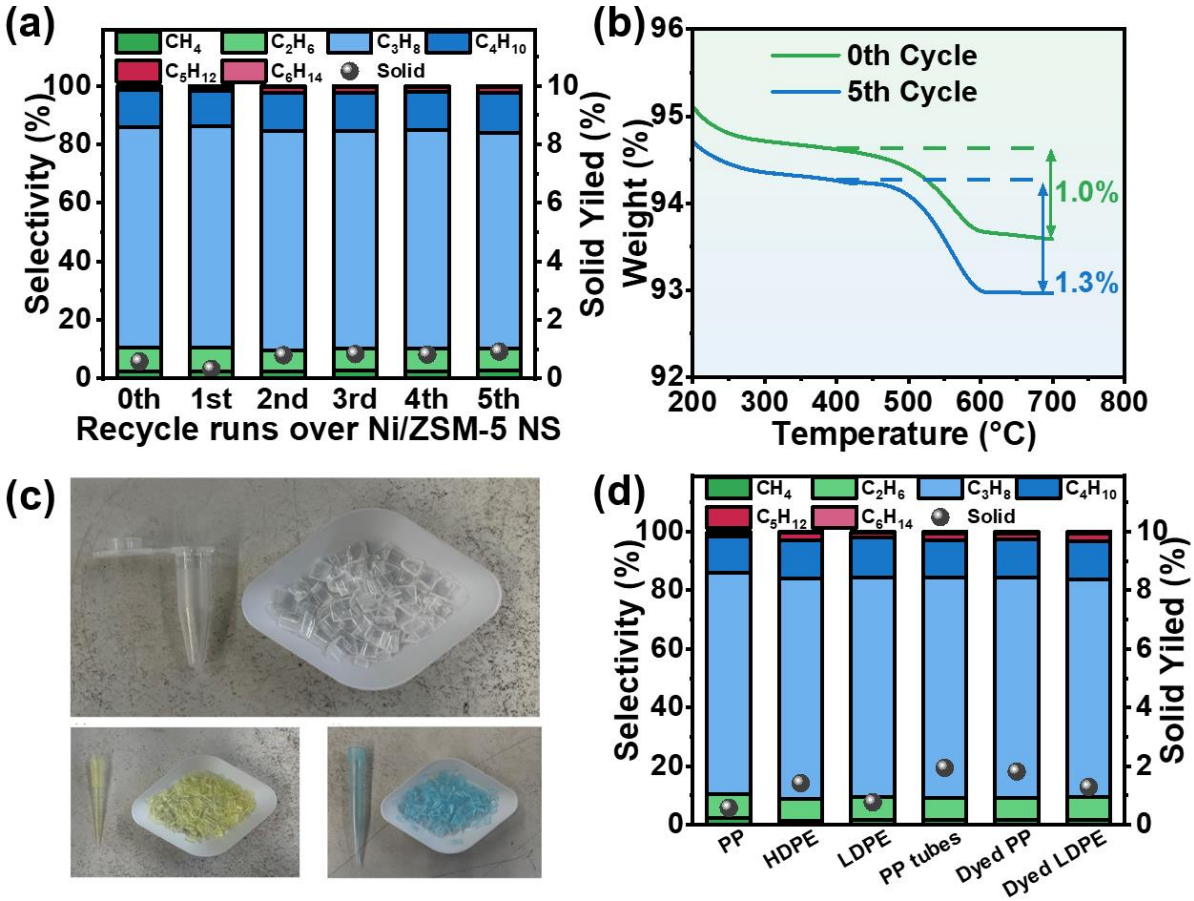

Figure 4.15 (a) Recyclability tests over Ni/ZSM-5 NS. (b) TG analysis profiles of spent Ni/ZSM-5 NS after 0th and 5th cycle of recyclability test. (c) Commercial plastics used for other plastic tests (White: commercial PP microtubes; Yellow: PP pipette tips; Blue: LDPE pipette tips). (d) Product distributions over Ni/ZSM-5 NS of different plastic types (pure PP, HDPE, LDPE, and commercial plastics). Reaction conditions: 260 °C, 30 bar H_2, 10 h, 0.2 g catalyst and 2 g PP for the initial recycling test, followed by the addition of only PP in the subsequent recycling

tests, or 2 g of other plastics, stirring speed 400 RPM. All the mass balances are within the range of 97 ± 3%.

Recognising that additives such as dyes and plasticisers, along with varying types of plastics, can influence catalytic behaviour, the evaluation of Ni/ZSM-5 NS was extended by testing its hydrocracking performance on a range of different plastics, including commercial ones, to assess its viability for practical plastic upcycling. As shown in Figure 4.15 (d), the catalyst exhibited consistent conversion and selectivity across various plastics, such as LDPE and HDPE, indicating that the product distribution is primarily governed by the molecular sieving effect of the catalysts regardless of the plastic types. Moreover, tests on laboratory plastics, including white PP microtubes, yellow PP pipette tips, and blue LDPE pipette tips (Figure 4.15 (c)), revealed similar propane selectivity and conversion levels to those observed in pure PP hydrocracking, suggesting that Ni/ZSM-5 NS is effective in decomposing PP even in the presence of additives. These results highlight the catalyst's versatility and efficiency in processing different plastic types, including commercial plastics, underscoring its significant potential for real-world plastic upcycling applications.

To gain a deeper understanding of the reaction mechanism, time-resolved studies on PP hydrocracking using Ni/ZSM-5 NS were conducted, as depicted in Figure 4.16 (a). The findings indicate a general increase in propane selectivity as the reaction time is extended from 2 to 10 h, followed by a slight decrease when the reaction time is prolonged to 12 h. In the initial 4 h, propane selectivity was relatively low, at approximately 62%, with a substantial amount of solid residues remaining. GPC profiles shown in Figure 4.16 (b) identify these residues as predominantly unreacted polymer. The polymer is likely preferentially adsorbed onto the active sites, impending access for other reaction intermediates or products, leading to molecular sieving primarily occurring over the polymer chains.[47] As the reaction continues from 4 to 8 h, most of the unreacted polymer is nearly completely consumed. During this period, medium molecular weight intermediates and some heavier gaseous products, such as butane and pentane, are also adsorbed onto the active sites, undergoing molecular sieving. This process raises propane selectivity to approximately 68%, as evidenced by the reduction in

butane and pentane selectivity during this phase. Between 8 to 10 h, with only medium molecular weight intermediates and gaseous products remaining, a higher proportion of heavier gaseous products can be readsorbed onto the active sites, where they undergo further hydrocracking and molecular sieving. This results in the highest propane selectivity, approximately 76%. However, extending the reaction time beyond this optimal point leads to overcrack of existing products, resulting in increased production of light products, such as methane and ethane, at the expense of heavier products like propane and butane. These findings emphasise the dynamic nature of the hydrocracking process over Ni/ZSM-5 NS, highlighting the importance of optimising reaction times to achieve the desired product distribution.

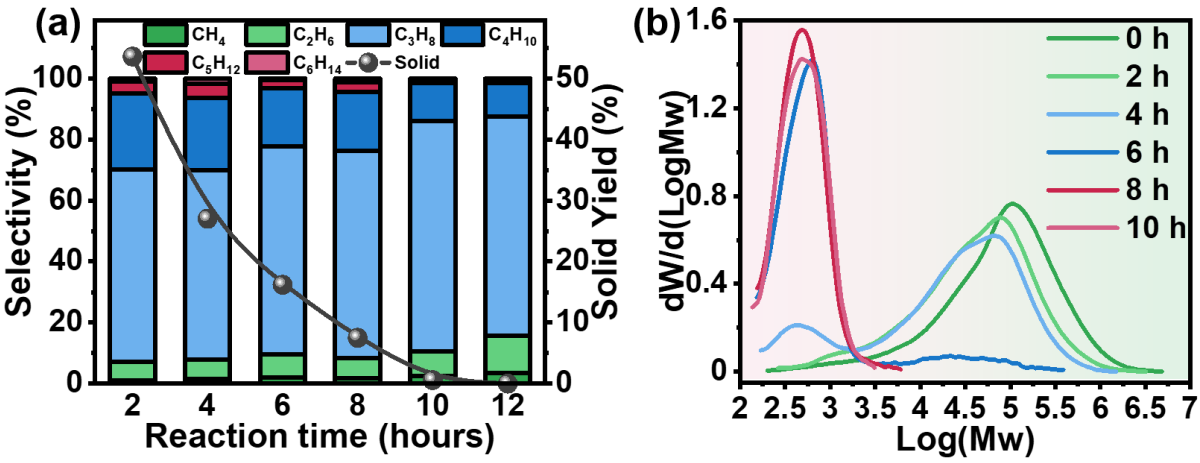

Figure 4.16 (a) Time-dependent reaction over Ni/ZSM-5 NS. (b) GPC profiles of solid residues over Ni/ZSM-5 NS after different reaction time. Reaction conditions: 260 °C, 30 bar H_2, 0.2 g catalyst and 2 g PP for different reaction time, stirring speed 400 RPM. All the mass balances are within the range of 97 ± 3%.

To further elucidate the mechanistic differences in PP hydrocracking between Ni/ZSM-5 and Ni/ZSM-5 NS, in-situ DRIFTS was employed, as presented in Figure 4.17 (a) and 4.17 (b). For Ni/ZSM-5 (Figure 4.17 (a)), primary cracking begins within the first 10 min, as indicated by the appearance of weak CH_3 bending (1370 cm^{-1}), CH_2 bending (1450 cm^{-1}), and C-H stretching (2800 to 3000 cm^{-1}) vibrations, which are characteristic of the PP framework.[48] These peak intensities remain stable throughout the 4-hours spectra collection, indicating sustained but

limited primary cracking without significant transition to secondary cracking. This behaviour can be attributed to the smaller surface area and pore volume of Ni/ZSM-5 (Figure 4.10 and Table 4.3), which limits the number of accessible active sites. Furthermore, the structure of Ni/ZSM-5 likely allows larger hydrocarbons to diffuse into the pores, where they become trapped, causing pore blockages and reduced mass transfer efficiency, thereby inhibiting further cracking.

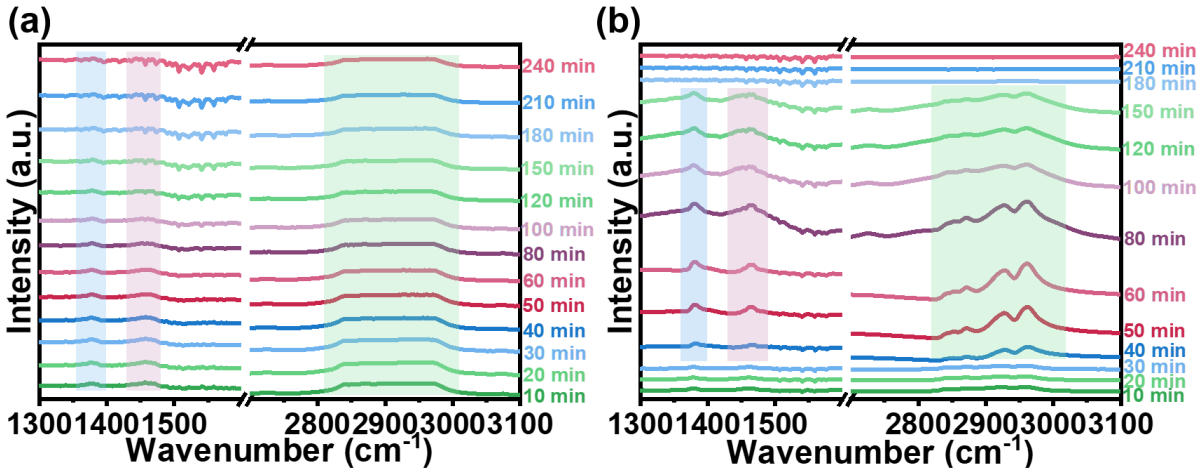

Figure 4.17 (a) In-situ DRIFTS analysis of 4 mg Ni/ZSM-5 catalyst mixed with 40 mg PP at 260 °C and 5 bar H_2, with a flow rate 5 mL min^{-1}. (b) In-situ DRIFTS analysis of 4 mg Ni/ZSM-5 NS catalyst mixed with 40 mg PP under identical conditions.

In contrast, the DRIFTS for Ni/ZSM-5 NS shows similar primary cracking within the first 30 min. However, from 40 to 150 min, there is a notable intensification of peak intensities, with the emergence of distinct and strong C-H stretching peaks (2840, 2870, 2920, 2960 cm^{-1}).[48] This period is indicative of predominant secondary cracking, wherein long-chain intermediates diffuse into the micropore channels, facilitating extensive C-C bond cleavage to produce the desired final products. The accelerated reaction kinetics observed with Ni/ZSM-5 NS can be attributed to its higher surface area and reduced diffusion distances, which enhance overall catalytic efficiency. After 180 to 240 min, the spectra exhibit minimal peak fluctuations, indicating the cessation of hydrocracking reactions. These findings underscore the critical role of catalyst structure in governing the hydrocracking mechanism and highlight the superior

performance of Ni/ZSM-5 NS in promoting both primary and secondary cracking processes due to its advantageous textural properties.

4.3 Conclusion

In this chapter, the effective hydrocracking of PP into propane was demonstrated, achieving a selectivity of approximately 76.3% using ZSM-5 NS. The reduced diffusion distances within the ZSM-5 NS structure plays a crucial role in mitigating coke accumulation and enhancing reaction kinetics when compared to conventional ZSM-5 zeolite. The introduction of non-noble-metals (Fe, Co, Ni, Cu, Zn) into the ZSM-5 NS matrix significantly boosts the catalytic performance, with Ni/ZSM-5 NS showing high conversion, selectivity for propane, and robust stability. Furthermore, this catalyst exhibits versatility by efficiently hydrocracking a variety of plastic types, including commercial plastics, underscoring its potential for industrial-scale plastic waste treatment. Collectively, these results demonstrate that Ni/ZSM-5 NS is an effective catalyst for transforming plastic waste into valuable propane, offering a potential solution for sustainable plastic waste management and contributing to the advancement of a circular economy.

4.4 Reference

1. Wang, H., and Edman Tsang, S.C. (2024). Recent advances in polyolefin plastic waste upcycling via mild heterogeneous catalysis route from catalyst development to process design. Cell Reports Physical Science *5*, 102075. 10.1016/j.xcrp.2024.102075.
2. Zheng, K., Wu, Y., Hu, Z., Wang, S., Jiao, X., Zhu, J., Sun, Y., and Xie, Y. (2023). Progress and perspective for conversion of plastic wastes into valuable chemicals. Chemical Society Reviews *52*, 8-29. 10.1039/D2CS00688J.
3. Europe, P. (2023). Annual production of plastics worldwide from 1950 to 2022 (in million metric tons). Plastics Europe.
4. Korley, L.T.J., Epps, T.H., Helms, B.A., and Ryan, A.J. (2021). Toward polymer upcycling—adding value and tackling circularity. Science *373*, 66-69. 10.1126/science.abg4503.
5. Law, K.L., and Narayan, R. (2022). Reducing environmental plastic pollution by designing polymer materials for managed end-of-life. Nature Reviews Materials *7*, 104-116. 10.1038/s41578-021-00382-0.

6. Geyer, R., Jambeck, J.R., and Law, K.L. (2017). Production, use, and fate of all plastics ever made. Science Advances *3*, e1700782. 10.1126/sciadv.1700782.
7. Zhang, Z., Wang, J., Ge, X., Wang, S., Li, A., Li, R., Shen, J., Liang, X., Gan, T., Han, X., et al. (2023). Mixed Plastics Wastes Upcycling with High-Stability Single-Atom Ru Catalyst. Journal of the American Chemical Society *145*, 22836-22844. 10.1021/jacs.3c09338.
8. Zhang, F., Zhao, Y., Wang, D., Yan, M., Zhang, J., Zhang, P., Ding, T., Chen, L., and Chen, C. (2021). Current technologies for plastic waste treatment: A review. Journal of Cleaner Production *282*, 124523. 10.1016/j.jclepro.2020.124523.
9. Sardon, H., and Dove, A.P. (2018). Plastics recycling with a difference. Science *360*, 380-381. 10.1126/science.aat4997.
10. Martín, A.J., Mondelli, C., Jaydev, S.D., and Pérez-Ramírez, J. (2021). Catalytic processing of plastic waste on the rise. Chem *7*, 1487-1533. 10.1016/j.chempr.2020.12.006.
11. Hou, Q., Zhen, M., Qian, H., Nie, Y., Bai, X., Xia, T., Laiq Ur Rehman, M., Li, Q., and Ju, M. (2021). Upcycling and catalytic degradation of plastic wastes. Cell Reports Physical Science *2*, 100514. 10.1016/j.xcrp.2021.100514.
12. Dong, Z., Chen, W., Xu, K., Liu, Y., Wu, J., and Zhang, F. (2022). Understanding the Structure–Activity Relationships in Catalytic Conversion of Polyolefin Plastics by Zeolite-Based Catalysts: A Critical Review. ACS Catalysis *12*, 14882-14901. 10.1021/acscatal.2c04915.
13. Wu, X., Wang, X., Zhang, L., Wang, X., Song, S., and Zhang, H. (2024). Polyethylene Upgrading to Liquid Fuels Boosted by Atomic Ce Promoters. Angewandte Chemie International Edition *63*, e202317594. 10.1002/anie.202317594.
14. Zhou, Q., Wang, D., Wang, Q., He, K., Lim, K.H., Yang, X., Wang, W.-J., Li, B.-G., and Liu, P. (2023). Mechanistic Understanding of Efficient Polyethylene Hydrocracking over Two-Dimensional Platinum-Anchored Tungsten Trioxide. Angewandte Chemie International Edition *62*, e202305644. 10.1002/anie.202305644.
15. Chu, M., Wang, X., Wang, X., Xu, P., Zhang, L., Li, S., Feng, K., Zhong, J., Wang, L., Li, Y., et al. (2024). Layered Double Hydroxide Derivatives for Polyolefin Upcycling. Journal of the American Chemical Society *146*, 10655-10665. 10.1021/jacs.4c00327.
16. Wang, C., Zhang, L., Huang, X., Zhu, Y., Li, G., Gu, Q., Chen, J., Ma, L., Li, X., He, Q., et al. (2019). Maximizing sinusoidal channels of HZSM-5 for high shape-selectivity to p-xylene. Nature Communications *10*, 4348. 10.1038/s41467-019-12285-4.
17. Yang, M., Li, B., Gao, M., Lin, S., Wang, Y., Xu, S., Zhao, X., Guo, P., Wei, Y., Ye, M., et al. (2020). High Propylene Selectivity in Methanol Conversion over a Small-Pore

SAPO Molecular Sieve with Ultra-Small Cage. ACS Catalysis *10*, 3741-3749. 10.1021/acscatal.9b04703.

18. Duan, J., Wang, H., Li, H., Liu, L., Fan, K., Meng, X., Zhang, Z., Wang, L., and Xiao, F.-S. (2023). Selective conversion of polyethylene wastes to methylated aromatics through cascade catalysis. EES Catalysis *1*, 529-538. 10.1039/D3EY00011G.
19. Liu, X., Shi, J., Yang, G., Zhou, J., Wang, C., Teng, J., Wang, Y., and Xie, Z. (2021). A diffusion anisotropy descriptor links morphology effects of H-ZSM-5 zeolites to their catalytic cracking performance. Communications Chemistry *4*, 107. 10.1038/s42004-021-00543-w.
20. Duan, J., Chen, W., Wang, C., Wang, L., Liu, Z., Yi, X., Fang, W., Wang, H., Wei, H., Xu, S., et al. (2022). Coking-Resistant Polyethylene Upcycling Modulated by Zeolite Micropore Diffusion. Journal of the American Chemical Society *144*, 14269-14277. 10.1021/jacs.2c05125.
21. Shen, K., Wang, N., Qian, W., Cui, Y., and Wei, F. (2014). Atmospheric pressure synthesis of nanosized ZSM-5 with enhanced catalytic performance for methanol to aromatics reaction. Catalysis Science & Technology *4*, 3840-3844. 10.1039/C4CY01010H.
22. Sing, K.S.W. (1985). Reporting physisorption data for gas/solid systems with special reference to the determination of surface area and porosity (Recommendations 1984). Pure and Applied Chemistry *57*, 603-619. doi:10.1351/pac198557040603.
23. Wang, Q., Xu, S., Chen, J., Wei, Y., Li, J., Fan, D., Yu, Z., Qi, Y., He, Y., Xu, S., et al. (2014). Synthesis of mesoporous ZSM-5 catalysts using different mesogenous templates and their application in methanol conversion for enhanced catalyst lifespan. RSC advances *4*, 21479-21491. 10.1039/C4RA02695K.
24. Yoo, W.C., Zhang, X., Tsapatsis, M., and Stein, A. (2012). Synthesis of mesoporous ZSM-5 zeolites through desilication and re-assembly processes. Microporous and mesoporous materials *149*, 147-157. 10.1016/j.micromeso.2011.08.014.
25. Zhang, W., Bao, X., Guo, X., and Wang, X. (1999). A high-resolution solid-state NMR study on nano-structured HZSM-5 zeolite. Catalysis Letters *60*, 89-94. 10.1023/A:1019061714047.
26. Seo, Y., Cho, K., Jung, Y., and Ryoo, R. (2013). Characterization of the surface acidity of MFI zeolite nanosheets by 31P NMR of adsorbed phosphine oxides and catalytic cracking of decalin. ACS catalysis *3*, 713-720. 10.1021/cs300824e.
27. Leung, K.C., Hong, S., Li, G., Xing, Y., Ng, B.K.Y., Ho, P.-L., Ye, D., Zhao, P., Tan, E., Safonova, O., et al. (2023). Confined Ru sites in a 13X zeolite for ultrahigh H2 production from NH3 decomposition. Journal of the American Chemical Society *145*, 14548-14561. 10.1021/jacs.3c05092.

28. Heeribout, L., Batamack, P., Dorémieux-Morin, C., Vincent, R., and Fraissard, J. (1996). Study of H-ZSM-5 acidity by 1H NMR: broad-line at 4 K and high resolution MAS at 300 K; Brønsted acidity scale and comparison with other zeolites. Colloids and Surfaces. A, Physicochemical and Engineering Aspects *115*, 229-237. 10.1016/0927-7757(96)03664-3.
29. Almutairi, S.M.T., Mezari, B., Magusin, P.C.M.M., Pidko, E.A., and Hensen, E.J.M. (2012). Structure and reactivity of Zn-modified ZSM-5 zeolites: The importance of clustered cationic Zn complexes. ACS Catalysis *2*, 71-83. 10.1021/cs200441e.
30. Rodríguez-González, L., Hermes, F., Bertmer, M., Rodríguez-Castellón, E., Jiménez-López, A., and Simon, U. (2007). The acid properties of H-ZSM-5 as studied by NH3-TPD and 27Al-MAS-NMR spectroscopy. Applied Catalysis A: General *328*, 174-182. 10.1016/j.apcata.2007.06.003.
31. Niwa, M., and Katada, N. (1997). Measurements of acidic property of zeolites by temperature programmed desorption of ammonia. Catalysis Surveys from Asia *1*, 215-226. 10.1023/A:1019033115091.
32. Wang, H., Yoskamtorn, T., Zheng, J., Ho, P.-L., Ng, B., and Tsang, S.C.E. (2023). Ce-Promoted PtSn-Based Catalyst for Hydrocracking of Polyolefin Plastic Waste into High Yield of Gasoline-Range Products. ACS Catalysis *13*, 15886-15898. 10.1021/acscatal.3c03996.
33. Cañizares, P., de Lucas, A., Dorado, F., Durán, A., and Asencio, I. (1998). Characterization of Ni and Pd supported on H-mordenite catalysts: Influence of the metal loading method. Applied catalysis. A, General *169*, 137-150. 10.1016/S0926-860X(98)00008-8.
34. Park, J.-H., Choung, J.-H., Nam, I.-S., and Ham, S.-W. (2008). N2O decomposition over wet- and solid-exchanged Fe-ZSM-5 catalysts. Applied Catalysis B: Environmental *78*, 342-354. 10.1016/j.apcatb.2007.09.020.
35. Yuan, E., Wu, G., Dai, W., Guan, N., and Li, L. (2017). One-pot construction of Fe/ZSM-5 zeolites for the selective catalytic reduction of nitrogen oxides by ammonia. Catalysis science & technology *7*, 3036-3044. 10.1039/C7CY00724H.
36. Ayodele, O.B. (2017). Influence of oxalate ligand functionalization on Co/ZSM-5 activity in Fischer Tropsch synthesis and hydrodeoxygenation of oleic acid into hydrocarbon fuels. Scientific Reports *7*, 10008-10014. 10.1038/s41598-017-09706-z.
37. Ihm, S.-K., Yi, K.-H., and Park, Y.-K. (1994). Aromatization of n-pentane over Ni-ZSM-5 catalysts. In Studies in Surface Science and Catalysis, J. Weitkamp, H.G. Karge, H. Pfeifer, and W. Hölderich, eds. (Elsevier), pp. 1765-1772. 10.1016/S0167-2991(08)63730-1.

38. De Lucas, A., Valverde, J.L., Dorado, F., Romero, A., and Asencio, I. (2005). Influence of the ion exchanged metal (Cu, Co, Ni and Mn) on the selective catalytic reduction of NOX over mordenite and ZSM-5. Journal of Molecular Catalysis. A, Chemical *225*, 47-58. 10.1016/j.molcata.2004.08.036.

39. Urquieta-González, E.A., Martins, L., Peguin, R.P.S., and Batista, M.S. (2002). Identification of extra-framework species on Fe/ZSM-5 and Cu/ZSM-5 catalysts typical microporous molecular sieves with zeolitic structure. Materials Research (São Carlos, São Paulo, Brazil) *5*, 321-327. 10.1590/S1516-14392002000300017.

40. Peng, C., Yan, R., Peng, H., Mi, Y., Liang, J., Liu, W., Wang, X., Song, G., Wu, P., and Liu, F. (2020). One-pot synthesis of layered mesoporous ZSM-5 plus Cu ion-exchange: Enhanced NH3-SCR performance on Cu-ZSM-5 with hierarchical pore structures. Journal of Hazardous Materials *385*, 121593-121603. 10.1016/j.jhazmat.2019.121593.

41. Zou, W., Xie, P., Hua, W., Wang, Y., Kong, D., Yue, Y., Ma, Z., Yang, W., and Gao, Z. (2014). Catalytic decomposition of N2O over Cu-ZSM-5 nanosheets. Journal of Molecular Catalysis. A, Chemical *394*, 83-88. 10.1016/j.molcata.2014.07.004.

42. Tamiyakul, S., Sooknoi, T., Lobban, L.L., and Jongpatiwut, S. (2016). Generation of reductive Zn species over Zn/HZSM–5 catalysts for n–pentane aromatization. Applied Catalysis. A, General *525*, 190-196. 10.1016/j.apcata.2016.07.020.

43. Li, J., Gong, Q., Liu, Y., Kang, R., Yang, C., Qiu, M., Hu, Z., and Zhu, Z. (2019). Insight into the formation of COX by-products in methanol-to-aromatics reaction over Zn/HZSM-5: Significantly affected by the chemical state of surface Zn species. ChemCatChem *11*, 4755-4764. 10.1002/cctc.201901226.

44. Niu, X., Gao, J., Miao, Q., Dong, M., Wang, G., Fan, W., Qin, Z., and Wang, J. (2014). Influence of preparation method on the performance of Zn-containing HZSM-5 catalysts in methanol-to-aromatics. Microporous and Mesoporous Materials *197*, 252-261. 10.1016/j.micromeso.2014.06.027.

45. Vance, B.C., Yuliu, Z., Najmi, S., Selvam, E., Granite, J.E., Yu, K., Ierapetritou, M.G., and Vlachos, D.G. (2024). Unlocking naphtha from polyolefins using Ni-based hydrocracking catalysts. Chemical Engineering Journal *487*, 150468. 10.1016/j.cej.2024.150468.

46. Liu, S., Kots, P.A., Vance, B.C., Danielson, A., and Vlachos, D.G. (2021). Plastic waste to fuels by hydrocracking at mild conditions. Science Advances *7*, eabf8283. 10.1126/sciadv.abf8283.

47. Vance, B.C., Kots, P.A., Wang, C., Hinton, Z.R., Quinn, C.M., Epps, T.H., Korley, L.T.J., and Vlachos, D.G. (2021). Single pot catalyst strategy to branched products via adhesive isomerization and hydrocracking of polyethylene over platinum tungstated

zirconia. Applied Catalysis B: Environmental *299*, 120483. 10.1016/j.apcatb.2021.120483.

48. Jung, M.R., Horgen, F.D., Orski, S.V., Rodriguez C, V., Beers, K.L., Balazs, G.H., Jones, T.T., Work, T.M., Brignac, K.C., Royer, S.-J., et al. (2018). Validation of ATR FT-IR to identify polymers of plastic marine debris, including those ingested by marine organisms. Marine Pollution Bulletin *127*, 704-716. 10.1016/j.marpolbul.2017.12.061.

Chapter 5 Sustainable Propane Production from Plastics with Stable W-Ni Catalysts

This chapter is adapted from the work by Haokun Wang, Sijie Huang, Lam Ka Yin, Guangchao Li, Ping-Luen Ho, Jiasi Li, and Shik Chi Edman Tsang, unpublished paper draft.*

5.1 Introduction

Since the advent of large-scale plastic production in the 1950s, these materials have become integral to modern life primarily due to their low cost, durability, and versatile applications across various industries.[1-4] However, the challenges associated with the unsustainable disposal, limited recyclability, and prolonged degradation of plastic waste have culminated in a serious global environmental issue.[5,6] Among the different types of plastic waste, PO plastics–including HDPE, LDPE, LLDPE, and PP–constitute over 60% of the total plastic content in municipal solid waste, largely due to their widespread use and cost-effectivesness.[7] Despite their abundance, PO plastics have traditionally been overlooked in recycling efforts compared to PET, primarily due to their complex physiochemical characteristics, such as high melt viscosities that hinder efficient heat and mass transfer, as well as chemically inert C-C bonds that resist degradation in harsh environments.[8,9]

Conventional mechanical recycling methods are generally energy-intensive and produce low-quality materials, leading to significant technical and economic challenges.[2,10,11] In contrast, chemical recycling has gained considerable attention as a promising alternative, with processes like hydrocracking, hydrogenolysis, metathesis, and related tandem reactions showing the potential to convert plastics into valuable products under milder conditions.[12] Despite these advances, several key challenges remain in the chemical recycling of PO plastics under mild conditions. Chief among these is the reliance on noble metals such as Pt,[10,13-18] and Ru,[19-21] which are costly and unsustainable. Furthermore, existing chemical recycling approaches predominantly yield broad-spectrum liquid products (e.g., gasoline,[13,15,17,18,22] long-chain alkyaromatics[14,19]) or low-value gaseous products (e.g.,

methane[21,23]) due to preferential hydrogenolysis pathways that cleavage terminal C-C bonds. While metathesis offers the possibility of selectively producing propylene under mild reaction conditions,[24,25] the requirement for ethylene as a co-reactant to convert PE into propylene limits its economic feasibility and production efficiency. Thus, precise control over product distribution remains a critical challenge, particularly in achieving targeted outcomes, such as converting PE to ethylene monomer or PP to propylene, which are essential for a fully circular economy. Additionally, current studies on catalyst stability are limited in scope, typically assessing only a few cycles, thereby restricting the applicability of these processes at an industrial scale.[26] A comprehensive investigation into catalyst stability and underlying mechanisms pathway is therefore essential.

In this chapter, a novel approach to upcycling PP into high-yield propane (approximately 68 wt%) using a solvent-free and noble-metal-free catalytic system was developed, marking a significant advancement, as propane has not previously reported as the primary product in PO plastic upcycling (see Figure 5.1). The propane generated by this method can be further dehydrogenated in commercially established processes, making it a suitable precursor for the production of PP, therefore closing the loop in the plastic life cycle.[27] The catalytic system is based on W-modified Ni nanoparticles supported on ZSM-5 zeolite. The incorporation of W serves multiple roles: it introduces additional BAS to enhance C-C bond cleavage, improve the dispersion of Ni nanoparticles to bolster both dehydrogenation and hydrogenation activities, and facilitates the formation of NiW clusters within the ZSM-5 micropores. These clusters effectively reduce the pore diameter, thereby trap aromatic intermediates and may drive the reaction cycle via the hydrocarbon pool mechanism, ultimately leading to propane as the predominant product. The catalyst system also demonstrated versatility, efficiently converting a range of plastic feedstocks–including LDPE, HDPE, mixed plastics, and even commercial plastics–into high yields of propane regardless of the plastic types. Stability tests confirmed that the catalyst maintained consistent performance in terms of conversion and selectivity over at least 10 cycles without sings of deactivation. Moreover, a life cycle

assessment indicated that this process offers substantial reductions in carbon emissions compared to conventional plastic waste treatment methods. This innovative strategy for converting plastic waste into propane represents a significant contribution to sustainable plastic recycling and underscores its potential to advance the circular economy.

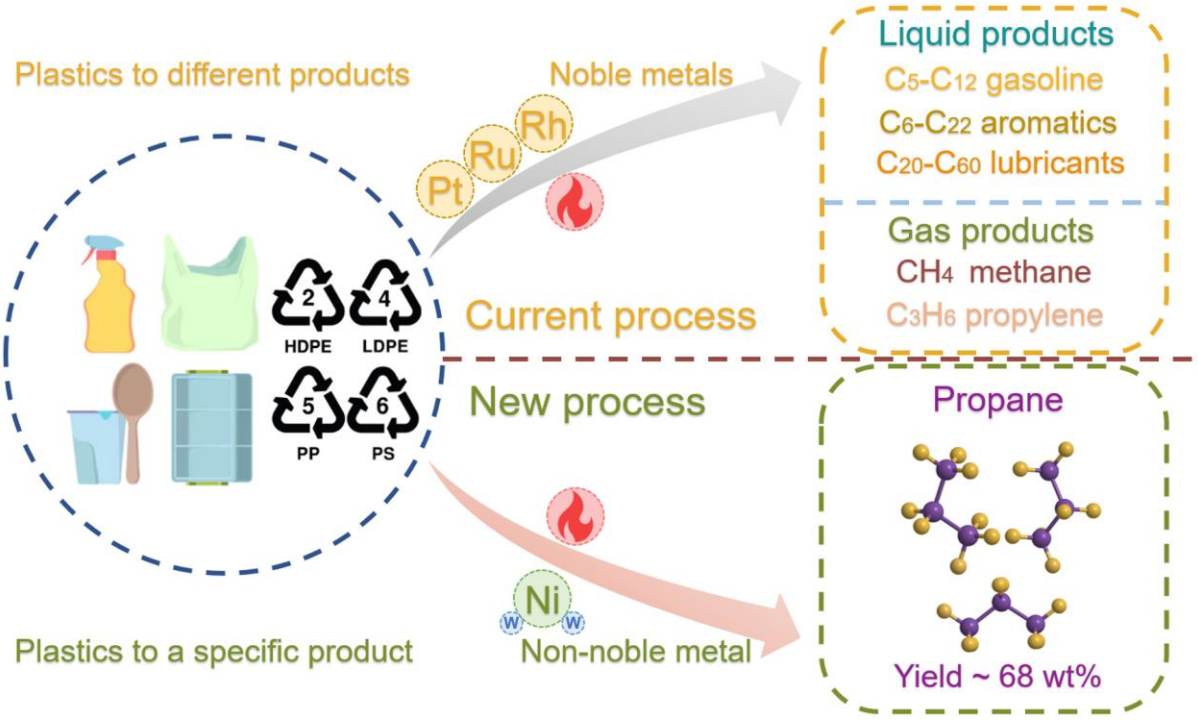

Figure 5.1 Schematic comparison between conventional plastic recycling processes and the novel approach for converting plastic to propane in this chapter.

5.2 Results and discussion

5.2.1 PP hydrocracking results

To precisely direct the hydrocracking of PP towards the selective production of propane–while minimising the generation of liquid-range hydrocarbons and lower-value methane–an investigation was initiated using a variety of zeolites with comparable Si/Al ratios. The unique pore structures of these zeolites enable effective molecular sieving, a feature widely adopted in industrial processes. Noteworthy examples include the shape-selective synthesis of p-xylene from xylene isomers during toluene alkylation over ZSM-5 zeolite,[28] as well as the selective production of propylene from hydrocarbons during MTO processes over SAPO-34 and ZSM-5 zeolites.[29]

As shown in Figure 5.2, the small-pore SAPO-34 zeolite (pore size ~ 0.38 nm) displayed high selectivity for propane without forming liquid products, but led to a substantial solid yield of approximately 85 wt% when subjected to 280 °C under 30 bar hydrogen for 8 h. In contrast, ZSM-5 zeolite, which has the same Si/Al ratio but a larger pore size (~ 0.56 nm), achieved high propane selectivity while significantly reducing the solid yield to 71 wt%. The comparable Si/Al ratios between ZSM-5 and SAPO-34 suggest that the differences in catalytic performance are primarily due to the enhanced diffusion limitations within the smaller pores of SAPO-34. When the pore size was further increased to that of Y zeolite (~0.74 nm), the solid yield became similar to that of ZSM-5, but the selectivity shifted towards butane, pentane, and heavier liquid hydrocarbons (C_{6+}). These initial screening tests highlight that while smaller pores effectively sieve products, they also impede the diffusion of larger hydrocarbon intermediates. On the other hand, large pores alleviate diffusion constraints but lack the precision in molecular sieving. Therefore, balancing diffusion restriction and molecular sieving is crucial to achieving both high conversion and selectivity towards propane. Based on these findings, ZSM-5 was selected for further investigation.

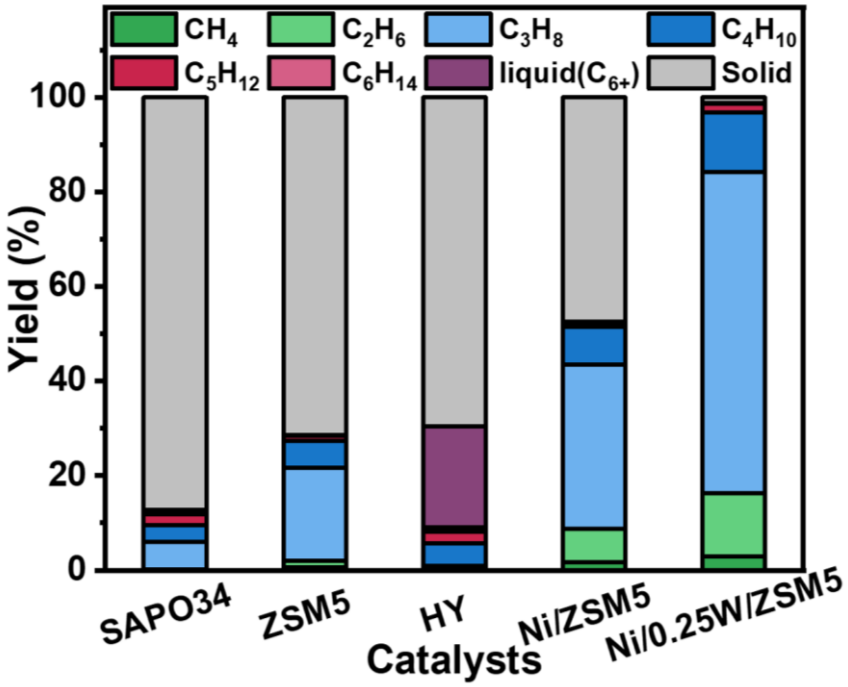

Figure 5.2 Initial catalysts screening for the hydrocracking of PP. Reaction conditions: 280 °C, 30 bar H_2, 8 h, 0.2 g catalyst mixed with 2 g PP (Mw ~ 181kDa), stirring speed 400 RPM. All mass balances are within the range of 97 ± 3%.

Rather than utilising noble metals, like Pt or Ru for C-H bond activation, the more abundant and cost-effective metal Ni was employed as a substitute. Incorporating Ni into ZSM-5 structure significantly reduced the solid yield from 71 wt% to 47 wt%, indicating an improvement in reducing undesirable byproducts, though the overall conversion of plastic feedstock to gaseous products remained limited (47 wt% solid yield). Remarkably, the subsequent addition of W to Ni nanoparticles further enhanced the catalytic performance, reducing the solid yield to approximately 1 wt% and achieving a propane yield of 68 wt%, demonstrating a significant improvement in product selectivity and conversion efficiency. This development is particularly notable since propane has not been previously reported as the primary product in plastic upcycling processes. Moreover, this catalyst operates within a temperature range (240 to 300 °C) typically associated with noble metals, rather than the higher temperatures (>350 °C) required for non-noble metal catalysts. Further investigation of the spent solid residues over various catalysts was conducted using GPC, as depicted in Figure 5.3. Compared to the molecular weight of virgin PP (Mw ~ 181 kDa), the application of

different catalysts progressively shifted the molecular weight to lower values. This observation indicates that the sequential incorporation of ZSM-5, Ni, and W enhances the efficiency C-C bond cleavage within the PP framework, consistent with the observed reduction in solid yield in Figure 5.2.

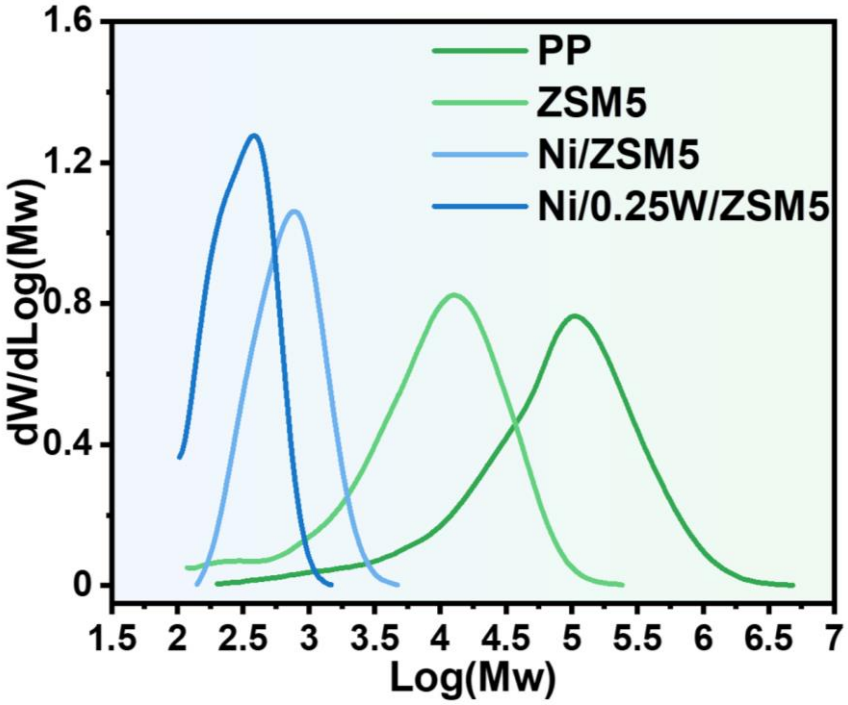

Figure 5.3 GPC analysis of virgin PP and solid residues resulting from PP upcycling with various catalysts.

To systematically evaluate the effects of varying reaction parameters on catalytic performance, a series of hydrocracking experiments under a range of conditions were conducted. As presented in Figure 5.4 (a), increasing W loading from 0 wt% to 0.25 wt% induces a shift in product distribution from solid residues towards gas-phase products, indicating that fine-tuning W content can effectively control the product outcome. However, exceeding this optimal W threshold results in a higher accumulation of solid residues, diverging from previously reported findings that suggest a continuous decrease in solid yield with increasing W loadings up to 1 wt%.[17] This deviation likely arises from changes in the synergetic interactions between acid and metal sites, as well as distinct variations in reaction mechanisms.

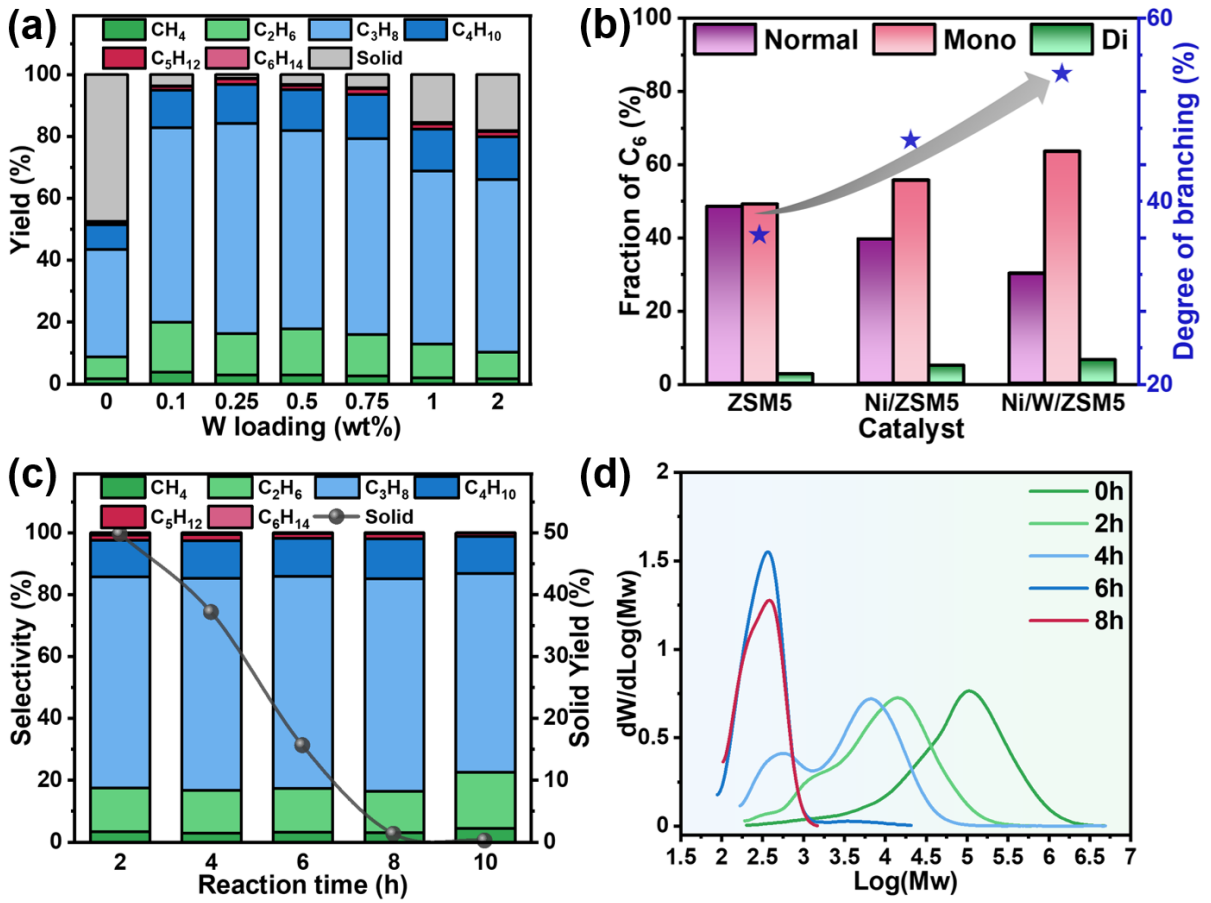

Figure 5.4 (a) Effect of W loading on different Ni/W/ZSM-5 catalysts. (b) Product branching analysis using various catalysts with n-octadecane as the model substrate. (c) Time-dependent reaction results over Ni/0.25W/ZSM-5 catalyst. (d) GPC analysis of solid residues produced over Ni/0.25W/ZSM-5 catalyst at different reaction times. Reaction conditions: 280 °C, 30 bar H_2, 8 h, 0.2 g catalyst mixed with 2 g PP (Mw ~ 181kDa), stirring speed 400 RPM, unless otherwise specified. All mass balances are within the range of 97 ± 3%.

To better understand the impact of different catalysts on product distribution, a detailed analysis of branching patterns was performed using the ratios of normal, mono-branched, and di-branched hexane, employing n-octadecane as model compound. The branching degree analysis, shown in Figure 5.4 (b), reveals that the proportion of normal hexane declines progressively from approximately 48% to 39% to 30 %, with the incremental incorporation of Ni and W into ZSM-5 framework. This suggests that the introduction of the C-H bond activation metal, Ni, promotes the generation of alkenes intermediates while reducing the strong adsorption of acidic sites, thereby enhancing both isomerisation and C-C bond cleavage.

Further modification with W enhances dehydrogenation/hydrogenation capabilities, leading to greater C-C bond cleavage and an increased formation of isomerised products.

To further investigate the temporal behaviour of the reactions catalysed by the Ni/0.25W/ZSM-5 catalyst, a series of time-resolved experiments were carried out, as depicted in Figure 5.4 (c). Notably, the selectivity of gaseous products remained largely unchanged from 2 to 8 h, even as solid yields progressively decreased over this frame. However, extending the reaction beyond 8 h (e.g., to 10 h) led to near-complete conversion of solid residues, accompanied by a shift in selectivity towards light gases, such as methane and ethane, at the expanse of heavier hydrocarbons like butane and pentane. This behaviour suggests that polymer chains preferentially adsorb over active sites compared to larger hydrocarbons, and once the PP polymers are fully reacted, larger gaseous products are adsorbed and subsequent converted into lighter fractions.

GPC analysis of the reacted PP at different reaction intervals further supports these observations. As shown in Figure 5.4 (d), the molecular weight of the remaining PP decreases steadily over time, eventually falling below 1 kDa after 8 h of reaction. These shifts in molecular weight sharply contrast with the behaviour observed in the Ru/ZSM-5 system, where the GPC profiles of solid residues remain largely unchanged relative to the virgin polymer over time.[19] This clear distinction suggests that once polymer chains are adsorbed onto the active sites, they undergo continuous C-C bonds cleavage to produce gaseous products. The molecular sieving properties of ZSM-5 ensures that only products fitting within its pore size can diffuse out, thereby promoting the exclusive formation of gas products as the reaction advances.

An in-depth examination of the polymer's molecular weight, as depicted in Figure 5.5 (a), indicates that the selectivity of gaseous product remains stable even as the molecular weight of PP feedstock increases, despite the corresponding accumulation of solid residues. The consistent product selectivity, regardless of PP molecular weight, underscores that ZSM-5's pore size governs product formation, largely independent of the polymer's molecular characteristics. However, the observed rise in solid yield with higher molecular weight PP can

be attributed to increased diffusion limitations. The elevated melting viscosity of higher molecular weight PP restricts effective catalyst-polymer interactions and impedes the release of cracking products from catalyst pores due to the formation of a more viscous polymer film.[30] This diffusion challenge can be mitigated by optimising the stirring conditions. As demonstrated in Figure 5.5 (b), increasing the stirring speed from 0 to 400 RPM substantially reduces the solid yield from approximately 15 wt% to 1 wt%, while maintaining stable product selectivity. Enhanced agitation alleviates diffusion barriers between the catalysts and molten polymer, thereby improving overall reaction kinetics.

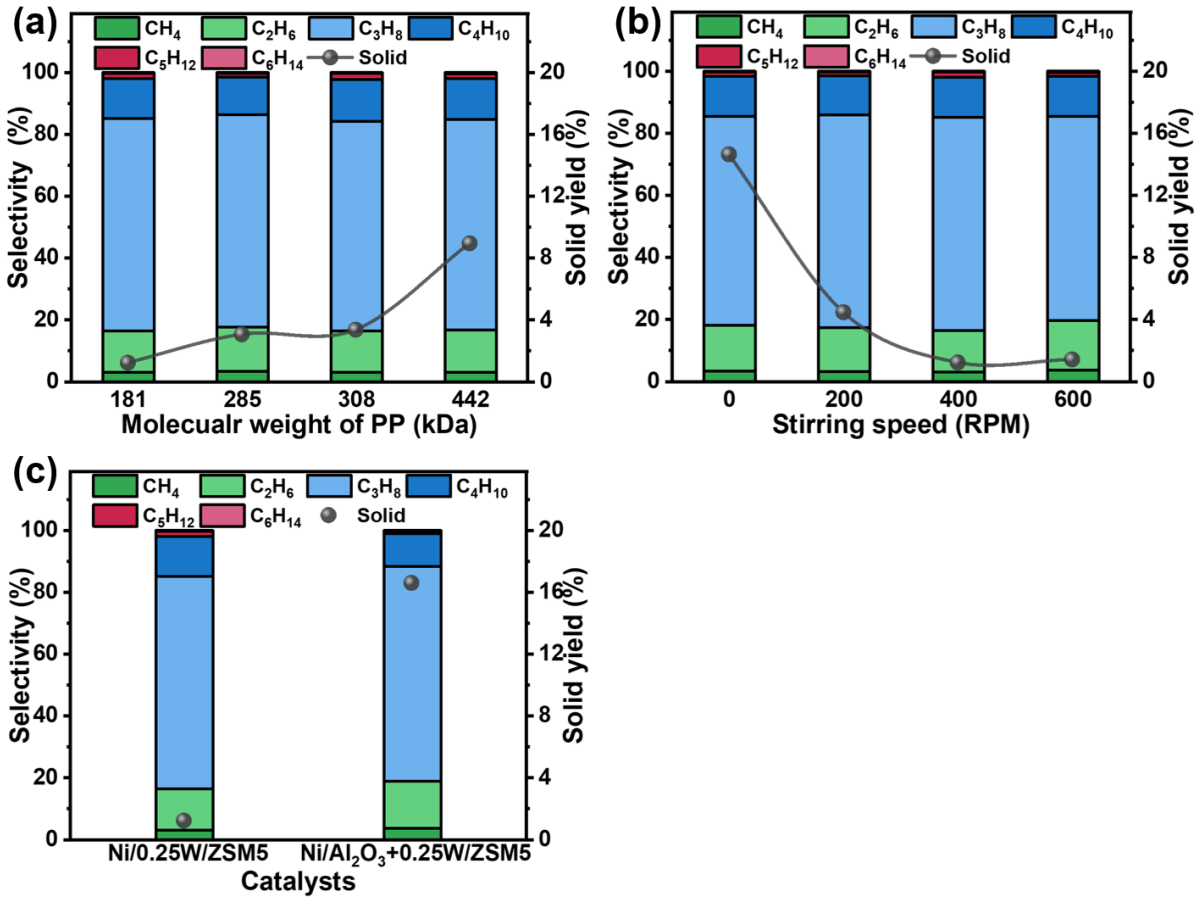

Figure 5.5 (a) Effect of molecular weight of PP plastic on catalytic performance over Ni/0.25W/ZSM-5. (b) Influence of stirring speed on catalytic performance over Ni/0.25W/ZSM-5. (c) Impact of metal-acid proximity on catalytic performance. Reaction conditions: 280 °C, 30 bar H_2, 8 h, 0.2 g catalyst mixed with 2 g PP (Mw ~ 181kDa), stirring speed 400 RPM, unless otherwise specified. All mass balances are within the range of 97 ± 3%.

Further analysis of the proximity between metal and acid sites underscores the critical role of diffusion in PP hydrocracking reactions. Compared to the intimate contact of metal and acid sites in the Ni/0.25W/ZSM-5 catalyst (Figure 5.5 (c)), the physical separation of these sites in the Ni/Al_2O_3 and 0.25W/ZSM-5 combination leads to a significantly higher solid yield (17 wt%). This finding suggests that an increased diffusion distance between metal and acid sites slows down reaction kinetics and results in greater solid accumulation.[15] However, the extended diffusion distance can also increase the residence time of intermediates within the ZSM-5's molecular sieving pores, leading to a marginal enhancement in propane selectivity.

To rigorously assess the long-term stability of the catalysts, a comprehensive set of stability assessments was conducted. Initially, the Ni/ZSM-5 catalyst exhibited solid yield and product selectivity comparable to those of the fresh catalyst. However, it suffered from marked deactivation by the second cycle (Figure 5.6 (a)). In contrast, the Ni/0.25W/ZSM-5 catalyst demonstrated remarkable stability, maintaining consistent catalytic performance over 10 successive cycles, as shown in Figure 5.6 (b). TG analysis provided insights into the different coke formation behaviours between the catalysts. Following the initial reaction, the Ni/ZSM-5 catalyst showed slighted higher coke deposition (1.6 wt%) compared to the Ni/0.25W/ZSM-5 catalyst (1.0 wt%), as presented in Figure 5.6 (c). However, with continued cycling, coke accumulation on the Ni/ZSM-5 catalyst escalated sharply, reaching approximately 2.4 wt% after just two cycles (Figure 5.6 (d)). In contrast, the Ni/0.25W/ZSM-5 catalyst effectively suppressed coke formation, with no noticeable increase in coke content even after 10 cycles (Figure 5.6 (d)). These results suggest that the W modification enhances the dehydrogenation and hydrogenation efficiency of Ni-based catalysts, thereby reducing the strong adsorption of reaction intermediates that typically lead to coke build-up. Further mechanistic studies are needed to fully elucidate the complex processes underlying this improved stability.

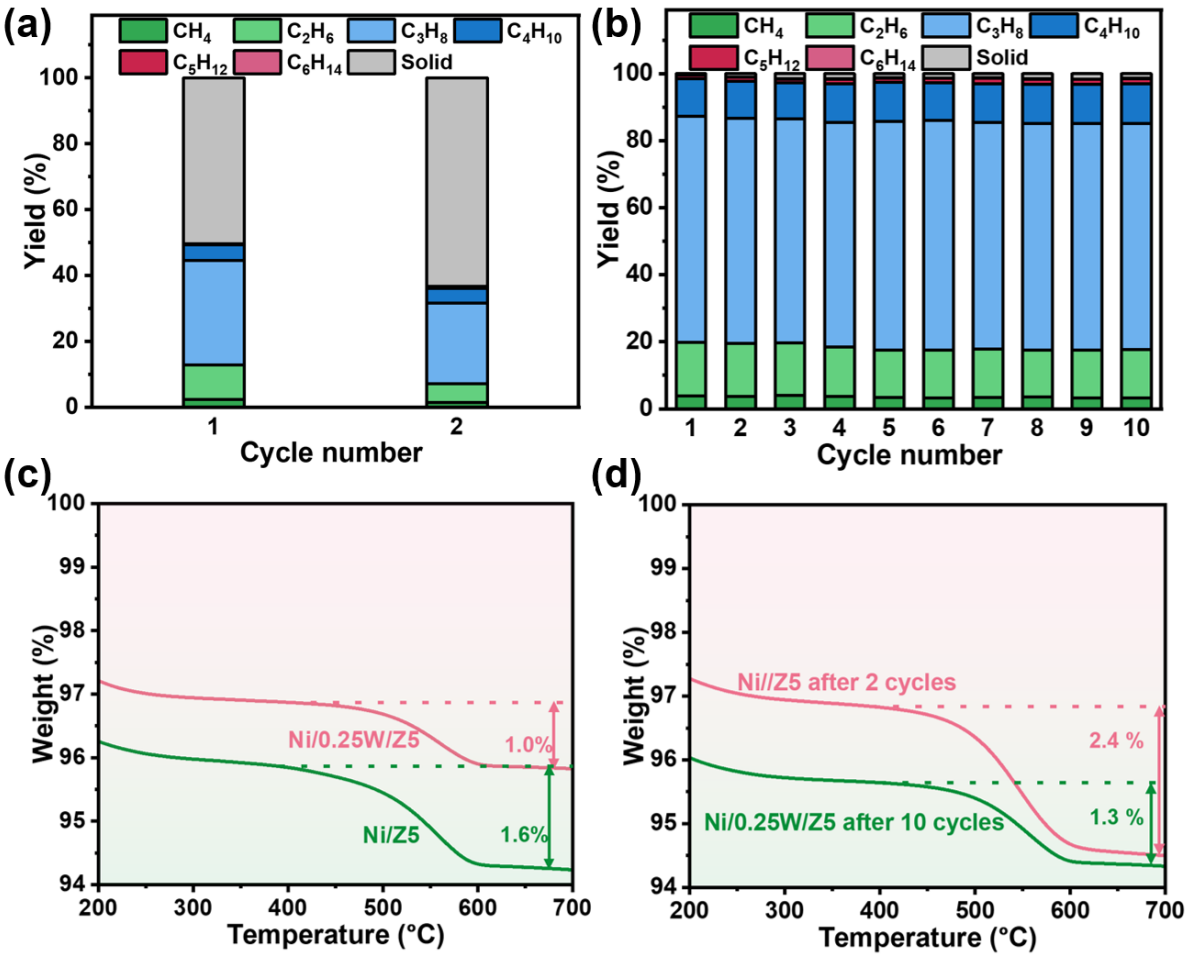

Figure 5.6 (a) Stability tests over Ni/ZSM-5. (b) Stability tests over Ni/0.25W/ZSM-5. (c) TG analysis results of Ni/ZSM-5 and Ni/0.25W/ZSM-5 catalysts after the initial reaction. (d) TG analysis results of Ni/ZSM-5 and Ni/0.25W/ZSM-5 catalysts after multiple cycle tests. Reaction conditions: 280 °C, 30 bar H_2, 8 h, 0.2 g catalyst mixed with 2 g PP (Mw ~ 181kDa) for the initial test, with only PP added during subsequent cycle tests, stirring speed 400 RPM. All mass balances are within the range of 97 ± 3%.

5.2.2 Characterisation of catalysts

To investigate the underlying factors responsible for the enhanced catalytic activity and stability achieved through W incorporation into Ni/ZSM-5 catalysts, an extensive series of characterisations were performed. HRTEM images of Ni/ZSM-5 and Ni/0.25W/ZSM-5 (Figure 5.7 (a) and 5.7 (b)) indicated that the introduction of Ni alone leads to the formation of relatively large Ni nanoparticles. However, the addition of W significantly improves Ni particle dispersion. Further insights were obtained through STEM dark-filed imaging combined with EDX spectroscopy mappings of Ni/0.25W/ZSM-5 (Figure 5.7 (c)). These analyses confirmed the

formation of well-distributed NiW clusters and homogenous distribution of metallic elements. Even after 10 reaction cycles, the dispersion of metallic particles remains consistent, as validated by HRTEM image (Figure 5.7 (d)) and STEM image with EDX (Figure 5.7 (e)) over Ni/0.25W/ZSM-5 catalyst, underscoring its exceptional stability.

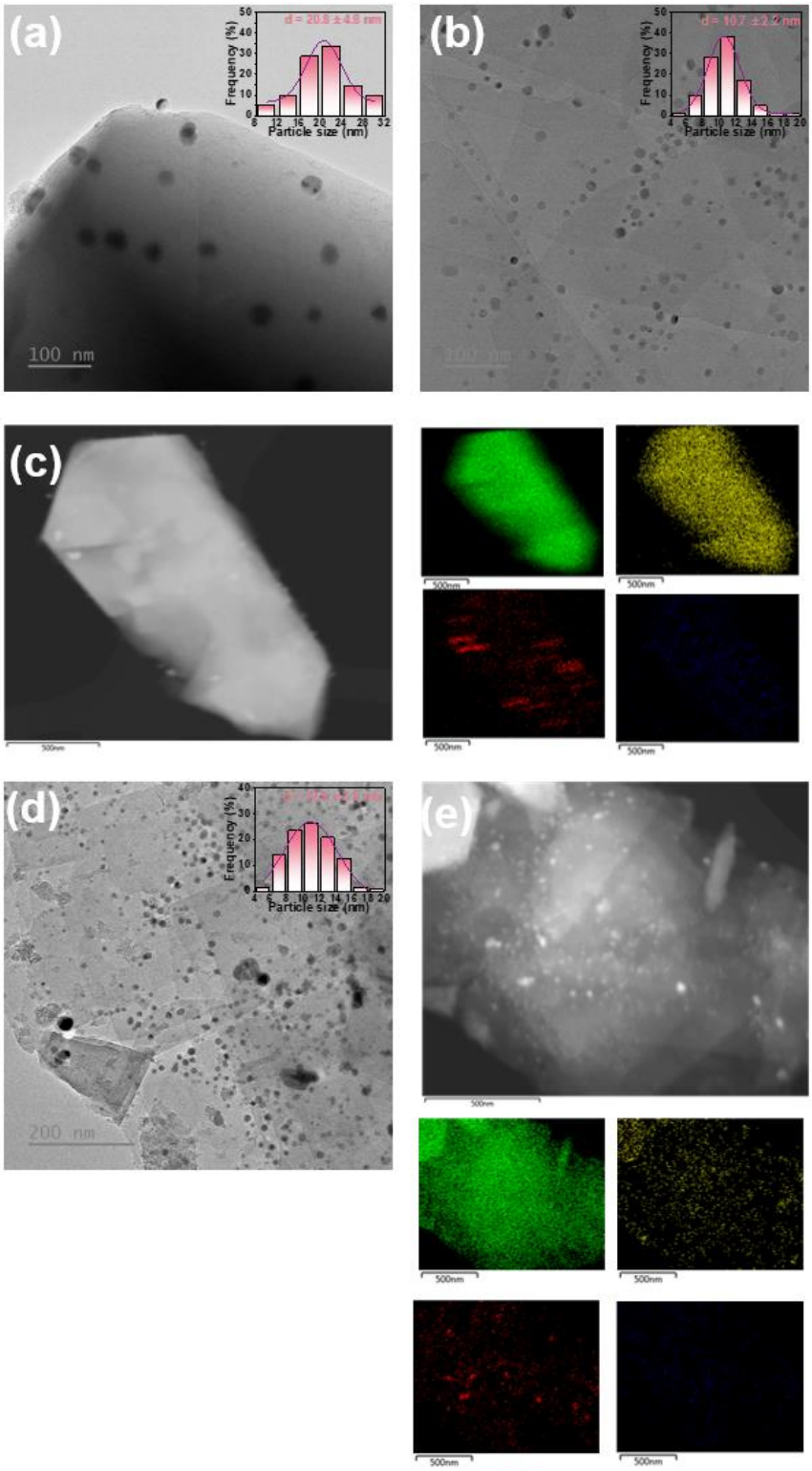

Figure 5.7 (a) HRTEM image of the fresh Ni/ZSM-5 catalyst with particle size distribution. (b) HRTEM image of the fresh Ni/0.25W/ZSM-5 catalyst with particle size distribution. (c) STEM dark-filed image of Ni/0.25W/ZSM-5 with EDX spectroscopy mappings (green: Si, yellow: Al, red: Ni, and blue: W). (d) HRTEM image of Ni/0.25W/ZSM-5 catalyst after 10 cycles with

particle size distribution. (e) STEM dark-field image of Ni/0.25W/ZSM-5 catalyst after 10 cycles, with EDX spectroscopy mappings (green: Si, yellow: Al, red: Ni, and blue: W).

Although larger Ni particle were detected in HRTEM for the Ni/ZSM-5 catalyst, the presence of smaller Ni species within the ZSM-5 channels was corroborated by XRD analysis (Figure 5.8). The reduced intensity of ZSM-5 peaks below 10° 2θ in the Ni/ZSM-5 pattern, relative to the parent ZSM-5, indicates that Ni species infiltrate the channels, potentially aggravating diffusion barrier for larger molecular intermediates.[31] Interestingly, the introduction of an optimal W loading (e.g., 0.25 wt%) mitigates this issue, as reflected in the recovery of low-angle peak intensities to levels comparable to those of the parent ZSM-5. This suggests the formation of smaller NiW clusters within the channels and a well-dispersed particle distribution on the external surface of zeolite. However, further increases in W loading could lead to a reduction in these peak intensities, indicating that formation of larger NiW clusters that could occupy the micropore channels.

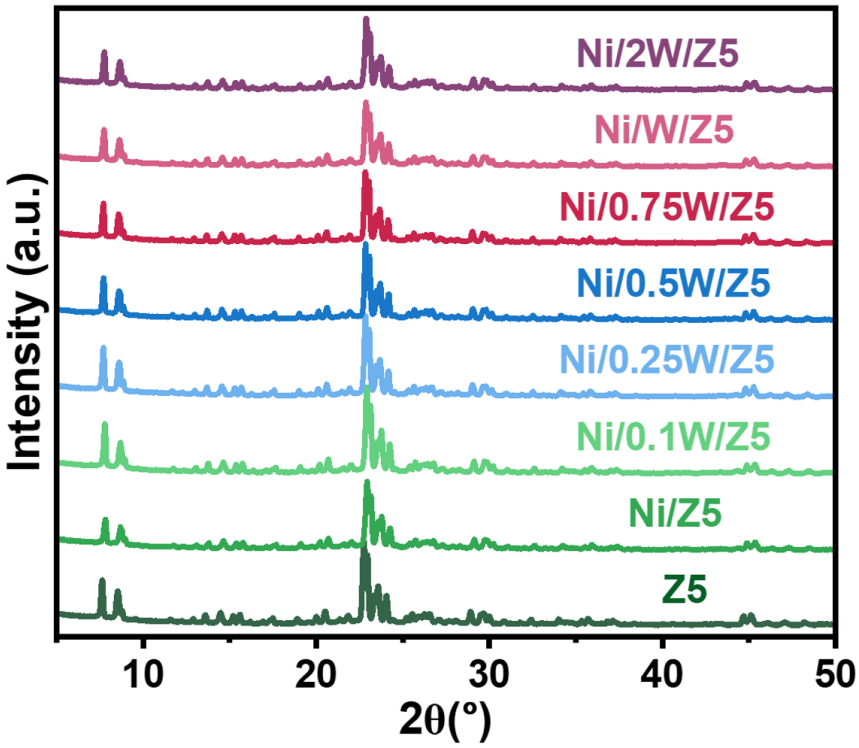

Figure 5.8 XRD patterns of all catalysts.

This interpretation is further supported by N_2 adsorption/desorption isotherms (Figure 5.9). Incorporation of Ni into ZSM-5 results in a decrease in both micropore and external surface areas compared to the parent ZSM-5, attributable to the presence of large Ni particles obstructing these areas (see Table 5.1). Additionally, Ni incorporation increases the average pore diameter from 29.6 Å to 30.5 Å, likely due to the expansion of large Ni nanoparticles that may block some micropores. Conversely, the formation of NiW clusters reduces particle size, preserving the N_2 adsorption/desorption characteristics. The presence of small NiW clusters within the micropores maintain the original micropore structure of ZSM-5, and even reduces the average pore diameter from 29.6 Å to 28.7 Å in the Ni/0.25W/ZSM-5 compared to the parent ZSM-5. These distinct differences in pore characteristics correlate strongly with the observed variations in catalytic performance between Ni/ZSM-5 and Ni/0.25W/ZSM-5 catalysts, which will be elaborated in the subsequent sections.

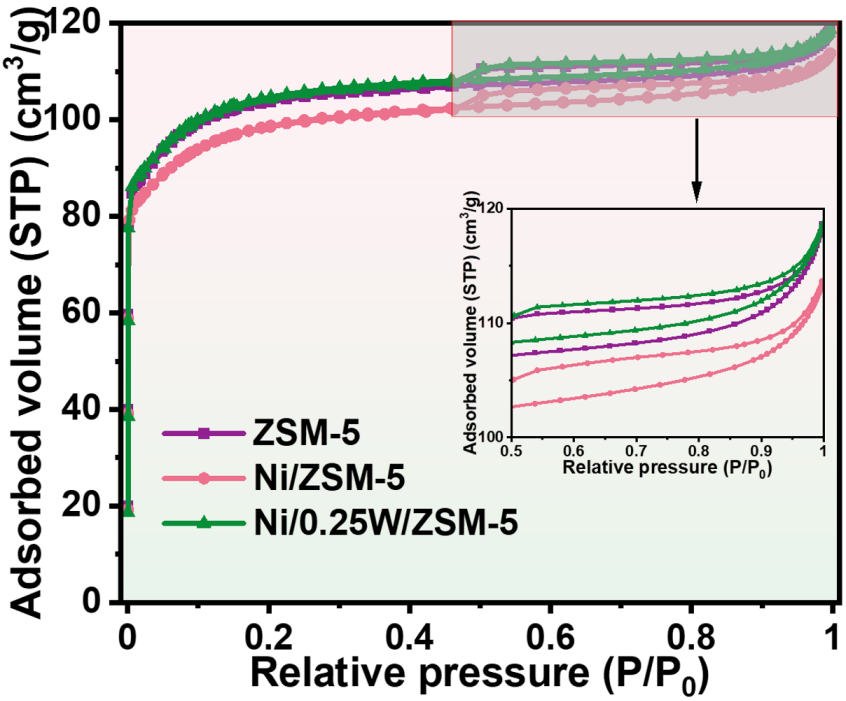

Figure 5.9 Nitrogen adsorption-desorption isotherms for ZSM-5, Ni/ZSM-5 and Ni/0.25W/ZSM-5 catalysts, with an enlarged inset highlighting the isotherms in the relative pressure range of 0.5 to 1.

Table 5.1 Summary of physiochemical characterisation of all catalysts.

Catalyst	Total area (m^2/g)[a]	Micropore area (m^2/g)	External area (m^2/g)	Pore volume (cm^3/g)[b]	Average pore size (Å)[c]
ZSM5	391	227	164	0.062	29.6
Ni/ZSM5	370	215	155	0.064	30.5
Ni/0.1W/ZSM5	373	217	156	0.061	28.4
Ni/0.25W/ZSM5	395	232	163	0.062	28.7
Ni/0.5W/ZSM5	375	219	156	0.065	29.1
Ni/0.75W/ZSM5	386	223	163	0.064	28.9
Ni/W/ZSM5	364	212	153	0.060	28.8
Ni/2W/ZSM5	366	213	153	0.063	28.9

[a] Measured by BET surface area.

[b] Measured by BJH adsorption cumulative volume of pores.

[c] Measured by BJH adsorption average pore diameter.

The acidity of the catalysts was characterised using NH_3-TPD and Py-IR spectroscopy, as depicted in Figure 5.10 (a), and Figure 5.10 (b), with fitting results consolidated in Table 5.2. The incorporation of W significantly enhances both the concentration and strength of weak and strong acid sites, as evidenced by the increased peak areas and elevated desorption temperatures. Notably, the addition of W to the Ni/ZSM-5 system preferentially increases the formation of BAS over LAS, as demonstrated in Figure 5.10 (b), this preferential enhancement of BAS facilitates the cleavage of C-C bonds during hydrocracking reactions.

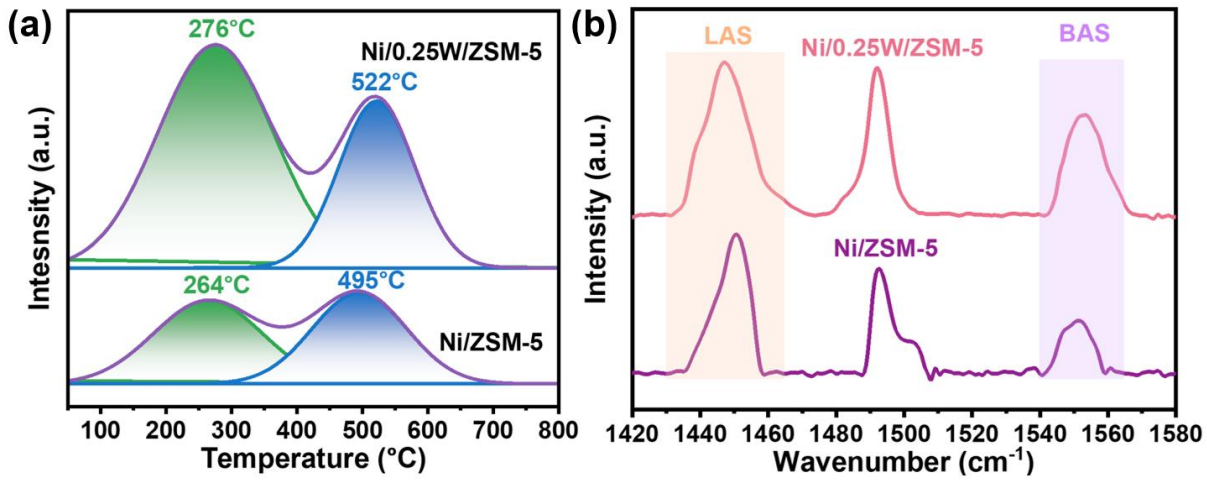

Figure 5.10 (a) NH_3-TPD profiles for Ni/ZSM-5 and Ni/0.25W/ZSM-5. (b) Py-IR results for Ni/ZSM-5 and Ni/0.25W/ZSM-5 at a desorption temperature of 350 °C.

Table 5.2 Summary of acidity results from NH_3-TPD and Py-IR.

Catalyst	Tm (°C) from NH_3-TPD		NH_3-TPD peak area (a.u.)	Acidity from Py-IR (μmol g cat^{-1})	
	I	II		LAS	BAS
Ni/ZSM-5	264	495	7.3	52.6	25.7
Ni/0.1W/ZSM-5	270	523	14.5	58.2	44.3
Ni/0.25W/ZSM-5	276	522	15.8	62.8	47.0
Ni/0.5W/ZSM-5	280	520	11.6	62.0	40.3
Ni/0.75W/ZSM-5	285	523	9.9	52.4	41.1
Ni/W/ZSM-5	270	527	9.1	53.1	36.3
Ni/2W/ZSM-5	270	522	6.3	50.8	20.2

To further clarify the electronic alternations brought about by W promoters, H_2-TPR experiments were conducted, as illustrated in Figure 5.11. The inclusion of W not only adjusts the acidity of the catalysts but also substantially influences their reduction profiles. The reduction peaks observed around 100 °C are linked to residual He trapped in the zeolite channels or within the TPR system itself, as NiO reduction typically does not occur at such low temperatures.[32] The primary reduction peaks at 479 °C and 614 °C for Ni/ZSM-5 catalyst correspond to NiO species located on the external surface and within the ZSM-5 micropores, respectively, consistent with literature findings.[33] The notable difference over 130 °C between

these reduction temperatures reflects the stronger metal-support interactions experienced for NiO confined within the ZSM-5 channels, compared to those situated on the external surface. The incorporation of just 0.25 wt% W brings about pronounced shifts in reduction behaviour, evidenced by both elevated reduction temperatures and increased peak areas. These shifts suggest that the formation of NiW clusters enhanced metal-support interactions, while the expanded peak areas indicate improved dispersion of Ni species, as corroborated by HRTEM imaging. This suggests that W promotes the generation of smaller metal particles and more robust metal-support interactions within the ZSM-5 channels. In contrast, larger and less interactive Ni nanoparticles confined within ZSM-5 channels would likely intensify diffusion constraints, prolong intermediates retention times, and contribute to coke build-up. Conversely, the smaller and more interactive NiW clusters alleviate such diffusion barriers, promoting more efficient passage of intermediates through the micropores, thereby minimising coke formation, and enhancing overall reaction kinetics.

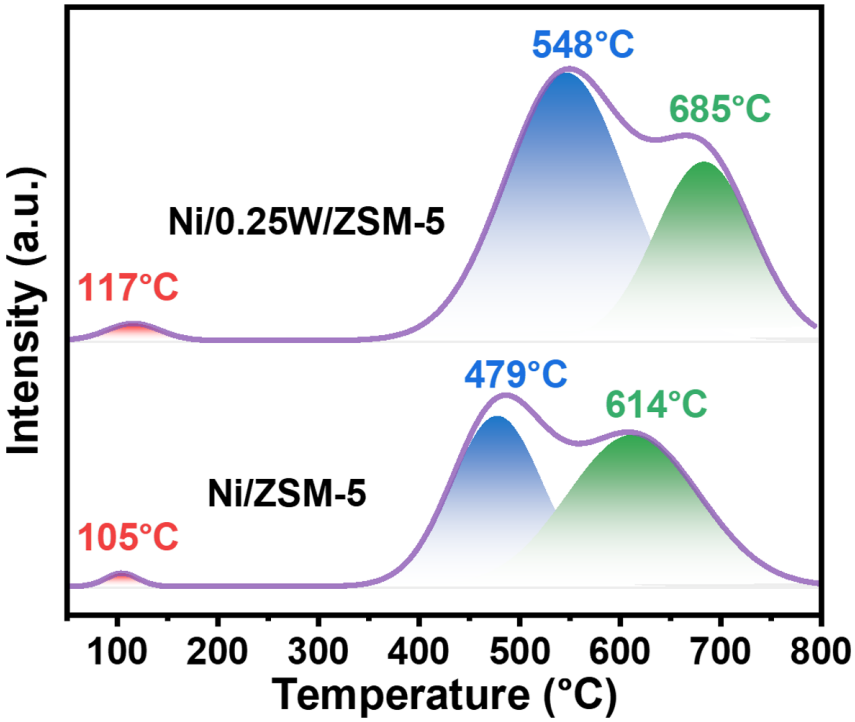

Figure 5.11 H_2-TPR results over Ni/ZSM-5 and Ni/0.25W/ZSM-5.

The electronic environments of the catalysts were further investigated through XPS, as depicted in Figure 5.12. The analysis revealed that three distinct Ni species–metallic Ni, Ni^{2+}, and Ni satellite peaks–in agreement with previous studies.[34,35] The introduction of W into the Ni/ZSM-5 catalyst system causes a shift in the binding energy of metallic Ni from 852.9 eV (in the absence of W) to lower values (e.g., 852.6 eV at 0.25% W loadings). This shift suggests electron donation from W to Ni species, leading to a more reduced state of metallic Ni, which in turn enhances dehydrogenation/hydrogenation activity and accelerates reaction kinetics. Notably, this modified electronic environment remains stable even after 10 catalytic cycles, suggesting durable metal-support interactions. The XPS spectra of the W 4f region were collected and analysed; however, the signal intensity was too low relative to background noise due to the low loading concentration of W (0.25 wt%). As a result, no reliable conclusions could be drawn from these data. Moreover, surface atomic ratios derived from XPS were not determined, as the primary focus of the XPS analysis was to investigate the electronic changes in the Ni species.

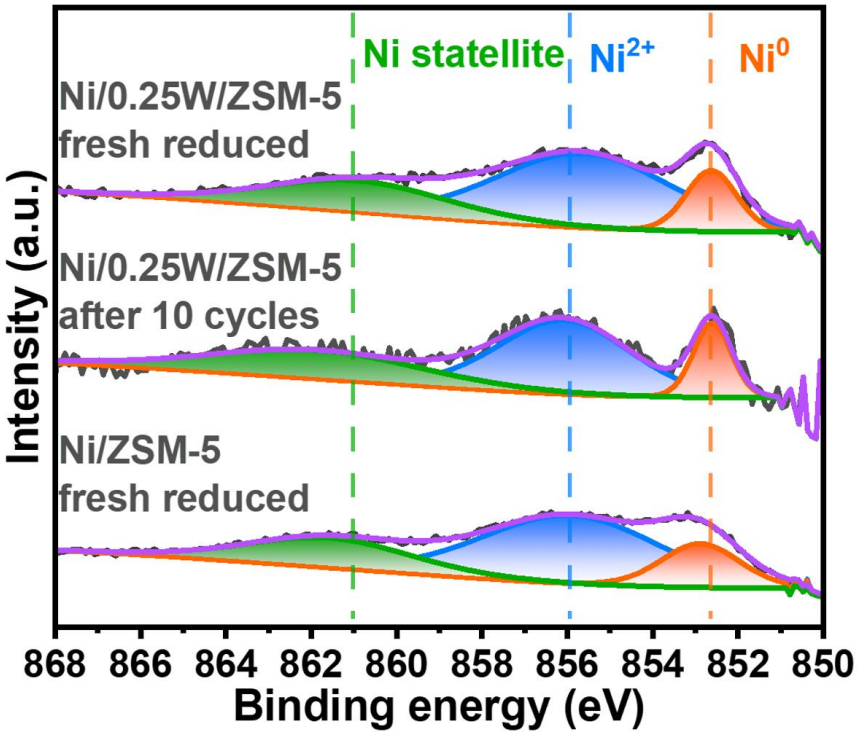

Figure 5.12 XPS patterns of Ni $2P_{3/2}$ for Ni/ZSM-5 (fresh) and Ni/0.25W/ZSM-5 (fresh and after 10 cycled reaction).

DRIFTS using CO as a probe molecule was employed to further verify the modifications in the Ni electronic environment upon W introduction (Figure 5.13 (a) and 5.13 (b)). The characteristic peaks around 2115 and 2170 cm^{-1}, attributed to physically adsorbed CO, gradually diminish upon N_2 purging.[36] However, the peaks near 1940 cm^{-1}, representative of CO chemisorption on metallic Ni surface,[37,38] exhibit a noticeable red shift from approximately 1943 to 1937 cm^{-1} after the addition of W, indicating the formation of more electron-rich Ni centres due to electron transfer from W to Ni.

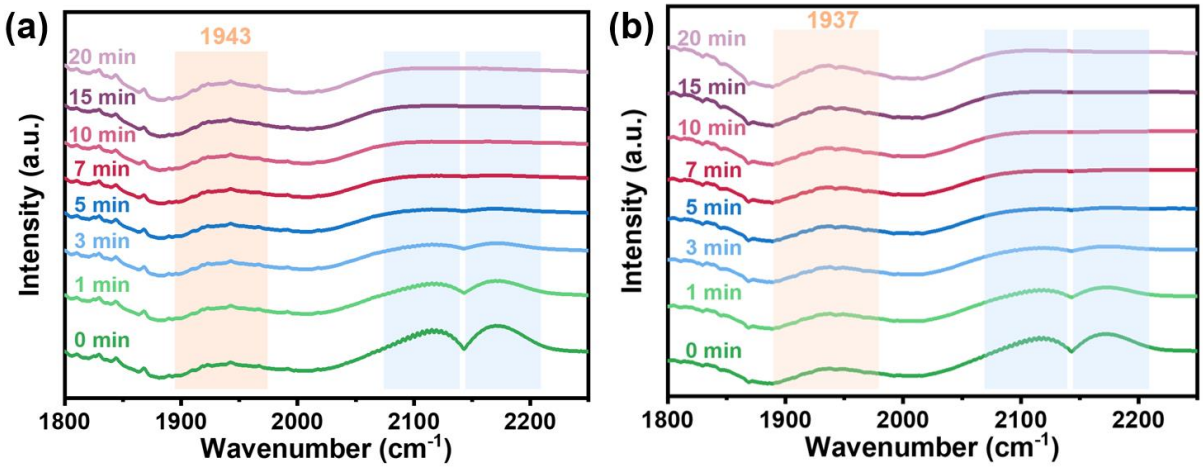

Figure 5.13 (a) DRIFTS of CO adsorption over Ni/ZSM-5 catalyst. (b) DRIFTS of CO adsorption over Ni/0.25W/ZSM-5 catalyst.

5.2.3 Reaction mechanism study

To gain deeper insights into the distinct mechanistic pathways of PP hydrocracking catalysed by various materials, in-situ DRIFTS analyses of PP mixtures with different catalysts were conducted. As shown in Figure 5.14 (a), the spectral data reveal two distinct reaction stages throughout the collection period. In the initial stage (5 to 160 min), hydrocracking activity over Ni/ZSM-5 catalysts is relatively limited, indicated by weak vibrations corresponding to CH_3 bending (1370 cm^{-1}), CH_2 bending (1445 cm^{-1}), and C-H stretching (2945 cm^{-1}), which are characteristic of the PP structure.[39] The restricted size of the zeolite micropores, relative to the macromolecular dimensions of PP, hinders the direct diffusion of the intact polymer into these micropores, limiting the reaction initiation. Therefore, this phase primarily involves the initial hydrocracking of the PP polymer into long-chain intermediates on the external surface

of ZSM-5, consistent with existing literature on polymer cracking over microporous zeolite-supported catalysts.[40,41]

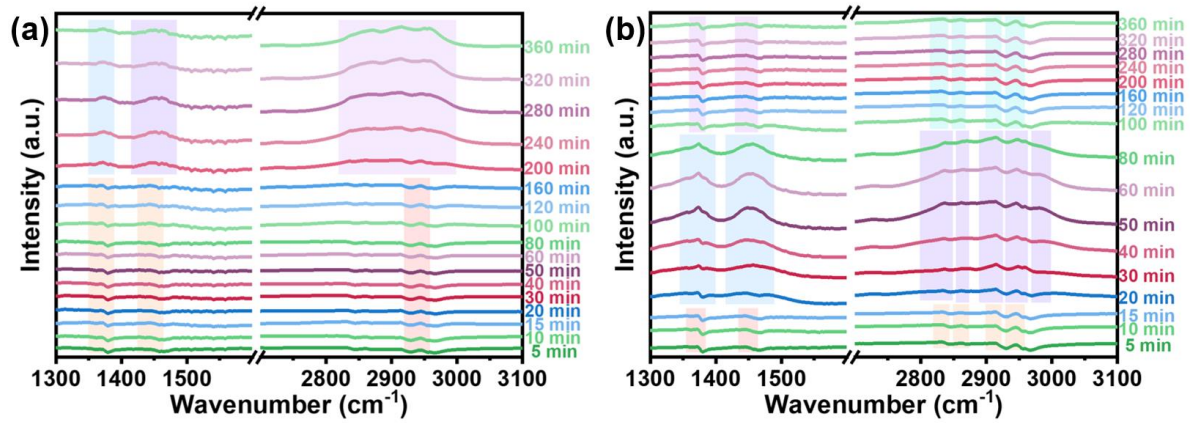

Figure 5.14 (a) In-situ DRIFTS analysis of 4 mg Ni/ZSM-5 catalyst mixed with 40 mg PP (Mw ~181 kDa) at 280 °C and 5 bar H_2, with a flow rate 10 mL min^{-1}. (b) In-situ DRIFTS analysis of 4 mg Ni/0.25W/ZSM-5 catalyst mixed with 40 mg PP (Mw ~181 kDa) under identical conditions of 280 °C and 5 bar H_2, with a flow rate of 10 mL min^{-1}.

In contrast, the subsequent reaction stage (from 200 to 360 min) is marked by a significant increase in hydrocracking activity, as indicated by stronger stretching and bending vibrations, along with the emergence of new, intense C-H stretching peaks (2840, 2870, 2920, 2960 cm^{-1}).[39] This shift in spectral features indicates that secondary hydrocracking becomes dominate in this phase, where long-chain intermediates enter the micropores, undergo C-C bond cleavage via strong BAS, leveraging the molecular sieving effect of the confined zeolite environment to produce final hydrocracked products. Interestingly, even after 6 h, the sustained intensity of various bending modes suggests that the reaction is still ongoing by the end of spectral data collection.

In comparison, the initial hydrocracking over Ni/0.25W/ZSM-5 catalyst occurs at a notably faster rate and with greater intensity than that observed for Ni/ZSM-5 catalyst. As depicted in Figure 5.14 (b), this phase exhibits stronger CH_3 bending, CH_2 bending, and C-H stretching vibrations from the PP framework, with significantly enhanced peak intensities. The intensification is especially evident in the C-H bond stretching regions (2830 to 2950 cm^{-1}),

which is much less prominent during the initial hydrocracking over Ni/ZSM-5 catalyst. Additionally, this primary hydrocracking phase is completed within 20 min, transitioning more rapidly to the secondary hydrocracking phase compared to the W-free catalyst. Two key factors likely account for this accelerated reaction. Firstly, the incorporation of W markedly enhances Ni nanoparticle dispersion and introduces additional BAS on the external surface of the zeolite, thereby significantly improving dehydrogenation/hydrogenation activity and facilitating C-C bond cleavage, ultimately accelerating reaction kinetics. Additionally, the presence of smaller NiW clusters within the channel reduces the diffusion barrier for intermediates entering the micropores compared to the larger Ni nanoparticle clusters in Ni/ZSM-5. During the secondary hydrocracking stage over Ni/0.25W/ZSM-5 catalyst (20 to 80 min), the hydrocracking activity further intensifies, remaining more robust than that over Ni/ZSM-5. This stage persists for approximately 1 h before gradually diminishing, with weaker vibration continuing for over 260 min without further changes. This suggests that the reaction concludes within 100 min–much faster than the reaction kinetics observed with Ni/ZSM-5 catalyst–aligning with the superior catalytic performances shown in Figure 5.2. However, unlike the complete disappearance of bending and stretching variations post-reaction, weak peaks persisted beyond 100 min and continued to the end of spectrum collection, indicating the presence of residual compounds within the zeolite framework.

To elucidate the relationship between these residual compounds and the reaction mechanisms, the spent Ni/ZSM-5 and Ni/0.25W/ZSM-5 catalysts were dissolved in chloroform and the resulting solutions were analysed using GC. As depicted in Figure 5.15 (a), the spent Ni/ZSM-5 catalyst retained traces of heavy gaseous products (C_5-C_6), likely due to undesorbed species, along with measurable quantities of heavier liquid hydrocarbons, such as C_7-C_9 alkanes and aromatic compounds in the liquid phase. After an 8-hours reaction with Ni/ZSM-5, minimal liquid products were detected, strongly suggesting that these heavier hydrocarbons acted as intermediates, strongly adsorbed on the catalyst surface, preventing their desorption as liquid products. In contrast, the liquid extracts from Ni/0.25W/ZSM-5 contained traces

amounts of C_5-C_6 products but exhibited a significantly higher concentration of aromatic compounds, particularly toluene and xylene, with minimal other liquid-range hydrocarbons (Figure 5.15 (b)). As confirmed by BET analysis in the previous section, while the introduction of Ni increased the average pore diameter of ZSM-5, the addition of W reduced the pore diameter significantly compared to the parent zeolite. This suggests that larger liquid alkanes and aromatics may undergo strong adsorption on the Ni/ZSM-5 surface, limiting the adsorption of macromolecular PP, thereby inhibiting effective primary hydrocracking. However, in the case of Ni/0.25W/ZSM-5, its narrowed pore structure likely confines aromatics species within the micropores, preventing their competitive adsorption with macromolecular PP, thus enhancing primary hydrocracking kinetics.

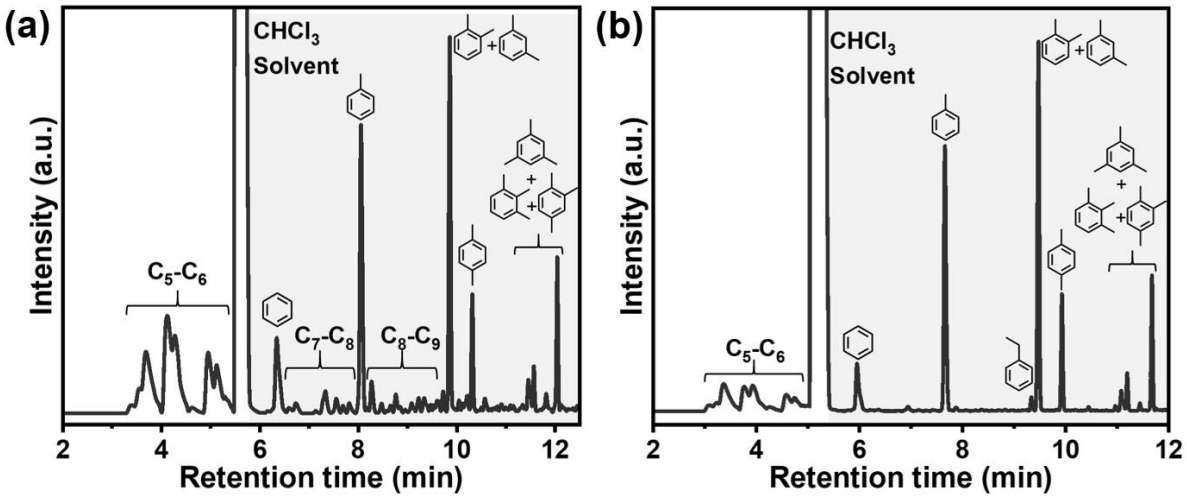

Figure 5.15 (a) GC profiles of the liquid solution obtained after dissolving the Ni/ZSM-5 catalyst post-reaction in $CHCl_3$ solvent. (b) GC profiles of the liquid solution obtained after dissolving the Ni/0.25W/ZSM-5 catalysts post-reaction in $CHCl_3$ solvent.

To further investigate this hypothesis, ^{13}C CP/MAS NMR experiments were conducted to analyse the trapped compounds within the spent catalysts. As shown in Figure 5.16, the chemical shifts at approximately 22, 27, and 46 ppm in the spent Ni/ZSM-5 correspond to ^{13}C nuclei in the CH_3, CH, and CH_2 groups, respectively, indicating the presence of unreacted PP polymer.[42] No aromatic hydrocarbons were detected in the spectra, suggesting that liquid-range intermediates (aromatics and liquid alkanes) identified by GC in Figure 5.15 (a) were

strongly adsorbed on catalyst surface, with only unreacted PP retained within the zeolite micropores. In contrast, the NMR spectrum for the spent Ni/0.25W/ZSM-5 exhibited similar chemical shifts between 20 and 50 ppm but with broader peaks, indicating superior hydrocracking performances and fewer PP residues within the micropores. Notably, a pronounced peak at around 130 ppm was observed, corresponding to confined aromatics within the zeolite micropores.[43] This direct evidence confirms that in Ni/0.25W/ZSM-5, aromatic species are confined within the micropores rather than on the surface, as seen in Ni/ZSM-5 , highlighting their different spatial distributions in two catalysts.

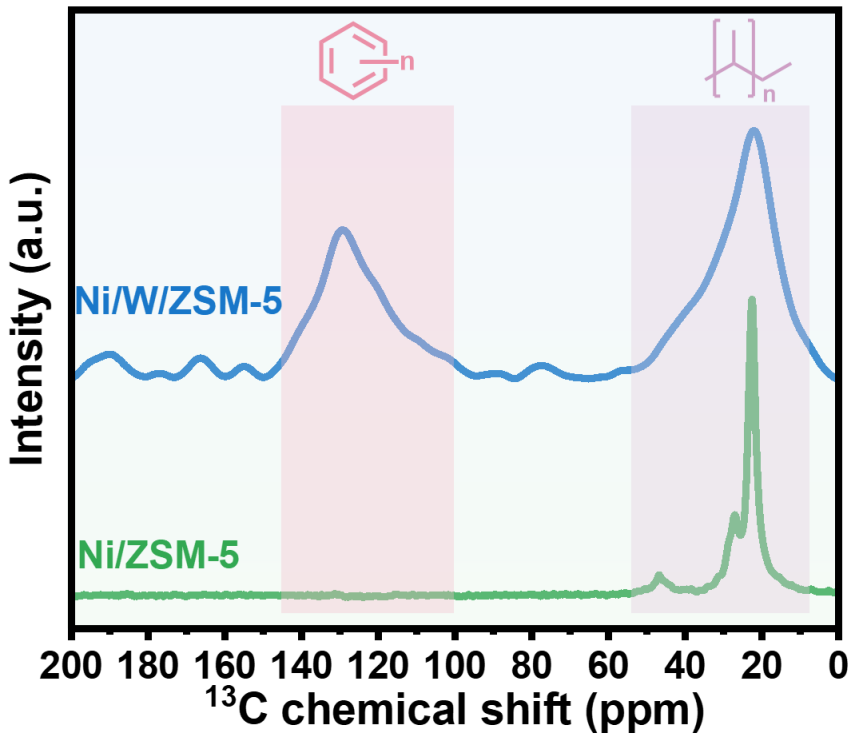

Figure 5.16 ^{13}C CP/MAS NMR spectra of trapped species collected from spent Ni/ZSM-5 and Ni/0.25W/ZSM-5 catalysts after the reaction.

It is well-established that aromatics are known to act as autocatalysts in MTO processes over zeolites like ZSM-5 through a hydrocarbon pool mechanism. This mechanism involves dual cycles: an aromatics-based cycle that primary produces ethene and propene, and an alkene methylation cycle responsible for generating propene and higher alkenes.[44] The product distributions in PP hydrocracking experiments (Figure 5.2) follow a similar pattern, with

propane as the dominant product and a combined yield of C_2-C_4 alkanes exceeding 94%. The key difference is that, in this system, the final products are saturated alkanes rather than olefins, likely due to the high-pressure hydrogen environment, which saturates the olefins to form alkane. It is therefore plausible that long-chain intermediates pass through the micropore and undergo alkylation with the confined aromatics, following a mechanism analogous to the MTO process. However, further experiments are underway to validate whether these confined aromatic species actively participate in the reaction, driving both reaction kinetics and selectivity towards propane.

5.2.4 Upcycling of other plastics and life-cycle assessment

To evaluate the catalytic performance of the Ni/0.25W/ZSM-5 catalyst across a diverse range of plastic feedstocks, further investigations to include LDPE, HDPE and various plastic mixtures were conducted, as presented in Figure 5.17. The resulting product distributions were closely aligned with those observed when using PP as the substrate, demonstrating the catalyst's versatility in upcycling a broad spectrum of PO plastics, including mixed plastic streams. Additionally, common laboratory plastics–such as pipettes, pipette tips, bottles, and microtubes–were efficiently processed under identical reaction conditions, despite the presence of additives and impurities like stabilisers, plasticisers, dyes.[26] These results strongly suggest the catalyst's significant potential for practical applications in recycling both pure and mixed plastic waste.

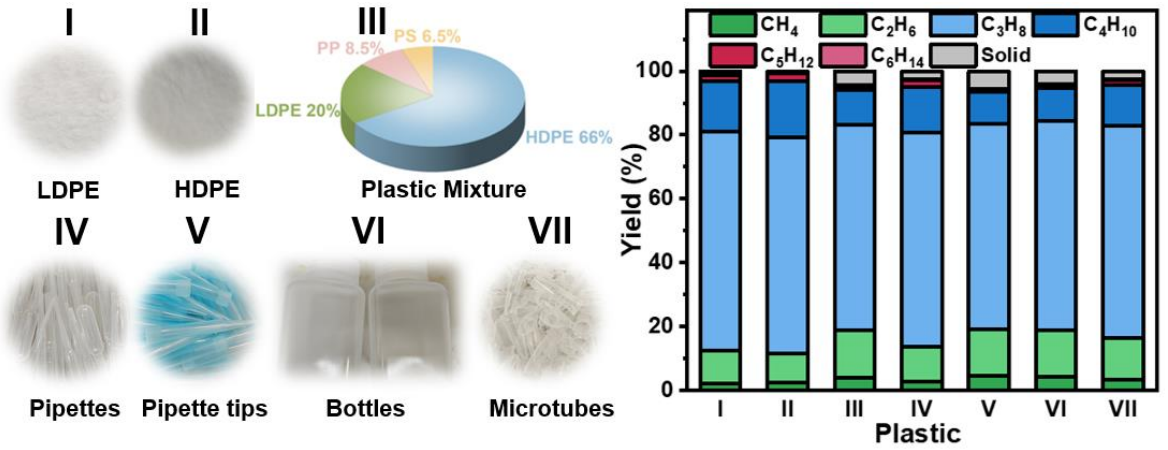

Figure 5.17 Catalytic performance of Ni/0.25W/ZSM-5 catalyst for LDPE, HDPE, a plastic mixture, and some commercial plastics in lab. Reaction conditions: 280 °C, 30 bar H_2, 8 h, 0.2 g catalyst mixed with 2 g plastics, stirring speed 400 RPM. All mass balances are within the range of 97 ± 3%.

Building on catalyst's strong performance and broad applicability across different plastic feedstocks, a process for hydrocracking plastic waste into propane was conceptualised, as illustrated in Figure 5.18, accompanied by a comprehensive LCA. The proposed process is divided into three key stages: reaction, product separation, and hydrogen recycling. In the first stage, plastic feedstock and hydrogen are fed into reactor R-1, where hydrocracking occurs under the same reaction conditions established in the lab experiments. The resulting gaseous effluent is then cooled to 37 °C and sent to distillation column DL-1 for fractionation. Heavier fractions (C_4 to C_6) are collected as bottom distillates, suitable for use as light gasoline or naphtha blends, while the lighter top distillates, mainly ethane and propane, are compressed to 27 bar and heated to 3 °C via pump P-1 and heater H-2, respectively, before being directed to a secondary distillation column to separate propane from ethane.[22,45] The overhead vapor streams from both distillation columns, consisting primarily of hydrogen and methane, are recombined and heated to 35 °C before entering membrane separator M-1 for hydrogen recovery. The reclaimed hydrogen is subsequently mixed with fresh hydrogen to maintain a continuous feed supply for hydrocracking. The envisioned plant is designed to process 2000 tons of plastic annually, yielding approximately 1280 tons of propane as the primary product,

along with secondary outputs including flare gas (13 wt%), ethane (9 wt%), and a C_4-C_6 mixture (16 wt%).

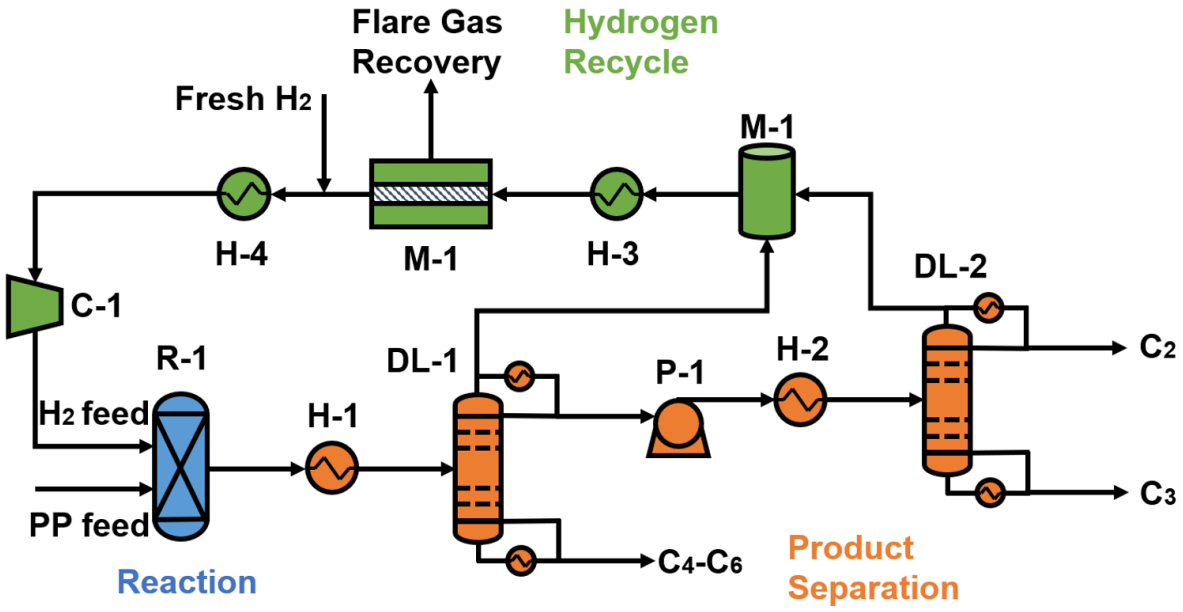

Figure 5.18 Process schematic illustrating the hydrocracking of PP to produce propane.

A comprehensive cradle-to-gate LCA was further conducted to rigorously evaluate the GWP of the proposed hydrocracking process compared to other common plastic disposal methods. As shown in Figure 5.19, the results indicate that, relative to conventional approaches such as landfilling (3.0 kg CO_2e/kg plastic) and incineration (2.9 kg CO_2e/kg plastic), the process achieves a more than 55% reduction in CO_2 emission.[46,47] Compared to other chemical recycling pathways, such as pyrolysis and gasification for producing high-value chemicals, this method offers over a 50% reduction in carbon emission.[48] Additionally, when benchmarked against similar hydrocracking process in literature that target naphtha as the primary product, this approach further reduces CO_2 emissions by approximately 0.7 kg CO_2e per kg of plastic treated.[45] This substantial reduction underscores the potential of PP-to-propane process to contribute to low-carbon solutions in plastic waste management. Furthermore, the integration of downstream propane dehydrogenation and subsequent repolymerisation offers the opportunity to convert propane back into PP, highlighting the

capability of this technology to support a circular economy and drive towards CO_2-neutral plastic treatment.

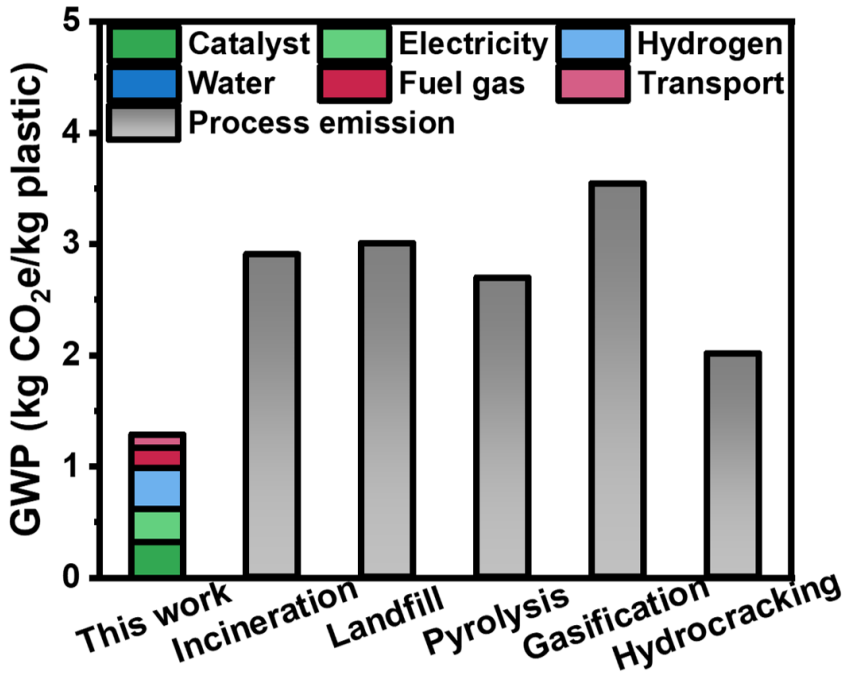

Figure 5.19 Comparative analysis of global warming potentials (GWP, kg CO_2e/kg plastic) for this process versus other plastic treatment methods.

5.3 Conclusion

In conclusion, this chapter presents a novel approach for upcycling of PP into propane using a solvent-free and noble-metal-free catalytic system, representing a significant advancement in the field of plastic recycling. This catalyst exhibited high efficacy, achieving selective conversion of PP to propane with a yield of approximately 68 wt%, while maintaining stability over at least 10 cycles without deactivation, thereby outperforming existing methods. The addition of W notably enhanced the dispersion of Ni nanoparticles, introduced additional BAS, and promoted the formation of NiW clusters within the ZSM-5 micropores. However, the ongoing experiments are being conducted to validate whether that the aromatics confined within zeolite channel can participate in the reaction, enhancing both reaction kinetics and selectivity towards propane.

Further catalytic evaluations on diverse plastics, including commercial waste, revealed the system's strong potential for practical application in upcycling mixed plastic streams. The LCA results further emphasised the significant reduction in carbon emissions offered by this process compared to conventional disposal methods. This research not only outlines a sustainable pathway for converting PP to propane, thereby contributing to the circular economy, but also demonstrates the feasibility of employing earth-abundant metals in catalytic processes traditionally dominated by noble metals. These insights are expected to guide future developments in plastic upcycling and sustainable catalysis.

5.4 Reference

1. Sardon, H., and Dove, A.P. (2018). Plastics recycling with a difference. Science *360*, 380-381. 10.1126/science.aat4997.
2. Korley, L.T.J., Epps, T.H., Helms, B.A., and Ryan, A.J. (2021). Toward polymer upcycling—adding value and tackling circularity. Science *373*, 66-69. 10.1126/science.abg4503.
3. Zheng, K., Wu, Y., Hu, Z., Wang, S., Jiao, X., Zhu, J., Sun, Y., and Xie, Y. (2023). Progress and perspective for conversion of plastic wastes into valuable chemicals. Chemical Society Reviews *52*, 8-29. 10.1039/D2CS00688J.
4. Geyer, R., Jambeck, J.R., and Law, K.L. (2017). Production, use, and fate of all plastics ever made. Science Advances *3*, e1700782. 10.1126/sciadv.1700782.
5. Sullivan, K.P., Werner, A.Z., Ramirez, K.J., Ellis, L.D., Bussard, J.R., Black, B.A., Brandner, D.G., Bratti, F., Buss, B.L., Dong, X., et al. (2022). Mixed plastics waste valorization through tandem chemical oxidation and biological funneling. Science *378*, 207-211. 10.1126/science.abo4626.
6. Ellis, L.D., Rorrer, N.A., Sullivan, K.P., Otto, M., McGeehan, J.E., Román-Leshkov, Y., Wierckx, N., and Beckham, G.T. (2021). Chemical and biological catalysis for plastics recycling and upcycling. Nature Catalysis *4*, 539-556. 10.1038/s41929-021-00648-4.
7. Jia, X., Qin, C., Friedberger, T., Guan, Z., and Huang, Z. (2016). Efficient and selective degradation of polyethylenes into liquid fuels and waxes under mild conditions. Science Advances *2*, e1501591. 10.1126/sciadv.1501591.
8. Vollmer, I., Jenks, M.J.F., Roelands, M.C.P., White, R.J., van Harmelen, T., de Wild, P., van der Laan, G.P., Meirer, F., Keurentjes, J.T.F., and Weckhuysen, B.M. (2020). Beyond Mechanical Recycling: Giving New Life to Plastic Waste. Angewandte Chemie International Edition *59*, 15402-15423. 10.1002/anie.201915651.

9. Bin Jumah, A., Anbumuthu, V., Tedstone, A.A., and Garforth, A.A. (2019). Catalyzing the Hydrocracking of Low Density Polyethylene. Industrial & Engineering Chemistry Research *58*, 20601-20609. 10.1021/acs.iecr.9b04263.
10. Tennakoon, A., Wu, X., Paterson, A.L., Patnaik, S., Pei, Y., LaPointe, A.M., Ammal, S.C., Hackler, R.A., Heyden, A., Slowing, I.I., et al. (2020). Catalytic upcycling of high-density polyethylene via a processive mechanism. Nature Catalysis *3*, 893-901. 10.1038/s41929-020-00519-4.
11. Peng, Y., Yang, J., Deng, C., Deng, J., Shen, L., and Fu, Y. (2023). Acetolysis of waste polyethylene terephthalate for upcycling and life-cycle assessment study. Nature Communications *14*, 3249. 10.1038/s41467-023-38998-1.
12. Lee, K., Jing, Y., Wang, Y., and Yan, N. (2022). A unified view on catalytic conversion of biomass and waste plastics. Nature Reviews Chemistry *6*, 635-652. 10.1038/s41570-022-00411-8.
13. Liu, S., Kots, P.A., Vance, B.C., Danielson, A., and Vlachos, D.G. (2021). Plastic waste to fuels by hydrocracking at mild conditions. Science Advances *7*, eabf8283. 10.1126/sciadv.abf8283.
14. Zhang, F., Zeng, M., Yappert, R.D., Sun, J., Lee, Y.-H., LaPointe, A.M., Peters, B., Abu-Omar, M.M., and Scott, S.L. (2020). Polyethylene upcycling to long-chain alkylaromatics by tandem hydrogenolysis/aromatization. Science *370*, 437-441. 10.1126/science.abc5441.
15. Han, X., Zhou, X., Ji, T., Zeng, F., Deng, W., Tang, Z., and Chen, R. (2024). Boosting the catalytic performance of metal–zeolite catalysts in the hydrocracking of polyolefin wastes by optimizing the nanoscale proximity. EES Catalysis *2*, 300-310. 10.1039/D3EY00180F.
16. Vance, B.C., Kots, P.A., Wang, C., Hinton, Z.R., Quinn, C.M., Epps, T.H., Korley, L.T.J., and Vlachos, D.G. (2021). Single pot catalyst strategy to branched products via adhesive isomerization and hydrocracking of polyethylene over platinum tungstated zirconia. Applied Catalysis B: Environmental *299*, 120483. 10.1016/j.apcatb.2021.120483.
17. Sun, M., Zhu, L., Liu, W., Zhao, X., Zhang, Y., Luo, H., Miao, G., Li, S., Yin, S., and Kong, L. (2022). Efficient upgrading of polyolefin plastics into C5–C12 gasoline alkanes over a Pt/W/Beta catalyst. Sustainable Energy & Fuels *6*, 271-275. 10.1039/D1SE01778K.
18. Wang, H., Yoskamtorn, T., Zheng, J., Ho, P.-L., Ng, B., and Tsang, S.C.E. (2023). Ce-Promoted PtSn-Based Catalyst for Hydrocracking of Polyolefin Plastic Waste into High Yield of Gasoline-Range Products. ACS Catalysis *13*, 15886-15898. 10.1021/acscatal.3c03996.

19. Du, J., Zeng, L., Yan, T., Wang, C., Wang, M., Luo, L., Wu, W., Peng, Z., Li, H., and Zeng, J. (2023). Efficient solvent- and hydrogen-free upcycling of high-density polyethylene into separable cyclic hydrocarbons. Nature Nanotechnology. 10.1038/s41565-023-01429-9.
20. Kots, P.A., Vance, B.C., Quinn, C.M., Wang, C., and Vlachos, D.G. (2023). A two-stage strategy for upcycling chlorine-contaminated plastic waste. Nature Sustainability *6*, 1258-1267. 10.1038/s41893-023-01147-z.
21. Zhang, Z., Wang, J., Ge, X., Wang, S., Li, A., Li, R., Shen, J., Liang, X., Gan, T., Han, X., et al. (2023). Mixed Plastics Wastes Upcycling with High-Stability Single-Atom Ru Catalyst. Journal of the American Chemical Society *145*, 22836-22844. 10.1021/jacs.3c09338.
22. Cen, Z., Han, X., Lin, L., Yang, S., Han, W., Wen, W., Yuan, W., Dong, M., Ma, Z., Li, F., et al. (2024). Upcycling of polyethylene to gasoline through a self-supplied hydrogen strategy in a layered self-pillared zeolite. Nature Chemistry *16*, 871-880. 10.1038/s41557-024-01506-z.
23. Wang, M., Gao, Y., Yuan, S., Deng, J., Yang, J., Yan, J., Yu, S., Xu, B., and Ma, D. (2024). Complete hydrogenolysis of mixed plastic wastes. Nature Chemical Engineering *1*, 376-384. 10.1038/s44286-024-00064-y.
24. Conk, R.J., Hanna, S., Shi, J.X., Yang, J., Ciccia, N.R., Qi, L., Bloomer, B.J., Heuvel, S., Wills, T., Su, J., et al. (2022). Catalytic deconstruction of waste polyethylene with ethylene to form propylene. Science *377*, 1561-1566. 10.1126/science.add1088.
25. Wang, N.M., Strong, G., DaSilva, V., Gao, L., Huacuja, R., Konstantinov, I.A., Rosen, M.S., Nett, A.J., Ewart, S., Geyer, R., et al. (2022). Chemical Recycling of Polyethylene by Tandem Catalytic Conversion to Propylene. Journal of the American Chemical Society *144*, 18526-18531. 10.1021/jacs.2c07781.
26. Wang, H., and Edman Tsang, S.C. (2024). Recent advances in polyolefin plastic waste upcycling via mild heterogeneous catalysis route from catalyst development to process design. Cell Reports Physical Science, 102075. 10.1016/j.xcrp.2024.102075.
27. Carter, J.H., Bere, T., Pitchers, J.R., Hewes, D.G., Vandegehuchte, B.D., Kiely, C.J., Taylor, S.H., and Hutchings, G.J. (2021). Direct and oxidative dehydrogenation of propane: from catalyst design to industrial application. Green Chemistry *23*, 9747-9799. 10.1039/D1GC03700E.
28. Wang, C., Zhang, L., Huang, X., Zhu, Y., Li, G., Gu, Q., Chen, J., Ma, L., Li, X., He, Q., et al. (2019). Maximizing sinusoidal channels of HZSM-5 for high shape-selectivity to p-xylene. Nature Communications *10*, 4348. 10.1038/s41467-019-12285-4.
29. Yang, M., Li, B., Gao, M., Lin, S., Wang, Y., Xu, S., Zhao, X., Guo, P., Wei, Y., Ye, M., et al. (2020). High Propylene Selectivity in Methanol Conversion over a Small-Pore

SAPO Molecular Sieve with Ultra-Small Cage. ACS Catalysis *10*, 3741-3749. 10.1021/acscatal.9b04703.

30. Rejman, S., Vollmer, I., Werny, M.J., Vogt, E.T.C., Meirer, F., and Weckhuysen, B.M. (2023). Transport limitations in polyolefin cracking at the single catalyst particle level. Chemical Science *14*, 10068-10080. 10.1039/D3SC03229A.
31. Zhang, Y., Zhou, Y., Liu, H., Wang, Y., Xu, Y., and Wu, P. (2007). Effect of La addition on catalytic performance of PtSnNa/ZSM-5 catalyst for propane dehydrogenation. Applied Catalysis A: General *333*, 202-210. 10.1016/j.apcata.2007.07.049.
32. Cañizares, P., de Lucas, A., Dorado, F., Durán, A., and Asencio, I. (1998). Characterization of Ni and Pd supported on H-mordenite catalysts: Influence of the metal loading method. Applied catalysis. A, General *169*, 137-150. 10.1016/S0926-860X(98)00008-8.
33. Van der Borght, K., Galvita, V.V., and Marin, G.B. (2015). Ethanol to higher hydrocarbons over Ni, Ga, Fe-modified ZSM-5: Effect of metal content. Applied Catalysis A: General *492*, 117-126. 10.1016/j.apcata.2014.12.020.
34. Telkar, M.M., Nadgeri, J.M., Rode, C.V., and Chaudhari, R.V. (2005). Role of a co-metal in bimetallic Ni–Pt catalyst for hydrogenation of m-dinitrobenzene to m-phenylenediamine. Applied Catalysis A: General *295*, 23-30. 10.1016/j.apcata.2005.07.050.
35. Akri, M., Zhao, S., Li, X., Zang, K., Lee, A.F., Isaacs, M.A., Xi, W., Gangarajula, Y., Luo, J., Ren, Y., et al. (2019). Atomically dispersed nickel as coke-resistant active sites for methane dry reforming. Nature Communications *10*, 5181. 10.1038/s41467-019-12843-w.
36. Chu, M., Wang, X., Wang, X., Xu, P., Zhang, L., Li, S., Feng, K., Zhong, J., Wang, L., Li, Y., et al. (2024). Layered Double Hydroxide Derivatives for Polyolefin Upcycling. Journal of the American Chemical Society *146*, 10655-10665. 10.1021/jacs.4c00327.
37. Vance, B.C., Najmi, S., Kots, P.A., Wang, C., Jeon, S., Stach, E.A., Zakharov, D.N., Marinkovic, N., Ehrlich, S.N., Ma, L., and Vlachos, D.G. (2023). Structure–Property Relationships for Nickel Aluminate Catalysts in Polyethylene Hydrogenolysis with Low Methane Selectivity. JACS Au *3*, 2156-2165. 10.1021/jacsau.3c00232.
38. Vogt, C., Kranenborg, J., Monai, M., and Weckhuysen, B.M. (2020). Structure Sensitivity in Steam and Dry Methane Reforming over Nickel: Activity and Carbon Formation. ACS Catalysis *10*, 1428-1438. 10.1021/acscatal.9b04193.
39. Jung, M.R., Horgen, F.D., Orski, S.V., Rodriguez C, V., Beers, K.L., Balazs, G.H., Jones, T.T., Work, T.M., Brignac, K.C., Royer, S.-J., et al. (2018). Validation of ATR FT-IR to identify polymers of plastic marine debris, including those ingested by marine organisms. Marine Pollution Bulletin *127*, 704-716. 10.1016/j.marpolbul.2017.12.061.

40. Wu, X., Wang, X., Zhang, L., Wang, X., Song, S., and Zhang, H. (2024). Polyethylene Upgrading to Liquid Fuels Boosted by Atomic Ce Promoters. Angewandte Chemie International Edition *63*, e202317594. 10.1002/anie.202317594.
41. Feng, J., Duan, J., Hung, C.-T., Zhang, Z., Li, K., Ai, Y., Yang, C., Zhao, Y., Yu, Z., Zhang, Y., et al. (2024). Micelles Cascade Assembly to Tandem Porous Catalyst for Waste Plastics Upcycling. Angewandte Chemie International Edition *63*, e202405252. 10.1002/anie.202405252.
42. Bunn, A., Cudby, M.E.A., Harris, R.K., Packer, K.J., and Say, B.J. (1982). High resolution 13C n.m.r. spectra of solid isotactic polypropylene. Polymer *23*, 694-698. 10.1016/0032-3861(82)90053-2.
43. Salehirad, F., and Anderson, M.W. (1996). Solid-State13C MAS NMR Study of Methanol-to-Hydrocarbon Chemistry over H-SAPO-34. Journal of Catalysis *164*, 301-314. 10.1006/jcat.1996.0386.
44. Olsbye, U., Svelle, S., Bjørgen, M., Beato, P., Janssens, T.V.W., Joensen, F., Bordiga, S., and Lillerud, K.P. (2012). Conversion of Methanol to Hydrocarbons: How Zeolite Cavity and Pore Size Controls Product Selectivity. Angewandte Chemie International Edition *51*, 5810-5831. 10.1002/anie.201103657.
45. Li, L., Luo, H., Shao, Z., Zhou, H., Lu, J., Chen, J., Huang, C., Zhang, S., Liu, X., Xia, L., et al. (2023). Converting Plastic Wastes to Naphtha for Closing the Plastic Loop. Journal of the American Chemical Society *145*, 1847-1854. 10.1021/jacs.2c11407.
46. Kilgore, G. (2024). 2023 Plastic Carbon Footprint: Official Emissions Numbers + Calculator. https://8billiontrees.com/carbon-offsets-credits/carbon-ecological-footprint-calculators/plastic-carbon-footprint/.
47. GAIA (2023). Plastic is Carbon Unwrapping the "net zero" myth. https://www.no-burn.org/wp-content/uploads/2021/11/Plastic-is-Carbon-Oct2021.pdf.
48. Xayachak, T., Haque, N., Lau, D., Parthasarathy, R., and Pramanik, B.K. (2023). Assessing the environmental footprint of plastic pyrolysis and gasification: A life cycle inventory study. Process Safety and Environmental Protection *173*, 592-603. 10.1016/j.psep.2023.03.061.

Chapter 6 Lanthanum-Group Elements Promoted PtGa Catalysts for Propane Dehydrogenation: Exploring Key Performance Descriptors

This chapter is adapted from the work by Haokun Wang, Xuelei Pan, Yanjie Wang, Bryan Ng, and Shik Chi Edman Tsang, published in Applied Catalysis A: General in 2024.[1] The figures and tables are reproduced with permission. Copyright 2025 CC-BY 4.0.[1]*

6.1 Introduction

Propylene is a crucial chemical feedstock, ranking as the second most significant raw material in the petrochemical industry.[2] It serves as a key precursor element in the manufacture of major synthetic materials, including plastics, synthetic rubbers, and synthetic fibres.[3] Moreover, propylene is further processed into other essential industrial chemicals, such as acetone and isopropanol.[2,4] Traditional methods of propylene production, such as fluid catalytic cracking (FCC) and steam cracking (SC), accounted for over 80% of global propylene output in 2016. However, these processes are associated with low atom efficiency, reliance on toxic reagents, use of non-renewable feedstocks, and frequent catalyst regeneration, making them less environmentally friendly and sustainable.[4,5] Emerging technologies, such as direct propane dehydrogenation, offer a promising alternative, addressing the drawbacks of conventional methods by eliminating toxic chemicals and reducing by-product formation under optimised operation conditions.[4]

The growing demand for propylene, projected to increase annually by 2% to 3% by 2030, coupled with the surge in PP consumption during the COVID-19 pandemic, particularly in the production of surgical masks, underscores the pressing need for alternative propylene production methods, including propane dehydrogenation.[6-8] Moreover, as demonstrated in Chapters 4 and 5, two stable and efficient catalytic approaches have already been developed for upcycling of PP waste into high yields of propane. To achieve a truly circular economy, further investigation into the dehydrogenation of propane back into propylene is essential.

In the field of propane dehydrogenation, while the process offers significant environmental advantages, its endothermic nature requires high operating temperatures (550–700 °C).[6] These demanding conditions present challenges in maintaining catalytic activity, selectivity and stability.[9] Thus, the development of a catalyst that balances active, selectivity, and stability is crucial for the sustainability of this process. Currently, commercial propane dehydrogenation catalysts are predominantly either Pt-based or CrO_x-based.[7] CrO_x-based catalysts, though cost-effective and high active, are associated with significant toxicity and environmental hazards, promoting the search for alternative metal oxide with reduced or no chromium content.[7,9] On the other hand, Pt-based catalysts excel in activating C-H bonds while minimising unwanted C-C bond breakage, and they are environmentally friendlier. However, their susceptibility to coking, sintering, and high cost necessitates the development of more selective and stable Pt-based systems, particularly through the inclusion of suitable promoters.[4,7,10]

Among various promoters, Sn and Ga have been particularly effective in enhancing Pt-based catalysts for propane dehydrogenation, as evidenced by their use in commercial processes such as Oleflex ($PtSn/Al_2O_3$), Dow FCDh ($PtGa/Al_2O_3$), and other commercial technologies like STAR and PDH.[11] The addition of Sn or Ga improves propane selectivity, reduces the acidity of the support, and facilitates the migration of coke away from the active Pt sites, primarily due to the well-documented ‘‘geometric effect’’ and ‘‘electronic effect’’.[12,13] Despite these advances, the catalytic performance of PtSn or PtGa systems still requires further optimisation to lower operational costs and improve the efficiency of catalyst regeneration and separation processes in industrial settings. To address these challenges, researchers have investigated other promoters aimed at enhancing the thermal stability, fine-tuning the acid-base properties of the support, and optimising metal-support interactions in PtSn and PtGa systems. Promoters explored include alkaline earth metals like Mg,[14] Ca,[15] as well as various transition metals, such as Zn,[16,17] Co,[17] In,[18] Fe,[18] La,[18-20] Ce,[18,20] Y,[20] and others. Although these studies have improved catalytic performance, the complex relationship between the

modified microenvironments of active sites by promoters and their initial catalytic behaviours remains poorly understood, which is critical for the rational design of heterogeneous catalysts. Recently, both experimental and theoretical studies have begun to shed light on these correlations in reactions like ethylene hydrogenation,[21] and acetylene hydrochlorination.[22] This progress highlights the need for further exploration of these interactions in other industrial reactions and catalysts, such as PtGa systems used in propane dehydrogenation.

In this chapter, the use of four lanthanide promoters–La, Ce, Pr, and Nd–at varying loadings (1 wt%, 3 wt%, and 5 wt%) was explored to modify the commercial PtGa/γ-Al_2O_3 catalyst for propane dehydrogenation. The modified catalysts demonstrate enhanced conversion, selectivity, and stability compared to the commercial PtGa/γ-Al_2O_3 catalyst. Additionally, the mechanisms by which these promoters influence the catalyst enable precise control over the microenvironments of the active sites. This work facilitates the identification of key performance descriptors and construction of structure-activity relationships, offering insights for optimising commercial PtGa/γ-Al_2O_3 catalyst in propane dehydrogenation.

6.2 Results and discussion

6.2.1 Physicochemical properties of catalysts

As depicted in Figure 6.1, the XRD patterns of the PtGa/γ-Al_2O_3 catalyst display distinct diffraction peaks at 37.7°, 45.8°, and 66.9°, which correspond to the (311), (400), and (440) crystal planes of γ-Al_2O_3.[23] Upon incorporating lanthanide elements into the PtGa system, a noticeable shift of these primary diffraction peaks towards lower angles is observed in all-modified catalysts, signifying an expansion in the lattice parameters.[24] This lattice expansion is attributed to the larger ionic diameter of these promoter cations relative to Al^{3+}, leading to the substitution of some Al^{3+} ions in the γ-Al_2O_3 lattice, and consequent structural dilation. Notably, no diffraction peaks corresponding to Pt, Ga, or the lanthanide promoters are detected, indicating that these elements are highly dispersed across the γ-Al_2O_3 support.

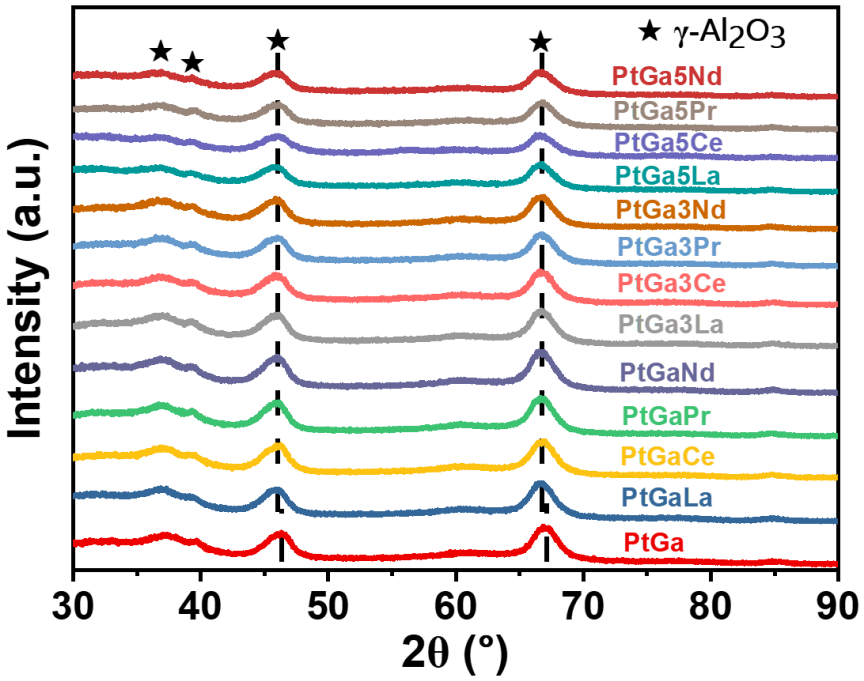

Figure 6.1 XRD patterns of all catalysts.

This conclusion is further corroborated by HRTEM image of the PtGa/γ-Al_2O_3 catalyst (Figure 6.2), which reveals a relatively uniform distribution of metallic particles with an average particle size of approximately 1.7 nm.

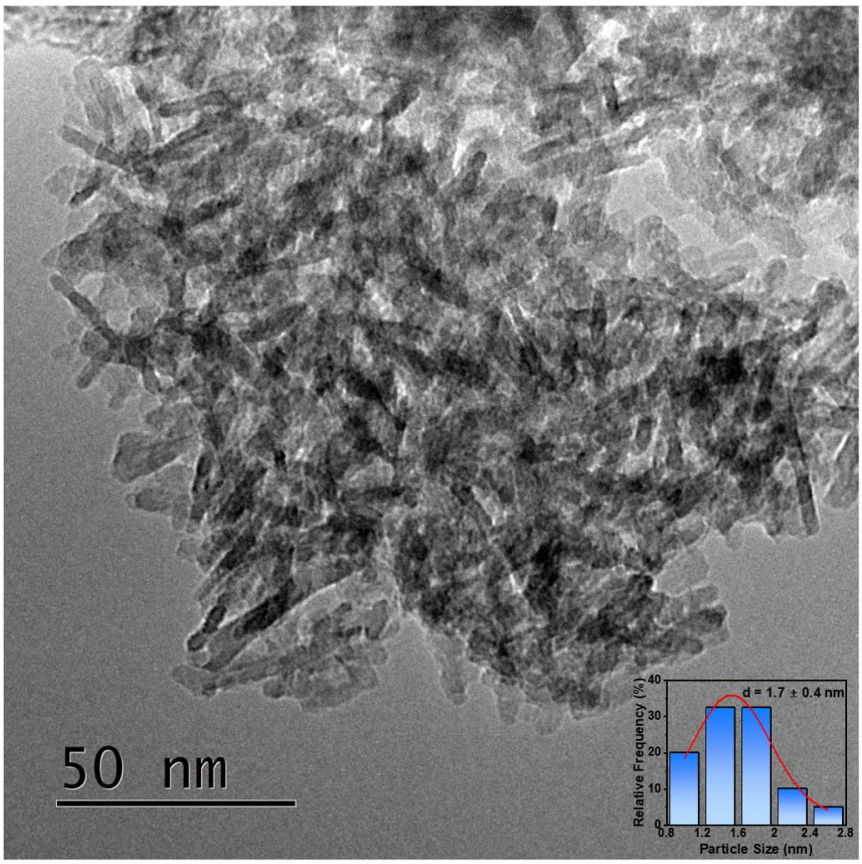

Figure 6.2 HRTEM image of $PtGa/Al_2O_3$ catalyst with particle size distribution.

Additional insights into the textural properties, including specific surface area and pore size distribution of all catalysts, were obtained through nitrogen adsorption-desorption isotherms (Figure 6.3 (a) and (b)). Interestingly, all catalysts exhibit consistent adsorption-desorption isotherm patterns and similar pore size distributions. Importantly, the introduction of different lanthanide promoters (La, Ce, Pr, Nd) up to 5 wt% does not significantly alter the specific surface area or pore characteristics across the catalysts (Table 6.1). These observations collectively highlight the mesoporous nature of γ-Al_2O_3 support, as evidenced by the type IV isotherms and the absence of significant micropore volume according to the t-plot analysis.

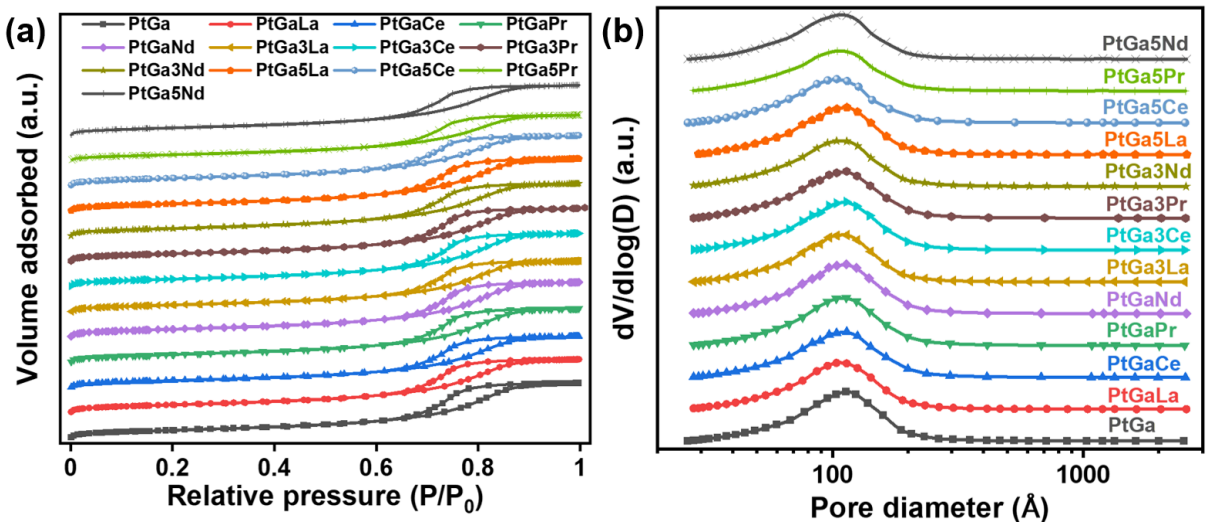

Figure 6.3 (a) N_2 adsorption-desorption isotherms of all catalysts. (b) Pore size distribution of all catalysts.

Table 6.1 Physicochemical characterisation of PtGa-based catalysts.

Catalyst	Specific area (m^2g^{-1})[a]	Pore volume (cm^3g^{-1})[b]	Average pore size (nm)[c]
$PtGa/Al_2O_3$	192	0.50	9.63
$PtGaLa/Al_2O_3$	198	0.48	9.10
$PtGaCe/Al_2O_3$	180	0.47	9.61
$PtGaPr/Al_2O_3$	195	0.49	9.36
$PtGaNd/Al_2O_3$	197	0.50	9.42
$PtGa3La/Al_2O_3$	179	0.47	9.64
$PtGa3Ce/Al_2O_3$	191	0.48	9.45
$PtGa3Pr/Al_2O_3$	195	0.48	9.22
$PtGa3Nd/Al_2O_3$	194	0.48	9.19
$PtGa5La/Al_2O_3$	184	0.48	9.60
$PtGa5Ce/Al_2O_3$	192	0.46	8.90
$PtGa5Pr/Al_2O_3$	180	0.44	9.03
$PtGa5Nd/Al_2O_3$	188	0.45	9.04

[a] Measured by BET surface area

[b] Measured by BJH adsorption cumulative volume of pores

[c] Measured by adsorption average pore diameter

To access the reducibility of the different supported catalysts, H_2-TPR experiments were conducted, with the resulting profiles shown in Figure 6.4 (a) and (b). As illustrated in Figure 6.4 (a), when Pt is supported solely on γ-Al_2O_3, a distinct reduction peak appears around 303 °C, indicating the straightforward reduction of Pt oxides to metallic Pt, typically occurring below 400 °C over Al_2O_3.[25] In contrast, the reduction of Ga oxides on the same support is more challenging, as evidenced by the higher temperature of 466 °C (Figure 6.4 (a)). This aligns with the reduction behaviour observed for Ga/ZSM5 catalysts, where an intense reduction peak occurs between 400 °C and 600 °C, corresponding to the initial reduction of Ga^{3+} to Ga^{+}, as confirmed by TPR-microbalance studies and theoretical calculations.[26,27] When Pt and Ga are co-supported on Al_2O_3, two prominent reduction peaks are detected at 317 °C and 518 °C, respectively. Wang et al. (2016) reported similar reduction peaks for PtGa/Al_2O_3, albeit at lower temperatures (239 °C and 440 °C), likely due to differences in Ga content, which can significantly influence the TPR profiles of bimetallic catalysts.[25,28] The first reduction peak, occurring at a slightly higher temperature (317 °C) compared to Pt alone (303 °C), suggests the simultaneous reduction of Pt and a fraction of Ga that are in close proximity, likely forming intermetallic PtGa species.[29] The higher temperature peak is likely associated with the reduction of a more isolated Ga species, which remains spatially distinct from Pt but is reduced with the assistant of Pt.[28] This phenomenon, where Pt facilitates the reduction of remote Ga oxides even on separate grains, is well documented.[30-32] The proposed mechanism involves the dissociation of H_2 on metallic Pt sites, with the resulting atomic hydrogen driving Ga reduction at elevated temperatures. Overall, the two distinct reduction peaks corresponds to two types of Ga species: one in close contact with Pt and the other dispersed on the support.[28]

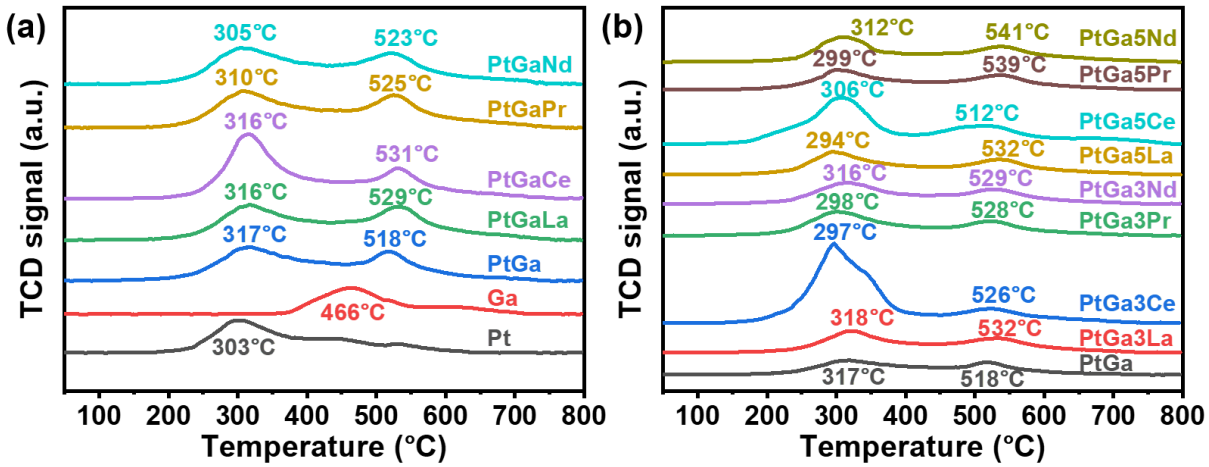

Figure 6.4 (a) and (b) H_2-TPR over different catalysts.

The introduction of various lanthanide promoters (La, Ce, Pr, Nd) at low loading (1 wt%) in Figure 6.4 (a) leads to a progressive shift of the first reduction peak towards lower temperatures, while the second peak shifts to higher temperatures compared to the unmodified PtGa catalyst. The lower temperatures of the first peaks suggest that these promoters enhance the reduction of the intimately associated Pt-Ga species, facilitating the formation of PtGa alloys. The increased surface coverage by promoters may hinder the Pt-facilitated reduction of more remote Ga species, leading to an increase in the second reduction temperatures. Similar effects have been observed by Vu et al. (2011), who noted enhanced Pt reduction when La and Ce were added to Pt/Al_2O_3.[20] This reduction in the first peak temperature is attributed to an electron-donating effect, where increased electron density conglomeration on the Pt surface facilitates electron transfer from Ga to Pt. This phenomenon has been observed in La-modified PtSn systems as well, where it is linked to the Lewis basicity of ionic lanthanide oxides.[32]

Among the promoters, Ce-promoted PtGa catalyst stand out not only lowering the first reduction temperature but also by nearly doubling the peak area, accompanied by a broader peak range. This indicates a unique interaction between Pt, Ga, and Ce on the support. Recent studies identified a similar strong interactions between Pt, Sn and Ce on amorphous SiAl support.[33] The observed reduction temperature decrease with Ce suggests a robust Lewis

base interaction with PtGa, coupled with distinctive metal-support interactions. This is attributed to an enhanced hydrogen spillover effect from Pt to a more distant Ga species via surface cerium oxides. Additionally, the preferential interaction of Pt and ceria, as opposed to alumina, may also play a role.[34] As a result, the total hydrogen consumption in the first peak significantly increases at the expense of second peak, indicating a higher extent of PtGa alloy formation, which could lead to enhanced catalytic performances when ceria is used as a promoter.

Upon increasing the promoter loadings to 3 wt% and 5 wt% (Figure 6.4 (b)), the shift in the first peak temperatures become more pronounced, indicating an enhanced promotion of the reduction of Pt and Ga in intimate contact. This suggests that both the type and concentration of promoters significantly influence their reducibility.[20,35] Similar to the strong interactions observed between Pt, Ga, and Ce at low promoter loading (1 wt%), these interactions intensify at higher loadings (3 wt% and 5 wt%), as evidenced by the increased peak area and broader peak ranges. While the broadest peak is observed at 5 wt% Ce loading, suggesting the strongest interactions, the largest peak area is found at 3 wt% Ce loading. Interestingly, when Ce loading increases from 3 wt% to 5 wt%, the first reduction peak shifts to a higher temperature, while the second peak shifts to a lower temperature. This indicates that excessive Ce deposition disrupts the intimate-interaction between Pt and Ga (likely due to high affinity of Pt for Ce) but has minimal impact on the reduction of remote Ga species. Conversely, the electron-donating effects of other promoters (La, Pr, and Nd) are amplified as their concentration increases, as reflected by higher hydrogen consumption in the first reduction peaks at 5 wt% compared to 3 wt%.

To further investigate the concentration and strength of acids sites, NH_3-TPD was performed, with profiles presented in Figure 6.5. The resulting NH_3-TPD curves were deconvolved for semiquantitative analysis, and the fitting results are summarised in Table 6.2. Across all catalysts, three distinct desorption peaks are observed within the temperature range of 50 °C to 600 °C, corresponding to weak acid sites (red dashed lines), medium acid sites (blue

dashed lines), and strong acid sites (green dashed lines) based on their desorption strengths. The introduction of different promoters reveals a consistent trend: all promoted catalysts show a reduction in both the concentration and the strength of acid sites across all three categories. This is supported by the lower total peak area and decreased desorption temperatures reported in Table 6.2. Intriguingly, as the promoter loading increases, the overall acidity decreases uniformly without alternating the relative proportions of each type of acid sites. This suggests that the promoters primarily affect the total acidity rather than selectively targeting specific acid site.

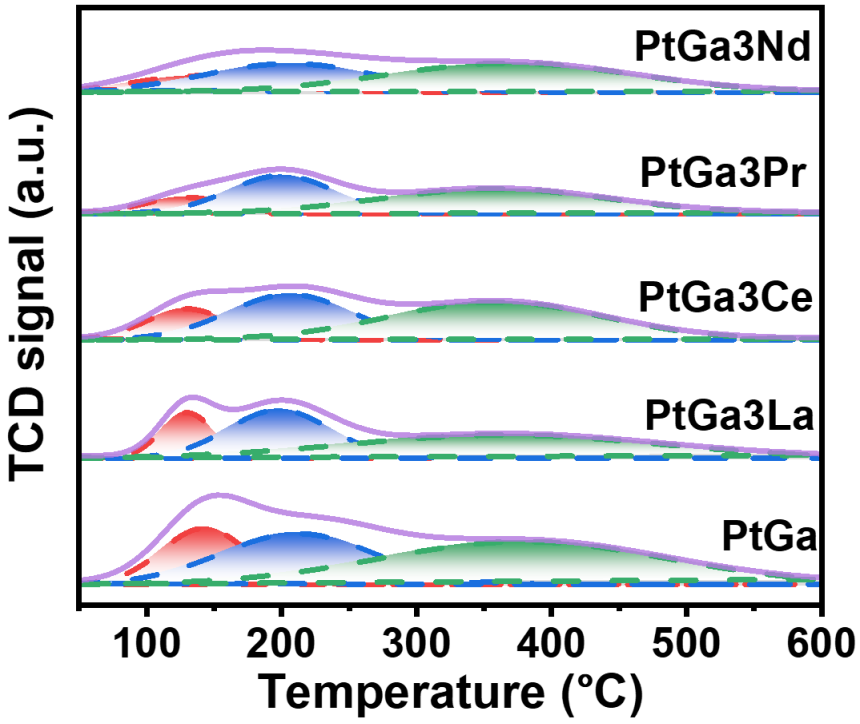

Figure 6.5 NH_3-TPD profiles on PtGa/Al_2O_3 and 3 wt% loading promoted catalysts.

Table 6.2 Summary of acidity results from NH_3-TPD and Py-IR at 200 °C.

Catalyst	T_M (°C)			Total area (a.u.)	Peak fraction (%)			LAS concentration from Py-IR (μmol g cat^{-1})
	I	II	III		I	II	III	
PtGa	143	212	379	28	19	32	49	57.6
PtGaLa	132	207	371	20	13	39	48	43.7
PtGaCe	132	204	361	20	14	38	48	43.4
PtGaPr	138	210	368	21	14	39	47	44.8
PtGaNd	141	207	375	24	13	37	50	52.7
PtGa3La	130	198	365	16	16	35	49	33.0
PtGa3Ce	130	206	359	18	15	35	50	40.9
PtGa3Pr	129	200	358	12	12	37	51	26.8
PtGa3Nd	139	206	370	16	15	35	50	33.2
PtGa5La	135	201	370	14	14	34	52	30.4
PtGa5Ce	131	202	355	14	14	36	50	30.1
PtGa5Pr	132	202	363	16	16	34	50	33.8
PtGa5Nd	140	212	372	18	15	36	49	38.1

Given the limitations of NH_3-TPD in distinguishing the precise nature of acid sites, Py-IR spectroscopy was conducted at 200 °C to access the concentration of BAS and LAS. As shown in Figure 6.6, the adsorption peaks around 1450 cm^{-1} are attributed to LAS-pyridine interactions, while BAS (peaks around 1550 cm^{-1}) is nearly absent, indicating that the acidity in all catalysts is predominantly due to LAS. The concentration of LAS was quantified using Beer-Lambert-Bouguer law,[36] and the results are presented in Table 6.2. The trends in LAS concentration measured by Py-IR are consistent with those observed in NH_3-TPD, showing a gradual decrease in LAS concentration with increasing promoter content. Similar reductions in acidity have been observed with increasing La content in ZSM-5 zeolite,[37] which were attributed to pore blockage by La_2O_3 deposition and the creation of new basic sites on the support surface. However, in this study, promoter loading up to 5 wt% did not significantly affect the specific surface area and pore size distribution, as confirmed by adsorption/desorption isotherms and pore size measurements (Figure 6.3 and Table 6.1).

Therefore, the observed decrease in acidity is likely attributed to the formation of new basic sites rather than any structural alternations to the support.

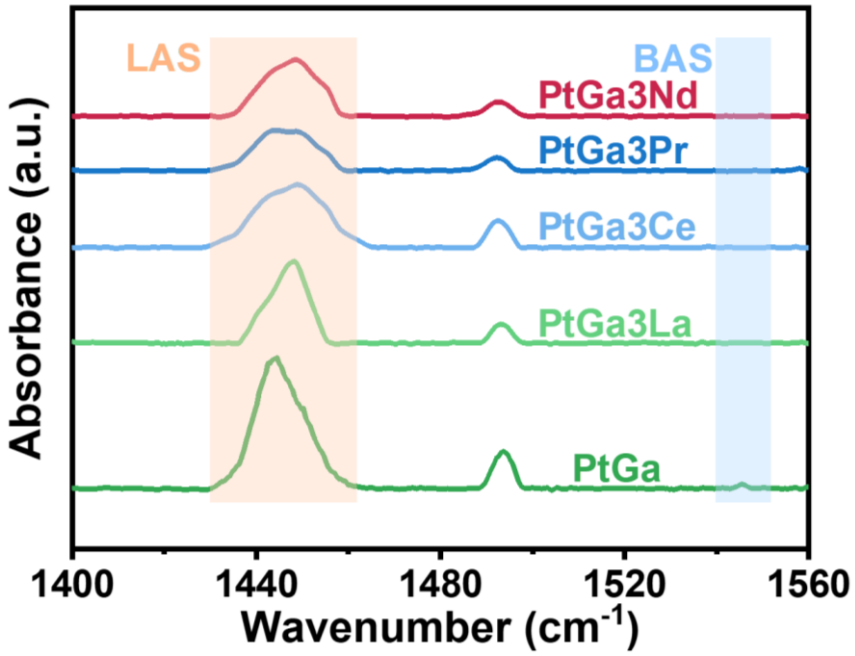

Figure 6.6 Py-IR profiles on $PtGa/Al_2O_3$ and 3 wt% loading promoted catalysts at 200 °C.

Previous research has demonstrated that incorporating La into the ZSM-5 support enhances its basicity, as confirmed by CO_2-TPD analysis.[38,39] A newly emerged peak around 70 °C indicated the presence of surface basic sites generated with the introduction of La promoters. Furthermore, the CO_2 adsorption capacity associated with these peak increases with higher La loadings, suggesting that these new basic sites are directly attributed to La incorporation. The origin of these sites is linked to the predominantly ionic nature of lanthanide oxides bonds, a consequence of the elements' electronegativity. Lanthanide oxides are characterised by basicity comparable to that of alkali metal oxides, but they avoid the surface contamination typically caused by alkali ions. The introduction of these basic sites can hinder the re-adsorption of propylene and reduce deep cracking, thereby enhancing propylene selectivity. Additionally, the reduction in both the concentration and strength of acid sites offers further benefits to catalytic performance by minimising side reactions like isomerisation and

polymerisation, which are generally catalysed by acidic centres and are primary contributors to coke formation.[40]

The interaction between Pt and various promoters was also explored by examining electronic environment of Pt atoms using CO-FTIR spectroscopy, as shown in Figure 6.7. The spectra for all catalysts display a dominant peak between 2057 cm^{-1} to 2070 cm^{-1}, corresponding to CO linearly bonded to exposed metallic Pt site.[41] Introducing an suitable amount of promoter results in a red shift in the adsorption peak, moving from 2070 cm^{-1} for PtGa catalyst to 2057 cm^{-1} for the PtGa3La catalyst. This shift indicates a modified electronic interaction where electrons from surface Pt atoms occupy the 2π antibonding orbital of CO, leading to the formation of Pt-C bonds and a concomitant weaking of C-O bond energy. The basic promoters further enhance the electron density of Pt particles, contributing to the red shift in CO adsorption by reducing C-O bond strength. According to Blyholder's classic model on CO bonding to metal surfaces,[42] smaller Pt particles have a lower average coordination number, which also reduces bonding energy, potentially aiding in the improved dispersion of Pt promoted by these promoters. Interestingly, the CO peak frequency shifts from 2057 cm^{-1} for La-promoted catalyst to 2066 cm^{-1} for Nd-promoted systems. This trend may be attributed to the gradual increase in electronegativity from La to Nd, which reduces the ability to increase the electron density on Pt particles.

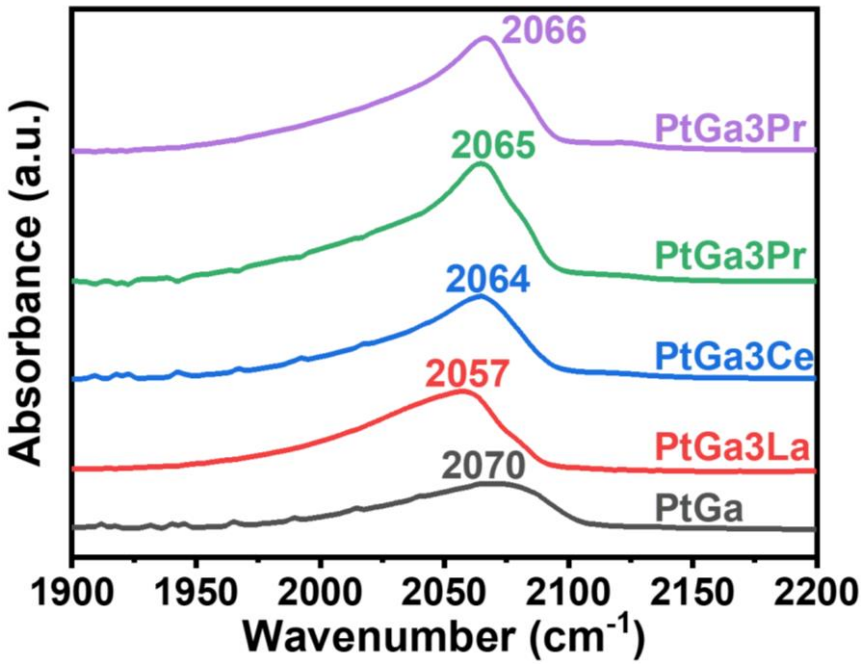

Figure 6.7 CO-FTIR spectra on PtGa/Al_2O_3 and 3 wt% loading promoted catalysts.

6.2.2 Catalytic performances in propane dehydrogenation

Figures 6.8 and 6.9 depict propane conversion and propylene selectivity as functions of time on stream (TOS) for various modified catalysts at 600 °C under distinct reaction conditions. Using a first-order deactivation model,[43] the deactivation rate and estimated catalyst lifetimes for each catalyst under different reaction conditions were determined, with the results summarised in Table 6.3. As shown in Figure 6.8 (a)-(d), catalysts promoted by La, Ce, Pr, and Nd consistently display superior conversion, selectivity, and stability compared to the commercial PtGa catalyst under hydrogen cofeeding conditions. Notably, the PtGa3Nd catalyst achieves an initial conversion of 43.6%, substantially higher than the unmodified PtGa catalyst's 30.1%. Interestingly, for each promoter, the highest conversion is typically achieved at a moderate loading (3wt%), expect for the Ce-promoted catalyst, where the maximum conversion is observed at a higher loading (5 wt%). This trend likely stems from the increasingly robust interactions between Pt, Ga, and Ce with increasing Ce content, a phenomenon less evident with other promoters.

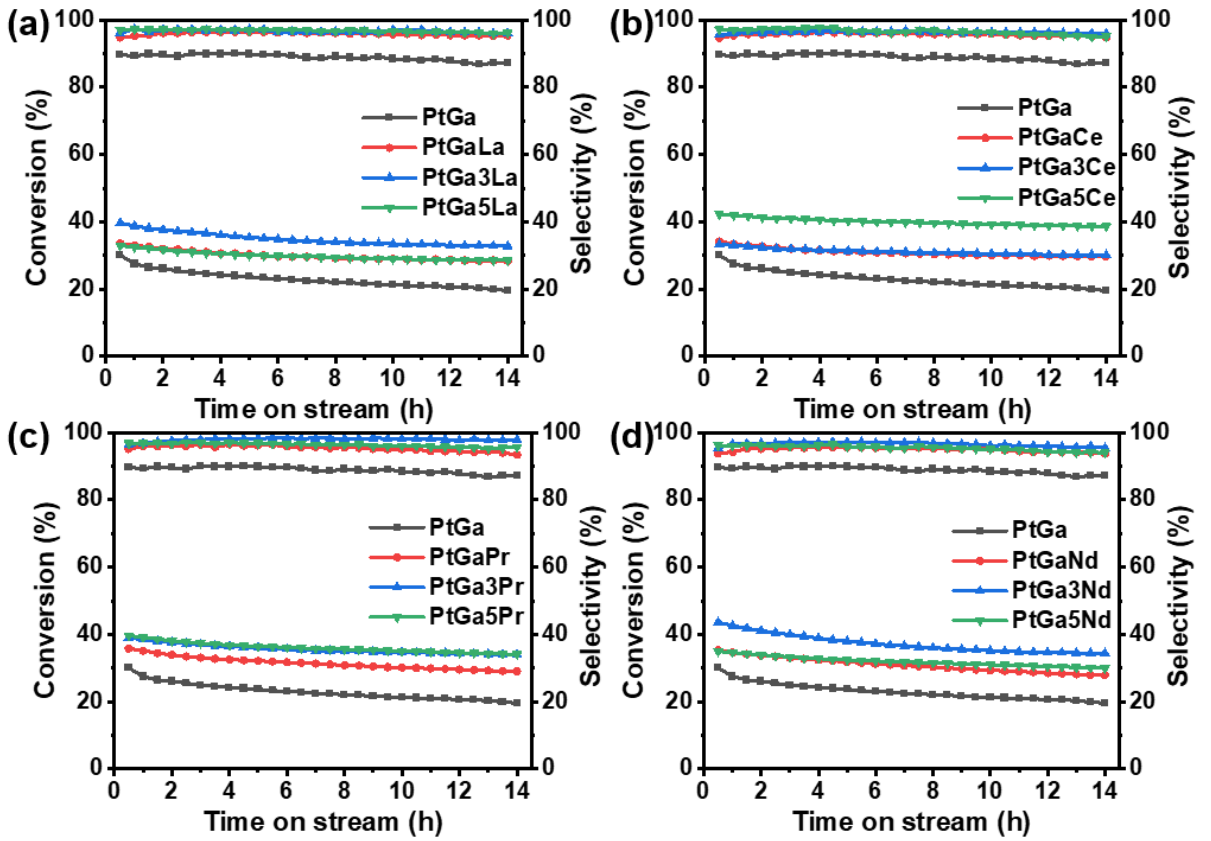

Figure 6.8 (a) Catalytic performances over La-modified $PtGa/Al_2O_3$ catalysts with different La loadings under hydrogen cofeeding. (b) Catalytic performances over Ce-modified $PtGa/Al_2O_3$ catalysts with different Ce loadings under hydrogen cofeeding. (c) Catalytic performances over Pr-modified $PtGa/Al_2O_3$ catalysts with different Pr loadings under hydrogen cofeeding. (d) Nd-modified $PtGa/Al_2O_3$ catalysts with different Nd loadings under hydrogen cofeeding. Reaction conditions: 600 °C, total flow rate of 25 mL min^{-1} containing 10 vol % H_2, 20 vol % C_3H_8, and balanced with N_2. The WHSV of propane was maintained at 5.4 h^{-1}, with a carbon balance exceeding 98%.

Table 6.3 Deactivation rate and expected lifetime for each catalyst under different conditions.

Catalyst	Deactivation rate (h^{-1})	Expected catalyst life (h)
PtGa/Al_2O_3(H_2)	0.042	23.7
PtGaLa/Al_2O_3(H_2)	0.018	54.9
PtGaCe/Al_2O_3(H_2)	0.015	66.1
PtGaPr/Al_2O_3(H_2)	0.023	43.8
PtGaNd/Al_2O_3(H_2)	0.025	39.3
PtGa3La/Al_2O_3(H_2)	0.022	45.4
PtGa3Ce/Al_2O_3(H_2)	0.011	92.4
PtGa3Pr/Al_2O_3(H_2)	0.016	63.3
PtGa3Nd/Al_2O_3(H_2)	0.029	34.9
PtGa5La/Al_2O_3(H_2)	0.016	64.3
PtGa5Ce/Al_2O_3(H_2)	0.011	90.6
PtGa5Pr/Al_2O_3(H_2)	0.018	56.7
PtGa5Nd/Al_2O_3(H_2)	0.017	59.1
PtGa/Al_2O_3(no H_2)	0.082	12.2
PtGa3La/Al_2O_3(no H_2)	0.031	32.2
PtGa3Ce/Al_2O_3(no H_2)	0.015	69.1
PtGa3Pr/Al_2O_3(no H_2)	0.023	43.7
PtGa3Nd/Al_2O_3(no H_2)	0.038	26.0

Regarding propylene selectivity, the PtGa3Pr catalyst exhibits the highest selectivity, surpassing 98%, which is approximately 10% higher than the commercial PtGa catalyst. Although PtGa3Pr offers the best selectivity, the overall selectivity variation across different loadings or promoters is minimal. However, catalyst stability is significantly influenced by both promoter types and loadings. As presented in Table 6.3, PtGa3Ce emerges as the most stable catalyst, with a deactivation rate of approximately 0.011 h^{-1}, a 74% reduction compared to the commercial PtGa catalyst (0.042 h^{-1}) under hydrogen cofeeding conditions. Additionally, the deactivation rate tends to decrease as promoter loading increases, with Ce-modified catalysts consistently showing greater stability than those modified with other promoters at equivalent loadings, suggesting a link between stronger interactions and enhanced stability.

Although hydrogen cofeeding effectively mitigates coke formation and improves catalyst stability, it also limits the conversion equilibrium.[44,45] Consequently, harsher reaction conditions without hydrogen cofeeding were investigated to meet industrial production demands. As shown in Figure 6.9 (a), the same propane flow rate (WHSV = 5.4 h^{-1}) was applied without hydrogen to re-evaluate catalyst performance. The initial propane conversion slightly increased compared to hydrogen cofeeding conditions for all catalysts, indicating the presence of hydrogen restricts the conversion equilibrium. However, catalyst stability decreased significantly without hydrogen. The PtGa/Al_2O_3 catalyst exhibited nearly double the deactivation rate compared to hydrogen conditions (see Table 6.3), while all modified catalysts experienced around a 30% to 40% increase in deactivation rate, still demonstrating better coking-resistance than the nonmodified PtGa/Al_2O_3 catalyst. Despite the improved stability achieved through promoter addition, deactivation remained a challenge in the absence of hydrogen. Coke deposition and gradual deactivation are well-known issues in Pt-based propane dehydrogenation catalysts, necessitating periodic catalyst regeneration to achieve a viable catalyst lifespan in industrial applications.[46,47] To further assess long-term stability, extended tests with regular regeneration cycles were performed after 14-hours reaction periods, as shown in Figure 6.9 (b). The PtGa/Al_2O_3 exhibited significant losses in activity and selectivity after regeneration, whereas the PtGa3Pr/Al_2O_3 catalyst maintained performance over four consecutive cycles, confirming its superior stability during regeneration. The enhanced stability could effectively extend catalyst lifetime and reduce the frequency of regeneration, providing valuable slights for industrial applications.

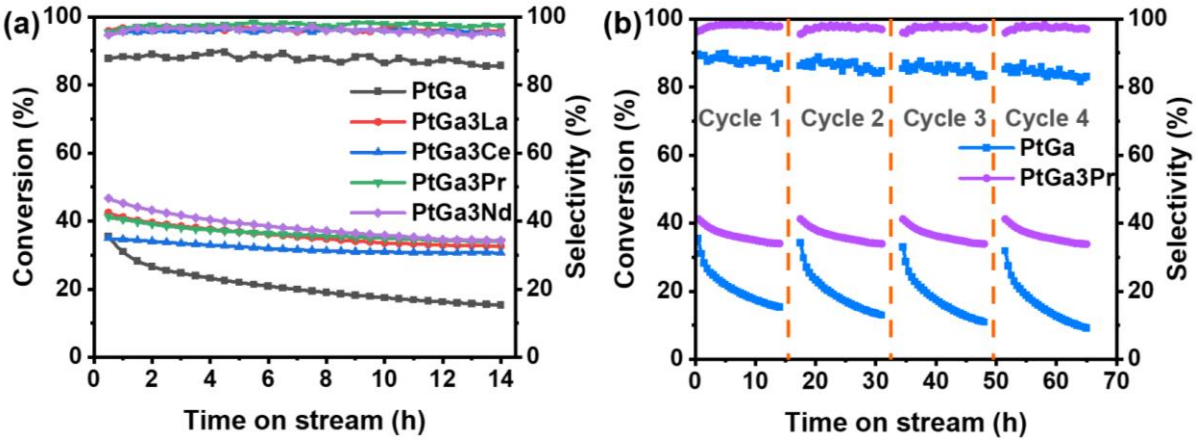

Figure 6.9 (a) Catalytic performances over La, Ce, Pr, and Nd-modified PtGa/Al_2O_3 catalysts under hydrogen-free conditions. (b) Catalytic performances over PtGa/Al_2O_3 and PtGa3Pr/Al_2O_3 catalysts under hydrogen-free conditions for long-term stability tests across four reaction-regeneration cycles. Reaction conditions: 600 °C, total flow rate 25 mL min^{-1} containing 20 vol % C_3H_8 and balanced with N_2. Regarding the regeneration cycles, after each 14-hours reaction, the catalysts were regenerated by feeding 20 mL min^{-1} air for 1 h at 600 °C, followed by reduction in 20 mL min^{-1} H_2 flow for 2 h before the next cycle. The WHSV of propane was maintained at 5.4 h^{-1}, with a carbon balance exceeding 98%.

6.2.3 Exploring the key catalytic performance descriptors

To enhance the catalytic performance of the commercial PtGa catalyst for propane dehydrogenation, a series of promoters (La, Ce, Pr, and Nd) at varying loadings (1 wt%, 3 wt%, and 5 wt%) were introduced. Despite these systematic modifications, the discernible correlations between specific microenvironmental changes over active sites and their direct influence on catalytic performance remain unclear. Thus, this section focuses on identifying the critical performance descriptors for these modified catalysts in the context of this industrially relevant reaction (see Figure 6.10).

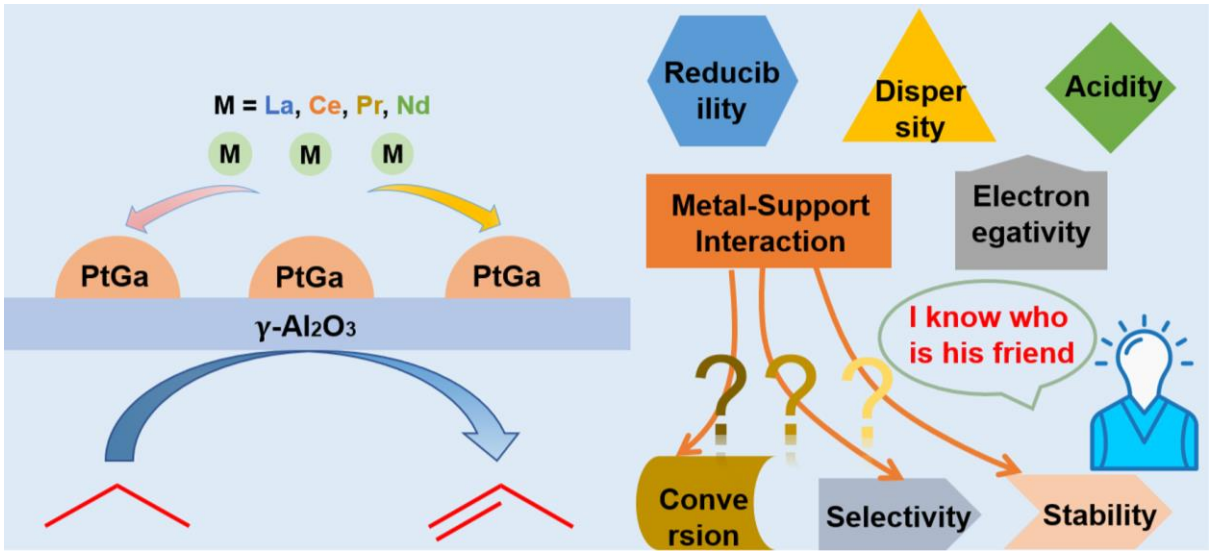

Figure 6.10 The schematic objective of this chapter.

6.2.3.1 Exploring the key propane conversion descriptors

It is widely acknowledged that Pt nanoparticles function as the primary active sites for propane dehydrogenation, with the presence of a secondary Sn or Ga promoter playing a crucial role in determining overall catalytic activity.[25,48] Therefore, variations in the microenvironment within the resulting PtGa alloy can serve as significant descriptor of conversion performance. The introduction of low promoter loading (1 wt%) substantially enhances the reducibility of intimate-contact PtGa species compared to the commercial PtGa catalyst. This is reflected in the increased hydrogen consumption observed in the first reduction peak of H_2-TPR profile (see Figure 6.4 (a)). For La, Pr, and Nd promoters, this improvement is attributed to the electron-donating effect, where the accumulation of electron density on the Pt surface facilitates electron transfer from Ga to Pt.[49] When the promoter loading is increased to 3 wt%, this electron-pushing effect is further amplified, as indicated by the lower reduction temperatures and the notably higher hydrogen consumption in the first reduction peak compared to low loadings. Consequently, the enhanced reducibility of PtGa species corresponds to improved propane conversion, as shown in Figure 6.8.

However, further increasing the promoter loading to 5 wt% does not necessarily lead to higher conversion, despite the enhanced reducibility of PtGa species (see Figure 6.8). This is likely

due to the growing difficulty in reducing other localised Ga species at high promoter loadings. As shown in Figure 6.4 (a) and (b), when La, Pr, and Nd loadings are increased from 1 wt% to 3 wt%, the reducibility of these localised Ga spices remains relatively constant, as indicated by the similar temperatures and hydrogen consumption associated with the second reduction peak in TPR profile. Yet, at higher promoter loadings (especially 5 wt% Pr and Nd), the reduction temperatures for these peaks increase significantly, reaching approximately 540 °C. According to the literature, the formation of PtGa alloy proceeds through a stepwise process: initially, the fast formation of Pt clusters at low temperatures from readily reducible isolated Pt oxides, followed by the reaction of Pt nanoparticles with isolated Ga^{3+} sites to generate alloyed PtGa particles.[9,50] Hence, the presence of a large amount of promoters, which act as a physical barriers, hinders the reduction of Ga^{3+} species, ultimately inhibiting PtGa alloy formation and lowering overall propane dehydrogenation conversion. The observed lower temperatures for the first reduction peak at high loadings could be attributed to the reduced participation of Ga species in the formation of PtGa alloys.

Although the reducibility serves as an effective conversion descriptor for catalysts modified with La, Pr, and Nd, Ce-modified catalysts exhibit distinct behaviours due to strong metal-support interactions. The reduction profiles of Ce-modified catalysts differ notably from those of the other three promoters, as shown in Figure 6.4 (a) and (b). As the Ce loading increases up to 5 wt%, both reduction peaks broaden, indicating stronger interactions between Pt, Ga, and Ce on the support. This continued intensification of interactions is likely linked to higher dispersion, which in turn contributes to enhanced propane conversion. In conclusion, while reducibility is a key conversion descriptor for this reaction, the role of metal-support interactions, particularly in Ce-modified catalysts, must not be overlooked.

6.2.3.2 Exploring the key propylene selectivity descriptors

In examining key descriptor for propylene selectivity in propane dehydrogenation, it is essential to consider the influence of major side reactions such as cracking, hydrogenolysis, olefin isomerisation, and olefin polymerisation.[35,40] These reactions predominantly occur on

acid sites, and therefore, establishing a relationship between total acid sites and propylene selectivity becomes crucial. Remarkably, a strong linear relationship was observed when comparing the total acid concentration, derived from NH_3-TPD profiles, to propylene selectivity across various modified catalysts under hydrogen conditions (Figure 6.11 (a)). This finding suggests that total acid concentration serves as a reliable indicator of propylene selectivity, where a lower acid concentration effectively enhances selectivity by mitigating side reactions catalysed by acidic centres. Similar conclusions was drawn by Mitran et al. (2009), who demonstrated a direct relationship between surface basicity (from CO_2-TPD data) and propylene selectivity at both 500 °C and 550 °C.[51] The enhanced desorption of propylene from less acidic surface, due to its electron-donating nature, likely explains this trend by preventing subsequent side reactions (as further confirmed through in-situ DRIFTS).

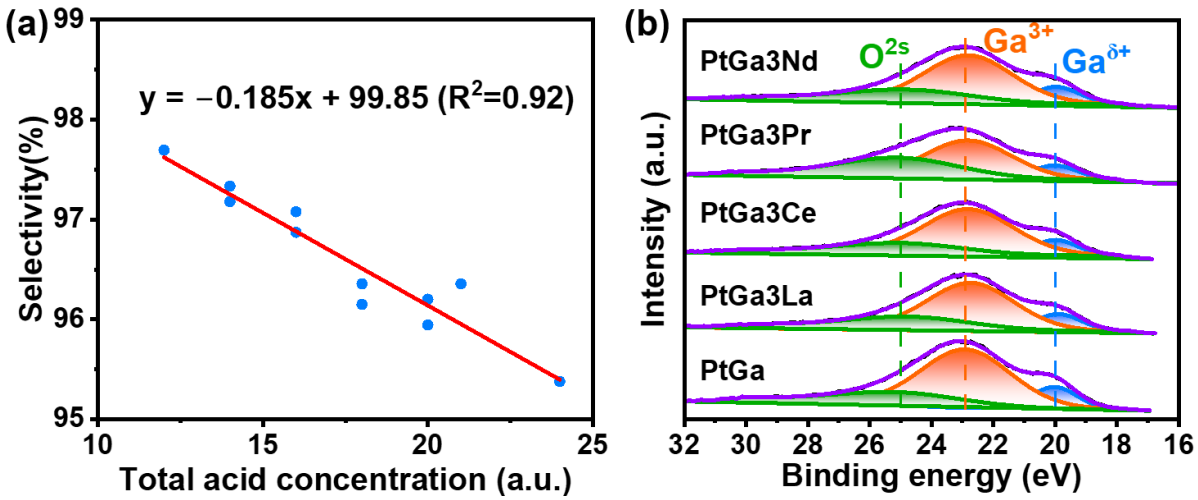

Figure 6.11 (a) Linear fitting of total acid concentration from NH_3-TPD and propylene selectivity. (b) XPS spectra of Ga 3d over different PtGa catalysts.

While total acid concentration is an effective predictor of propylene selectivity, it is also important to consider the well-known ‘‘geometric effect’’ induced by the Sn/Ga promoter. This effect can partially block surface Pt sites, resulting in smaller Pt ensembles that minimise the occurrence of undesirable side-reactions.[12,48,52] To gain deeper insight into the role of Ga in the propylene selectivity, the surface chemical properties of Ga are further investigated using XPS (Figure 6.11 (b)). The semi-quantitative analysis of XPS spectra is summarised in Table

6.4. In the Ga 3d spectra, an asymmetry peak emerges around 20.0 eV, attributed to reduced $Ga^{\delta+}$ species ($\delta < 2$) emerges, while higher binding energy peaks at around 25.0 eV and 22.8 eV correspond to O^{2-} 2s and Ga^{3+} species, respectively.[6,53,54] Although the binding energy of Ga does not significantly shift upon promoter introduction, the relative proportions of each Ga species show notable variation. With the exception of $PtGa3Ce/Al_2O_3$, which exhibits the highest Ga content, all modified catalysts display a reduction in the Ga^{3+} to reduced $Ga^{\delta+}$ ratio, with the Pr-promoted catalyst showing the lowest Ga^{3+} ratio at around 52% (see Table 6.4). This observation can be linked to the strong interactions among Pt, Ga, and Ce, which facilitate the extensive reduction of Ga^{3+} species. The consistent reduction in Ga^{3+} content across other promoted catalysts aligns with conclusions drawn from H_2-TPR analysis, indicating that promoter addition enhances the deeper reduction of Ga species. More importantly, the significantly lowest Ga^{3+} content in the Pr-modified catalyst, reflecting its reduced $Ga^{3+}/Ga^{\delta+}$ ratio, suggests that a higher proportion of Ga species are reduced, leading to more effective decoration of Pt sites. This in turn strengthens the ensemble effect, resulting in smaller Pt ensembles and explaining the superior propylene selectivity observed with Pr as the promoter compared to others. In summary, while total acid concentration remains a robust descriptor of propylene selectivity, the surface chemical properties of Ga provide additional valuable insights into selectivity trends.

Table 6.4 The semi-quantitative fitting results of XPS spectra over Ga 3d.

Catalyst	$Ga^{\delta+}$ (%)	Ga^{3+} (%)	O^{2s} (%)	$Ga^{3+}/Ga^{\delta+}$
$PtGa/Al_2O_3$	20.0 (12.6)	22.9 (66.1)	25.0 (21.3)	5.25
$PtGa3La/Al_2O_3$	19.9 (12.3)	22.7 (64.2)	24.6 (23.5)	5.22
$PtGa3Ce/Al_2O_3$	20.0 (11.2)	22.8 (67.4)	25.0 (21.5)	6.02
$PtGa3Pr/Al_2O_3$	20.0 (10.5)	22.8 (52.0)	25.0 (37.5)	4.95
$PtGa3Nd/Al_2O_3$	20.0 (12.4)	22.8 (64.0)	24.7 (23.6)	5.16

6.2.3.3 Exploring the key stability descriptors

In evaluating key stability descriptors, coke deposition is widely recognised as the principal factor leading to catalyst deactivation in propane dehydrogenation.[25,55,56] To quantify the extent

of coke accumulation, TG analysis was conducted on all spent catalysts following a 14-hours reaction under hydrogen conditions (Figure 6.12 (a)). The TG profiles reveal three distinct stages. In stage I (room temperature to 200 °C), all spent catalysts exhibit weight losses, with minimal differences between samples, which is mainly attributed to the removal of moisture and surface-adsorbed species. In stage II (200 °C to 350 °C), weight remains almost stable across all samples, with only minor variations likely due to surface dihydroxylation of the support. The most significant weight loss occurs in stage III (350 °C to 700 °C), where differences between catalysts become evident. The unmodified PtGa/Al_2O_3 catalyst shows the highest weight loss at approximately 9.5 %, whereas the PtGa3Ce/Al_2O_3 exhibits the lowest loss, around 1.0 wt% (summarised in Table 6.5). The addition of promoters substantially reduces coke formation, and this effect is more pronounced with increasing promoter loading. This reduction in coke content is partially attributed to the diminished acid concentration that accompanies promoter addition, which suppresses side reactions like cracking that contribute to coke formation. Additionally, promoter introduction affects propylene desorption, limiting deep dehydrogenation and subsequent coke formation, as later confirmed by DRIFTS analysis.

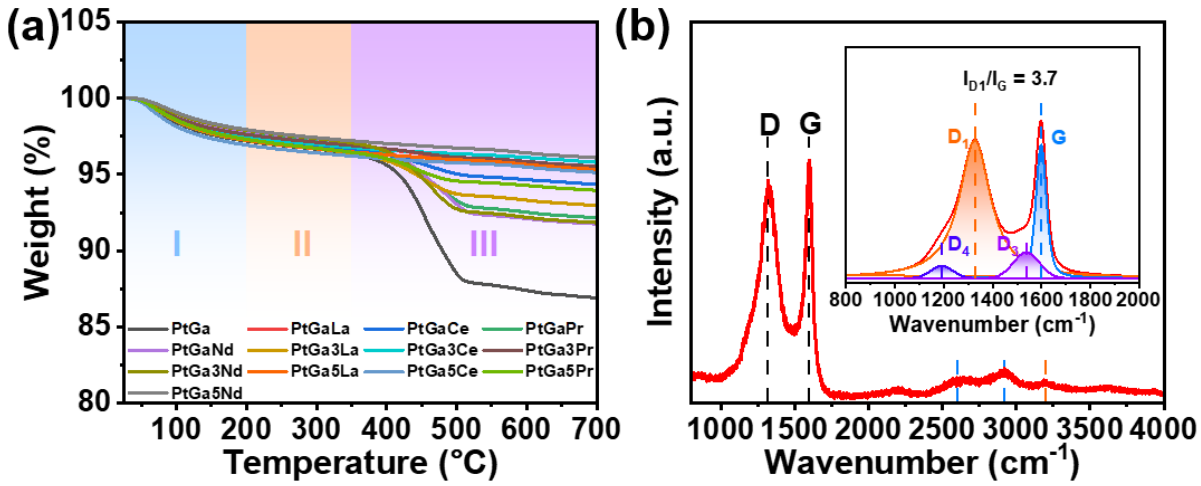

Figure 6.12 (a) TG analysis results for all spent catalysts. (b) Raman spectra of the spent PtGa/Al_2O_3 catalyst, with an enlarged inset highlighting the deconvolution peaks in the wavenumber range from 800 to 2000 cm^{-1}.

Table 6.5 Summary of coke content from TG analysis and Raman fitting results over all spent catalysts.

Catalyst	Coke content (%)	Raman band position (cm^{-1})		I_G/I_{D1}
		D_1	G	
PtGa	9.5	1327.1	1598.4	3.7
PtGaLa	1.4	1324.6	1600.4	2.9
PtGaCe	2.3	1329	1601.1	3.1
PtGaPr	4.8	1325.9	1599.1	1.9
PtGaNd	5.3	1329.2	1600.3	2.7
PtGa3La	3.4	1324.3	1599.4	2.8
PtGa3Ce	1.0	1326.2	1598.4	3.5
PtGa3Pr	1.4	1328.2	1601	3.3
PtGa3Nd	5.2	1327.1	1600.7	3.5
PtGa5La	1.2	1326.3	1598.9	3.5
PtGa5Ce	1.1	1330.9	1599.3	4.4
PtGa5Pr	2.5	1331.2	1596.2	3.9
PtGa5Nd	1.1	1330.3	1597.9	3.9

To further investigate the nature of the coke, Raman spectroscopy was performed on all spent catalysts (Figure 6.12 (b)). The Raman spectrum of the spent $PtGa/Al_2O_3$ catalyst displays 5 identical characteristic peaks at 1320, 1600, 2604, 2921, 3199 cm^{-1}. Peaks between 2600 and 3000 cm^{-1} (highlighted with blue dashed lines) are associated with the vibration modes of C-H bonds in aliphatic hydrocarbons (indicative of robust coke), while the peak at 3199 cm^{-1} (highlighted with an orange dashed line) corresponds to C-H bonds vibrations in aromatic structure (indicative of graphitic coke).[57,58] Therefore, the Raman analysis suggests that the coke contains both aliphatic and aromatic hydrocarbon components. To further understand the detailed composition of coke, the Raman peaks between 1200 and 1650 cm^{-1}, where carbonaceous material spectra overlap, were deconvoluted.[59] The deconvolution results for the $PtGa/Al_2O_3$ and other promoted catalysts are summarised in Table 6.5. Four distinct bands are identified as D_4, D_1, D_3, and G bands, following established nomenclature.[60] The G band near 1580 cm^{-1} corresponds to the ideal graphitic lattice vibration with E_{2g} symmetry, while the

D_1 band around 1350 cm^{-1} represents defect, including in-plane disorder and heteroatoms (associated with robust coke).[61,62] In contrast, the D_3 band is linked to amorphous carbon, and the D_4 band indicates a highly disordered graphitic structure.[63] In Figure 6.12 (b), the G band is observed at 1598.4 cm^{-1}, which is slightly higher than the position for a perfect graphite crystal (1575 cm^{-1}), implying that coke may be composed of graphite-like carbon species. The introduction of promoters shifts the G band to higher wavenumbers, indicating smaller crystallite size compared to the coke formed on $PtGa/Al_2O_3$ catalyst.[64] Furthermore, the addition of promoters reduces the I_G/I_{D1} ratio, suggesting a lower degree of graphitisation in the coke, particularly at low and moderate promoter loadings.[65]

Given the diverse nature of coke species, the removal of coke particularly graphitic coke typically requires higher temperatures, which accounts for the weight loss observed in stage III of the TG analysis to coke.[66] Establishing a relationship between coke content and the projected catalyst lifespan across various catalysts is essential, as illustrated in Figure 6.13 (a). A strong linear correlation is observed when fitting coke content against expected catalyst life; however, Ce-modified catalysts deviate from this trend, demonstrating a longer lifespan at similar coke levels compared to other promoted catalysts. This deviation is likely due to the distinct and robust metal-support interactions observed in Ce-modified catalysts, as evidenced by the H_2-TPR profiles shown in Figure 6.4 (a) and (b). While coke accumulation has been extensively recognised as the primary factor in propane dehydrogenation deactivation, the sintering of Pt active sites also plays a crucial role.[6,43,67] HRTEM image of spent $PtGa/Al_2O_3$ catalyst (Figure 6.14) shows a significant increase in particle size compared to the fresh catalyst, indicating considerable sintering of Pt species during prolonged high-temperature reactions. In contrast, the strong interactions between Pt, Ga, and Ce effectively mitigate Pt sintering, as the robust Pt-O-Ce bonds weaken the Pt-Pt interactions while reinforcing Pt-O bonds, thereby hindering sintering, as confirmed by both experimental and theoretical studies.[68,69] These strong interactions contribute to reduced Pt centre sintering, thus extending catalyst life, as reflected in Figure 6.13 (a). To further explore the relationship between coke

content and expected catalyst life, the effects of strong metal-support interactions were isolated by excluding Ce-modified catalysts and refitting the correlation between coke content and catalyst life (Figure 6.13 (b)). As anticipated, a more precise linear relationship emerges, confirming that coke accumulation is a key factor in catalyst stability deterioration. In summary, while coke content serves as a crucial catalyst stability descriptor, it is significantly modulated by metal-support interactions.

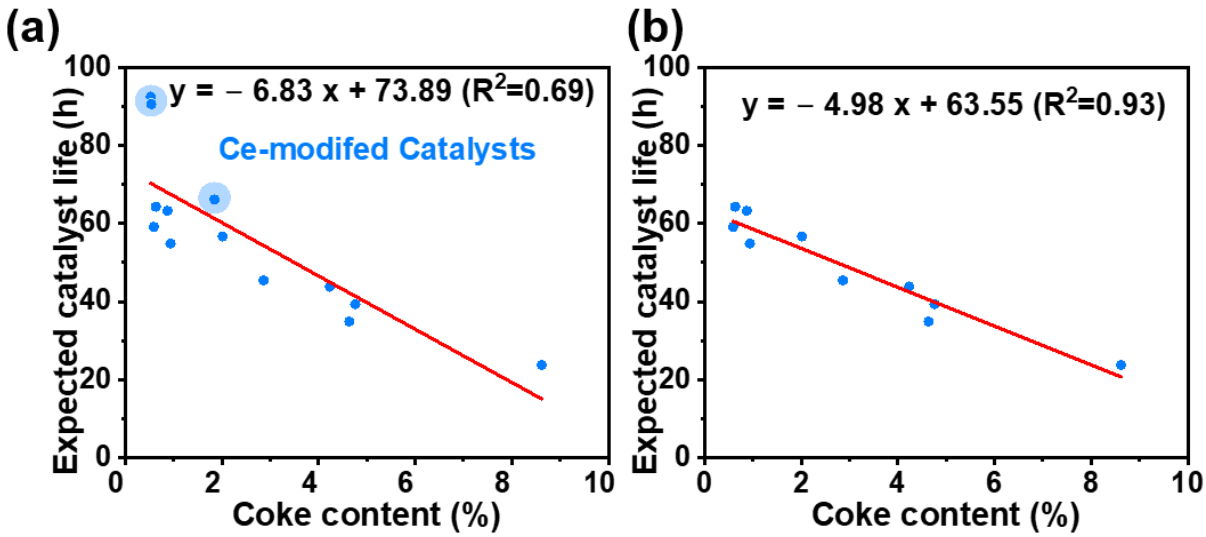

Figure 6.13 (a) Linear fitting of coke content against the expected catalyst life over all catalysts. (b) Linear fitting of coke content against the expected catalyst life over all catalysts excluding Ce-modified catalysts.

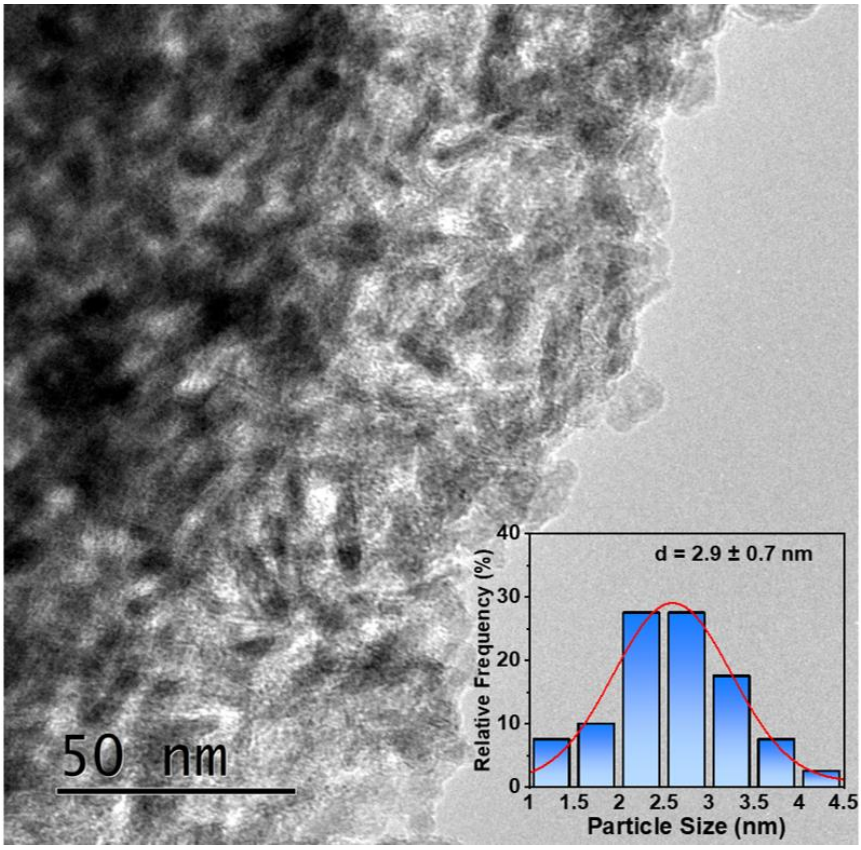

Figure 6.14 HRTEM image of spent $PtGa/Al_2O_3$ catalyst with particle size distribution.

To gain deeper insight into the coke formation mechanism, DRIFTS using propylene as a probe molecule was conducted to investigate propylene's interaction over different catalysts, as shown in Figure 6.15 (a) and (b). The peaks around 1650 cm^{-1} correspond to the C=C bond stretching vibrations in propylene, while the peaks near 1450 cm^{-1} represent aromatic ring skeletal vibrations.[70] On the $PtGa/Al_2O_3$ catalyst, the desorption peak for C=C bond stretching remains unchanged after reaching 250 °C, whereas on $PtGa3Pr/Al_2O_3$ catalyst, the corresponding peak stabilises at 150 °C. These temperature-dependent differences indicate the propylene desorption is more facile on promoted catalysts than on the commercial $PtGa/Al_2O_3$ catalyst. Additionally, as the temperature increases, the intensity of the aromatic ring skeletal vibrations intensifies, suggesting that the strong interaction between Pt and the π-electrons of propylene drives deep dehydrogenation of propylene into coke precursors.[44] The more facile desorption of propylene from Pt sites enhances propylene selectivity and reduces coke formation, leading to improved catalytic performances.

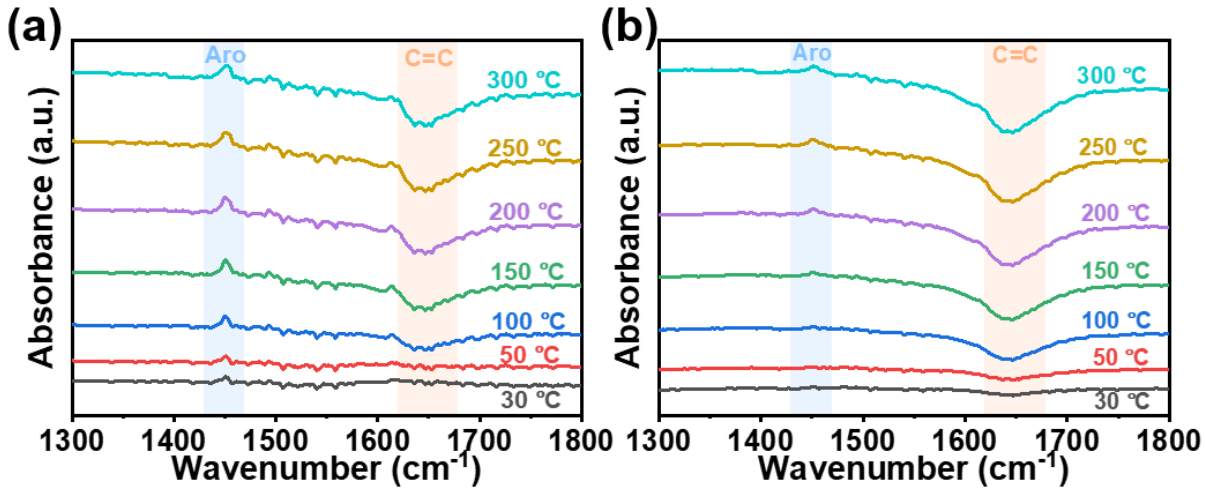

Figure 6.15 (a) DRIFTS of C_3H_6 adsorption over $PtGa/Al_2O_3$ catalyst at different temperatures. (b) DRIFTS of C_3H_6 adsorption over $PtGa3Pr/Al_2O_3$ catalyst at different temperatures.

6.3 Conclusion

In this chapter, the performance enhancement of commercial $PtGa/Al_2O_3$ catalyst for propane dehydrogenation by incorporating four distinct promoters–La, Ce, Pr, and Nd–at varying loadings (1 wt%, 3 wt%, and 5 wt%) was investigated. All modified catalysts exhibited notable improvements in conversion, selectivity, and stability compared to the unmodified $PtGa/\text{-}Al_2O_3$ catalyst. Through this study, clear structure-activity relationships linked to key performance descriptors were identified. While reducibility emerged as an effective descriptor for conversion, the role of metal-support interactions, particularly in the case of Ce-modified catalysts, was shown to be critically important. Additionally, total acid concentration proved to be a robust predictor of propylene selectivity, although the surface chemical properties of Ga also significantly influenced selectivity trends. In terms of stability, coke content was found to be a reliable descriptor; however, strong metal-support interactions were identified as a key factor in enhancing stability.

The comprehensive exploration of these performance descriptors in propane dehydrogenation not only facilitates the rational design of commercial catalysts but also provides a robust framework for deriving catalytic descriptors that could be extended to other industrial processes. This research offers valuable insights into optimising catalytic performance and

deepening the understanding of the complex interrelationships between catalyst composition, structure, and activity. Such insights are instrumental in advancing the development of more efficient catalytic systems for industrial applications.

6.4 Reference

1. Wang, H., Pan, X., Wang, Y., Ng, B.K.Y., and Tsang, S.C.E. (2025). Lanthanum-group elements promoted PtGa catalysts for propane dehydrogenation: Exploring key performance descriptors. Applied Catalysis A: General *691*, 120055. 10.1016/j.apcata.2024.120055.
2. Feng, F., Zhang, H., Chu, S., Zhang, Q., Wang, C., Wang, G., Wang, F., Bing, L., and Han, D. (2023). Recent progress on the traditional and emerging catalysts for propane dehydrogenation. Journal of Industrial and Engineering Chemistry *118*, 1-18. 10.1016/j.jiec.2022.11.001.
3. Liang, K., Zeng, X., Ma, R., Zou, G., Dang, L., and Li, S. (2023). A theoretical investigation of propane dehydrogenation on Pt and Ni-based alloys. Journal of Catalysis *428*, 115162. 10.1016/j.jcat.2023.115162.
4. Carter, J.H., Bere, T., Pitchers, J.R., Hewes, D.G., Vandegehuchte, B.D., Kiely, C.J., Taylor, S.H., and Hutchings, G.J. (2021). Direct and oxidative dehydrogenation of propane: from catalyst design to industrial application. Green Chemistry *23*, 9747-9799. 10.1039/D1GC03700E.
5. Akah, A., Williams, J., and Ghrami, M. (2019). An Overview of Light Olefins Production via Steam Enhanced Catalytic Cracking. Catalysis Surveys from Asia *23*, 265-276. 10.1007/s10563-019-09280-6.
6. Wang, P., Yao, J., Jiang, Q., Gao, X., Lin, D., Yang, H., Wu, L., Tang, Y., and Tan, L. (2022). Stabilizing the isolated Pt sites on PtGa/Al2O3 catalyst via silica coating layers for propane dehydrogenation at low temperature. Applied Catalysis B: Environmental *300*, 120731. 10.1016/j.apcatb.2021.120731.
7. Chen, S., Chang, X., Sun, G., Zhang, T., Xu, Y., Wang, Y., Pei, C., and Gong, J. (2021). Propane dehydrogenation: catalyst development, new chemistry, and emerging technologies. Chemical Society Reviews *50*, 3315-3354. 10.1039/D0CS00814A.
8. Kilmartin-Lynch, S., Saberian, M., Li, J., Roychand, R., and Zhang, G. (2021). Preliminary evaluation of the feasibility of using polypropylene fibres from COVID-19 single-use face masks to improve the mechanical properties of concrete. Journal of Cleaner Production *296*, 126460. 10.1016/j.jclepro.2021.126460.
9. Payard, P.A., Rochlitz, L., Searles, K., Foppa, L., Leuthold, B., Safonova, O.V., Comas-Vives, A., and Copéret, C. (2021). Dynamics and Site Isolation: Keys to High

Propane Dehydrogenation Performance of Silica-Supported PtGa Nanoparticles. JACS Au *1*, 1445-1458. 10.1021/jacsau.1c00212.

10. Yang, F., Zhang, J., Shi, Z., Chen, J., Wang, G., He, J., Zhao, J., Zhuo, R., and Wang, R. (2022). Advanced design and development of catalysts in propane dehydrogenation. Nanoscale *14*, 9963-9988. 10.1039/D2NR02208G.
11. Qu, Z., and Sun, Q. (2022). Advances in zeolite-supported metal catalysts for propane dehydrogenation. Inorganic Chemistry Frontiers *9*, 3095-3115. 10.1039/D2QI00653G.
12. Chen, S., Pei, C., Sun, G., Zhao, Z.-J., and Gong, J. (2020). Nanostructured Catalysts toward Efficient Propane Dehydrogenation. Accounts of Materials Research *1*, 30-40. 10.1021/accountsmr.0c00012.
13. Yang, M.-L., Zhu, Y.-A., Zhou, X.-G., Sui, Z.-J., and Chen, D. (2012). First-Principles Calculations of Propane Dehydrogenation over PtSn Catalysts. ACS Catalysis *2*, 1247-1258. 10.1021/cs300031d.
14. Li, B., Xu, Z., Jing, F., Luo, S., and Chu, W. (2017). Facile one-pot synthesized ordered mesoporous Mg-SBA-15 supported PtSn catalysts for propane dehydrogenation. Applied Catalysis A: General *533*, 17-27. 10.1016/j.apcata.2016.12.026.
15. Gao, X.-Q., Yao, Z.-H., Li, W.-C., Deng, G.-M., He, L., Si, R., Wang, J.-G., and Lu, A.-H. (2023). Calcium-Modified PtSn/Al2O3 Catalyst for Propane Dehydrogenation with High Activity and Stability. ChemCatChem *15*, e202201691. 10.1002/cctc.202201691.
16. Wu, X., Zhang, Q., Chen, L., Liu, Q., Zhang, X., Zhang, Q., Ma, L., and Wang, C. (2020). Enhanced catalytic performance of PtSn catalysts for propane dehydrogenation by a Zn-modified Mg(Al)O support. Fuel Processing Technology *198*, 106222. 10.1016/j.fuproc.2019.106222.
17. Naseri, M., Tahriri Zangeneh, F., and Taeb, A. (2019). The effect of Ce, Zn and Co on Pt-based catalysts in propane dehydrogenation. Reaction Kinetics, Mechanisms and Catalysis *126*, 477-495. 10.1007/s11144-018-1470-5.
18. Qiu, Y., Li, X., Zhang, Y., Xie, C., Zhou, S., Wang, R., Luo, S.-Z., Jing, F., and Chu, W. (2019). Various Metals (Ce, In, La, and Fe) Promoted Pt/Sn-SBA-15 as Highly Stable Catalysts for Propane Dehydrogenation. Industrial & Engineering Chemistry Research *58*, 10804-10818. 10.1021/acs.iecr.9b01413.
19. Wang, G., Lu, K., Yin, C., Meng, F., Zhang, Q., Yan, X., Bing, L., Wang, F., and Han, D. (2020). One-Step Fabrication of PtSn/γ-Al2O3 Catalysts with La Post-Modification for Propane Dehydrogenation. Catalysts *10*, 1042. 10.3390/catal10091042.
20. Vu, B.K., Song, M.B., Ahn, I.Y., Suh, Y.-W., Suh, D.J., Kim, W.-I.L., Koh, H.-L., Choi, Y.G., and Shin, E.W. (2011). Propane dehydrogenation over Pt–Sn/Rare-earth-doped Al2O3: Influence of La, Ce, or Y on the formation and stability of Pt–Sn alloys. Catalysis Today *164*, 214-220. 10.1016/j.cattod.2010.10.007.

21. He, H., Canning, G.A., Nguyen, A., Dasgupta, A., Meyer, R.J., Rioux, R.M., and Janik, M.J. (2023). Active-site isolation in intermetallics enables precise identification of elementary reaction kinetics during olefin hydrogenation. Nature Catalysis *6*, 596-605. 10.1038/s41929-023-00978-5.
22. Kaiser, S.K., Fako, E., Surin, I., Krumeich, F., Kondratenko, V.A., Kondratenko, E.V., Clark, A.H., López, N., and Pérez-Ramírez, J. (2022). Performance descriptors of nanostructured metal catalysts for acetylene hydrochlorination. Nature Nanotechnology *17*, 606-612. 10.1038/s41565-022-01105-4.
23. Wu, J., Zhao, G., Song, M., Wang, H., Wei, Y., Chen, X., Wang, G., and Yan, Z. (2022). Nanosheets-stacked Al2O3-flower anchoring Pt catalyst for intensified ethylene production from ethane dehydrogenation. Fuel *329*, 125381. 10.1016/j.fuel.2022.125381.
24. Prasetya, A.D., Rifai, M., Mujamilah, and Miyamoto, H. (2020). X-ray diffraction (XRD) profile analysis of pure ECAP-annealing Nickel samples. Journal of Physics: Conference Series *1436*, 012113. 10.1088/1742-6596/1436/1/012113.
25. Wang, T., Jiang, F., Liu, G., Zeng, L., Zhao, Z.-j., and Gong, J. (2016). Effects of Ga doping on Pt/CeO2-Al2O3 catalysts for propane dehydrogenation. AIChE Journal *62*, 4365-4376. 10.1002/aic.15339.
26. Liu, R.-l., Zhu, H.-q., Wu, Z.-w., Qin, Z.-f., Fan, W.-b., and Wang, J.-g. (2015). Aromatization of propane over Ga-modified ZSM-5 catalysts. Journal of Fuel Chemistry and Technology *43*, 961-969. 10.1016/S1872-5813(15)30027-X.
27. Price, G.L., and Kanazirev, V. (1990). Ga2O3/HZSM-5 propane aromatization catalysts: Formation of active centers via solid-state reaction. Journal of Catalysis *126*, 267-278. 10.1016/0021-9517(90)90065-R.
28. Jablonski, E.L., Castro, A.A., Scelza, O.A., and de Miguel, S.R. (1999). Effect of Ga addition to Pt/Al2O3 on the activity, selectivity and deactivation in the propane dehydrogenation. Applied Catalysis A: General *183*, 189-198. 10.1016/S0926-860X(99)00058-7.
29. de La Bretèque, P. (1974). Gallium bulletin bibliographique (La Société).
30. Filez, M., Redekop, E.A., Galvita, V.V., Poelman, H., Meledina, M., Turner, S., Van Tendeloo, G., Bell, A.T., and Marin, G.B. (2016). The role of hydrogen during Pt–Ga nanocatalyst formation. Physical Chemistry Chemical Physics *18*, 3234-3243. 10.1039/C5CP07344H.
31. Redekop, E.A., Galvita, V.V., Poelman, H., Bliznuk, V., Detavernier, C., and Marin, G.B. (2014). Delivering a Modifying Element to Metal Nanoparticles via Support: Pt–Ga Alloying during the Reduction of Pt/Mg(Al,Ga)Ox Catalysts and Its Effects on Propane Dehydrogenation. ACS Catalysis *4*, 1812-1824. 10.1021/cs500415e.

32. Zhang, T., Pei, C., Sun, G., Chen, S., Zhao, Z.-J., Sun, S., Lu, Z., Xu, Y., and Gong, J. (2022). Synergistic Mechanism of Platinum-GaOx Catalysts for Propane Dehydrogenation. Angewandte Chemie International Edition *61*, e202201453. 10.1002/anie.202201453.

33. Wang, H., Yoskamtorn, T., Zheng, J., Ho, P.-L., Ng, B., and Tsang, S.C.E. (2023). Ce-Promoted PtSn-Based Catalyst for Hydrocracking of Polyolefin Plastic Waste into High Yield of Gasoline-Range Products. ACS Catalysis *13*, 15886-15898. 10.1021/acscatal.3c03996.

34. Pitchon, V., Zins, J.F., Hilaire, L., and Maire, G. (1996). Influence of platinum on the reducibility of rare earth oxides supported on alumina. Reaction Kinetics and Catalysis Letters *59*, 203-209. 10.1007/BF02068114.

35. Yu, C., Ge, Q., Xu, H., and Li, W. (2006). Effects of Ce addition on the Pt-Sn/γ-Al2O3 catalyst for propane dehydrogenation to propylene. Applied Catalysis A: General *315*, 58-67. 10.1016/j.apcata.2006.08.038.

36. Zholobenko, V., Freitas, C., Jendrlin, M., Bazin, P., Travert, A., and Thibault-Starzyk, F. (2020). Probing the acid sites of zeolites with pyridine: Quantitative AGIR measurements of the molar absorption coefficients. Journal of Catalysis *385*, 52-60. 10.1016/j.jcat.2020.03.003.

37. Sugi, Y., Kubota, Y., Komura, K., Sugiyama, N., Hayashi, M., Kim, J.H., and Seo, G. (2006). Shape-selective alkylation and related reactions of mononuclear aromatic hydrocarbons over H-ZSM-5 zeolites modified with lanthanum and cerium oxides. Applied Catalysis A: General *299*, 157-166. 10.1016/j.apcata.2005.10.024.

38. Yoshimura, Y., Kijima, N., Hayakawa, T., Murata, K., Suzuki, K., Mizukami, F., Matano, K., Konishi, T., Oikawa, T., Saito, M., et al. (2001). Catalytic Cracking of Naphtha to Light Olefins. Catalysis Surveys from Japan *4*, 157-167. 10.1023/A:1011463606189.

39. Wakui, K., Satoh, K.-i., Sawada, G., Shiozawa, K., Matano, K.-i., Suzuki, K., Hayakawa, T., Murata, K., Yoshimura, Y., and Mizukami, F. (1999). Catalytic cracking of n-butane over rare earth-loaded HZSM-5 catalysts. Journal of The Japan Petroleum Institute *42*, 307-314. 10.1627/jpi1958.42.307.

40. Xue, M., Zhou, Y., Zhang, Y., Liu, X., Duan, Y., and Sheng, X. (2012). Effect of cerium addition on catalytic performance of PtSnNa/ZSM-5 catalyst for propane dehydrogenation. Journal of Natural Gas Chemistry *21*, 324-331. 10.1016/S1003-9953(11)60372-1.

41. Barth, R., Pitchai, R., Anderson, R.L., and Verykios, X.E. (1989). Thermal desorption-infrared study of carbon monoxide adsorption by alumina-supported platinum. Journal of Catalysis *116*, 61-70. 10.1016/0021-9517(89)90075-4.

42. Blyholder, G. (1964). Molecular Orbital View of Chemisorbed Carbon Monoxide. The Journal of Physical Chemistry *68*, 2772-2777. 10.1021/j100792a006.

43. Nakaya, Y., Hirayama, J., Yamazoe, S., Shimizu, K.-i., and Furukawa, S. (2020). Single-atom Pt in intermetallics as an ultrastable and selective catalyst for propane dehydrogenation. Nature Communications *11*, 2838. 10.1038/s41467-020-16693-9.

44. Lian, Z., Si, C., Jan, F., Zhi, S., and Li, B. (2021). Coke Deposition on Pt-Based Catalysts in Propane Direct Dehydrogenation: Kinetics, Suppression, and Elimination. ACS Catalysis *11*, 9279-9292. 10.1021/acscatal.1c00331.

45. Zhang, Y., and Aly, M. (2022). Effect of CO2 on activity and coke formation over gallium-based catalysts for propane dehydrogenation. Applied Catalysis A: General *643*, 118795. 10.1016/j.apcata.2022.118795.

46. Sun, C., Luo, J., Cao, M., Zheng, P., Li, G., Bu, J., Cao, Z., Chen, S., and Xie, X. (2018). A comparative study on different regeneration processes of Pt-Sn/γ-Al2O3 catalysts for propane dehydrogenation. Journal of Energy Chemistry *27*, 311-318. 10.1016/j.jechem.2017.09.035.

47. Alcala, R., Dean, D.P., Chavan, I., Chang, C.-W., Burnside, B., Pham, H.N., Peterson, E., Miller, J.T., and Datye, A.K. (2023). Strategies for regeneration of Pt-alloy catalysts supported on silica for propane dehydrogenation. Applied Catalysis A: General *658*, 119157. 10.1016/j.apcata.2023.119157.

48. Deng, L., Wang, J., Wu, Z., Liu, C., Qing, L., Liu, X., Xu, J., Zhou, Z., and Xu, M. (2022). Effects of second metals (M = Fe, Cu, Ga, In, Sn) on the geometric and electronic properties of platinum for the direct dehydrogenation of propane. Journal of Alloys and Compounds *909*, 164820. 10.1016/j.jallcom.2022.164820.

49. Zhang, Y., Zhou, Y., Liu, H., Wang, Y., Xu, Y., and Wu, P. (2007). Effect of La addition on catalytic performance of PtSnNa/ZSM-5 catalyst for propane dehydrogenation. Applied Catalysis A: General *333*, 202-210. 10.1016/j.apcata.2007.07.049.

50. Brack, E., Plodinec, M., Willinger, M.-G., and Copéret, C. (2023). Implications of Ga promotion and metal–oxide interface from tailored PtGa propane dehydrogenation catalysts supported on carbon. Chemical Science *14*, 12739-12746. 10.1039/D3SC04711C.

51. Mitran, G., Urda, A., Tanchoux, N., Fajula, F., and Marcu, I.-C. (2009). Propane Oxidative Dehydrogenation Over Ln–Mg–Al–O Catalysts (Ln = Ce, Sm, Dy, Yb). Catalysis Letters *131*, 250-257. 10.1007/s10562-009-0057-1.

52. Wang, Z., Chen, Y., Mao, S., Wu, K., Zhang, K., Li, Q., and Wang, Y. (2020). Chemical Insight into the Structure and Formation of Coke on PtSn Alloy during Propane Dehydrogenation. Advanced Sustainable Systems *4*, 2000092. 10.1002/adsu.202000092.

53. Kashif, M., Yuan, M., Abduallah, M., and Su, Y. (2020). Fully selective catalytic oxidation of NO to NO2 over most active Ga-PCH catalyst. Journal of Environmental Chemical Engineering *8*, 103524. 10.1016/j.jece.2019.103524.

54. Collins, S.E., Baltanás, M.A., Garcia Fierro, J.L., and Bonivardi, A.L. (2002). Gallium–Hydrogen Bond Formation on Gallium and Gallium–Palladium Silica-Supported Catalysts. Journal of Catalysis *211*, 252-264. 10.1006/jcat.2002.3734.

55. Gao, X.-Q., Li, W.-C., Qiu, B., Sheng, J., Wu, F., and Lu, A.-H. (2022). Promotion effect of sulfur impurity in alumina support on propane dehydrogenation. Journal of Energy Chemistry *70*, 332-339. 10.1016/j.jechem.2022.02.048.

56. Zhang, Y., Zhou, Y., Tang, M., Liu, X., and Duan, Y. (2012). Effect of La calcination temperature on catalytic performance of PtSnNaLa/ZSM-5 catalyst for propane dehydrogenation. Chemical Engineering Journal *181-182*, 530-537. 10.1016/j.cej.2011.11.055.

57. Korhonen, S.T., Airaksinen, S.M.K., Bañares, M.A., and Krause, A.O.I. (2007). Isobutane dehydrogenation on zirconia-, alumina-, and zirconia/alumina-supported chromia catalysts. Applied Catalysis A: General *333*, 30-41. 10.1016/j.apcata.2007.08.040.

58. Chua, Y.T., and Stair, P.C. (2003). An ultraviolet Raman spectroscopic study of coke formation in methanol to hydrocarbons conversion over zeolite H-MFI. Journal of Catalysis *213*, 39-46. 10.1016/S0021-9517(02)00026-X.

59. McGregor, J., Huang, Z., Parrott, E.P.J., Zeitler, J.A., Nguyen, K.L., Rawson, J.M., Carley, A., Hansen, T.W., Tessonnier, J.-P., Su, D.S., et al. (2010). Active coke: Carbonaceous materials as catalysts for alkane dehydrogenation. Journal of Catalysis *269*, 329-339. 10.1016/j.jcat.2009.11.016.

60. Sadezky, A., Muckenhuber, H., Grothe, H., Niessner, R., and Pöschl, U. (2005). Raman microspectroscopy of soot and related carbonaceous materials: Spectral analysis and structural information. Carbon *43*, 1731-1742. 10.1016/j.carbon.2005.02.018.

61. Liu, J., Zhao, Z., Xu, C., Duan, A., Jiang, G., Gao, J., Lin, W., and Wachs, I.E. (2008). In-situ UV-Raman study on soot combustion over TiO2 or ZrO2-supported vanadium oxide catalysts. Science in China Series B: Chemistry *51*, 551-561. 10.1007/s11426-008-0027-2.

62. Sattler, J.J.H.B., Beale, A.M., and Weckhuysen, B.M. (2013). Operando Raman spectroscopy study on the deactivation of Pt/Al2O3 and Pt–Sn/Al2O3 propane dehydrogenation catalysts. Physical Chemistry Chemical Physics *15*, 12095-12103. 10.1039/C3CP50646K.

63. Han, Z., Li, S., Jiang, F., Wang, T., Ma, X., and Gong, J. (2014). Propane dehydrogenation over Pt–Cu bimetallic catalysts: the nature of coke deposition and the role of copper. Nanoscale *6*, 10000-10008. 10.1039/C4NR02143F.

64. Dresselhaus, M.S., Dresselhaus, G., Jorio, A., Souza Filho, A.G., and Saito, R. (2002). Raman spectroscopy on isolated single wall carbon nanotubes. Carbon *40*, 2043-2061. 10.1016/S0008-6223(02)00066-0.

65. Dumont, M., Chollon, G., Dourges, M.A., Pailler, R., Bourrat, X., Naslain, R., Bruneel, J.L., and Couzi, M. (2002). Chemical, microstructural and thermal analyses of a naphthalene-derived mesophase pitch. Carbon *40*, 1475-1486. 10.1016/S0008-6223(01)00320-7.

66. Wang, H.-Z., Sun, L.-L., Sui, Z.-J., Zhu, Y.-A., Ye, G.-H., Chen, D., Zhou, X.-G., and Yuan, W.-K. (2018). Coke Formation on Pt–Sn/Al2O3 Catalyst for Propane Dehydrogenation. Industrial & Engineering Chemistry Research *57*, 8647-8654. 10.1021/acs.iecr.9b00867.

67. Srinath, N.V., Longo, A., Poelman, H., Ramachandran, R.K., Feng, J.-Y., Dendooven, J., Reyniers, M.-F., and Galvita, V.V. (2021). In Situ XAS/SAXS Study of Al2O3-Coated PtGa Catalysts for Propane Dehydrogenation. ACS Catalysis *11*, 11320-11335. 10.1021/acscatal.1c03146.

68. Ning, Q., Zhang, H., He, Y., Chen, Z., Liu, S., and Ren, J. (2019). Suppression of platinum sintering on Pt–M/ZSM-22 (M = Ce, La, and Re) catalyst for n-dodecane isomerization. New Journal of Chemistry *43*, 13967-13978. 10.1039/C9NJ03194D.

69. Ahmed, F., Alam, M.K., Muira, R., Suzuki, A., Tsuboi, H., Hatakeyama, N., Endou, A., Takaba, H., Kubo, M., and Miyamoto, A. (2010). Adsorption and dissociation of molecular hydrogen on Pt/CeO2 catalyst in the hydrogen spillover process: A quantum chemical molecular dynamics study. Applied Surface Science *256*, 7643-7652. 10.1016/j.apsusc.2010.06.021.

70. Zhang, W., Wang, H., Jiang, J., Sui, Z., Zhu, Y., Chen, D., and Zhou, X. (2020). Size Dependence of Pt Catalysts for Propane Dehydrogenation: from Atomically Dispersed to Nanoparticles. ACS Catalysis *10*, 12932-12942. 10.1021/acscatal.0c03286.

Chapter 7 Conclusion and Outlook

7.1 Conclusion

In this thesis, two pathways have been systematically developed and demonstrated, comprising four complementary approaches for the upcycling of PO plastic waste, primarily PE and PP, into valuable products. The first route focuses on an efficient and stable plastic-to-gasoline conversion system, achieved using Ce-modified PtSn catalysts. In the second route, two catalytic systems–ZSM-5 NS and W-modified Ni/ZSM-5–were optimised to upcycle plastic into propane. This process is followed by a propane dehydrogenation step using lanthanide-promoted PtGa/Al_2O_3 catalysts, ultimately yielding a two-step plastic-to-propylene process. Together, these pathways provide an integrated framework for efficient and sustainable conversion of plastic waste into valuable products, contributing to advancements in circular economy and environmental sustainability.

Plastic upcycling has only recently emerged as a highly active research area, gaining significant attention particularly since 2019, following the publication of high-quality studies in *Nature* and *Science*. These pioneering works have attracted numerous researchers to tackle the critical and urgent challenges in plastic recycling and upcycling.[1] Despite the rapid increase in the volume of research in this filed, efforts remain concentrated on three primary pathways–hydrocracking, hydrogenolysis, and metathesis–under mild reaction conditions. While many innovative catalytic materials have been developed, with detailed investigations into reaction mechanisms, parameters, there is still a persistent need for further improvements in catalytic efficiency, specifically in terms of conversion and product selectivity. Moreover, catalyst stability has often been overlooked in these upcycling systems, despite its crucial importance for long-term industrial applications. Further research must address this gap by developing more robust catalysts and thoroughly investigating the mechanisms behind catalyst deactivation. In response to these research gaps, four complementary approaches have been developed aimed at advancing the efficiency and stability of these catalytic systems, ultimately bringing them closer to practical and industrial-scale applications.

Chapter 7 Conclusion and Outlook

In this thesis, the research background and experimental methodologies were laid out in Chapters 1 and 2, providing a foundation for the exploration of catalytic hydrocracking systems. Chapter 3 introduces a series of strategies aimed at enhancing the efficiency and stability of plastic-to-gasoline hydrocracking route through the incorporation of various promoters. Initially, Sn was employed as a promoter in the Pt/SiAl system to boost dehydrogenation and hydrogenation activity. The presence of Sn led to the formation of smaller Pt ensembles and increased electron density around Pt atoms, characteristics that have made PtSn-based catalysts widely effective in propane dehydrogenation.[2,3] As anticipated, the inclusion of Sn lowered solid yield while improving selectivity towards liquid fuel products. Further optimisation was achieved with the introduction of an appropriate amount of Ce as a promoter, leading to nearly complete conversion of HDPE and a yield of gasoline-range hydrocarbons exceeding 77 wt%. Detailed characterisations revealed that the addition of Ce enhanced both the concentration and strength of BAS, thereby facilitating skeletal rearrangement and β-scission during the hydrocracking process. Moreover, the introduction of Ce promoted the reduction of Pt oxides, resulting in a higher ratio of metallic Pt, and concurrently suppressed the formation of metallic Sn, which is known to poison catalytic activity. This improvement led to enhanced dehydrogenation and hydrogenation performance. Stability tests demonstrated that Ce-modified catalysts exhibited significantly greater resistance to deactivation, which was attributed to enhanced resistance to coke formation and the ability to facilitate coke migration, likely due to stronger metal-support interactions. In summary, the introduction of Ce was shown to be a highly effective approach for improving both the catalytic efficiency and stability of plastic-to-gasoline hydrocracking system.

Chapter 4 shifts focus towards enhancing the efficiency and stability of hydrocracking by modifying the morphology of ZSM-5 zeolite. While conventional hydrocracking processes, as demonstrated in Chapter 3, typically produce liquid-range hydrocarbons, fine-turning the product distributions remains a significant challenge. Zeolites, well-known for their molecular sieving properties, offer a potential solution due to their widespread use in industrial

applications. However, conventional ZSM-5 zeolites are hindered by extended diffusion pathways within their micropores, slowing reaction kinetics, particularly for macromolecular intermediates derived from polymers, and leading to undesirable side reactions and coke formation. To address these issues, ZSM-5 NS catalysts were developed, featuring significantly reduced b-axis and c-axis dimensions compared to traditional ZSM-5, resulting in shorter diffusion pathways within both straight and sinusoidal channels. Hydrocracking of PP using ZMS-5 NS exhibited approximately 20 wt% lower solid yield compared to conventional ZSM-5, along with slightly higher propane selectivity and significantly improved catalyst stability. Given the comparable acidities of two zeolites, as confirmed by NH_3-TPD and NMR analyses, the enhanced conversion was primarily attributed to the reduced diffusion paths in ZSM-5 NS, which accelerated reaction kinetics and minimising solid formation. The improved propane selectivity in ZSM-5 NS was likely due to its narrower average pore diameter, allowing for more precise molecular sieving. The enhanced stability of ZSM-5 NS was linked to its larger specific surface area and shorter pore channels, providing more accessible acid sites while mitigating pore blockage and coke accumulation. Further optimisation was achieved through the introduction of non-noble metals (Fe, Co, Ni, Cu, and Zn) onto ZSM-5 NS, with Ni/ZSM-5 NS standing out for its superior conversion and selectivity. Mechanistic studies elucidated the crucial role of reduced diffusion pathways in both primary cracking and second cracking processes, contributing to the catalyst's superior performance. Overall, modifying the morphology of catalysts, particularly ZSM-5, proved to be an effective strategy for enhancing both the efficiency and stability of plastic-to-propane hydrocracking system.

Building on the development of an efficient and stable plastic-to-propane system through catalyst morphology modification in Chapter 4, Chapter 5 explores the impact of incorporating W into Ni/ZSM-5 system to further enhance catalytic performances. The results show that the addition of W significantly reduced the solid yield from 47 wt% to around 1 wt%. This improvement can be attributed to the enhanced dispersion of Ni nanoparticles and the introduction of additional BAS, which collectively promote dehydrogenation, hydrogenation,

and C-C bond cleavage, thereby intensifying the hydrocracking process. Furthermore, the W-modified Ni/ZSM-5 catalyst exhibited exceptional stability, maintaining similar catalytic performance even after 10 reaction cycles. In contrast, the unmodified Ni/ZSM-5 catalyst showed noticeable deactivation after just 2 cycles, with lower yield and increased coke formation. It is strongly suggested that this enhanced stability is linked to the interaction between aromatics trapped within the zeolite micropores and the distinct pore dynamics between Ni/ZSM-5 and Ni/0.25W/ZSM-5. However, further investigation is required to fully understand the underlying factors contributing to their different stability profiles. Overall, the inclusion of W has proved to be a highly effective strategy for improving both the efficiency and stability of plastic-to-propane hydrocracking system.

Extending the advancements made in plastic-to-propane hydrocracking system discussed in Chapters 4 and 5, Chapter 6 focuses on furthering the circular economy by developing efficient and stable propane dehydrogenation approach for propylene production. Four promoters–La, Ce, Pr, and Nd–were introduced at varying loadings to enhance the catalytic performances of the commercial PtGa/Al_2O_3 catalyst. All modified catalysts exhibited significant improvements in conversion, selectivity, and stability compared to the unmodified PtGa/Al_2O_3 catalyst. The enhancement in conversion can be attributed to the increased reducibility of PtGa species due to the electron-donating effect of La, Pr, and Nd promoters, as well as the strong metal-support interaction in the presence of Ce. The improvement in selectivity is primarily due to the reduced concentration and strength of acid sites, particularly LAS, which effectively mitigate side reactions catalysed by these acid centres. With regard to stability, the promoters were shown to effectively reduce the amount of coke by facilitating easier desorption of propylene, thereby inhibiting its deep dehydrogenation into coke precursors. Additionally, the strong metal-support interactions in the Ce-modified catalysts further contributed to the reduced sintering of Pt centres, thus improving overall stability. In conclusion, the introduction of La, Ce, Pr, and Nd as promoters has been demonstrated to significantly enhance both the efficiency and stability of propane dehydrogenation systems through distinct mechanisms.

7.2 Further work and outlook

While this thesis has successfully developed strategies to enhance the efficiency and stability of PO plastic upcycling systems, further research is necessary to address remaining questions. In Chapter 4, the modification of ZSM-5 zeolite morphology resulted in notable improvements in solid yield and stability. This was achieved by reducing the lengths of both the straight and sinusoidal channels within the zeolite. Although shortening these diffusion channels clearly reduced the diffusion pathways for reaction intermediates, it remains unclear which channel primarily facilitates the passage of intermediates. To better understand the reaction mechanism, additional reference materials should be synthesised, such as ZSM-5 with reduced b-axis thickness but same c-axis thickness and vice versa. This will allow for a more detailed investigation into the specific roles of each channel plays during the plastic hydrocracking reaction. Moreover, previous studies have examined the effects of progressively altering the lengths of b-axis or c-axis thickness on overall reaction kinetics and catalytic performance.[4-6] Therefore, it is should be beneficial to develop zeolites with varying micropore channel lengths to explore the relationship between channel length and catalytic performance more comprehensively.

In Chapter 5, while the introduction of W into the Ni/ZSM-5 system was shown to significantly enhance catalytic performance, particularly in terms of stability, the underlying mechanisms remain unclear. Specifically, it is uncertain whether the improved stability is linked to the interactions between trapped aromatics within the zeolite's micropores and reaction intermediates. To gain a deeper understanding of this relationship, further experiments are needed to elucidate the precise role that these trapped aromatics play in the reaction pathways and how they influence catalyst stability.

While Chapters 4 and 5 developed two efficient and stable approaches for converting plastic into high yields of propane, and Chapter 6 focused on propane dehydrogenation, this thesis has not fully explored the integration of these two reactions into a seamless process. Achieving direct plastic-to-propylene conversion requires effective coupling of both reactions. However,

the significant differences in reaction parameters–such as temperatures, pressure, gas atmosphere, reactor configurations–and the need of separation of multiple products, making this integration challenging with current laboratory capabilities. To bridge this gap, further work should focus on optimising the existing systems and incorporating advanced separation technologies to facilitate the coupling of these two reactions, ultimately enabling a continuous plastic-to-propylene conversion system.

In addition to the catalytic strategies and systems developed in this thesis, numerous other approaches have been proposed to enhance the efficiency and stability of hydrocracking for mitigating PO plastic waste. Key developments include the optimisation of the MAB and control of metal-acid proximity, as outlined in Chapter 1. While hydrocracking is a widely applied technique for the upcycling of PO plastics, the limited understanding of catalyst deactivation mechanisms continues to hinder the development of more stable catalytic systems. Further research must delve deeper into the mechanisms of deactivation in PO hydrocracking, which will facilitate the design of more stable and efficient catalysts.[1] Moreover, further explorations into the use of alternative promoters and the adjustment of particle size for C-H bond activation metals presents an opportunity to fine-tune catalytic performance.

In contrast, hydrogenolysis has also been investigated as an effective pathway for the upcycling of PO plastics, with significant efforts focused on enhancing selectivity for liquid-range hydrocarbons by minimising methane formation. Approaches include modifying the geometrical and electronic properties of active metals, adjusting the basicity of the supports, and utilising confinement effects.[7] Further advancements, such as the application of single-atom catalyst or high-entropy alloys, could offer potential improvements to hydrogenolysis systems due to their unique properties.[8,9] While metathesis has been shown to be a viable route for PO plastic upcycling, research on fully heterogeneous catalytic systems remain sparse. More studies are required to explore catalyst design and reaction mechanisms, similarly to the partially developed pathway of selective oxidation, which effectively converts PO plastics into valuable acids.[10,11]

Beyond catalyst development, advancements in reactor design and process engineering are also pivotal for achieving efficient and stable catalytic systems to address the challenges associated with PO plastic waste. The highly viscous nature of PO plastic melts during reactions imposes significant mass transfer limitations, hindering reaction kinetics.[12,13] Thus, designing reactors with enhanced internal mixing, developed catalysts with improved pore accessibility, and exploring strategies to reduce polymer melt viscosity are essential steps towards overcoming these barriers. Recent studies have demonstrated the substantial influence of mixing strategies, with reports indicating up to an 85% improvement in catalytic conversion and a 40% increase in selectivity for the hydrogenolysis of HDPE and PP.[14] Optimising power numbers to achieve effective mixing presents a promising avenue for further enhancing catalytic performance. Similarly, addressing the heat transfer limitations during the upcycling of macromolecular plastics is critical. The incorporation of solvents has also been shown to significantly enhance both heat and mass transfer; however, solvent choice can greatly impact reaction outcomes, as reported in literature.[15] Further research should prioritise addressing these heat and mass transfer challenges to advance the development of more efficient and stable catalytic systems capable of effectively managing PO plastic waste.

In conclusion, the integration of catalyst development, in-depth mechanistic studies, and optimised reactor and process design presents a promising route for creating highly efficient and stable systems to tackle the pressing issue of PO plastic waste management. These advancements are essential for driving forward sustainable plastic upcycling technologies, with the potential to substantially lower environmental impact and pave the way for a more sustainable future.

7.3 Reference

1. Wang, H., and Edman Tsang, S.C. (2024). Recent advances in polyolefin plastic waste upcycling via mild heterogeneous catalysis route from catalyst development to process design. Cell Reports Physical Science *5*, 102075. 10.1016/j.xcrp.2024.102075.

2. Chen, S., Pei, C., Sun, G., Zhao, Z.-J., and Gong, J. (2020). Nanostructured Catalysts toward Efficient Propane Dehydrogenation. Accounts of Materials Research *1*, 30-40. 10.1021/accountsmr.0c00012.
3. Chen, S., Chang, X., Sun, G., Zhang, T., Xu, Y., Wang, Y., Pei, C., and Gong, J. (2021). Propane dehydrogenation: catalyst development, new chemistry, and emerging technologies. Chemical Society Reviews *50*, 3315-3354. 10.1039/D0CS00814A.
4. Zhang, J., Zhou, A., Gawande, K., Li, G., Shang, S., Dai, C., Fan, W., Han, Y., Song, C., Ren, L., et al. (2023). b-Axis-Oriented ZSM-5 Nanosheets for Efficient Alkylation of Benzene with Methanol: Synergy of Acid Sites and Diffusion. ACS Catalysis *13*, 3794-3805. 10.1021/acscatal.2c06384.
5. Zhang, J., Ren, L., Zhou, A., Li, W., Shang, S., Liu, Y., Jia, Z., Liu, W., Zhang, A., Guo, X., and Song, C. (2022). Tailored Synthesis of ZSM-5 Nanosheets with Controllable b-Axis Thickness and Aspect Ratio: Strategy and Growth Mechanism. Chemistry of Materials *34*, 3217-3226. 10.1021/acs.chemmater.2c00001.
6. Liu, X., Shi, J., Yang, G., Zhou, J., Wang, C., Teng, J., Wang, Y., and Xie, Z. (2021). A diffusion anisotropy descriptor links morphology effects of H-ZSM-5 zeolites to their catalytic cracking performance. Communications Chemistry *4*, 107. 10.1038/s42004-021-00543-w.
7. Sun, J., Dong, J., Gao, L., Zhao, Y.-Q., Moon, H., and Scott, S.L. (2024). Catalytic Upcycling of Polyolefins. Chemical Reviews *124*, 9457-9579. 10.1021/acs.chemrev.3c00943.
8. George, E.P., Raabe, D., and Ritchie, R.O. (2019). High-entropy alloys. Nature Reviews Materials *4*, 515-534. 10.1038/s41578-019-0121-4.
9. Zhang, H., Liu, G., Shi, L., and Ye, J. (2018). Single-Atom Catalysts: Emerging Multifunctional Materials in Heterogeneous Catalysis. Advanced Energy Materials *8*, 1701343. 10.1002/aenm.201701343.
10. Wang, K., Jia, R., Cheng, P., Shi, L., Wang, X., and Huang, L. (2023). Highly Selective Catalytic Oxi-upcycling of Polyethylene to Aliphatic Dicarboxylic Acid under a Mild Hydrogen-Free Process. Angewandte Chemie International Edition *62*, e202301340. 10.1002/anie.202301340.
11. Zhang, Q., He, J., Wei, X., Shen, C., Ye, P., An, W., Liu, X., Li, H., Xu, S., Su, Z., and Wang, Y.-Z. (2024). Oxidative Upcycling of Polyethylene to Long Chain Diacid over Co-MCM-41 Catalyst. Angewandte Chemie International Edition *63*, e202407510. 10.1002/anie.202407510.
12. Rejman, S., Vollmer, I., Werny, M.J., Vogt, E.T.C., Meirer, F., and Weckhuysen, B.M. (2023). Transport limitations in polyolefin cracking at the single catalyst particle level. Chemical Science *14*, 10068-10080. 10.1039/D3SC03229A.

13. Wang, H., Huang, S., and Tsang, S.C.E. (2025). Heterogeneous catalysis strategies for polyolefin plastic upcycling: co-reactant-assisted and direct transformation under mild conditions. Chemical Communications. 10.1039/D4CC05471G.
14. Jaydev, S.D., Martín, A.J., Garcia, D., Chikri, K., and Pérez-Ramírez, J. (2024). Assessment of transport phenomena in catalyst effectiveness for chemical polyolefin recycling. Nature Chemical Engineering. 10.1038/s44286-024-00108-3.
15. Jia, C., Xie, S., Zhang, W., Intan, N.N., Sampath, J., Pfaendtner, J., and Lin, H. (2021). Deconstruction of high-density polyethylene into liquid hydrocarbon fuels and lubricants by hydrogenolysis over Ru catalyst. Chem Catalysis *1*, 437-455. 10.1016/j.checat.2021.04.002.